

HIROSHIMA UNIVERSITY

DOCTORAL THESIS

**An experimental study on the upper bounds
of Bell's inequality violations and quantum
contextuality**

Author:
Kengo MATSUYAMA

Supervisor:
Holger F. HOFMANN

*A thesis submitted in fulfillment of the requirements
for the degree of Doctor of Science*

in the

**Quantum Frontier Group
Graduate school of Advanced Science and Engineering**

February 19, 2024

Declaration of Authorship

I, Kengo MATSUYAMA, declare that this thesis titled, “An experimental study on the upper bounds of Bell’s inequality violations and quantum contextuality” and the work presented in it are my own. I confirm that:

- This work was done wholly or mainly while in candidature for a research degree at this University.
- Where any part of this thesis has previously been submitted for a degree or any other qualification at this University or any other institution, this has been clearly stated.
- Where I have consulted the published work of others, this is always clearly attributed.
- Where I have quoted from the work of others, the source is always given. With the exception of such quotations, this thesis is entirely my own work.
- I have acknowledged all main sources of help.

Signed:

Date:

HIROSHIMA UNIVERSITY

Abstract

Graduate school of Advanced Science and Engineering

Doctor of Science

An experimental study on the upper bounds of Bell's inequality violations and quantum contextuality

by Kengo MATSUYAMA

In this thesis, experimental evidence is used to explore the upper limits of a CHSH-type Bell's inequality violation and the quantum contextuality by an operationally optimized input state. In the first experiment, the question of whether the upper limit of the CHSH-type Bell inequality violation obtained by experiment is consistent with the theoretical Cirelson bound is clarified by introducing a POVM measurement of polarization and varying the ratio of the measurement errors for two complementary polarization physical properties. A measurement outcome with an extremely low number of events appears in the joint probability distribution that includes the complementary polarization physical properties. Careful analysis of the measurement errors associated with this measurement outcome shows that any quantum correlation that exceeds the Cirelson bound requires negative measurement probabilities. Since it is impossible to obtain a negative probability in a real experiment, it is clear that the upper limit of Bell's inequality breaking that can be achieved in practice is the Cirelson bound, and that the Cirelson bound is limited by the uncertainty limit of the measurement. In the second experiment, we investigate whether quantum states exhibiting quantum correlations such that quantum contextuality appears in the experimental data can be realized operationally. The possibility of preparing a quantum state preparation such that it shows quantum contextuality based entirely on experimentally observed characteristics is investigated. An input state can be prepared by imposing certain deterministic conditions on quantum states showing non-local correlations that the degree of entanglement variable polarization entangled photon pairs source. The two experimental parameters of the experimental setup are optimized based on actual measurements. We refer to this method of optimization as adaptive input state control. Adaptive input state control returns parameter values that automatically account for non-trivial imperfections that the experimental setup may contain. Such a method not only enables an operational verification of quantum contextuality, but can also make significant contributions to the solution of recent technical problems in quantum information technologies by providing a method of optimizing the quantum state input generated in the presence of a number of unspecified error sources.

Acknowledgements

I would like to express my deepest gratitude to Prof. Hofmann and Prof. Inuma. I learned a great deal about the spirit and skills necessary to be a physics researcher from Prof. Hofmann, as well as his attitude toward research. Prof. Inuma helped me in a wide range of aspects of experimental research, including financial support and discussions, etc. By sharing their experiences with me, I was able to learn the qualities necessary for a researcher. I would like to express my gratitude to all the people who have helped me in various situations outside of research, including the university staff, friends (especially N. Aramoto, K. Ueda, Goddess A. Tomoishi, Princess M. Yamaguchi, T. Yamaguchi, Queen H. Murakami, N. Murakami, M. Furusawa, K. Kobayakawa, T. Kobayakawa, Y. Miyagami, S. Miyagami), and family. It is because of the support of so many people that I have been able to do my best so far. Thank you very much. My study was supported by JST SPRING, Grant Number JPMJSP2132.

Contents

Declaration of Authorship	iii
Abstract	v
Acknowledgements	vii
1 Introduction	1
1.1 Introduction	1
2 Upper bound of the Bell's inequality and adaptive input state control of a contextual quantum state	5
2.1 Bell correlations investigated by joint measurements	5
2.1.1 Joint measurement of complementary polarization physical properties	5
2.1.2 Observation of the Bell correlations using joint measurements	7
2.2 Operational preparation of an input state	8
2.2.1 Consistency paradox using deterministic conditions	9
2.2.2 Adaptive input state control for Frauchiger and Renner's thought experiment	10
3 Preparation for the experiment	13
3.1 Preparation for the first experiment	13
3.1.1 Experimental setup	13
3.1.2 Performance of the setup and the interferometer visibility	14
3.2 Preparation for the second experiment	17
3.2.1 Experimental setup	17
3.2.2 Performance of the setup and the trade off relation between a local polarization and entanglement witness	17
4 Experimental results for the upper bound of the Bell's inequality violation	25
4.1 Measurement visibility of the complementary polarizations	25
4.2 Joint statistical distributions of the complementary polarizations	29
4.3 Local and Non-local correlations of the maximally entangled photons	32
5 Experimental results for the quantum state preparation by adaptive input state control	35
5.1 Optimization of ϕ_M	35
5.2 Optimization of ϕ_S	37
5.3 Probabilities in several measurement context	38
6 Discussion and consideration	43
6.1 On the joint probability distributions resulting in Bell's inequality violation observed from the joint measurements	43
6.1.1 Relation between the joint statistical distributions and the measurement visibilities	43

6.1.2	Flipping probability of the four polarization physical properties . . .	45
6.1.3	Relation between the flipping probability of B and the joint probability distribution	45
6.1.4	Reconstruction of the intrinsic joint probabilities in one system . . .	49
6.1.5	Reconstruction of the intrinsic joint probabilities in both systems . .	53
6.1.6	Estimation of the initial state	54
6.1.7	Evaluation of the properties of the estimated quantum state	59
6.1.8	Relation between the measurement uncertainties and the Bell correlations	60
6.2	Adaptive and operation input state control using different measurement contexts	64
6.2.1	Estimation of the input state and the evaluation of its properties . . .	65
6.2.2	Relation between $P(0;a), P(a;0)$ and the correlations	67
6.2.3	Relation between $P(1;1)$ and the correlations	68
6.2.4	Relation between $P(a;a)$ and the correlations	69
6.2.5	Contrast of the four contextual probabilities	70
6.2.6	Bell correlations in the consistency paradox	72
7	Conclusion	75
7.1	Experiment to explore the cause of the upper bound of Bell's inequality . .	75
7.2	Experiment to demonstrate the adaptive input state control	76
A	EPR paradox	79
B	Cirel'son bound	81
C	PR-box	85
D	POVM measurement	89
E	Bit flip model	93
F	Three-box paradox	95
G	GHZ paradox	97
H	Hardy's paradox	99
I	Bloch sphere	103
J	Verification of the Bell's inequality violation	107
K	Derivation of Bell's inequalities	109
K.1	Original Bell's inequality	109
K.2	CHSH-type Bell's inequality	110
L	Semiconductor laser	111
L.1	Inverted distribution	111
L.2	Optical resonator	113
L.3	Semiconductor laser	114
M	Single mode fiber	117

N Polarization beam splitter	123
N.1 Boundary conditions and relation between electric and magnetic fields . . .	123
N.2 Fresnel equations and Brewster angle	124
N.3 Reflectance and Transmittance of the light intensity	126
N.4 Characteristic matrix	128
N.5 Structure of a PBS	132
O Wave Plate	135
P Dichroic mirror	141
P.1 Symmetric multi-layer system	141
P.2 Transmittance in a reflection band and transmission band	142
Q Glan-Taylor prism	143
R Band pass filter	145
S Single photon counting module	149
T Spontaneous parametric down conversion	151
T.1 Crystals which can cause nonlinear optical effect	151
T.2 Electromagnetic waves propagating in nonlinear crystals	152
U Phase matching	155
V Gaussian beam	159
W Construction of polarization entangled photon paris source	163
W.1 Determination of the dimensions of the entire experimental setup	163
W.2 Shaping of the spatial modes of the light emitted from the optical fiber . .	163
W.3 Fixing the position of the optical components and checking the photon pair generation	166
W.4 Fine tuning of the interferometer	167
X Hanbury Brown-Twiss experiment	169
X.1 Ratio of single photon with weak coherent light	169
X.2 Ratio of single photon with down-converted photons	170
Y Technical know-how for the optical experiment	173
Y.1 Adjustment of an optical axis	173
Y.2 Calibration of a HWP	174
Y.3 Adjustment of a collimation lens	175
Y.4 Measurement of polarization physical properties	175
Z Data analysis and rest	177
Z.1 Errors that experimental data includes	177
Z.1.1 Residuals, deviations and errors	177
Z.1.2 Propagation of errors	178
Z.2 Poisson distribution	179
Z.3 Frequently used functions and knowledge of Mathematica to analysis the experimental data	180
Z.3.1 Analytical calculations	181
Z.3.2 Algebraic calculations	184

Z.3.3	Illustration of tables and graphs	185
Z.3.4	Useful websites, applications and tools	187
Reference		189

List of Figures

2.1	Schematics of a joint measurement of complementary polarization physical properties. $\hat{\rho}$ is an initial state, \hat{E}_m is POVM element, \hat{X} and \hat{Y} are complementary physical properties whose values are $x, y \in \{0, 1\}$, $m = 1, 2, 3, 4$ are the labels to distinguish the difference measurement outcomes, $(\pm 1, \pm 1)$ means (x, y)	6
2.2	Joint statistical distributions that can be evaluated in an experiment to validate Bell's inequality by introducing a joint measurement. The yellow squares are the results of the measurement where $b = +2$ and the green squares are the results of the measurement where $b = -2$. The position of the physical property values correspond to $P(x_A, y_A; x'_B, y'_B)$, where the sign means ± 1 , the ";" means that the measurement systems are non-local.	8
3.1	Setup for the first experiment. It consists of three parts: the part for generating polarization entanglement photon pairs (surrounded by dotted lines), the part for measurement (surrounded by red and blue), and the part for signal processing.	14
3.2	Electrical pulses after DISCRIMINATOR. (a) Pulse waveform immediately after the SPCM1 signal and Logic Level Adapter passes through the DISCRIMINATOR (b) Pulse waveform immediately after the SPCM2 signal and Logic Level Adapter passes through the DISCRIMINATOR.	15
3.3	Delay curves evaluated before the first experiment. The positive area of Delay Time on the horizontal axis means multiplying the delay to the pulses from SPCM1, while the negative area means multiplying the delay to the pulses from SPCM2. The value on the vertical axis is the counting rate.	16
3.4	Setup for the second experiment. It also consists of three parts: the part for generating polarization entanglement photon pairs (surrounded by dotted lines), the part for measurement (surrounded by red and blue), and the part for signal processing. Compared to the setup in the first experiment shown in FIG. 3.1, fewer optical components realizes higher stability.	18
3.5	Electrical pulses after DISCRIMINATOR. (a) Pulse waveform immediately after the SPCM1 signal and Logic Level Adapter passes through the DISCRIMINATOR (b) Pulse waveform immediately after the SPCM2 signal and Logic Level Adapter passes through the DISCRIMINATOR.	19
3.6	Delay curves evaluated before the second experiment. The positive area of Delay Time on the horizontal axis means multiplying the delay to the pulses from SPCM1, while the negative area means multiplying the delay to the pulses from SPCM2. The value on the vertical axis is the counting rate.	20

3.7	Degree of local polarization in HV basis against experimental parameter ϕ_S . The local polarization is given by Eq. 3.9. Blue dots show $P(x_A = +; x_B = +) + P(x_A = +; x_B = -) - P(x_A = -; x_B = +) - P(x_A = -; x_B = -)$, yellow dots show $P(x_A = +; x_B = +) - P(x_A = +; x_B = -) + P(x_A = -; x_B = +) - P(x_A = -; x_B = -)$ and green dots show their average. This result indicates that system A and B are symmetric.	22
3.8	Trade-off relation between C_X and W_E in all range of ϕ_S . X is a polarization physical property composed of HV polarization, V_X shows the interferometer visibility given by Eq. (3.1), C_X is the local polarization given by Eq. (3.9) and W_E is the entanglement witness represented as Eq. (6.62).	23
4.1	On the Bloch sphere (see Appendix I), two complementary polarization physical properties that are (a) jointly measured in system A, and (b) measured in system B. Red arrows are POVM elements selected in system A. The blue arrows indicate the POVM elements selected in system B. θ_J is the joint measurement parameter, and in this experiment the parameter values are always the same for systems A and B. $x = +1$ corresponds to H polarization, $x = -1$ to V polarization, $y = +1$ to P polarization, and $y = -1$ to M polarization. x' and y' are polarization physical properties that lie exactly in between them.	26
4.2	Measurement visibilities of (a) X_A and Y_A , (b) X'_B and Y'_B against the joint measurement parameter, θ_J . At $\theta_J = 0^\circ$, the X_A and the X'_B are measured precisely, at $\theta_J = 90^\circ$, the Y_A and the Y'_B are measured precisely, and at $\theta_J = 45^\circ$, all four polarization physical properties are measured with the same accuracy.	29
4.3	Trade-off relation between the measurement visibilities of complementary polarization (a) between X_A and Y_A ; (b) between X'_B and Y'_B . The blue dots represent experimental values and the red curve represents an arc whose radius is 1.	30
4.4	Joint statistical distributions obtained in the experiment to investigate Bell's inequality with the joint measurements. All counts are measured for 10 seconds. Orange represents outcomes of $b = +2$ and green represents ones of $b = -2$. The 3D plots and the positions of the outcomes correspond, and the arrangement of the sixteen measurement outcomes follows the joint statistical distribution presented in FIG. 2.2.	31
4.5	Four non-local correlations against the joint measurement parameter θ_J	32
4.6	Local correlations against the joint measurement parameter. Blue dots show the local correlation of the complementary polarizations in system A, yellow dots show the one in system B.	33
5.1	Variation of (0;0) and (0;1) and optimal ϕ_M results when $\phi_S = 22.5^\circ$ is fixed. The blue and yellow data points are the counts per 10[s] of (0;0) and (0;1), respectively, and the blue and yellow lines are the results of linear fitting to the respective data points; since the resolution of the HWP2 setting angle for setting ϕ_M is $\approx 0.2^\circ$, the optimal ϕ_M value is shown to the first decimal place.	36
5.2	(a) Values of $P(1;1)$ for nine ϕ_S . (b) Fitting results with quadratic functions for five points near $\phi_S = 22.5^\circ$	37
5.3	Probability measured using $\{0,1\}$ -basis in systems A and B. $\phi_S = 0^\circ$ represents the product state and $\phi_S = 45^\circ$ the maximum entangled state.	38

5.4	Probability measured using $\{0, 1\}$ -basis in one system, using $\{a, b\}$ -basis in the other system. $\phi_S = 0^\circ$ represents the product state and $\phi_S = 45^\circ$ the maximum entangled state.	39
5.5	(a) Values of $P(1; 1)$ for nine ϕ_S . (b) Fitting results with quadratic functions for five points near $\phi_S = 22.5^\circ$	40
6.1	Value of flipping probability of B against the joint measurement parameter θ_J	48
6.2	$(\mp, \pm; \pm, \pm), (\pm, \pm; \pm, \mp)$ for the flipping probability of B for each of the four measurements. The values on the horizontal axis are obtained by substituting Eq. (6.1) and Eq. (6.2) into Eq. (6.14) and Eq. (6.16), while the probabilities on the vertical axis are the joint probabilities derived from FIG. 4.4. Different $P_{Bflip}(m)$ corresponds to different θ_J . The fitting results were performed for all data points.	50
6.3	Reconstructed joint probability distribution by eliminating the measurement uncertainties from system A. Note that these probability distributions still have the measurement uncertainties in system B.	52
6.4	Reconstructed joint probability distribution by eliminating the measurement uncertainties from system A and B.	55
6.5	Experimental and predicted values of local correlations of complementary physical properties. The specific values of the parameters in Eq. (6.51) and Eq. (6.52) are $\alpha = 0.98$, $\gamma = 0.2^\circ$, and $\phi = 5^\circ$	58
6.6	Experimental and predicted values of the four Bell correlations. The values of the parameters to be substituted into Eqs. (6.54)-(6.57) are $\alpha = 0.98$, $\gamma = 0.2^\circ$, and $\phi = 5^\circ$	58
6.7	Predictions of the four Bell correlations derived using Eqs. (6.42), (6.63)-(6.66), and Eqs.(6.47)-(6.50), and experimental values derived from the results in FIG. 6.3. As described in the subsec. 6.1.6, the parameter values are set such that $\alpha = 0.98$, $\gamma = 0.2^\circ$, and $\phi = 5^\circ$	61
6.8	The predicted values of the four Bell correlations derived using Eq. (6.42), Eqs. (6.63)-(6.70), and the experimental values derived from the joint probability distribution in FIG. 6.4. As described in the subsec. 6.1.6, the parameter values are set such that $\alpha = 0.98$, $\gamma = 0.2^\circ$, and $\phi = 5^\circ$	62
6.9	Mean values of B with and without measurement uncertainty. $\langle B \rangle_1$ is the average value obtained directly from FIG. 4.4, $\langle B \rangle_2$ is the average value obtained from (6.3), and $\langle B \rangle_3$ is the average value obtained from FIG. 6.4. The values of the parameters used to derive the predictions are $\alpha = 0.98$, $\gamma = 0.2^\circ$, and $\phi = 5^\circ$	63
6.10	Experimental and predicted values for C_X , V_X , and W_E . The horizontal axis is ϕ_S [deg], which represents the degree of entanglement, with $\phi_S = 0^\circ$ representing the product state and $\phi_S = 45^\circ$ the end state. The predictions have some range because they reflect the range of statistical errors that Eqs. (6.73)-(6.75) have.	66
6.11	Comparison of experimental and predicted values for $P(0; a) + P(a; 0)$. "Exp" is derived from the raw data shown in TAB. 5.2. "Predi" is the range of values that could change due to statistical errors when Eqs. (6.73)-(6.75) are substituted into Eq. (6.80).	68
6.12	Comparison of experimental and predicted values of $P(1; 1)$. The "Exp" is identical to that shown in FIG. 5.5, and the "Predi" is the value described by Eq. (6.83), with possible regions of variation in the range of (0.969 ± 0.013) and (0.935 ± 0.011)	69

6.13	Comparison of experimental and predicted values of $P(a; a)$. "Exp" represents the experimental value of $P(a; a)$ derived from TAB. 5.2, and "Predi" represents the predicted value of $P(a; a)$ that can be taken when Eqs. (6.73)-(6.75) are substituted into Eq. (6.86).	70
6.14	Comparison of experimental and predicted values of the contrast function. The horizontal axis is ϕ_S , which represents the degree of entanglement, and the vertical axis is the contrast function defined by Eq. (6.87).	71
6.15	Experimental and predicted values of Bell correlation in the consistency paradox; "Exp" can be evaluated from the counts in TAB. 5.2; "Predi" represents the predicted values, substituting $C_X = 0.968 \cos 2\phi_S, V_X = 0.968, V_Y = -0.935 \sin 2\phi_S$ in Eqs. (6.99)-(6.102).	73
6.16	EPR correlation whose definition is given by Eq. (6.103)." Exp" is the experimental value evaluated using Eqs. (6.91)-(6.94), and "Predi" is the prediction obtained by substituting $C_X = 0.968 \cos 2\phi_S, V_X = 0.968, V_Y = -0.935 \sin 2\phi_S$ in Eqs. (6.99)-(6.102).	74
B.1	Relation among the measured four polarization physical properties.	82
B.2	Result of plotting θ_0 against Eq. (B.10). The blue curve represents the result of Eq. (B.10), the red line represents ± 2	83
C.1	Four kind of joint probability distribution in Bell's inequality experiment, which can achieve EPR correlation 4. (a) \hat{X}_A measured in system A and \hat{X}'_B measured in system B (b) \hat{X}_A measured in system A and \hat{Y}'_B measured in system B (c) \hat{Y}_A measured in system A and \hat{X}'_B measured in system B (d) \hat{Y}_A measured in system A and \hat{Y}'_B measured in system B. These joint probability distributions satisfy the condition of the relativistic causality shown in FIG. C.1.	86
C.2	Superquantum correlation function Popescu and Rhorlich proposed in their paper. θ is an angle between two spin vectors, one is measured in system A and the other is measured in system B. The vertical axis shows the value of correlation of the two spin physical properties.	87
E.1	Relation between two complementary polarization physical property in Bloch sphere. The x, y are the value of \hat{X}, \hat{Y} . The θ_j is the joint measurement parameter. Arrows labeled with $i (i = 1, 2, 3, 4)$ are the four measurement outcomes in the joint measurements explained in Subsec. 2.1.1.	93
E.2	Change in the statistical distribution of the polarization physical property \hat{X} due to performing a measurement with errors, where N_{int} is the number of counts that would have been obtained by a precise measurement and N is the number of counts obtained by a measurement with errors.	94
H.1	Thought experiment of Hardy's paradox. The $ e^\pm\rangle$ is the quantum state showing the existence of the electron and positron, the $ u^\pm\rangle$ and $ v^\pm\rangle$ are the path physical properties, the $ D^\pm\rangle$ and $ C^\pm\rangle$ means the detection of the particles.	100
I.1	Bloch sphere and a quantum state. The red arrow shows the expectation value of $\hat{\sigma}_Z$, the blue arrow is the expectation value of $\hat{\sigma}_X$ and the green arrow is corresponding to the one of $\hat{\sigma}_Y$. A quantum state described by $\hat{\rho}$ is corresponding to one arrow whose starting point is the origin in the Bloch sphere. This black arrow is called Bloch vector.	104

J.1	Experimental results of statistical distributions obtained in an experiment to verify Bell's inequality using precision measurements. All values were obtained from a 10-second measurement. (a) \hat{X}_A was measured in system A and \hat{X}'_B in system B. (b) \hat{X}_A was measured in system A and \hat{Y}'_B in system B. (c) \hat{Y}_A was measured in system A and \hat{X}'_B in system B. (d) \hat{Y}_A was measured in system A and \hat{Y}'_B in system B.	108
L.1	Energy level diagram for inverted distribution. When electrons are excited from the E_1 level to the E_3 level, some fall directly to the E_1 level, but some relax to the E_2 level; if a material is used that stays in the E_2 level for a long time, the number of electrons in E_2 is larger than the number in E_1 , and an inverted distribution is realized between E_1 and E_2	112
L.2	Principle of laser oscillation. An inverted distribution medium of length L_{sub} and gain constant the G is placed in an optical resonator. The R is the reflectance of the mirror and the L_{cav} is the length of the optical resonator. Red arrows show laser light.	113
L.3	Energy band diagram of a double heterostructure, where A represents the n-type clad layer, B represents the active layer, and C represents the p-type clad layer. n-type clad layers contain many electrons, while p-type clad layers contain many holes. The band-junction energy of the active layer is smaller than that of the p- and n-type semiconductors, allowing electrons and holes to accumulate more efficiently. The transitions of electrons produced in this active layer generate photons.	114
M.1	Schematic of an optical fiber and the refractive index distribution. n_1 is the refractive index of the core with radius a , n_2 is the refractive index of the cladding with radius b . n_0 is the refractive index of air, which is approximately equal to that of a vacuum.	118
N.1	A virtual micro-rectangle on the boundary surface of a medium with different refractive indices, where dh is the micro-height and dl is the micro-width.	123
N.2	The relation among incident, reflected, and transmitted light at the interface between two media with different refractive indices. In this figure, the electric field is assumed to oscillate perpendicular to the incident plane. The direction of oscillation of the magnetic field perpendicular to the electric field is parallel to the plane of incidence, where θ_i , θ_r , and θ_t are the angle of incidence, reflection, and refraction, respectively.	125
N.3	An electromagnetic wave with cross-section area S incident on a medium with refractive index n_1 into a medium with refractive index n_2 . the area at the boundary between the two media is S' . θ_i is the angle of incidence and θ_t is the angle of refraction. S'' is the cross-section area of transmitted light.	127

N.4 A situation in which an electromagnetic wave is incident perpendicularly from a medium with a refractive index of n_0 to a thin film with a refractive index of n and reaches a substrate with a refractive index of n_m . Vector of $+$ and $-$ define two directions. a and b are labels of boundary surfaces. Y is optical admittance, d is the width of thin film. Arrows near the electric field indicate the propagation direction of electromagnetic wave, not the direction of oscillation of the electric field. The direction of oscillation of the magnetic field is perpendicular to the direction of electromagnetic oscillation. 129

N.5 Schematic diagram of the concept of expansion into a multi-layer membrane. First, the incident light enters the thin film of the characteristic matrix M_1 , then interacts with the thin film of the characteristic matrix M_2 . Finally, some of the light reaches the substrate with a gradient admittance of η_m 131

N.6 Schematic diagram of the structure of PBS. Dielectric multi-layers and glue are applied to the oblique side of the right-angle prism. The p-polarized component of the incident light is transmitted and the s-polarized component is reflected. 132

O.1 Relation between the Slow and Fast axes with respect to the $\{H, V\}$ -basis. θ_S is the angle between the direction of H polarization and the Slow axis, and \vec{k} is the wavenumber vector of the electromagnetic wave incident on the waveplate. 136

O.2 Specific polarization state on the Bloch sphere (black arrows). The red arrow represents the expected value of HV polarization, the blue arrow represents the expected value of PM polarization, and the green arrow represents the expected value of RL polarization. The colored plane is the plane containing the Bloch vector representing the polarization state and the axis representing the expected value of RL polarization (green arrow). 138

O.3 Relation between a given polarization state (dark black arrows) and the polarization state after transformation by the QWP(thin black arrow). The yellow arrow represents the direction of the S-axis of the QWP, the black dashed arrow represents the unitary transformation of the QWP. 139

O.4 Relation between a given polarization state (black arrows) and the polarization state after conversion by HWP. The yellow arrows represent the orientation of the S-axis of the HWP, and the black dashed arrows represent the unitary transformation of the HWP; the polarization state after transformation by the HWP is consistent with the H polarization state. . . 140

R.1 A model of multi-layers to realize narrow band BPF. It consists of two multi-layers A and B composed of a dielectric and a thin metal film, and a spacer layer sandwiched between them. n_0 is the refractive index of the medium into which light is incident, n_m is the refractive index of the substrate, and n is the refractive index of the spacer layer. 146

S.1 Forward and reverse bias voltages applied to the p-n junction. (a) A p-n junction diode with a forward bias voltage applied. This diode works as a light emitting diode (LED) (b) p-n junction diode with reverse bias voltage applied. This diode works as a photodiode. 150

- U.1 Geometric relation between the phase matching angle and the refractive index distribution such that angular phase matching is satisfied. The A, B, and C axes make Cartesian coordinate defined in a uniaxial crystal. This Cartesian coordinate is defined so that polarization components parallel to the A and B axes perceive the same refractive index but polarization components parallel to the C axis perceive different refractive indices. $n_o^{(\omega)}$ is the refractive index for electromagnetic waves with an angular frequency of ω , and $n_e^{(2\omega)}$ is the refractive index for electromagnetic waves with an angular frequency of 2ω . The distance from the center of the coordinates to the circle or ellipse corresponds to the value of the refractive index. The subscripts "o" and "e" correspond to ordinary and extra-ordinary light, where ordinary light has an oscillating component parallel to the AB plane and extra-ordinary light oscillates in a direction perpendicular to both the wavenumber vector and ordinary light. It can be seen that when the electromagnetic wave propagates at an angle θ_{PM} deviating from the C axis, the values of the refractive index perceived by ordinary light and extra-ordinary light are equal. Such an angle is called the phase matching angle. 156
- U.2 Intensity changes of light generated in a nonlinear crystal in the case of (a) non-phase matching, (b) quasi phase matching and (c) angular phase matching. If the phase matching condition is not achieved, the intensity of the light produced inside the crystal will start to decrease as the pump light propagates $\pi/\Delta k$. If a crystal is used in which the direction of polarization reverses when the light propagates for a decreasing length, the intensity of the generated light will continue to increase. Such a crystal is called a periodically poled crystal. 157
- V.1 The envelope of the fundamental Gaussian beam propagating in the z-axis direction in space. ω_0 is the beam radius at the beam waist, z_R is the Rayleigh length, and θ is the beam spread angle. 161
- W.1 Photo of presetting of all optics. This setup is corresponding to the one shown in FIG. 3.4. There are no HWP2 and GT in front of the FC1 and FC2. 164
- W.2 Results of spacial mode matching. The horizontal axis is defined as the position of the PPKTP at $z = 0$, with the upstream side being negative and the downstream side being positive. The vertical axis represents the beam radius at position z . The beam radius is defined as the distance that is $1/e^2$ times the maximum beam intensity. All points are experimental data and curves are the result of fitting to experimental data. The experimental data are given as the average of the cross-section of the intensity distribution in the direction of horizontal polarization and in the direction of vertical polarization. 165
- X.1 Schematic of the experimental setup for evaluating the ratio of single photon; light incident on the NPBS enters FC1 with a 50% probability and FC2 with a 50% probability. What is done in signal processing is the same as what is described in Subsec. 3.1.1. $N_{1,2}$ are the number of photon counts measured in SPCM1,2, and N_C is the number of coincidence counts. 170

X.2	Experimental setup for measuring the ratio of single photons using a down-converted photon pair as a source. The symbol \otimes means that the output is a coincidence counts. Thus, N_1 represents the coincidence of SPCM1 and SPCM3, N_2 represents the coincidence of SPCM2 and SPCM3, and N_C represents the coincidence of N_1 and N_2 . FC3 corresponds to FC2 in FIG. 3.4. Signal photon P_S uses photons incident on FC1 in FIG. 3.4. When detecting single photons, GT and HWP2 immediately before FC1 and FC2 in FIG. 3.4 were removed.	171
Y.1	(a)Height ruler for an optical axis. (b) Transverse ruler for an optical axis.	174
Y.2	Schematic of optical axis adjustment using two pinholes in the Sagnac interferometer.	175

List of Tables

3.1	Coincidence counts in the basis of and evaluated immediately before the first experiment. The counting time is 10 seconds. $0^\circ, 90^\circ, 45^\circ$ and 135° means four polarization physical properties X, Y, X' and Y'	16
3.2	Coincidence counts in HV basis and PM basis evaluated immediately before the second experiment. The counting time is 10 seconds. 0° and 90° means two polarization physical properties X and Y	18
3.3	Count rates of the four measurement outcomes for X above and Y below. X is the polarization physical property composed of HV polarization and Y is the polarization physical property composed of PM polarization. The \pm sign means ± 1	21
3.4	Numerical results of C_X, V_X, W_E for each ϕ_S , and the total coherence $\sqrt{C_X^2 + W_E^2}$	21
4.1	Correspondence between measured polarization physical quantities and actual polarization angles, where X, Y, X' and Y' are four different polarization physical quantities and \pm represents the measured result ± 1 . The angle in real space represents the rotation angle when the light is viewed from the approaching direction, with H polarization as the reference and counterclockwise as the positive direction.	26
4.2	Raw data of the joint measurement of X_A and Y_A . The label of the joint outcomes follow the form of $N(X_A, Y_A; X_B, Y_B)$. Note that X, Y and X', Y' are totally different polarization. "." means that the value of the corresponding polarization is not considered. All values are measured for 10 seconds. . .	27
4.3	Raw data of the joint measurement of X'_B and Y'_B . The label of the joint outcomes follow the form of $N(X'_A, Y'_A; X'_B, Y'_B)$. Note that X, Y and X', Y' are totally different polarization. "." means that the value of the corresponding polarization is not considered. All values are measured for 10 seconds. . .	28
4.4	Results of the joint measurement when an eigenstate is prepared in which the eigenvalue of a physical property is $+1$	28
4.5	Numerical results of the measurement visibility of X_A, Y_A, X'_B, Y'_B	29
4.6	Results of the joint measurement when an eigenstate is prepared in which the eigenvalue of a physical quantity is $+1$	33
5.1	Results of optimal ϕ_M against each ϕ_S . These results are measurement results, and also setting value of the ϕ_M . This is the reason why they are shown without errors.	36
5.2	Absolute counts with respect to $(f_A; f_B), (f_A; w_B), (w_A; f_B)$ and (w_A, w_B) for each ϕ_S . All counts were obtained from a 10-second measurement. . .	37
5.3	Numerical results of $P(0; a)$ and $P(a; 0)$ for nine ϕ_S	40
6.1	Numerical results of the flipping probability of X_A, Y_A, X'_B, Y'_B	45
6.2	Numerical results of the flipping probability of B that the sixteen outcomes have.	48
6.3	Numerical results of the four Bell correlations in FIG. 6.7.	62

6.4	Numerical results of the four Bell correlations in FIG. 6.8.	63
6.5	Numerical results of the four Bell correlations in FIG. 6.9.	64
6.6	Ratio of $\langle B \rangle_1$ and $\langle B \rangle_2$ to θ_j and ratio of $\langle B \rangle_2$ and $\langle B \rangle_3$	64
6.7	Results of purity, fidelity, and negativity for the density matrix estimated from the experimental results. For a density matrix in Eq. (6.58) and Eq. (6.60) and for ρ_2 in Eq. (6.59), the density matrix in Eq. (6.72) is substituted for V_X , C_X , and V_Y derived from TAB. 3.3, and for ρ_1 in Eq. (6.59), $V_X = 1$, $V_Y = -\sin 2\phi_S$, and the density matrix substituting $C_X = \cos 2\phi_S$ was used.	66
6.8	Numerical results for the contrast function. The contrast function is defined by Eq. (6.87) and all experimental values are derived from the numerical data in TAB. 5.2.	72
D.1	Comparison of the conditions between PVM and POVM measurement. \hat{P}_i is projection operator defined by $ \phi_m\rangle \langle \phi_m $, \hat{E}_m is a POVM element. δ_{mn} is Kronecker delta.	90
X.1	Experimental results with weak coherent light. The measurement time was 100 seconds, and measurements were taken both with and without the laser turned on.	170
X.2	Experimental results with down-converted photons. The measurement time was 100 seconds.	171

List of Abbreviations

AISC	Adaptive Input State Control
BPF	Band Pass Filter
DHWP	Double Half-Wave Plate
DPBS	Polarization Beam Splitter
FC	Fiber Coupler
FWHM	Full Width at Half maximum
GT	Glan Taylor prism
H pol.	Horizontal polarization
HWP	Half-Wave Plate
LED	Light Emitting Diode
M pol.	Minus polarization. 135° linear polarization
NIM	Nuclear Instrument Module
P pol.	Plus polarization. 45° linear polarization
PBS	Polarization Beam Splitter
Pol C	Polarization Controller
POVM	Positive Operator Valued Measure
PVM	Projection Valued Measure
SHG	Second Harmonic Generation
SMF	Single Mode Fiber
SPCM	Single Photon Counting Module
SPDC	Spontaneous Parametric Down Conversion
SPF	Short Pass Filter
SVA	Slowly Varying Amplitude
TTL	Transistor Transistor Logic
V pol.	Vertical polarization

Chapter 1

Introduction

1.1 Introduction

In 1935, A. Einstein, B. Podolsky, and N. Rosen submitted a remarkable paper that would later cause crucial controversy[1](see Appendix A). The EPR paradox is a paradox in which the phenomena that could occur if quantum mechanics is correct contradict the classically correct assumption of reality and locality. EPR have argued that if these assumptions that must of course be true are correct, they cannot explain the behavior of particles in an entangled state of the position and the momentum; therefore, the quantum mechanical description of nature is not complete. Although the EPR paradox raised the essential question of whether the quantum mechanical description of physics is complete or not, it could not go beyond the realm of an interpretative problem because of the difficulty of experimental verification.

In 1957, D. Bohm and Y. Aharonov developed the thought experiment on the EPR paradox and proposed a variant of the EPR paradox that the spin of the two particles are measured instead of their position and momentum[2]. This thought experiment measuring spin not only redefined the problem in a realistically demonstrable framework, but was also a key factor in J. S. Bell's later submission of his landmark paper[3]. D. Bohm also extended L. de Broglie's wave theory[4] and proposed a non-local realistic quantum theory that is valid for many-body systems[5, 6], but it has been pointed out that it is inconsistent with theory of relativity because it admits non-locality in the sense that it assumes the existence of physical influences beyond the speed of light.

In 1964, J. S. Bell proposed an inequality to determine whether local realism claimed by EPR or quantum mechanics was correct, providing a tool to end the long-running controversy[3]. Bell's inequality must be satisfied if local realism is correct, but if the prediction of quantum mechanics is correct, the Bell's inequality is violated. Since the inequality proposed in the paper was not in a form suitable for experiment, attempts were subsequently made by many researchers to improve the inequality. The most important and most realistic of these inequalities is the CHSH inequality, which stands for the initials J. Clauser, M. Horne, A. Shimony, and R. Holt and consists of four different correlations for a two-particle system with two degrees of freedom[7].

In 1972, J. Clauser and S. J. Freedman performed the first experimental verification of Bell's inequality of the CHSH-type using photon polarization and observed a violation of Bell's inequality, but noted that the distance between the two measurement devices was not far enough apart so that the measurement made in one system could have physical effects on the other system that were consistent with theory of relativity[8]. In 1981 and 1982, a research group led by A. Aspect conducted an experiment in a form that resolved this locality loop-hole. Aspect's group used cascade radiation of calcium atoms to generate polarization entanglement and observed the violation of Bell's inequality at a distance between the detectors[9, 10]. Since then, many follow-up experiments have successively reported violations of Bell's inequality, which are now understood phenomenologically

as EPR correlations[11–34]. On the other hand, the physical postulate that explains the non-local correlations of entanglement has not yet been clarified, and remains one of the most profound unsolved problems in physics.

After the violation of Bell’s inequality was confirmed, it was a natural question to wonder how large quantum correlations could increase; in 1980, Cirel’son provided an upper bound on the quantum mechanical EPR correlations, later known as the Cirel’son bound[35](see Appendix B). In 1994, S. Popescu and D. Rohrlich showed that quantum correlations beyond the Cirel’son bound can be realized by assuming non-locality that satisfies relativistic causality[36](see Appendix C). The upper bounds that EPR correlations can achieve depend on the physical principle assumed, and the question of how far EPR correlation can be achieved in actual experiments has remained unresolved. In this context, the motivation for the first experiment in this study is to provide experimental evidence that the Cirel’son bound is a realistically achievable upper bound for the EPR correlation.

We chose a joint measurement of complementary physical properties as a foothold to experimentally investigate the upper limits of EPR correlation[37–40]. Although the conventional idea of measurement is that it is impossible to measure complementary physical properties simultaneously, it is possible to obtain information on two physical properties simultaneously to the extent that the uncertainty principle is not violated. When performing such a measurement, it is necessary to discuss a property of the measurement device called measurement uncertainty. Measurement uncertainty is the property that the statistics obtained from a joint measurement always include measurement errors that would not be included in a precise measurement. Recent studies have suggested that the upper bound of the EPR correlation is limited by the local measurement uncertainty limit[41]. Thus, in order to experimentally explore the relation between the measurement uncertainty limit and the upper limit of the EPR correlation, it is necessary to introduce a joint measurement of a physical quantity in a complementary two-level system and to obtain a joint statistical distribution of the complementary physical properties.

In the first experiment discussed in this thesis, photon pairs are generated using spontaneous parametric down-conversion inside a Sagnac interferometer to prepare the maximum entangled state of photon polarization[42–45]. By performing conventional Bell’s inequality verification experiments on the photon pairs, we confirm that EPR correlations are achieved to the extent that a violation of Bell’s inequality is observed. Up to this point, the experiment is the same as the numerous Bell inequality violation experiments. We introduce a POVM measurement (see Appendix D) for the two measurement systems and perform a measurement uncertainty limited joint measurement of two complementary polarization properties. We introduce a parameter that determines which of the two complementary polarization properties is measured accurately, the joint measurement parameter, and we evaluate the measurement visibility for several different setting of the joint measurement parameter. The results show that for the two-level system, the value of measurement visibilities is independent of the initial quantum state. Next, we perform joint measurements in the two measurement systems at several different joint measurement parameters and evaluate the joint statistical distributions of all four polarization physical properties, including the complementary polarization physical property. Noting the property that the statistical distributions obtained by joint measurements contain measurement uncertainties, we discuss the relation between the joint probability of a particular measurement outcome and the measurement uncertainty. Two types of joint probability distributions are related by the spin-flip model (see Appendix E), one with and one without the effect of measurement uncertainty, and the fact that if there is an EPR correlation that exceeds the Cirel’son boundary, then realistically a negative probability must be obtained in the experiment. This provides strong experimental evidence

that the Cirel'son bound is an upper bound on the EPR correlations that can be achieved in the real world.

The origin of the second experiment discussed in this thesis dates back to the time when the violation of Bell's inequality began to be accepted as experimental fact. One of the problems that EPR thought experiments with particle spin have is that the relation between measurement outcomes becomes unclear because of the need to evaluate statistical averages. When there is a strong correlation, for example, when the measurement outcome of physical property A is a , the measurement outcome of physical property B is always b , the relation or logical relation between the measurement outcomes becomes clear. Some examples of paradoxes arising from such reasons is the three box paradox[46, 47](see Appendix F), GHZ paradox[48](see Appendix G) and Hardy's paradox[49, 50](see Appendix H), GHZ paradox and Hardy's paradox have been confirmed in various experiments [51–55]. Paradoxes such as these, in which results deduced from deterministic conditions based on non-contextual logic contradict conclusions predicted from quantum mechanics, are named consistency paradox here. Theoretically, it is characterized by the fact that the inconsistency is derived after only one trial because no statistical values are required, but experimentally, it is no different from an experiment to verification of the Bell's inequality with respect to the process of obtaining data, since a statistical distribution must be obtained. However, due to the experimental incompleteness that the experimental setup involves, it is very difficult to prepare deterministic conditions in a real experiment. Although L. Hardy himself cited as one of its features the fact that inequalities such as Bell's inequality are no longer needed in order to verify the truth, the statistical and systematic errors that experimental results invariably contain forced him to evaluate discriminant formulas described as inequalities[54]. L. Mandel's group is similarly conducting experiments to test local realism based on deterministic conditions, but since it is impossible to realize deterministic conditions, they are analyzing the errors that the statistics contain[52].

The thought experiment proposed by Frauchiger and Renner in 2018 is another example of such a consistency paradox[56]. Originally conceived as an extension of Wigner's friend's thought experiment[57, 58] and proposed to demonstrate the No-go theorem, it has been noted that this thought experiment is a special case of Hardy's paradox: In Frauchiger and Renner's thought experiment, a total of four observers appear and, based on non-contextual logic, the consistency between the measurement outcomes the observers obtain is discussed. As a result, it is argued that the three plausible physical assumptions cannot hold at the same time, since no matter what measurement outcomes are acquired, inconsistencies cannot be avoided. An interesting aspect of this thought experiment is that the initial state is determined by correlations between physical properties. This is convenient for experimentally investigating quantum contextuality, which is considered one of the fundamental properties of the quantum world. Quantum contextuality, also known as the BKS theorem, an acronym for Bell's paper[59] and S. Kochen and E. P. Specker's paper[60], is a no-go theorem that asserts that the values of two or more physical properties with different measurement contexts cannot be determined precisely and simultaneously. Since Frauchiger and Renner's thought experiment is precisely about the relation between measurement outcomes obtained in different measurement contexts, it seems a suitable scenario for considering quantum contextuality.

One of the problems with the previous paradoxes is that the discussion starts from a single quantum state whose physical meaning is not well understood at the beginning. Attempting to faithfully reproduce something whose physical meaning is not well understood often involves technical difficulties, and the verification of Frauchiger and Renner's thought experiment was one such example[31]. Furthermore, the difficulty of actual realizing deterministic conditions in this verification experiment ultimately led to

the evaluation of inequalities, such as Bell's inequality, in which the relation between measurement outcomes is ambiguous. In quantum mechanics, the gap between theoretically assumed unrealistic situations and experimental incompleteness often tends to be large. Some theories adopt physical interpretations as principles, as if they are assumed to be unprovable, and there is a need to reexamine the question of what empirical science is all about. Moves to bridge this gap can be seen in the experiments to verify Bell's inequality, an example of which is the various loop-hole experiments[18, 20–23, 26]. Loop-hole problems are logical loopholes caused by the fact that the physical conditions realized in the experiment do not match the physical conditions assumed in the theory, and because of this loop-hole problem, many follow-up experiments were required to verify Bell's inequality. Such a loop-hole problem can be solved by attempting to bring the experimental situation as close as possible to that of a theory, but on the other hand, it would be desirable to have a framework for experiments that would allow contradictions to be shown even under the experimental imperfections, and a way to reduce the technical difficulties associated with input state preparation. If there were a way to do this, it would not only give a boost to fundamental experimental research, which is becoming more and more complicated every year, but might also contribute to the development of quantum information technology.

In the second experiment discussed in this paper, we propose a completely new initial state preparation method, Adaptive input state control (AISC), and demonstrate it along the lines of Frauchiger and Renner's thought experiment. The validity of AISC is judged by the strength of the quantum contextuality, by introducing a figure of merit. In actual experiments, we will prepare an entanglement source with variable degree of entanglement, and evaluate the local degree of polarization and entanglement witness to see if the degree of entanglement is really controlled. Next, local polarization rotation is applied to the two generated entanglement photons in order to optimize two of the three physical conditions assumed in Frauchiger and Renner's thought experiment. By aligning the counts of two particular measurement outcomes, quantum interference effects reduce the frequency at which one particular measurement result is detected. The symmetry of the physical system automatically optimizes the second physical condition; the third physical condition is optimized by finding the degree at which the counts are minimized while varying the degree of entanglement. Prior research has shown that there is only one quantum state for which that particular three physical conditions are imposed[61]. After optimizing the experimental parameters, the inequalities derived from the non-contextual logic are evaluated to see if quantum contextuality appears. The results show that quantum contextuality appears over a wide range of degrees of entanglement, indicating that AISC is effective as an operational definition of an input state preparation method.

The structure of this paper is as follows. Chapter 2 describes the theoretical framework for describing the joint measurements in the Bell experiment in the first experiment and the strategy of AISC in the second experiment. Chapter 3 describes the principles of the experimental setup and summarizes the results of the performance evaluation of the setup in preparation for conducting the experiments. Chapter 4 presents the results of the first experiment, Chapter 5 presents the results of the second experiment, and Chapter 6 provides a discussion of those results. Chapter 7 presents the conclusions of this paper.

Chapter 2

Upper bound of the Bell's inequality and adaptive input state control of a contextual quantum state

2.1 Bell correlations investigated by joint measurements

In this section, strategies are described for how to experimentally explore what determines the upper bounds of the Bell's inequality. The Bell's inequality is violated by a number of experiments. However, the current situation is that the Cirel'son bound, which is a quantum mechanical upper bound, is still a matter of controversy, such as why it is such a value and the PR-box argument, which suggests the possibility of crossing the Cirel'son bound. In order to overcome this situation, the first experiment is aimed at obtaining experimental evidence to answer the problem of why the Cirel'son boundary is an upper bound of the Bell's inequality.

2.1.1 Joint measurement of complementary polarization physical properties

The introduction of joint measurements of complementary polarization physical properties may provide new insights compared to the evaluation of Bell correlations using only precise measurements. A joint measurement is a measurement that simultaneously obtains information on complementary physical properties. In this subsection, we describe joint measurements of complementary photon polarizations. FIG. 2.1 is a schematic diagram of the flow of obtaining measurement outcomes by joint measurements of complementary polarization physical properties. Polarization is a two-level system in air medium; therefore, a joint measurement of two complementary physical properties yields $2 \times 2 = 4$ measurement outcomes. In conventional POVM measurements, it is not possible to describe what value of the physical property each measurement outcome corresponds to, but here we consider that it is a combination of four different eigenvalues. Instead, we interpret that the statistical numbers resulting from the joint measurements have measurement errors, and that the errors affects the final average value. The average value including the measurement error is closer to the result obtained when all measurements are completely random than the average value without the error. Note that the measurement error here does not mean statistical error. It is necessary to quantitatively evaluate how much error each measurement outcome has, so as a measure of the precision of a joint measurement, we define the measurement visibility defined by

$$V_{\Xi} := \frac{\langle \Xi \rangle_{joint}}{\langle \hat{\Xi} \rangle_{precise}}, \quad (2.1)$$

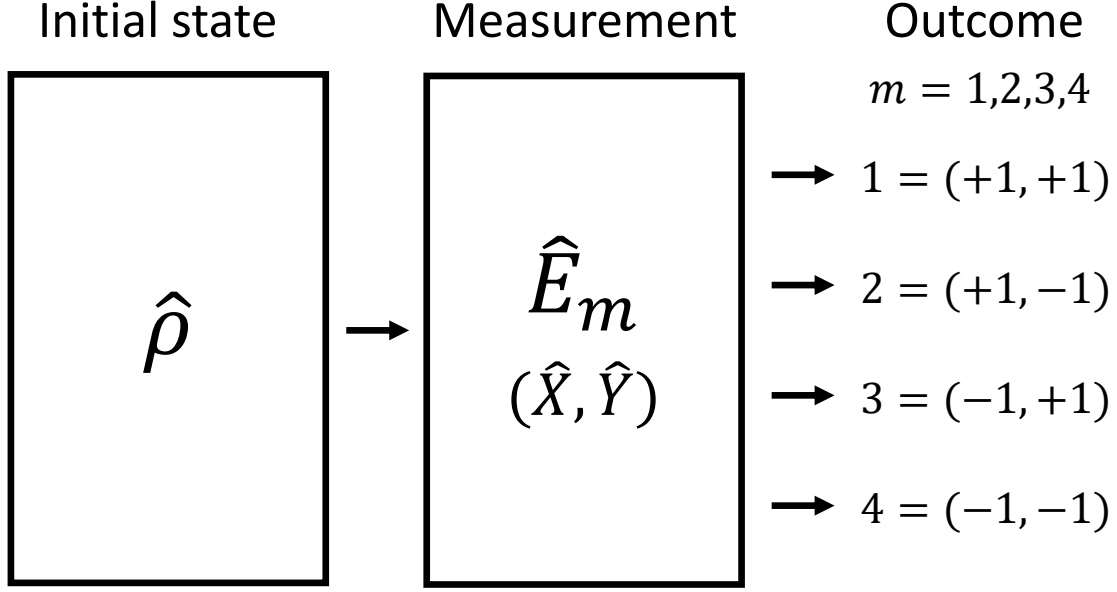


FIGURE 2.1: Schematics of a joint measurement of complementary polarization physical properties. $\hat{\rho}$ is an initial state, \hat{E}_m is POVM element, \hat{X} and \hat{Y} are complementary physical properties whose values are $x, y \in \{0, 1\}$, $m = 1, 2, 3, 4$ are the labels to distinguish the difference measurement outcomes, $(\pm 1, \pm 1)$ means (x, y) .

where Ξ is a specific polarization physical property, $\langle \Xi \rangle_{joint}$ is the average value of Ξ evaluated in the joint measurement, and $\langle \hat{\Xi} \rangle_{precise}$ is the average value of Ξ evaluated in the precise measurement.

Let us consider the specific form of the POVM element in order to clarify the relation between the measurement visibilities and the average of the physical property obtained in the experiment. From an experimentally obtained joint probability distribution, the four relations with respect to the average are given by

$$\langle X \rangle_{joint} = P(+, +) + P(+, -) - P(-, +) - P(-, -) \quad (2.2)$$

$$\langle Y \rangle_{joint} = P(+, +) - P(+, -) + P(-, +) - P(-, -) \quad (2.3)$$

$$\langle XY \rangle_{joint} = P(+, +) - P(+, -) - P(-, +) + P(-, -) \quad (2.4)$$

$$1 = P(+, +) + P(+, -) + P(-, +) + P(-, -), \quad (2.5)$$

where all joint probabilities are $P(x, y)$, and $x, y \in \{+1, -1\}$ are the values of the physical properties \hat{X} and \hat{Y} . Using Eqs. (2.1)-(2.5), the four probabilities are given by

$$P(+, +) = \frac{1}{4} (1 + V_X \langle \hat{X} \rangle_{precise} + V_Y \langle \hat{Y} \rangle_{precise} + \langle XY \rangle_{joint}) \quad (2.6)$$

$$P(+, -) = \frac{1}{4} (1 + V_X \langle \hat{X} \rangle_{precise} - V_Y \langle \hat{Y} \rangle_{precise} - \langle XY \rangle_{joint}) \quad (2.7)$$

$$P(-, +) = \frac{1}{4} (1 - V_X \langle \hat{X} \rangle_{precise} + V_Y \langle \hat{Y} \rangle_{precise} - \langle XY \rangle_{joint}) \quad (2.8)$$

$$P(-, -) = \frac{1}{4} (1 - V_X \langle \hat{X} \rangle_{precise} - V_Y \langle \hat{Y} \rangle_{precise} + \langle XY \rangle_{joint}). \quad (2.9)$$

It would not be easy to physically consider what $\langle XY \rangle_{joint}$ means. From the uncertainty principle of physical properties, $\hat{X}\hat{Y} = i\hat{Z}$ holds, so mathematically $\langle XY \rangle_{joint}$ is equal to the average value of the physical property \hat{Z} in the joint measurements multiplied

by an imaginary unit. However, since the POVM elements assumed in this experiment are completely insensitive to \hat{Z} , the average value obtained by the joint measurement is expected to be zero even if the average value in a precise measurement is not zero. Thus, if we assume that the relational relation in $\hat{X}\hat{Y} = i\hat{Z}$ is correct, the probabilities described by Eqs. (2.6)-(2.9) are given by

$$P(\pm, \pm) = \frac{1}{4} (1 \pm V_X \langle \hat{X} \rangle_{precise} \pm V_Y \langle \hat{Y} \rangle_{precise}). \quad (2.10)$$

Working back the form of the POVM elements from Eq. (2.10), they are given by

$$\hat{E}_m = \frac{1}{4} (\hat{I} \pm V_X \hat{X} \pm V_Y \hat{Y}). \quad (2.11)$$

Regarding the probability $P(-, -)$, it can be likely negative because the measurement visibility satisfies $0 \leq V_X, V_Y \leq 1$ and the average of the polarization physical property is maximally +1. However, obtaining a negative probability in the actual experiment never happens, a restraint condition is necessary given by

$$V_X^2 + V_Y^2 \leq 1, \quad (2.12)$$

named measurement uncertainty limit[62, 63].

2.1.2 Observation of the Bell correlations using joint measurements

In the verification of the Bell's inequality, there are the four non-local correlations among the four physical properties of the two level system. The Bell's inequality is given by

$$-2 \leq \langle \hat{X}_A \hat{X}'_B \rangle - \langle \hat{X}_A \hat{Y}'_B \rangle + \langle \hat{Y}_A \hat{X}'_B \rangle + \langle \hat{Y}_A \hat{Y}'_B \rangle \leq 2, \quad (2.13)$$

where $\hat{X}, \hat{Y}, \hat{X}'$ and \hat{Y}' are the four different physical quantities, and A and B are labels for the measurement system. It is impossible to simultaneously observe the four Bell correlations. In other word, it is impossible to precisely observe a physical property given by

$$\hat{B} \equiv \hat{X}_A \hat{X}'_B - \hat{X}_A \hat{Y}'_B + \hat{Y}_A \hat{X}'_B + \hat{Y}_A \hat{Y}'_B. \quad (2.14)$$

The joint measurements described in subsec. 2.1.1 are introduced into the experiment of Bell's inequality. The eigenvalues of the eigenstates of this operator \hat{B} include $\pm 2\sqrt{2}$, and in the following we assume eigenstates whose eigenvalue is $-2\sqrt{2}$.

Using the joint measurements of the complementary physical properties, \hat{X}_A and \hat{Y}_A can be measured in system A, \hat{X}'_B and \hat{Y}'_B can be measured in system B, taking simultaneous measurements of system A and B allows us to simultaneously obtain the values of the four physical properties; therefore, it is possible to obtain the value of \hat{B} given by

$$b = x_A x'_B - x_A y'_B + y_A x'_B + y_A y'_B, \quad (2.15)$$

where lowercase letters mean the value of the physical property represented by uppercase letters, and $x, y, x', y' \in \{+1, -1\}$. To reconcile this with the experimental fact of Bell's inequality violation, the effect of measurement uncertainty must be taken into account. The joint measurement of complementary physical properties brings the statistics obtained in the experiment closer to a random result, so that the absolute value of the mean of the physical properties is smaller. Bell's inequality, which would have been defeated if the four Bell correlations had been measured independently using only precision

Outcomes of system A

$P(x_A, y_A; x'_B, y'_B)$		$x_A = +1$ $y_A = +1$	$x_A = +1$ $y_A = -1$	$x_A = -1$ $y_A = +1$	$x_A = -1$ $y_A = -1$
		Outcomes of system B	$x'_B = +1$ $y'_B = +1$	$P(+, +; +, +)$	$P(+, -; +, +)$
$x'_B = +1$ $y'_B = -1$	$P(+, +; +, -)$		$P(+, -; +, -)$	$P(-, +; +, -)$	$P(-, -; +, -)$
$x'_B = -1$ $y'_B = +1$	$P(+, +; -, +)$		$P(+, -; -, +)$	$P(-, +; -, +)$	$P(-, -; -, +)$
$x'_B = -1$ $y'_B = -1$	$P(+, +; -, -)$		$P(+, -; -, -)$	$P(-, +; -, -)$	$P(-, -; -, -)$

FIGURE 2.2: Joint statistical distributions that can be evaluated in an experiment to validate Bell's inequality by introducing a joint measurement. The yellow squares are the results of the measurement where $b = +2$ and the green squares are the results of the measurement where $b = -2$. The position of the physical property values correspond to $P(x_A, y_A; x'_B, y'_B)$, where the sign means ± 1 , the ";" means that the measurement systems are non-local.

measurements, becomes smaller in the mean value of \hat{B} due to measurement uncertainties, and eventually the inequality is no longer violated.

The evaluated joint statistical distribution yields the joint probability distribution shown in FIG. 2.2: all sixteen measurements correspond to either $b = \pm 2$; therefore, a joint probability distribution in FIG. 2.2 can provides the average of \hat{B} ,

$$\langle \hat{B} \rangle = 2P(b = +2) - 2P(b = -2), \quad (2.16)$$

where $P(b = +2)$ is the sum of probabilities for the yellow squares and $P(b = -2)$ for the green squares. In this experiment, the result of Eq. (2.16) is expected to be negative because the eigenstate with eigenvalue of $-2\sqrt{2}$ will be prepared as the initial state. Thus, $P(b = -2) > P(b = +2)$ would hold. If the magnitude of the EPR correlation can further cross the Cirel'son bound, the difference between these two probabilities should widen further and the value of $\langle \hat{B} \rangle$ should be closer to -2 . Such a joint probability distribution should result in a measurement outcome with a count close to zero for the measurement outcomes with $b = +2$ in the joint statistical distribution, since the probability of a measurement outcome with $b = -2$ is larger and the probability of a measurement outcome with $b = +2$ is smaller. Such measurement results indicate that the magnitude of the EPR correlation is maximized, which should provide strong evidence as to whether the Cirel'son bound represents a realistic maximal correlation.

2.2 Operational preparation of an input state

This section describes the theoretical framework for the second experiment. Frauchiger and Renner presented the No-go theorem, which states that in order to explain the measurement outcomes by multiple measurers in a consistent manner along a time series,

three conditions that at first glance might be valid in classical dynamics are no longer valid simultaneously in quantum mechanics[56]. This result is important from two perspectives: first, the deterministic conditions are used in the thought experiment. A deterministic condition is an event that has a probability of 0 or 1. The thought experiment based on deterministic conditions ideally have the advantage of not requiring statistics and are characterized by the ability to discuss relation between different measurement outcomes rather than statistical averages. The second is that the initial state is inferred based on the results of measurements. In most cases, initial states are prepared based on theoretical predictions of quantum mechanics, but ideally, theoretical and experimental studies should be conducted independently. While it is important to conduct experiments to verify the theory, establishing methods and measurements that allow for independent experimental research will give us a glimpse into the true nature of the natural world, which we have not been able to see until now. The purpose of our research is to experimentally verify the possibility of preparing a quantum state which outcomes in a contradiction between quantum and classical dynamics based on measurement outcomes and relations between different measurement contexts.

2.2.1 Consistency paradox using deterministic conditions

A consistency paradox is a paradox in which the results predicted from classical mechanics contradict those predicted from quantum mechanics. In each of the two separated physical systems (System A and System B), physical properties of two complementary two-level systems are measured. If the two physical properties are common to systems A and B, and \hat{F}_i and \hat{W}_i ($i = A, B$) are the labeled subscripts that identify the systems, a prepared quantum state satisfies the three conditions given by

$$P(f_A = 0; w_B = a) = 0 \quad (2.17)$$

$$P(w_A = a; f_B = 0) = 0 \quad (2.18)$$

$$P(f_A = 1; f_B = 1) = 0, \quad (2.19)$$

where $f_i = 0, 1$ are measurement outcomes of \hat{F}_i ($i = A, B$), $w_i = a, b$ are measurement outcomes of \hat{W}_i ($i = A, B$). From Bayes' theorem, Eq. (2.17) implies that the result of \hat{F}_A is always 1 under the condition of $w_B = a$. Similarly, Eq. (2.18) shows that the result of \hat{F}_B will always be 1 if $w_A = a$. Eq. (2.19), on the other hand, implies that the simultaneous detection of 1 does not happen. Therefore, under non-contextual logic, which assumes that the value does not change depending on the measurement context, $P(w_A = a; w_B = a) = 0$ is expected since the simultaneous detection of a in both systems should never happen. This impossibility can be expressed as an inequality given by

$$P(a; a) \leq P(0; a) + P(a; 0) + P(1; 1), \quad (2.20)$$

where $P(x; y)$ represents the probability such that the value of \hat{F}_A or \hat{W}_A is x and the value of \hat{F}_B or \hat{W}_B is y . In an actual experiment, the three deterministic conditions represented by Eqs. (2.17) - (2.19) are not achievable because of the experimental imperfection. In such a situation, it is basically expected that the equality sign will not hold.

Eq. (2.20) can also be derived quantitatively by assuming the joint probabilities of the four physical properties, $\hat{F}_A, \hat{W}_A, \hat{F}_B$ and \hat{W}_B . The four joint probabilities in Eq. (2.20) can

be represented as

$$P(a; a) = P(0, a; 0, a) + P(0, a; 1, a) + P(1, a; 0, a) + P(1, a; 1, a) \quad (2.21)$$

$$P(0; a) = P(0, a; 0, a) + P(0, a; 1, a) + P(0, b; 0, a) + P(0, b; 1, a) \quad (2.22)$$

$$P(a; 0) = P(0, a; 0, a) + P(0, a; 0, b) + P(1, a; 0, a) + P(1, a; 0, b) \quad (2.23)$$

$$P(1; 1) = P(1, a; 1, a) + P(1, a; 1, b) + P(1, b; 1, a) + P(1, b; 1, b), \quad (2.24)$$

where the all joint probabilities follow the manner of $P(f_A, w_A; f_B, w_B)$. Since an experimentally obtained probability is definitely greater or equal to zero and less or equal to one, Eq. (2.21) is definitely less than the sum of Eqs. (2.22)-(2.24). All four joint probabilities included in Eq. (2.21) are included in the sum of Eqs. (2.22)-(2.24).

It is possible to show that Eq. (2.20) is equivalent to the Bell's inequality. Defining $|1\rangle, |b\rangle$ as eigenstates with eigenvalue 1 and $|0\rangle, |a\rangle$ as eigenstates with eigenvalue of -1 , considering how the four non-local correlations $\langle \hat{F}_A \hat{F}_B \rangle, \langle \hat{F}_A \hat{W}_B \rangle, \langle \hat{W}_A \hat{F}_B \rangle, \langle \hat{W}_A \hat{W}_B \rangle$ are expressed using the joint probability of the four physical properties as Eq. (2.21)-(2.24) results in the relation given by

$$\begin{aligned} & P(0; a) + P(a; 0) + P(1; 1) - P(a; a) \\ &= \frac{1}{4} (\langle \hat{F}_A \hat{F}_B \rangle + \langle \hat{F}_A \hat{W}_B \rangle + \langle \hat{W}_A \hat{F}_B \rangle - \langle \hat{W}_A \hat{W}_B \rangle + 2) \geq 0. \end{aligned} \quad (2.25)$$

Except for the assumption that the joint probability of all four physical properties is a real number between 0 and 1, Eq. (2.25) is not guaranteed. Conversely, if this inequality is violated, then either the probabilities must be negative, or the values of the physical properties must be other than eigenvalues, or both must be true.

2.2.2 Adaptive input state control for Frauchiger and Renner's thought experiment

The deterministic conditions expressed in Eqs. (2.17)-(2.19) is corresponding to the orthogonal relation in the Hilbert space,

$$\langle 0; a | \psi \rangle = 0 \quad (2.26)$$

$$\langle a; 0 | \psi \rangle = 0 \quad (2.27)$$

$$\langle 1; 1 | \psi \rangle = 0. \quad (2.28)$$

Regarding \hat{F} and \hat{W} as the complementary physical properties, the relation of the different eigenstates are given by

$$|a\rangle = \frac{1}{\sqrt{2}} (|0\rangle - |1\rangle) \quad (2.29)$$

$$|b\rangle = \frac{1}{\sqrt{2}} (|0\rangle + |1\rangle). \quad (2.30)$$

A quantum state such that Eqs. (2.26)-(2.28) are satisfied is unique, and leads to $P(a; a) = 1/12$ [61]. This paradox corresponds to a special case of Hardy's paradox of quantum contextuality and quantum non-locality. What is important in this example is that all three conditions determining the quantum state are experimentally measurable. My goal is to determine how to optimize the three conditions expressed in Eqs. (2.17)-(2.19), taking into account the unspecified imperfections of the experimental setup.

Quantum states that satisfy the three conditions in Eqs. (2.26)-(2.28) are non-maximal entanglement states; therefore, a physical system with a variable degree of entanglement is necessary to find the optimal degree of entanglement. An entanglement source using a Sagnac interferometer and spontaneous parametric downward conversion (SPDC) can change the degree of entanglement from the product state to the maximally entangled state by changing the polarization of the pump beam injected into the interferometer[42–45]. The polarizations of the photon pairs produced by SPDC is determined by the direction of the optical axes of the nonlinear crystal. Using a non-linear crystal that generated photon pairs have horizontal(H) and vertical(V) polarizations, the quantum state that the interferometer provides is given by

$$|\psi_0\rangle = \cos \phi_S |H; V\rangle - \sin \phi_S |V; H\rangle, \quad (2.31)$$

where ϕ_S is an experimentally variable parameter, changes the intensity ratio of pump beam between two light paths in the interferometer. It is easy to change the negative correlations to the positive correlations by inserting by flipping the polarization in one system, then the quantum state becomes

$$|\psi_0\rangle = \cos \phi_S |H; H\rangle - \sin \phi_S |V; V\rangle. \quad (2.32)$$

Such a conversion to positive correlation is due to the fact that the conditions in Eqs. (2.26)-(2.28) are symmetric with respect to the exchange of the system. Conversion from a quantum state with a certain degree of entanglement is achieved by applying local polarization rotation to the quantum state described by Eq. (2.32). The local polarization rotations are given by

$$|0\rangle = \hat{U}(\phi_M) |H\rangle \quad (2.33)$$

$$|1\rangle = \hat{U}(\phi_M) |V\rangle, \quad (2.34)$$

where ϕ_M is experimentally adjustable parameter and changes the rotation angle of a local polarization. AISC determines ϕ_M while holding Eq. (2.17) and Eq. (2.18). Using Eq. (2.26), Eq. (2.27) and Eq. (2.29) become

$$\langle 0; 1 | \psi \rangle = \langle 0; 0 | \psi \rangle \quad (2.35)$$

$$\langle 1; 0 | \psi \rangle = \langle 0; 0 | \psi \rangle. \quad (2.36)$$

These imply $P(0;0) = P(0;1) = P(1;0)$ in other words to the statistical data obtained in experiments. These conditions are achievable irrespective of the imperfection of the experimental setup. Since the optimal ϕ_M is determined under a certain ϕ_S , the condition $P(1;1) = 0$ corresponding to Eq. (2.28) is satisfied by varying ϕ_S . By optimizing these two parameters, it is possible to prepare a quantum state such that the three conditions expressed in Eqs. (2.17)-(2.19) are satisfied.

It is interesting to note so far that all the conditions necessary for input state preparation are achieved using only the $\{0, 1\}$ -basis. While quantum state preparation usually requires measurements in different basis to confirm quantum correlations, AISC uses only one measurement basis. This means that AISC has the potential to reveal relations between different measurement contexts.

Chapter 3

Preparation for the experiment

3.1 Preparation for the first experiment

3.1.1 Experimental setup

The first experiment investigates the cause of the reason why the Bell's inequality is limited by Cirel'son bound, quantum mechanical upper bound. FIG. 3.1 shows the schematic of the experimental setup for the first experiment. The semiconductor laser whose wave length is 405 [nm] is used to generate entangled photon pairs at the nonlinear crystal by spontaneous parametric down conversion (SPDC). This pump beam is efficiently injected into a single-mode fiber (SMF) using the two dielectric mirrors. Since the polarization beam splitter (PBS) extracts H polarization after the FC1, a polarization controller (Pol C) makes the pump beam of H polarization at the output of a fiber coupler (FC1). The intensity immediately after the FC1 was approximately 15 [mW]. The half-wave plate (HWP1) converts H polarization to diagonal polarization(P) polarization. The dichroic mirror (DM) transmits light near 405 [nm] and reflects light near 810 [nm]. The double polarization beam splitter (DPBS) is a polarizing beam splitter designed to act appropriately for light of two wavelengths, 405 [nm] and 810 [nm]; when P -polarized light is incident, the intensity is split roughly in half in the transmission and reflection directions. In the clockwise path, the pump beam is converted from V to H polarization by a double half-wave plate (DHWP) and reflected by a silver mirror before entering the PPKTP, which previous studies have shown to be most efficient at producing down-converted photon pairs when the temperature is kept at 18.5 [°C] and the H -polarized pump beam is injected[64]. Therefore, the temperature of the PPKTP is maintained at 18.5 [°C] by a temperature controller. In addition, the collimation lens inside FC1 is adjusted so that the pump laser creates a focal point roughly at the center of the PPKTP. The beam radius at the circumference store was $\omega_x = 132.2 \pm 1.8 [\mu m]$ in the direction parallel to the optical table and $\omega_y = 132.2 \pm 1.2 [\mu m]$ in the direction perpendicular to the optical table. The generated photon pairs are reflected by the silver mirror and then split by the DPBS, with the H -polarized photon propagating to the left and the V -polarized photon propagating downward. In the counterclockwise path, the generated photon pairs enter the DHWP, but since the H and V polarizations are only converted, the example of the relation between the polarizations of the photon pairs is not affected. In this case, the V -polarized photon propagates to the left and the H -polarized photon downward. In each path the polarization to be measured is selected by a half-wave plate (HWP2) and a Glan Taylor prism: the two gold mirrors efficiently inject the photon into fiber couplers (FC2 and FC3), and the band-pass filter (BPF) prevents the pump beam from entering the optical fiber. The two detected photons are each converted into an electrical pulse signal by a single-photon detector and signal processing is performed to count them. In the signal processing, the signal is converted from TTL to NIM by a logic level adapter and the signal width is converted to 30 [ns] by a DISCRIMINATOR. The shaped NIM

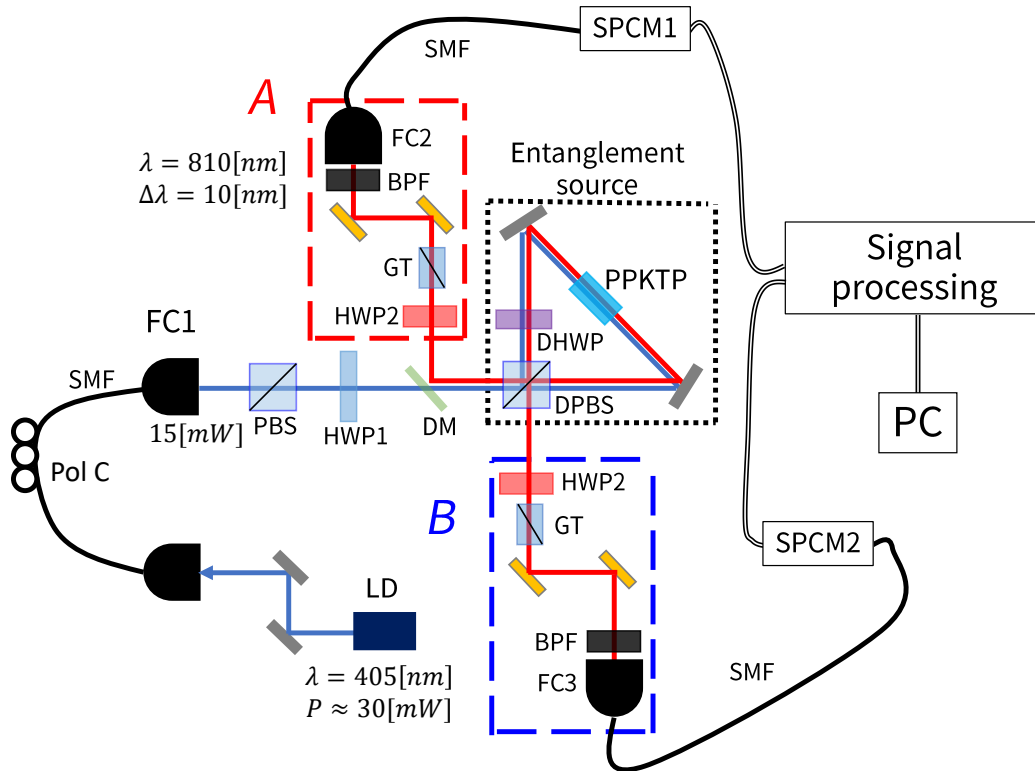


FIGURE 3.1: Setup for the first experiment. It consists of three parts: the part for generating polarization entanglement photon pairs (surrounded by dotted lines), the part for measurement (surrounded by red and blue), and the part for signal processing.

signal is simultaneously measured by the COINCIDENCE module. The collimation lens inside FC1 is adjusted so that the pump beam creates a beam waist at the center of the PPKTP; the collimation lenses inside FC2 and FC3 are designed so that the 810 [nm] laser light creates a beam waist at the center of the PPKTP too. The collimation lenses have a focal length such that the Rayleigh length of the pump beam and the Rayleigh length of the 810 [nm] laser light coincide. The silver mirrors are used inside the interferometer because they have high reflectivity for both 405 [nm] and 810 [nm] photons, and the gold mirrors are used immediately after the GT because they have high reflectivity for the 810 [nm] photon pairs but absorb the 405 [nm] noise source.

3.1.2 Performance of the setup and the interferometer visibility

Evaluation of the performance of an entanglement source is accomplished by counting the number of photons under specific conditions. Therefore, it is important to check the performance of the measuring instrument. The number of photons is converted into electrical pulses by the SPCMs, and the count of photons is corresponding to the number of rising pulses. It is necessary to know the number of dark counts because the measuring instrument produces pulses even if there is no light in the experimental environment, due to thermal fluctuations, defects in the crystal or bad insulation. The dark counts of SPCM1 and SPCM2 were 46 ± 7 [1/s] and 7080 ± 84 [1/s], respectively, which were checked immediately before the first experiment. The dark counts for SPCM2 have increased due to aging. That such dark counts have almost no effect in the coincidence

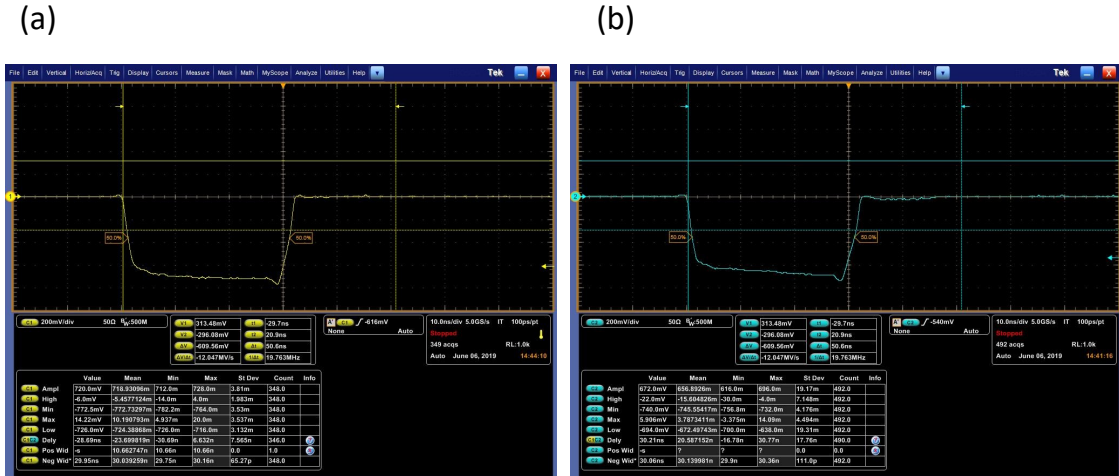


FIGURE 3.2: Electrical pulses after DISCRIMINATOR. (a) Pulse waveform immediately after the SPCM1 signal and Logic Level Adapter passes through the DISCRIMINATOR (b) Pulse waveform immediately after the SPCM2 signal and Logic Level Adapter passes through the DISCRIMINATOR.

count of entanglement photon pairs can be shown by evaluating the delay curves as explained later. The delay curve is achieved by intentionally applying a delay to the electrical pulse while making coincidence count in the absence of GT and HWP2 in FIG. 3.1. As shown in FIG. 3.2, the electrical pulse after DISCRIMINATOR has a width of 30.04 ± 0.06 [ns] and a height of -773 ± 4 [mV] on the System A and a width of 30.14 ± 0.11 [ns] and a height of -745 ± 4 [mV] on the System B. Both pulse signals have a width of roughly 30 [ns], so if entanglement photon pairs are really detected, the counts should drop to the same order of magnitude as the coincidence counts when greater than 30 [ns] delayed pulse is applied. FIG. 3.3 shows the results of the delay curves evaluated prior to conducting the first experiment. In the range of delay times from roughly -20 [ns] to 30 [ns], the two pulse signals are judged to overlap and the number of simultaneous measurements is roughly 1.9×10^4 [1/s], but outside that range, the count rate is roughly 10^2 [1/s]. At 2 [ns], roughly in the middle of the range where counting rates are higher, the single counts for SPCM1 and SPCM2 were 82305[1/s] and 75620[1/s], respectively. Therefore, the accidental coincidence count is $82305 \times 75620 \times 60 \times 10^{-9} \approx 373$ [1/s]. This is consistent with the order of magnitude of the number of coincidence counts in the region where the entanglement photon pairs are not coincidentally measured. FIG. 3.3 therefore provides evidence that the entanglement photon pairs are indeed being detected. Two more detailed features are not yet clear: First, the delay time is not symmetrical with respect to the $t = 0$ [ns] position. The second is that the count rate is slightly declining in the region where the entanglement photon pairs can be detected. We investigated the cause of this feature, but were unable to identify the cause.

Now that we have confirmed that the entanglement photon pairs are really detected, it is necessary to quantitatively evaluate how much quantum coherence these photon pairs have. Quantum coherence can be evaluated as the clarity of interference fringes, similar to the classical wave interference phenomenon. Photon pairs generated by SPDC are correlated in HV polarization in our case. If photon pairs have quantum coherence, then they should also be strongly correlated in PM polarization where M polarization is anti-diagonal linear polarization, which is complementary to the physical property of

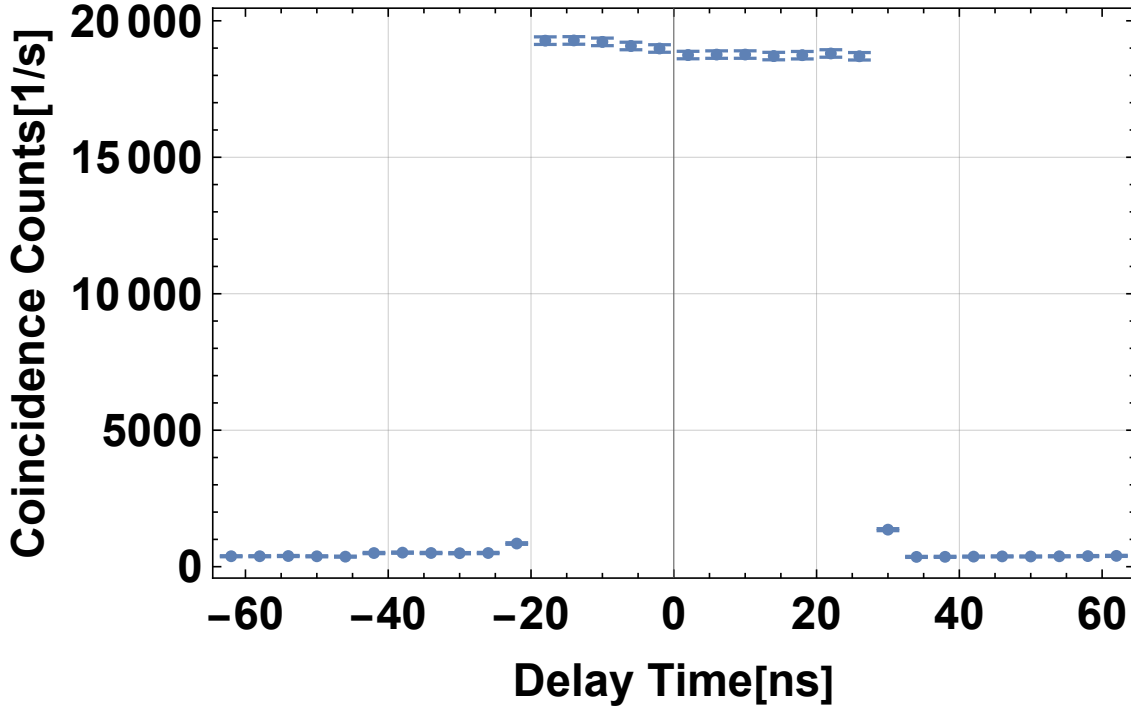


FIGURE 3.3: Delay curves evaluated before the first experiment. The positive area of Delay Time on the horizontal axis means multiplying the delay to the pulses from SPCM1, while the negative area means multiplying the delay to the pulses from SPCM2. The value on the vertical axis is the counting rate.

HV polarization. Therefore, the definition of the visibility of a photon pair is given by

$$V_{\Xi} := \frac{N_{++} + N_{--} - N_{+-} - N_{-+}}{N_{++} + N_{--} + N_{+-} + N_{-+}}, \quad (3.1)$$

where Ξ is a polarization physical property which has two outcomes of $+1$ and -1 , N_{+-}

TABLE 3.1: Coincidence counts in the basis of and evaluated immediately before the first experiment. The counting time is 10 seconds. $0^\circ, 90^\circ, 45^\circ$ and 135° means four polarization physical properties X, Y, X' and Y' .

Label of counts	0°	90°	45°	135°
N_{++}	711	1054	867	878
N_{--}	685	1150	878	881
N_{+-}	68283	68903	69438	69292
N_{-+}	68991	69531	70794	68985

is a coincidence counting rate that an outcome of $+1$ is obtained in System A and an outcome of -1 is obtained in System B. The results of the four coincidence counts in the four polarization physical properties $X(0^\circ), Y(90^\circ), X'(45^\circ)$ and $Y'(135^\circ)$ are shown in TAB. 3.1. Therefore, TAB. 3.1 and Eq. (3.1) give

$$V_X = -0.980 \pm 0.004 \quad (3.2)$$

$$V_Y = -0.969 \pm 0.004 \quad (3.3)$$

$$V_{X'} = -0.975 \pm 0.004 \quad (3.4)$$

$$V_{Y'} = -0.975 \pm 0.004. \quad (3.5)$$

These show the strong negative correlations, indicating that a quantum state is close to the singlet state.

3.2 Preparation for the second experiment

3.2.1 Experimental setup

The second experiment investigates how to prepare a quantum state that shows specific quantum correlations providing the appearance of quantum contextuality. As in the setup of the first experiment, it consists of three parts: generation of polarization entanglement, measurement of polarization, and signal processing. However, there are several changes as follows. First, the intensity of the semiconductor laser that outputs the pump light has been reduced by about 3 or 4 [mW] due to age-related deterioration. Second, the PBS placed immediately after the FC1 has been replaced by a GT for 405 [nm]. Third, the beam radius of the pump beam at PPKTP were $\omega_x = 166 \pm 3 [\mu\text{m}]$ in the direction parallel to the optical table and $\omega_y = 168 \pm 3 [\mu\text{m}]$ in the direction perpendicular to the optical table. In general, the extinction ratio of GTs is two orders of magnitude larger than that of PBSs, indicating that they can discriminate H and V polarization more precisely. A half-wave plate (HWP3) is placed on the downward path from the DPBS to convert between H and V polarizations. This converts the correlations that the photon pairs have from negative to positive correlations. Finally, in System A and System B, two mirrors were removed to allow the entanglement photon pairs source to be more stable. The adjustment to increase the photon pair counts becomes more difficult, but the stability of the setup as an entanglement source increases because the number of optical components is reduced. However, since gold mirrors were used for the two mirrors, they also played a role in absorbing the pump beam. To prevent the pump beam from entering the optical fiber and being measured as background, a long-pass filter (LPF) as well as a BPF were inserted into both FC2 and FC3. By inserting these two filters inside the two FCs, the space in front of the FCs can be secured. The situation in the subsequent part of the signal processing is exactly the same as in first experiment.

3.2.2 Performance of the setup and the trade off relation between a local polarization and entanglement witness

The dark counts for SPCM1 and SPCM2, confirmed just before the second experiment, were $52 \pm 7 [1/\text{s}]$ and $7289 \pm 85 [1/\text{s}]$, respectively; for SPCM1, the increase in dark counts is within the error margin, but for SPCM2 it is about 200 [1/s] more. As shown in FIG. 3.5, the electrical pulses sent from the two SPCMs are shaped by the DISCRIMINATOR. The electrical pulses after DISCRIMINATOR are $30.06 \pm 0.02 [\text{ns}]$ wide and $-918 \pm 10 [\text{mV}]$ high on the System A and $30.09 \pm 0.02 [\text{ns}]$ wide and $-902 \pm 11 [\text{mV}]$ high on the System B. Both pulses show roughly 30 [ns] in width, but the voltage values are about 150 [mV] smaller than in the first experiment. However, the shaped pulses are eventually converted to TTL signals and counted, so they can be measured without problems. FIG. 3.6 shows the results of the delay curve evaluated before conducting the second experiment. In the range of delay time from roughly $-22 [\text{ns}]$ to $30 [\text{ns}]$, two pulse signals are judged to overlap, and the number of simultaneous measurements is roughly $1.1 \times 10^4 [1/\text{s}]$, but outside that range, the counting rate is roughly in the order of $10^2 [1/\text{s}]$. At 2 [ns], roughly in the middle of the range of higher counting rates, the single counts for SPCM1 and SPCM2 were 56958 [1/s] and 60472 [1/s], respectively. Therefore, the accidental coincidence counts are $56958 \times 60472 \times 60 \times 10^{-9} \approx 207 [1/\text{s}]$. This indicates that the entanglement photon pairs of polarization were still detected just before the second

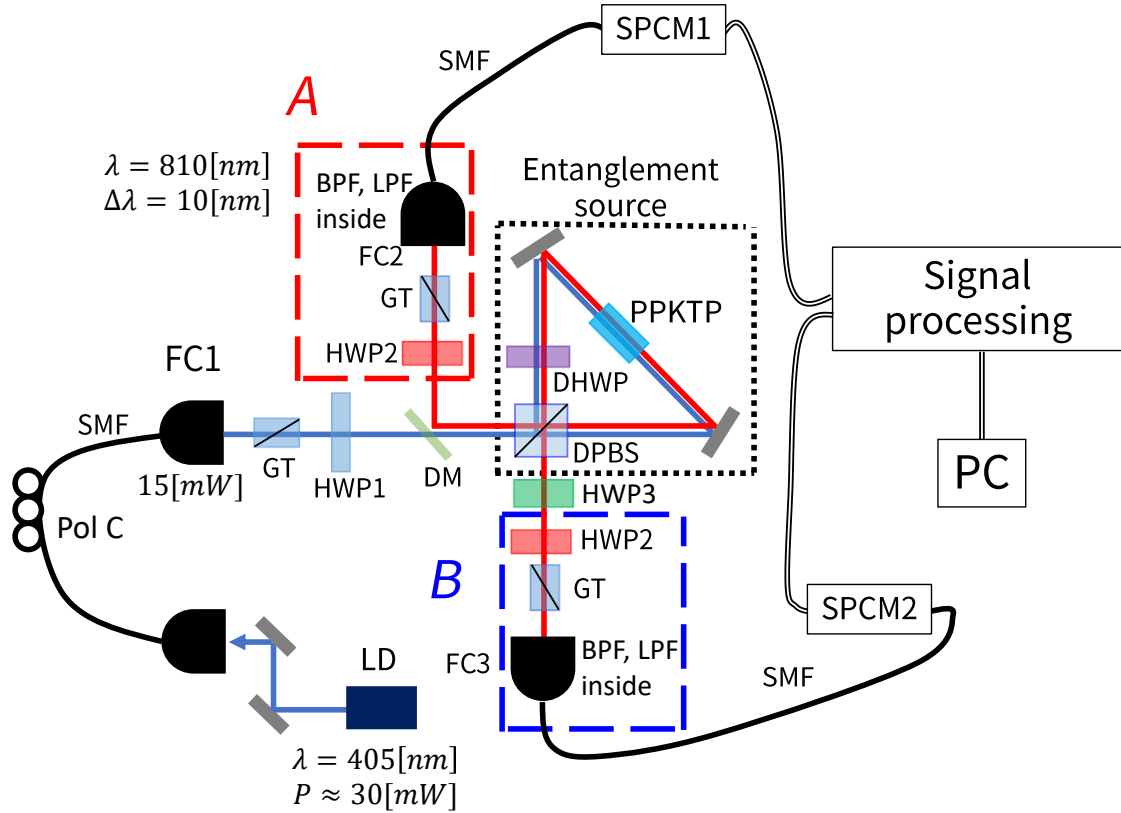


FIGURE 3.4: Setup for the second experiment. It also consists of three parts: the part for generating polarization entanglement photon pairs (surrounded by dotted lines), the part for measurement (surrounded by red and blue), and the part for signal processing. Compared to the setup in the first experiment shown in FIG. 3.1, fewer optical components realizes higher stability.

experiment. The most significant difference from the delay curve of the first experiment is the decrease in the single-count and coincidence count. The decrease is roughly one third as a count, which can be attributed to a decrease in the intensity of the pump beam due to aging and the change of the beam radius of the pump beam at the PPKTP. Higher pump beam energy densities produce more photon pairs because SPDC is a non-linear effect of polarization.

TABLE 3.2: Coincidence counts in HV basis and PM basis evaluated immediately before the second experiment. The counting time is 10 seconds. 0° and 90° means two polarization physical properties X and Y .

<i>Label of counts</i>	Counts in HV basis	Counts in PM basis
N_{++}	5902	207
N_{--}	5611	175
N_{+-}	109	5627
N_{-+}	81	5795

The quantum coherence of the entanglement photon pairs prepared in the second experiment can also be evaluated based on Eq. (3.1). TAB. 3.2 shows the number of coincidences in the HV and PM basis evaluated just before the second experiment. The number of coincidence counts is one order of magnitude smaller than in TAB. 3.1. The FC2 and FC3 are adjusted so that the number of N_{-+} and N_{+-} are equal when the pump

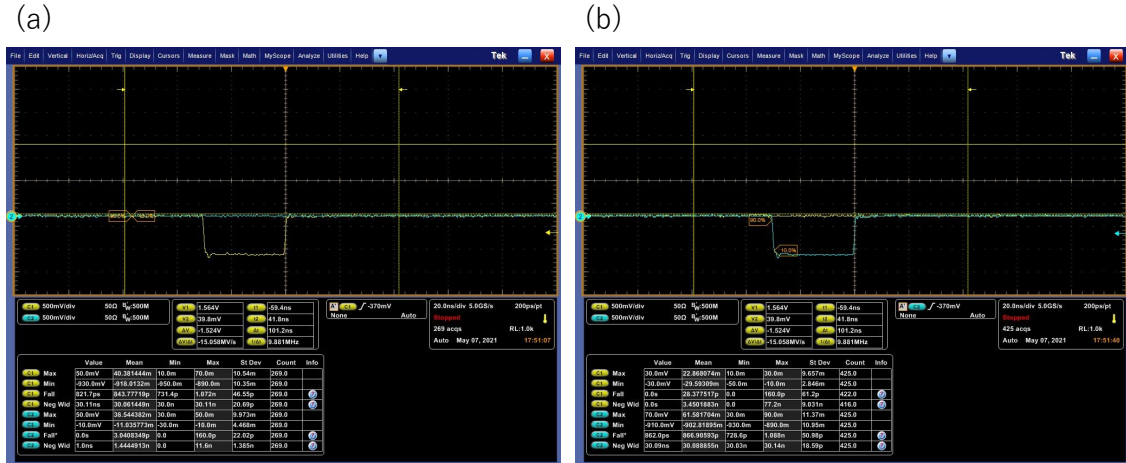


FIGURE 3.5: Electrical pulses after DISCRIMINATOR. (a) Pulse waveform immediately after the SPCM1 signal and Logic Level Adapter passes through the DISCRIMINATOR (b) Pulse waveform immediately after the SPCM2 signal and Logic Level Adapter passes through the DISCRIMINATOR.

beam is P polarized. As a result of such adjustment, the number of coincidence counts became one order of magnitude smaller. Although we were unable to determine the cause of this, the beam radius of the pump beam at the center of the PPKTP is thought to have a significant effect. Without polarization selection, the number of coincidences would be the same by an order of magnitude as shown in FIG. 3.3 and FIG. 3.6, but in the setup of the second experiment, the beam radius of the photon pair beams are also wider, which may have reduced the number of coincidences at the positions where $N_{-+} \approx N_{+-}$ is satisfied. The results of TAB. 3.2 and Eq. (3.1) provides

$$V_X = 0.968 \pm 0.013 \quad (3.6)$$

$$V_Y = -0.935 \pm 0.011. \quad (3.7)$$

Compared to the results obtained in the first experiment shown in Eq. (3.2) and Eq. (3.3), the interferometer visibilities are worse than the results in the first experiment. The reduced degrees of freedom for fine tuning made it difficult to increase the visibility in the PM polarization. There is room for improvement by devising the procedures and methods used to construct the setup.

In the second experiment, the degree of entanglement is changed from a product state to a maximally entangled state by transforming the polarization of the pump beam from V to P polarization with HWP1 in FIG. 3.4. This experimentally variable characteristic is parameterized with ϕ_S , and $\phi_S = 0^\circ$ is corresponding to V polarization and $\phi_S = 45^\circ$ is to P polarization of the pump beam. It is useful that there are indexes showing the degree of local polarizations and entanglements to know the actual performance of the experimental setup. As an index showing the entanglement, we introduce an entanglement witness described by

$$W_E \equiv V_X - V_Y - 1. \quad (3.8)$$

The minus sign in front of V_Y reflects the result of interference visibility shown in Eq. (3.7). Ideally speaking, the decrease of the degree of entanglement results in the increase

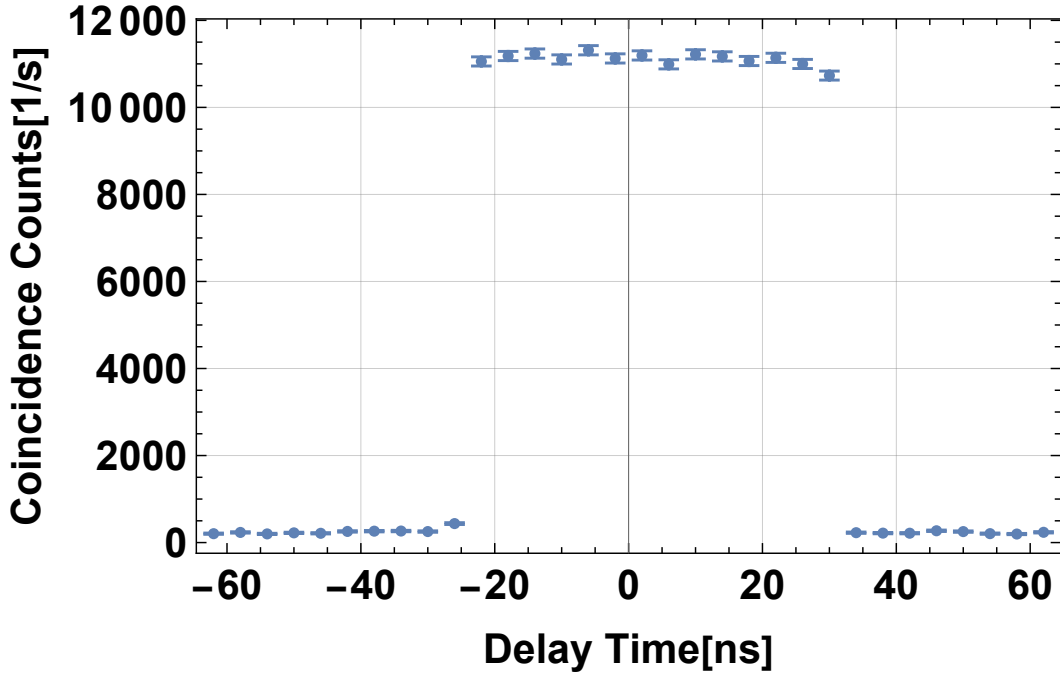


FIGURE 3.6: Delay curves evaluated before the second experiment. The positive area of Delay Time on the horizontal axis means multiplying the delay to the pulses from SPCM1, while the negative area means multiplying the delay to the pulses from SPCM2. The value on the vertical axis is the counting rate.

of the degree of the local polarization described by

$$C_{\Xi} \equiv \frac{N_{+} - N_{-}}{N_{+} + N_{-}}, \quad (3.9)$$

where N_{+} and N_{-} are the count rate of polarizations of $\zeta = +1$ and $\zeta = -1$, ζ is the value of Ξ . Since photon pairs produced by nonlinear crystals are strongly correlated between the original HV polarizations, the appropriate physical property for the degree of local polarization is X . The raw data needed to evaluate Eqs. (3.8) and (3.9) are shown in TAB. 3.3. When evaluating Eq. (3.9), $P(x_A = +; x_B = +) + P(x_A = +; x_B = -) - P(x_A = -; x_B = +) - P(x_A = -; x_B = -)$ for system A and $P(x_A = +; x_B = +) - P(x_A = +; x_B = -) + P(x_A = -; x_B = +) - P(x_A = -; x_B = -)$ for system B, and the average of these is $P(x_A = +; x_B = +) - P(x_A = -; x_B = -)$. To see how much these three differ, comparison of these three is shown in FIG. 3.7, showing that the three data points agree within the margin of error; henceforth, when evaluating local polarization, Eq. (3.9) shall be evaluated for each of systems A and B, and the average value of the two shall be shown.

The graphs and actual values of the degree of local polarization C_X , the interferometer visibility V_X with respect to X , and the degree of entanglement W_E are shown in FIG. 3.8 and TAB. 3.4. The V_X is a constant value within the error range; since the photon pairs generated in nonlinear crystals always have a strong negative correlation in HV polarization. The reason why it has a value close to $+1$ instead of -1 is because it is converted to a positive correlation by the HWP3 in FIG. 3.4. The reason why $+1$ is not included in the error range is due to imperfections in the mainly polarizers in the experimental setup. The C_X and the V_X are the same at $\phi_S = 0^\circ$, but V_X and W_E do not coincide at $\phi_S = 45^\circ$. This means that the local coherence represented by the local polarization is

TABLE 3.3: Count rates of the four measurement outcomes for X above and Y below. X is the polarization physical property composed of HV polarization and Y is the polarization physical property composed of PM polarization. The \pm sign means ± 1 .

$\phi_S[\text{deg}]$	$N(x_A = +; x_B = +)$	$N(x_A = +; x_B = -)$	$N(x_A = -; x_B = +)$	$N(x_A = -; x_B = -)$
0	11326	119	27	47
10	10379	115	26	379
175	10030	107	28	1101
20	9860	111	40	1336
225	9391	109	51	1666
25	9218	108	45	1947
275	9695	105	46	2415
35	7923	114	54	3689
45	5902	109	81	5611

$\phi_S[\text{deg}]$	$N(y_A = +; y_B = +)$	$N(y_A = +; y_B = -)$	$N(y_A = -; y_B = +)$	$N(y_A = -; y_B = -)$
0	3013	2926	2836	3033
10	1895	3657	3611	1853
175	1369	4353	4387	1342
20	1152	4711	4506	1182
225	1082	4655	4640	969
25	946	4854	4935	895
275	767	5327	5464	812
35	459	5651	5611	430
45	207	5629	5795	175

not completely transferred to the non-local coherence represented by the entanglement witness.

TABLE 3.4: Numerical results of C_X, V_X, W_E for each ϕ_S , and the total coherence $\sqrt{C_X^2 + W_E^2}$

$\phi_S[\text{deg}]$	V_X	C_X	W_E	$\sqrt{C_X^2 + W_E^2}$
0	0.975 ± 0.013	0.979 ± 0.013	-0.049 ± 0.017	0.980 ± 0.013
10	0.974 ± 0.013	0.918 ± 0.013	0.294 ± 0.017	0.963 ± 0.014
17.5	0.976 ± 0.013	0.793 ± 0.013	0.503 ± 0.017	0.938 ± 0.014
20	0.973 ± 0.012	0.751 ± 0.012	0.569 ± 0.016	0.943 ± 0.014
22.5	0.971 ± 0.012	0.689 ± 0.012	0.610 ± 0.017	0.920 ± 0.014
25	0.973 ± 0.012	0.642 ± 0.012	0.656 ± 0.016	0.918 ± 0.014
27.5	0.975 ± 0.012	0.594 ± 0.012	0.720 ± 0.016	0.933 ± 0.014
35	0.971 ± 0.011	0.359 ± 0.011	0.825 ± 0.016	0.900 ± 0.015
45	0.968 ± 0.011	0.025 ± 0.011	0.903 ± 0.016	0.903 ± 0.016

The generated photon pairs are strongly correlated for HV polarization, but for PM polarization which depends on the perfection of the interferometer. Thus, while C_X is affected by the imperfection status of the optical components, it is also affected by the imperfection of the interferometer for W_E , so that local coherence is not fully converted to non-local coherence. This feature is also evident in $\sqrt{C_X^2 + W_E^2}$ in TAB. 3.4. Originally, the value of $\sqrt{C_X^2 + W_E^2}$ is expected to be constant regardless of the value of ϕ_S , but it differs by a maximum of about 0.08. For $\phi_S = 0^\circ$, the value of $\sqrt{C_X^2 + W_E^2}$ is large because the interferometer imperfections do not take effect, but for $\phi_S = 45^\circ$, $\sqrt{C_X^2 + W_E^2}$ is small because interferometer imperfections take effect the most. It is clear that the C_X and W_E

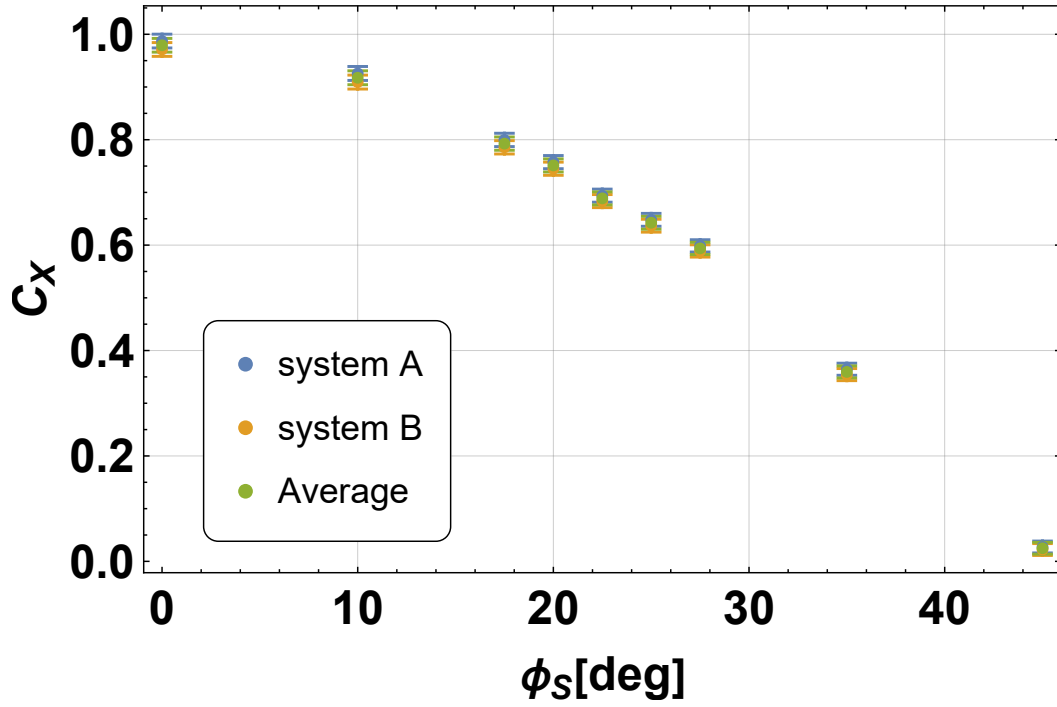


FIGURE 3.7: Degree of local polarization in HV basis against experimental parameter ϕ_s . The local polarization is given by Eq. 3.9. Blue dots show $P(x_A = +; x_B = +) + P(x_A = +; x_B = -) - P(x_A = -; x_B = +) - P(x_A = -; x_B = -)$, yellow dots show $P(x_A = +; x_B = +) - P(x_A = +; x_B = -) + P(x_A = -; x_B = +) - P(x_A = -; x_B = -)$ and green dots show their average. This result indicates that system A and B are symmetric.

have a trade-off relation. This is the evidence that the degree of entanglement can be controlled by varying ϕ_s .

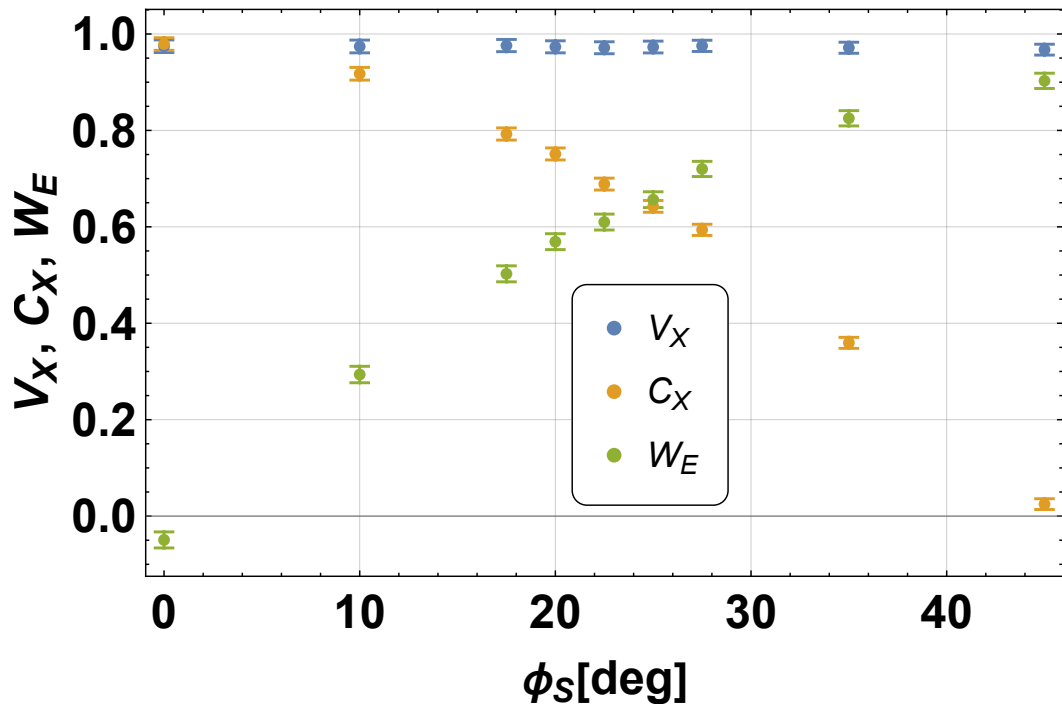


FIGURE 3.8: Trade-off relation between C_X and W_E in all range of ϕ_s . X is a polarization physical property composed of HV polarization, V_X shows the interferometer visibility given by Eq. (3.1), C_X is the local polarization given by Eq. (3.9) and W_E is the entanglement witness represented as Eq. (6.62).

Chapter 4

Experimental results for the upper bound of the Bell's inequality violation

4.1 Measurement visibility of the complementary polarizations

Since a joint measurement of two complementary physical properties contains errors in the measurement outcome, it is necessary to quantitatively evaluate how precisely the measurement was performed. Since Eq. (2.1) is independent of the initial state, arbitrary initial state is allowed to evaluate the measurement visibility for a physical property. Ξ takes two values because it is a polarization in the free space. In the first experiment, we prepared an eigenstate state where $\zeta = +1$ as an initial state. Since the photon pairs produced by the entanglement source has strong negative correlation, choosing the polarization corresponding to $\zeta = -1$ in one system means that the eigenstate corresponding to $\zeta = +1$ can be prepared in the other system. This manipulation of the quantum state of one particle of the entanglement by selecting the quantum state of the other particle is called quantum steering¹. In order to describe the experimental evaluation method of Eq. (2.1) in more detail, let us explain the process of deriving the $\langle \zeta \rangle_{joint}$ and the $\langle \hat{\Xi} \rangle_{precise}$. When the polarization corresponding to $\zeta = +1$ is prepared on the system A side, the polarization corresponding to $\zeta = -1$ is measured on the system B side. Thereafter, the polarization corresponding to $\zeta = -1$ will continue to be measured in system B until the end of the evaluation of the V_{Ξ} . Under this situation, the $\langle \hat{\Xi} \rangle_{precise}$ is given by

$$\begin{aligned} \langle \hat{\Xi} \rangle_{precise} &= P(\zeta_A = +1 | \zeta_B = -1) - P(\zeta_A = -1 | \zeta_B = -1) \\ &= \frac{P(+, \cdot; -, \cdot) - P(-, \cdot; -, \cdot)}{P(+, \cdot; -, \cdot) + P(-, \cdot; -, \cdot)}, \end{aligned} \quad (4.1)$$

where, let ζ^{\perp} be the complementary polarization physical property measured together with ζ , a center dot indicates that no distinction is made between the different values of ζ or ζ^{\perp} for this physical property. For example, $P(\zeta_A, \zeta_A^{\perp}; \zeta_B, \zeta_B^{\perp}) = P(\cdot, +; -, \cdot)$ means the joint probability such that the value of ζ_A is not considered, $\zeta_A^{\perp} = +1$, $\zeta_B = -1$ and the value of ζ_B^{\perp} is not , the measurement outcome in system A to the left of ";" and the

¹Quantum steering is a concept originally introduced for clustering quantum entanglement. The implication is that the quantum states of one system have such strong non-local correlations that measurements made on the other system can be used to infer the quantum state of the other system. It was proposed by Schrödinger[65, 66] and later developed by H. M. Wiseman, S. J. Jones, and A. C. Doherty[67].

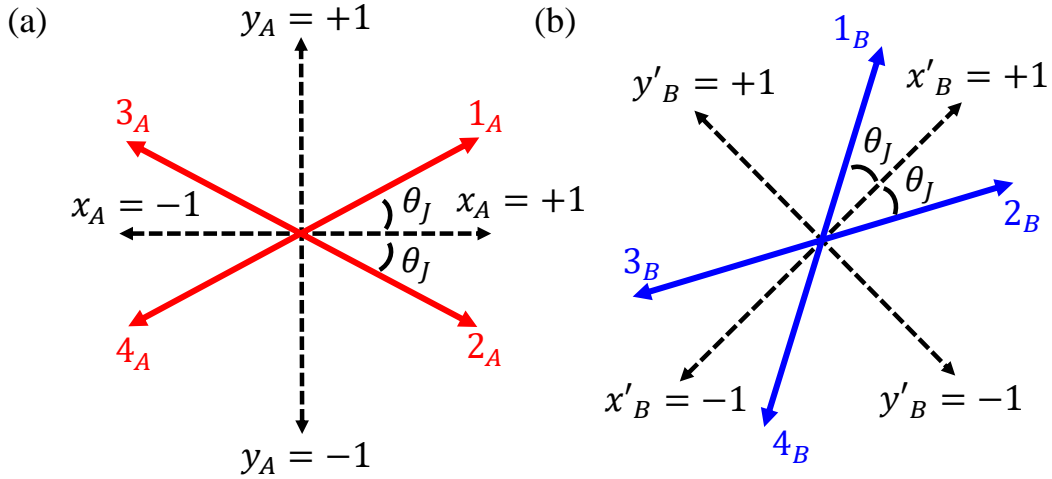


FIGURE 4.1: On the Bloch sphere (see Appendix I), two complementary polarization physical properties that are (a) jointly measured in system A, and (b) measured in system B. Red arrows are POVM elements selected in system A. The blue arrows indicate the POVM elements selected in system B. θ_J is the joint measurement parameter, and in this experiment the parameter values are always the same for systems A and B. $x = +1$ corresponds to H polarization, $x = -1$ to V polarization, $y = +1$ to P polarization, and $y = -1$ to M polarization. x' and y' are polarization physical properties that lie exactly in between them.

measurement outcome in system B to the right of ";". Regarding the $\langle \Xi \rangle_{joint}$, considered

$$\begin{aligned}
 \langle \Xi \rangle_{joint} &= P(\zeta_A = +1, \zeta_A^\perp = +1 | \zeta_B = -1) + P(\zeta_A = +1, \zeta_A^\perp = -1 | \zeta_B = -1) \\
 &\quad - P(\zeta_A = -1, \zeta_A^\perp = +1 | \zeta_B = -1) - P(\zeta_A = -1, \zeta_A^\perp = -1 | \zeta_B = -1) \\
 &= \frac{P(+, +; -, \cdot) + P(+, -; -, \cdot) - P(-, +; -, \cdot) - P(-, -; -, \cdot)}{P(+, +; -, \cdot) + P(+, -; -, \cdot) + P(-, +; -, \cdot) + P(-, -; -, \cdot)}, \quad (4.2)
 \end{aligned}$$

where, for example, $P(\zeta_A, \zeta_A^\perp; \zeta_B, \zeta_B^\perp) = P(-, +; -, \cdot)$ means the joint probability such that $\zeta_A = -1$, $\zeta_A^\perp = +1$, $\zeta_B = -1$ and the value of ζ_B^\perp is not considered.

Actual angle of polarization physical properties are defined as shown in TAB. 4.1. The

TABLE 4.1: Correspondence between measured polarization physical quantities and actual polarization angles, where X, Y, X' and Y' are four different polarization physical quantities and \pm represents the measured result ± 1 . The angle in real space represents the rotation angle when the light is viewed from the approaching direction, with H polarization as the reference and counterclockwise as the positive direction.

Physical property	Value	Angle in real space[deg]
\hat{X}	(+, -)	(0°, 90°)
\hat{Y}	(+, -)	(45°, 135°)
\hat{X}'	(+, -)	(22.5°, 112.5°)
\hat{Y}'	(+, -)	(67.5°, 157.5°)

\hat{X} is the polarization physical property with H and V polarization in the measurement outcomes, the \hat{Y} is the polarization physical property with P and M in the measurement outcomes, and the \hat{X}' , \hat{Y}' is the polarization physical property exactly in between the \hat{X}' and the \hat{Y}' . Setting a joint measurement of the \hat{X}, \hat{Y} in system A and \hat{X}', \hat{Y}' in system B,

the relation between polarization physical properties and joint measurement parameters is shown in FIG. 4.1. Note that FIG. 4.1 is displayed in the Bloch sphere, not in real space. There are four polarizations to be measured, one in each of the four directions between the two polarization physical properties measured in each system, corresponding to the four joint measurement outcomes of (x_A, y_A) or (x_B, y_B) .

To evaluate the performance of the joint measurements, we derive the measurement visibility for two polarization physical properties, the X_A and the Y_A for system A and the X'_B and the Y'_B for system B. Using the raw data in TAB. 3.1 and Eq. (4.1), $\langle \hat{E} \rangle_{precise}$ for the four polarization physical properties of X_A, Y_A, X'_B , and Y'_B become

$$\langle X_A \rangle_{precise} = 0.980 \pm 0.005 \quad (4.3)$$

$$\langle Y_A \rangle_{precise} = 0.967 \pm 0.005 \quad (4.4)$$

$$\langle X'_B \rangle_{precise} = 0.975 \pm 0.005 \quad (4.5)$$

$$\langle Y'_B \rangle_{precise} = 0.975 \pm 0.005. \quad (4.6)$$

These values agree with the results of Eqs. (3.2) - (3.5) within the error margin. The raw data for the joint measurement for the initial condition with $\zeta = +1$ is shown in TAB. 4.2 and TAB. 4.3. In the both case of $\theta = 0^\circ$ and $\theta = 90^\circ$, there are two measurement

TABLE 4.2: Raw data of the joint measurement of X_A and Y_A . The label of the joint outcomes follow the form of $N(X_A, Y_A; X_B, Y_B)$. Note that X, Y and X', Y' are totally different polarization. "." means that the value of the corresponding polarization is not considered. All values are measured for 10 seconds.

θ_J [deg]	$N(+, +; -, \cdot)$	$N(-, -; -, \cdot)$	$N(+, -; -, \cdot)$	$N(-, +; -, \cdot)$
0	69424	806	69424	806
10	69954	803	67873	1920
20	68667	1866	66187	3900
30	66806	4016	63672	6890
40	63845	6759	59595	10878
45	59130	10713	59315	9807
50	59836	10711	55013	15393
60	55245	15231	49979	20553
70	49713	20991	44246	26213
80	44133	26338	38088	32392
90	38672	32446	32446	38672
θ_J [deg]	$N(+, +; \cdot, -)$	$N(-, -; \cdot, -)$	$N(+, -; \cdot, -)$	$N(-, +; \cdot, -)$
0	31692	36206	31692	36206
10	37053	30964	26339	42451
20	42826	25472	20388	47723
30	48446	19556	15570	53071
40	53169	14908	10961	57011
45	59244	11033	11635	57952
50	57705	10705	7149	61292
60	60724	6941	4256	64260
70	64428	3926	2347	65707
80	66564	2239	1182	66870
90	67571	1113	1113	67571

outcomes that have the same coincidence counts. This means that the joint measurement is sensitive to only one of the two polarizations, which means that the measurements are equivalent to the precise measurements. Results in TAB. 4.2 and TAB.4.3 can provide the average obtained in the joint measurements of X_A and Y_A or X'_B and Y'_B as shown in TAB. 4.4. Therefore, the measurement visibilities of the four polarizations X_A, Y_A, X'_B

TABLE 4.3: Raw data of the joint measurement of X'_B and Y'_B . The label of the joint outcomes follow the form of $N(X'_A, Y'_A; X'_B, Y'_B)$. Note that X, Y and X', Y' are totally different polarization. "." means that the value of the corresponding polarization is not considered. All values are measured for 10 seconds.

θ_j [deg]	$N(-, \cdot; +, +)$	$N(-, \cdot; -, -)$	$N(-, \cdot; +, -)$	$N(-, \cdot; -, +)$
0	67938	931	67938	931
10	68686	868	66942	1961
20	67599	1902	65355	4049
30	65248	3786	61856	6957
40	61972	6860	58994	10810
45	59909	11082	59835	10639
50	59249	10382	53563	15331
60	54667	15158	48456	20381
70	49799	19745	43022	26410
80	44101	26143	37293	31795
90	38246	31296	31296	38246

θ_j [deg]	$N(\cdot, -; +, +)$	$N(\cdot, -; -, -)$	$N(\cdot, -; +, -)$	$N(\cdot, -; -, +)$
0	31717	36771	31717	36771
10	37509	31234	26249	42817
20	43618	25110	20796	47902
30	48973	20300	15664	53861
40	54105	14910	11147	57768
45	61237	9781	12578	57406
50	58717	10510	7190	62051
60	62623	6584	4331	65051
70	65060	3874	2182	67817
80	67703	1729	1048	68633
90	68228	952	952	68228

TABLE 4.4: Results of the joint measurement when an eigenstate is prepared in which the eigenvalue of a physical property is +1.

θ_j [deg]	$\langle X_A \rangle_{joint}$	$\langle Y_A \rangle_{joint}$	$\langle X'_B \rangle_{joint}$	$\langle Y'_B \rangle_{joint}$
0	0.977 ± 0.004	0.0000 ± 0.0027	0.973 ± 0.004	0.0000 ± 0.0027
10	0.961 ± 0.004	0.1623 ± 0.0027	0.959 ± 0.004	0.1658 ± 0.0027
20	0.918 ± 0.004	0.3276 ± 0.0028	0.914 ± 0.004	0.3319 ± 0.0028
30	0.8457 ± 0.0035	0.4859 ± 0.0030	0.8441 ± 0.0035	0.4818 ± 0.0030
40	0.7500 ± 0.0033	0.6197 ± 0.0032	0.7451 ± 0.0033	0.6222 ± 0.0032
45	0.7047 ± 0.0033	0.6759 ± 0.0032	0.6929 ± 0.0032	0.6829 ± 0.0032
50	0.6296 ± 0.0031	0.7391 ± 0.0034	0.6288 ± 0.0032	0.7443 ± 0.0034
60	0.4925 ± 0.0030	0.8356 ± 0.0035	0.4874 ± 0.0030	0.8425 ± 0.0035
70	0.3312 ± 0.0028	0.908 ± 0.004	0.3358 ± 0.0028	0.913 ± 0.004
80	0.1667 ± 0.0027	0.950 ± 0.004	0.1683 ± 0.0027	0.960 ± 0.004
90	0.0000 ± 0.0027	0.968 ± 0.004	0.0000 ± 0.0027	0.972 ± 0.004

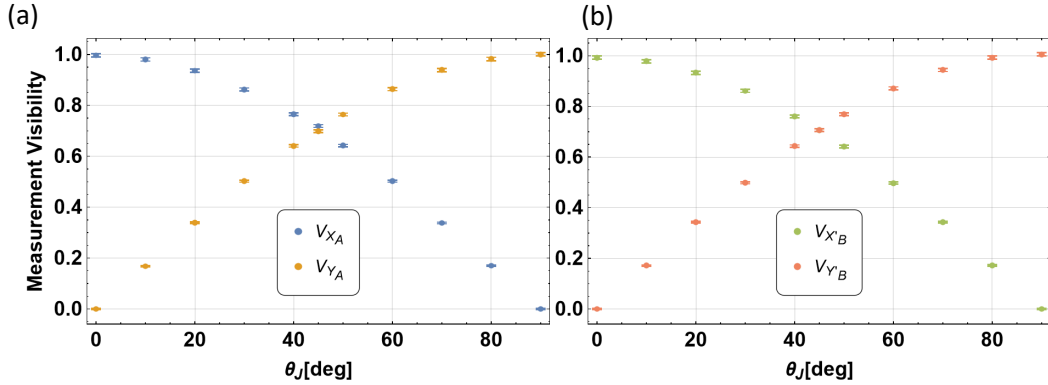


FIGURE 4.2: Measurement visibilities of (a) X_A and Y_A , (b) X'_B and Y'_B against the joint measurement parameter, θ_J . At $\theta_J = 0^\circ$, the X_A and the X'_B are measured precisely, at $\theta_J = 90^\circ$, the Y_A and the Y'_B are measured precisely, and at $\theta_J = 45^\circ$, all four polarization physical properties are measured with the same accuracy.

and Y'_B are obtained from Eqs. (2.1), (4.3) - (4.6), TAB. 4.4 as shown in FIG. 4.2 and TAB. 4.5. It can be seen that a clear trade-off relation between the measurement visibilities of

TABLE 4.5: Numerical results of the measurement visibility of X_A, Y_A, X'_B, Y'_B .

θ_J [deg]	V_{X_A}	V_{Y_A}	$V_{X'_B}$	$V_{Y'_B}$
0	0.997 ± 0.007	0.0000 ± 0.0028	0.992 ± 0.007	0.0000 ± 0.0028
10	0.981 ± 0.007	0.1678 ± 0.0030	0.978 ± 0.007	0.1714 ± 0.0030
20	0.936 ± 0.006	0.3387 ± 0.0035	0.933 ± 0.006	0.3432 ± 0.0035
30	0.863 ± 0.006	0.502 ± 0.004	0.861 ± 0.006	0.498 ± 0.004
40	0.765 ± 0.005	0.641 ± 0.005	0.760 ± 0.005	0.643 ± 0.005
45	0.719 ± 0.005	0.699 ± 0.005	0.707 ± 0.005	0.706 ± 0.005
50	0.642 ± 0.005	0.764 ± 0.005	0.641 ± 0.005	0.770 ± 0.005
60	0.502 ± 0.004	0.864 ± 0.006	0.497 ± 0.004	0.871 ± 0.006
70	0.3379 ± 0.0034	0.939 ± 0.006	0.3425 ± 0.0034	0.944 ± 0.006
80	0.1700 ± 0.0029	0.982 ± 0.007	0.1717 ± 0.0029	0.993 ± 0.007
90	0.0000 ± 0.0027	1.000 ± 0.007	0.0000 ± 0.0027	1.005 ± 0.007

the complementary physical properties is manifested in both systems A and B. To clarify the relation between the complementary polarization in each system, FIG. 4.3 is a graph with the measurement visibilities assigned to the horizontal and vertical axes. It can be seen that all data points are on arcs of radius one. This means that it is not possible to perform joint measurements beyond this uncertainty limit. These results certainly show the measurement uncertainty limit as shown in Eq. (2.12). If the measurement visibilities depended on the initial state, the experimental values would not have ridden on a circle of radius one, as shown in FIG. 4.3 because the initial state is not a pure state, as shown in Eqs. (3.2)-(3.5).

4.2 Joint statistical distributions of the complementary polarizations

The experiment to verify Bell's inequality using joint measurements are accomplished by joint measurements of the complementary relations the X_A and the Y_A , or the X'_B and the Y'_B . By changing the joint measurement parameter θ_J , one can change which of

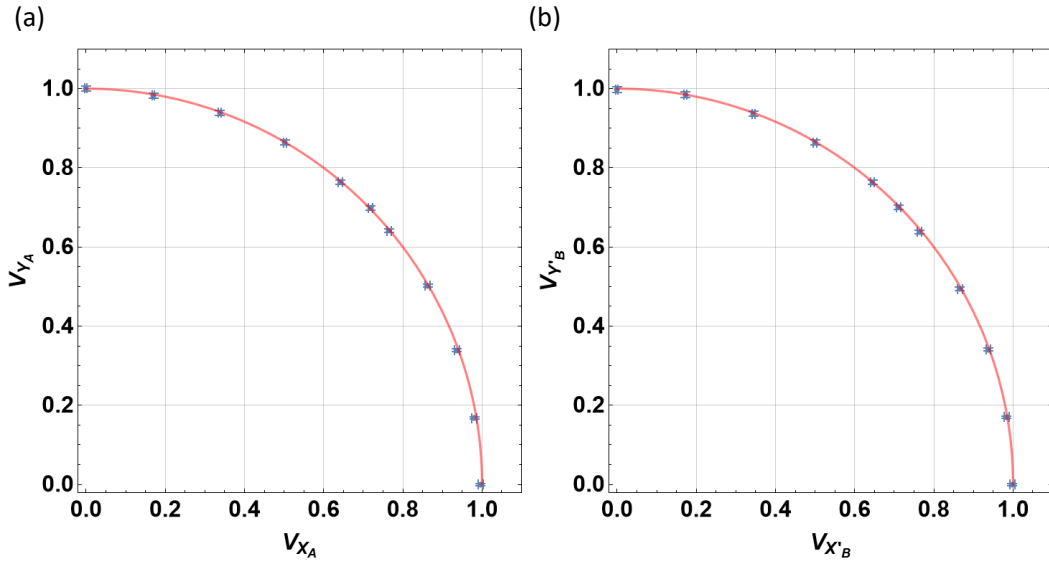


FIGURE 4.3: Trade-off relation between the measurement visibilities of complementary polarization (a) between X_A and Y_A ; (b) between X'_B and Y'_B . The blue dots represent experimental values and the red curve represents an arc whose radius is 1.

the complementary polarizations is measured more accurately. The joint measurement parameters set for systems A and B are strictly independent, but in this experiment they are varied so that they always have the same value. The condition that one of the four outcomes is selected at random is achieved by unifying the measurement time interval of the four outcomes.

FIG. 4.4 shows the results of the joint statistical distribution obtained in the experiment. The joint statistical distribution of the $\theta_J = 45^\circ$ case is the most easily understandable because the four polarization physical properties are measured with the same accuracy. The most interesting feature is that the counts of the eight measurements with $b = +2$ are almost identical, and the counts of the eight measurements with $b = -2$ are almost identical as well. This means that the joint statistical distribution depends only on the value of \hat{B} . The situation in which all four polarization physical properties are measured with the same accuracy is the same as in a conventional Bell's inequality verification using only precise measurements (see Appendix J). One more thing that can be said about the shape of the joint statistical distribution is that the counts of the measurement outcomes corresponding to $b = +2$ are not very close to zero. This suggests that even lower counts for the measurement outcomes where $b = +2$ could lead to more stronger quantum correlations, so the experimental data cannot conclude whether the Cirel'son bound is a realistic upper limit for Bell's inequality. Therefore, joint measurements with the same measurement uncertainty for all polarizations are insufficient to provide experimentally innovative facts about the upper bound of Bell's inequality, and there is a need to survey in detail the results for different balances of measurement uncertainty among the complementary polarizations.

Centered at $\theta_J = 45^\circ$, the closer $\theta_J = 0^\circ$, the more accurately X_A and X'_B are measured, and the closer $\theta_J = 90^\circ$, the more accurately Y_A and Y'_B are measured. The case of $\theta_J = 0^\circ$ is equivalent to a precise measurement for X_A and X'_B , and has no sensitivity to Y_A and Y'_B . As evidence of this, the counts of the measurement outcomes that would invert the values of X_A or X'_B are different, but the counts that would invert the results of Y_A or Y'_B are the same. Conversely, the case $\theta_J = 90^\circ$ is equivalent to a precise measurement of Y_A

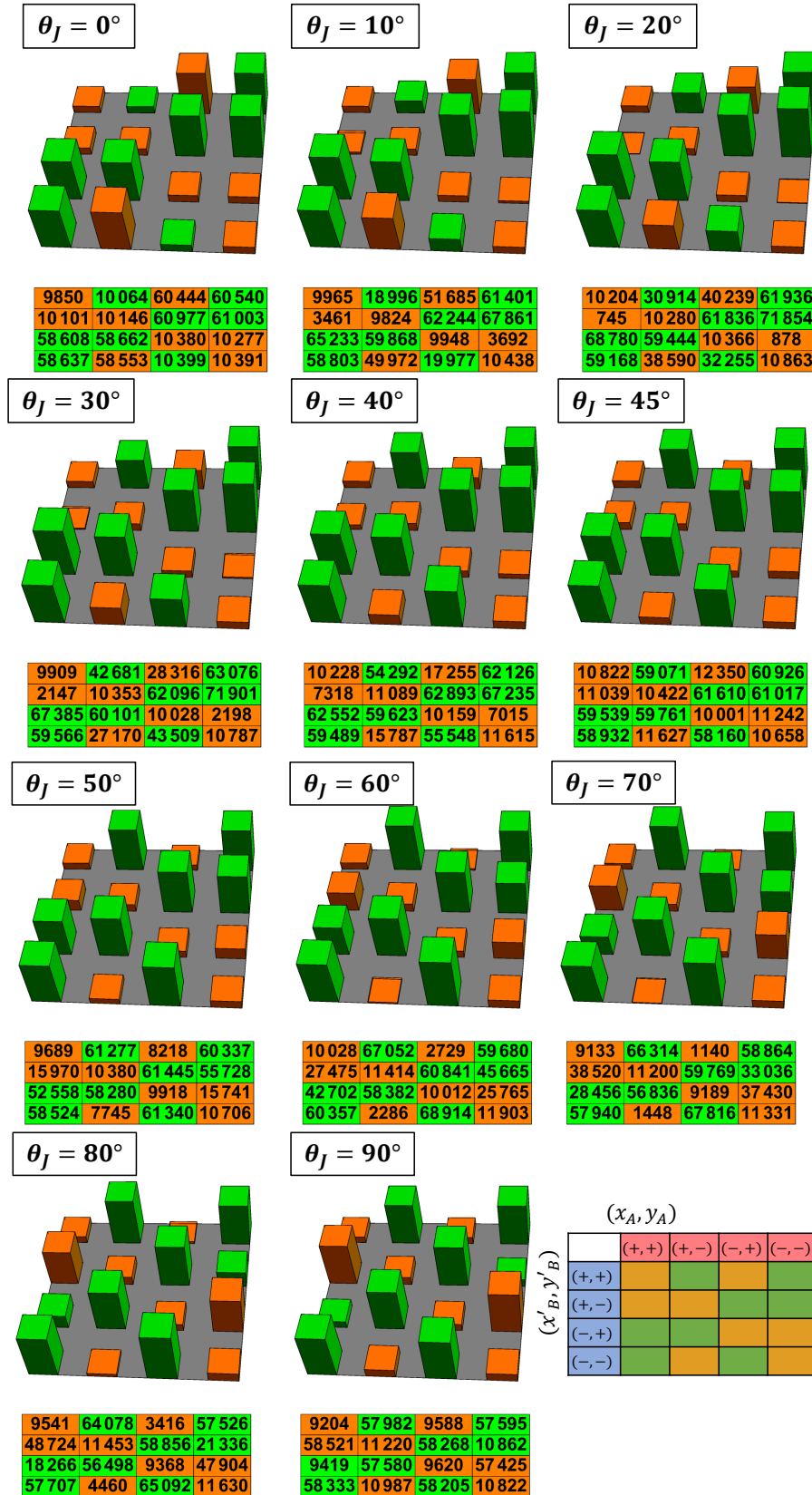


FIGURE 4.4: Joint statistical distributions obtained in the experiment to investigate Bell's inequality with the joint measurements. All counts are measured for 10 seconds. Orange represents outcomes of $b = +2$ and green represents ones of $b = -2$. The 3D plots and the positions of the outcomes correspond, and the arrangement of the sixteen measurement outcomes follows the joint statistical distribution presented in FIG. 2.2.

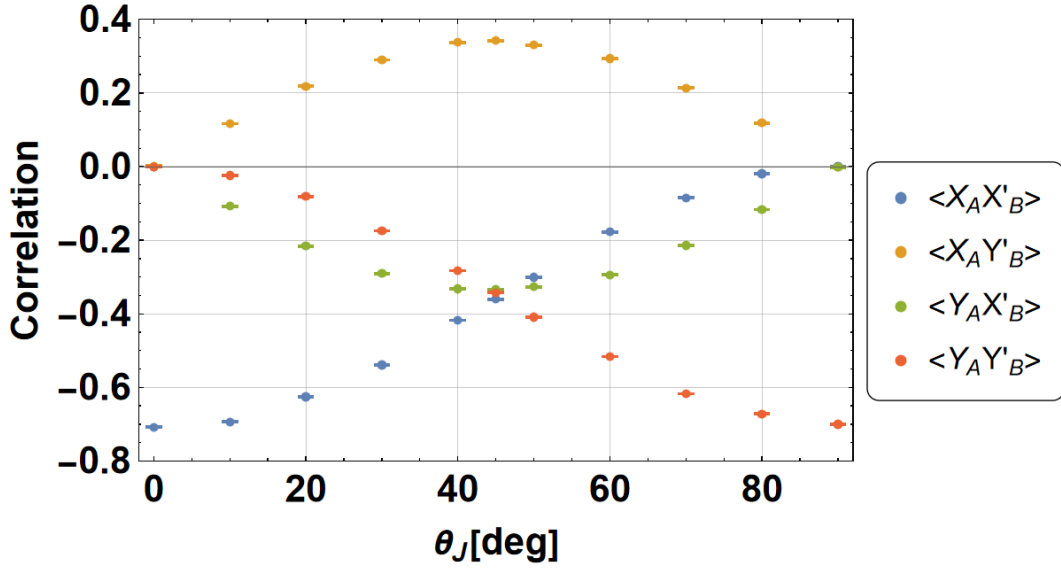


FIGURE 4.5: Four non-local correlations against the joint measurement parameter θ_J .

and Y'_B and has no sensitivity at all to X_A and X'_B , as evidenced by the nearly identical counts of measurement outcomes that would invert the values of X_A or X'_B .

The most noteworthy point when looking over all the joint statistical distributions is the measurement outcomes at two points, $\theta_J = 20^\circ$ and 70° , where the counts are significantly lower. It is important to note that the joint measurement is a measurement including measurement uncertainties in the measurement outcomes, and the fact that the counts are approaching zero despite the measurement uncertainty suggests that the quantum correlation is maximal. A detailed discussion of the behavior of the joint statistical distributions and the significant decrease of the counts in the specific outcomes when the joint measurement parameters are changed will be presented in Chapter 6.

4.3 Local and Non-local correlations of the maximally entangled photons

The various correlations that photon pairs have can be examined by deriving the joint probability distribution from the joint statistical distributions obtained in the experiment. To obtain the joint probability distributions, the counts from all sixteen measurements are added together and the sixteen counts are divided. The four Bell correlations are described according to the notation shown in FIG. 2.2 as given by

$$\langle X_A X'_B \rangle = P(+, \cdot; +, \cdot) - P(+, \cdot; -, \cdot) - P(-, \cdot; +, \cdot) + P(-, \cdot; -, \cdot) \quad (4.7)$$

$$\langle X_A Y'_B \rangle = P(+, \cdot; \cdot, +) - P(+, \cdot; \cdot, -) - P(-, \cdot; \cdot, +) + P(-, \cdot; \cdot, -) \quad (4.8)$$

$$\langle Y_A X'_B \rangle = P(\cdot, +; +, \cdot) - P(\cdot, +; -, \cdot) - P(\cdot, -; +, \cdot) + P(\cdot, -; -, \cdot) \quad (4.9)$$

$$\langle Y_A Y'_B \rangle = P(\cdot, +; \cdot, +) - P(\cdot, +; \cdot, -) - P(\cdot, -; \cdot, +) + P(\cdot, -; \cdot, -). \quad (4.10)$$

The four non-local correlations given by these equations are evaluated and shown graphically in FIG. 4.5.

At $\theta_J = 0^\circ$, since only X_A and X'_B are measured accurately and the sensitivity is zero for Y_A and Y'_B , the values of the three non-local correlations other than $\langle X_A X'_B \rangle$ are zero. Similarly, at $\theta_J = 90^\circ$, only Y_A and Y'_B are measured, so the values of correlations other

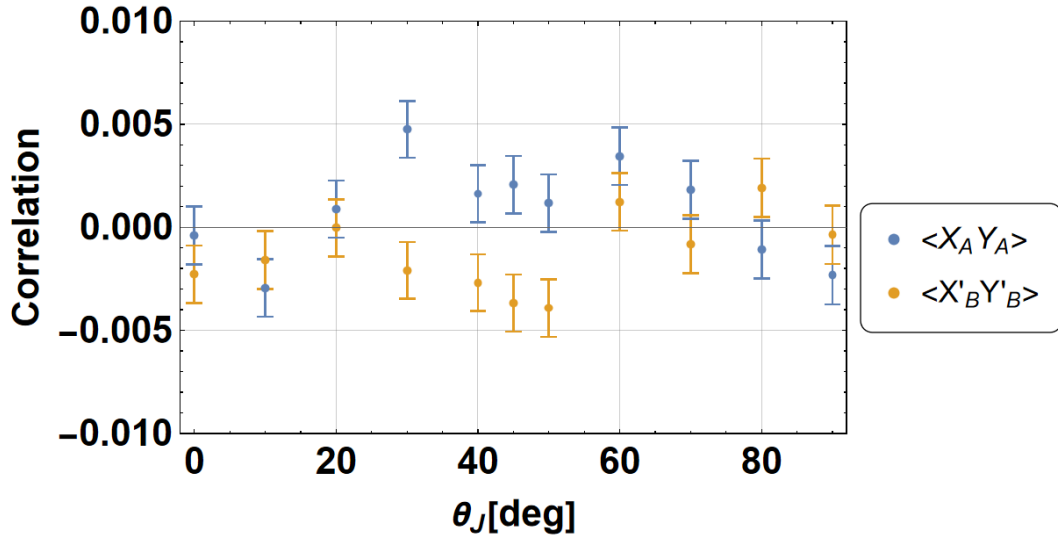


FIGURE 4.6: Local correlations against the joint measurement parameter. Blue dots show the local correlation of the complementary polarizations in system A, yellow dots show the one in system B.

than $\langle Y_A Y'_B \rangle$ are zero. If any one of the four non-local correlations in the Bell's inequality is measured accurately, the other three non-local correlations will be zero. As the joint measurement parameter approaches 45° , the other three non-local correlations that had zero values begin to increase or decrease. $\theta_J = 45^\circ$, the sensitivity of the measurement to the four polarization physical properties is the same, so the magnitudes of the four correlations are approximately the same, but the magnitude of their average value is smaller than the average value obtained by the precise measurement results (see Appendix B). How the measurement errors are related to the values of these correlations will be discussed in Chapter 6.

$\langle B \rangle$ can be evaluated by the sum or difference of the four correlations, or from the probability $P(b = +2)$ and the probability $P(b = -2)$. The values of the four non-local correlations and the average value of B derived from them are summarized in TAB. 4.6. The $\langle B \rangle$ does not exceed 2, which is not surprising since it is the average value

TABLE 4.6: Results of the joint measurement when an eigenstate is prepared in which the eigenvalue of a physical quantity is +1.

$\theta_J [deg]$	$\langle X_A X'_B \rangle$	$\langle X_A Y'_B \rangle$	$\langle Y_A X'_B \rangle$	$\langle Y_A Y'_B \rangle$	$\langle B \rangle$
0	-0.7080 ± 0.0014	0.0016 ± 0.0014	-0.0009 ± 0.0014	-0.0005 ± 0.0014	-0.7110 ± 0.0028
10	-0.6936 ± 0.0014	0.1168 ± 0.0014	-0.1078 ± 0.0014	-0.0240 ± 0.0014	-0.9422 ± 0.0028
20	-0.6252 ± 0.0014	0.2181 ± 0.0014	-0.2160 ± 0.0014	-0.0809 ± 0.0014	-1.1402 ± 0.0028
30	-0.5392 ± 0.0014	0.2898 ± 0.0014	-0.2902 ± 0.0014	-0.1742 ± 0.0014	-1.2934 ± 0.0028
40	-0.4174 ± 0.0014	0.3374 ± 0.0014	-0.3322 ± 0.0014	-0.2828 ± 0.0014	-1.3698 ± 0.0028
45	-0.3603 ± 0.0014	0.3422 ± 0.0014	-0.3332 ± 0.0014	-0.3426 ± 0.0014	-1.3782 ± 0.0028
50	-0.3008 ± 0.0014	0.3302 ± 0.0014	-0.3267 ± 0.0014	-0.4087 ± 0.0014	-1.3664 ± 0.0028
60	-0.1771 ± 0.0014	0.2933 ± 0.0014	-0.2944 ± 0.0014	-0.5161 ± 0.0014	-1.2809 ± 0.0028
70	-0.0849 ± 0.0014	0.2133 ± 0.0014	-0.2137 ± 0.0014	-0.6173 ± 0.0014	-1.1292 ± 0.0028
80	-0.0188 ± 0.0014	0.1186 ± 0.0014	-0.1169 ± 0.0014	-0.6722 ± 0.0014	-0.9265 ± 0.0028
90	0.0007 ± 0.0014	-0.0017 ± 0.0014	-0.0015 ± 0.0014	-0.7004 ± 0.0014	-0.6996 ± 0.0028

of $b = \pm 2$. Introducing an uncertainty limited joint measurement of complementary physical properties does not cause the Bell's inequality violation.

Since the joint statistical distribution obtained in the experiment contains information on all four polarizations, we can also obtain local correlations as shown in FIG. 4.6. It

is certain that the local correlations have values less than 0.01 for all values of the θ_j . It is interesting that it is an opposite relation where the non-local correlation shows large values while the local correlation is small. The meaning of these behavior will also be discussed in Chapter 6.

Chapter 5

Experimental results for the quantum state preparation by adaptive input state control

5.1 Optimization of ϕ_M

Quantum correlations describe the relation between different measurement contexts, related by quantum coherence. The optimization of the ϕ_M exploits exactly such quantum correlations. Eq. (2.17) and Eq. (2.18) are satisfied in the experiment for the optimization of the ϕ_M . Since the quantum states of the photon pairs produced by the entanglement source are symmetric with respect to the exchange between systems A and B, if one of the two conditions is satisfied, the other is automatically satisfied ideally. Therefore, we determine the ϕ_M so that the detection frequency of the two measurement outcomes (0;0) and (0;1) is the same as explained in Subsec. 2.2.2.

The ϕ_M can be controlled by HWP2 in FIG. 3.4 and is the angle of rotation from H polarization of the local linear polarization. Thus, $\phi_M = 0^\circ$ is equivalent to H polarization and $\phi_M = 45^\circ$ is equivalent to P polarization; the angle of the ϕ_M always represents the eigenstate $|0\rangle$ of $f = -1$, which can be used as a reference for the eigenstates of \hat{F} and \hat{W} . To maintain symmetry between systems 1 and 2, the set angles of HWP2 for systems A and B are adjusted so that they are always the same. If the ϕ_S is fixed to a certain value and then the ϕ_M is rotated, the ϕ_M will appear such that the detection frequency of (0;0) and (0;1) is the same. To accurately determine such a ϕ_M , we obtain three counts in each neighborhood of the ϕ_M such that $N(0;0) \approx N(0;1)$. Since the difference between the three ϕ_M is small, we assume that the rate of change of (0;0) and (0;1) relative to the ϕ_M is constant and fit each with a linear function. Fitting each of them with a linear function, the intersection of the fitting results of (0;0) and (0;1) should give the optimal ϕ_M for a particular ϕ_S .

As an example, FIG. 5.1 shows a graph evaluating the optimal ϕ_M when $\phi_S = 22.5^\circ$ is fixed. The fitting lines for the two data points (0;0) and (0;1) intersect at $\phi_M = 31.4^\circ$, which exactly represents the optimal ϕ_M for $\phi_S = 22.5^\circ$. Such an analysis was performed for nine points, $\phi_S = 0, 10, 17.5, 20, 22.5, 25, 27.5, 35, 45[deg]$, and the results of evaluating the optimal ϕ_M for each ϕ_S are shown in TAB. 5.1. The optimal ϕ_M are shown on the order of 0.1 because the resolution of HWP2 is roughly 0.2° .

Whether $P(0;a)$ and $P(a;0)$ are really small values can be checked according to the optimal ϕ_M shown in TAB. 5.1 by actually evaluating these probabilities. The results of the probabilities are presented in Sec. 5.3.

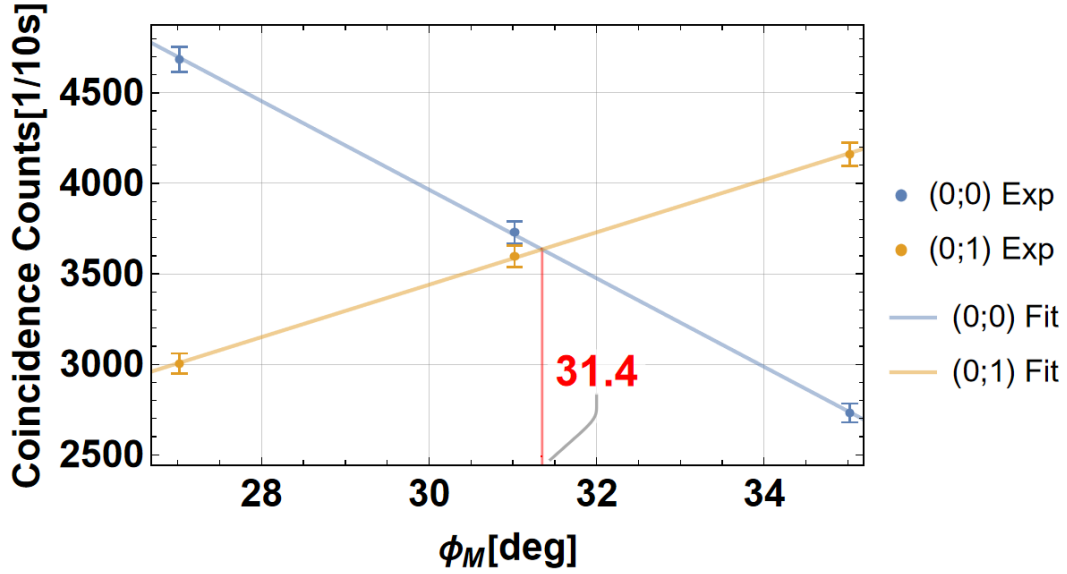


FIGURE 5.1: Variation of (0;0) and (0;1) and optimal ϕ_M results when $\phi_S = 22.5^\circ$ is fixed. The blue and yellow data points are the counts per 10[s] of (0;0) and (0;1), respectively, and the blue and yellow lines are the results of linear fitting to the respective data points; since the resolution of the HWP2 setting angle for setting ϕ_M is $\approx 0.2^\circ$, the optimal ϕ_M value is shown to the first decimal place.

TABLE 5.1: Results of optimal ϕ_M against each ϕ_S . These results are measurement results, and also setting value of the ϕ_M . This is the reason why they are shown without errors.

ϕ_S [deg]	ϕ_M [deg]
0	46.3
10	38.8
17.5	33.7
20	32.7
22.5	31.3
25	30.5
27.5	29.5
35	26.7
45	22.2

5.2 Optimization of ϕ_S

The optimization of ϕ_S is achieved by measuring $(1;1)$ in the range $0^\circ \leq \phi_S \leq 45^\circ$ and finding the ϕ_S such that its probability is minimized. Since we evaluated the optimal ϕ_M for nine ϕ_S as shown in TAB. 5.1, it is possible to predict what linear polarizations $f = 0,1$ and $w = a,b$ correspond to at each point. TAB. 5.2 shows the raw data of the counts obtained in the experiment.

TABLE 5.2: Absolute counts with respect to $(f_A; f_B)$, $(f_A; w_B)$, $(w_A; f_B)$ and (w_A, w_B) for each ϕ_S . All counts were obtained from a 10-second measurement.

$\phi_S[\text{deg}]$	$N(0;0)$	$N(0;1)$	$N(1;0)$	$N(1;1)$	$N(0;a)$	$N(0;b)$	$N(1;a)$	$N(1;b)$
0	3431	2989	3484	3354	88	5933	81	6119
10	3201	3377	3556	954	88	6510	564	4120
17.5	3527	3560	3979	231	125	7071	1442	2727
20	3496	3465	3993	155	113	7114	1782	2299
22.5	3688	3638	3661	172	118	7240	2159	1862
25	3624	3573	3967	240	145	7293	2492	1635
27.5	3952	3917	3977	285	136	7723	2990	1440
35	3631	3609	3803	1002	163	7020	4105	584
45	3565	3394	3408	3513	136	6444	6401	114

$\phi_S[\text{deg}]$	$N(a;0)$	$N(a;1)$	$N(b;0)$	$N(b;1)$	$N(a;a)$	$N(a;b)$	$N(b;a)$	$N(b;b)$
0	36	38	6223	5824	40	38	95	12072
10	95	417	6453	3788	304	144	292	10224
17.5	79	1353	7323	2519	752	608	774	9123
20	79	1616	7264	2237	959	756	870	8649
22.5	71	2086	7501	1748	1148	959	1098	8196
25	98	2380	7434	1511	1357	1112	1210	7791
27.5	97	2850	7842	1359	1586	1357	1579	7697
35	106	4083	7199	671	2153	1964	2037	5691
45	123	6317	6107	144	3430	3370	3318	3483

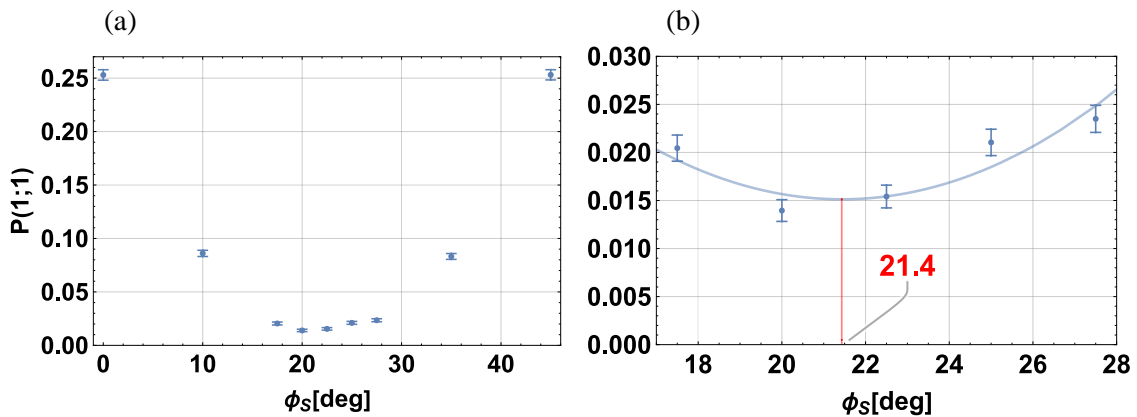


FIGURE 5.2: (a) Values of $P(1;1)$ for nine ϕ_S . (b) Fitting results with quadratic functions for five points near $\phi_S = 22.5^\circ$.

$P(1;1)$ was evaluated based on the relation given by

$$P(1;1) = \frac{N(1;1)}{N(0;0) + N(0;1) + N(1;0) + N(1;1)}. \quad (5.1)$$

FIG. 5.1(a) shows that the ϕ_S such that $P(1;1)$ is a minimum is near the middle of the product state and the maximally entanglement state. Judging only from the measured values, the minimum value of $P(1;1)$ is $P(1;1) = 0.0140 \pm 0.0011$ at $\phi_S = 20^\circ$. One way to determine the optimal ϕ_S in this situation was to fit the five data points near the center with a quadratic function. The minimum value of $P(1;1)$ indicated by the fitting results was $P(1;1) = 0.0151 \pm 0.0016$ at $\phi_S = 21.4^\circ$ as shown in FIG. 5.1 (b). If the measurement outcomes were completely random, the probability would be 0.25, so the deviation from the ideal situation is

$$\frac{0.25 - (0.0151 \pm 0.0016)}{0.25} = 0.940 \pm 0.006. \quad (5.2)$$

This value is consistent with the value of $\sqrt{C_X^2 + W_E^2}$ in TAB. 3.4 at $\phi_S = 20^\circ, 22.5^\circ$. The optimal ϕ_M corresponding to this point was not evaluated experimentally, but can be evaluated by the method described in Sec. 5.1.

5.3 Probabilities in several measurement context

TAB. 5.2 can provide sixteen joint probabilities obtained from a total of four eigenstate combinations of \hat{F} and \hat{W} . All joint probabilities should reflect the contextual correlation of the initial states. Therefore, in this section, we discuss the relation between the different measurement contexts and their consistency with the assumed three deterministic conditions.

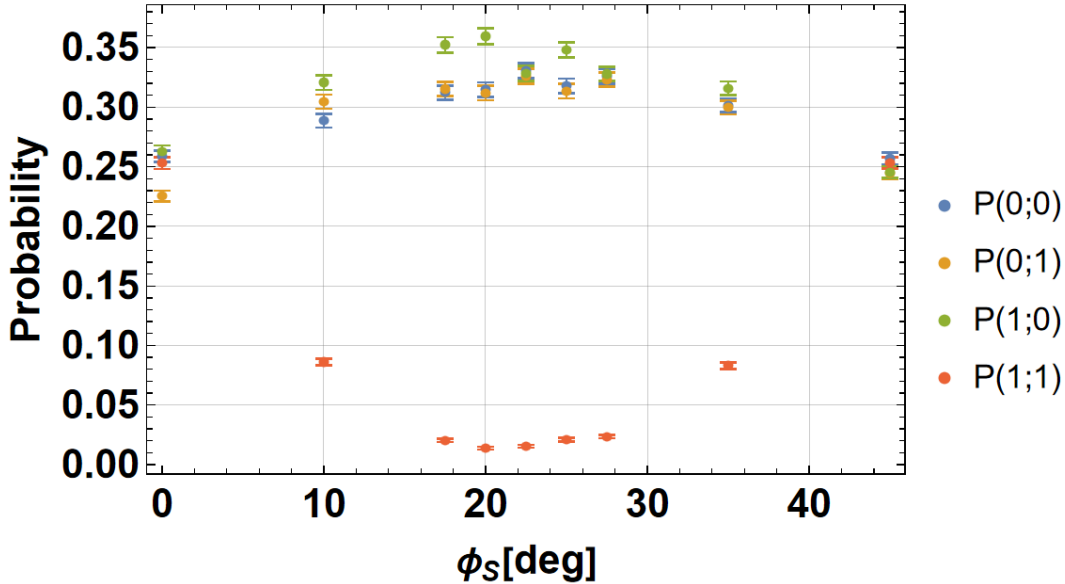


FIGURE 5.3: Probability measured using $\{0,1\}$ -basis in systems A and B. $\phi_S = 0^\circ$ represents the product state and $\phi_S = 45^\circ$ the maximum entangled state.

Since the $\{0,1\}$ -basis was only used to prepare the quantum state satisfying the three conditions shown in Eqs. (2.17)-(2.19), the imperfections of the experimental setup is

easily understandable in the results using the $\{0, 1\}$ -basis for both system A and B. FIG. 5.3 shows the results for $P(f_A; f_B)$. Since the optimal ϕ_M such that $N(0; 0) \approx N(0; 1)$ is satisfied was found, $P(0; 0)$ and $P(0; 1)$ agree within the margin of error except for two points at $\phi_S = 0^\circ, 10^\circ$. Although there is naturally a possibility that there was some human error with respect to the two points of $\phi_S = 0, 10[\text{deg}]$, it can be seen that $P(0; 0)$ and $P(0; 1)$ are in good agreement, at least in the neighborhood of ϕ_S where $P(1; 1)$ is the minimum value. On the other hand, just because $P(0; 0)$ and $P(0; 1)$ agree does not mean that $P(0; 0)$ and $P(1; 0)$ agree; the nine data points show no systematic trend as to whether $P(0; 0)$ and $P(1; 0)$ agree, which may be caused by some systematic errors. One of the most suspicious causes is the calibration method of HWP1 in FIG. 3.4. HWP1 defines $\phi_S = 45^\circ$ as the angle at which the ratio of transmitted to reflected light intensity at DPBS is the same. The phase difference that HWP1 gives to the pump light is not exactly π , so the systematic error is largest when $\phi_S = 0^\circ$. To reduce this discrepancy between $P(0; 0)$ and $P(1; 0)$, an adjustment method without using the assumption that system A and B are symmetrical is desirable. The true benefit of AISC can only be realized when idealistic assumptions can be completely removed from the total manipulations.

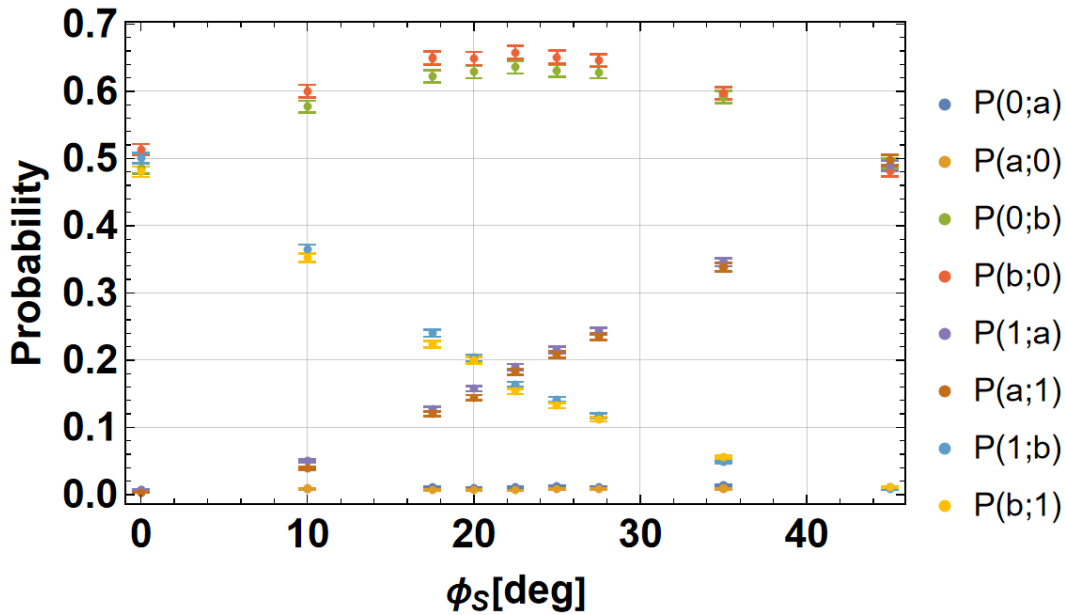


FIGURE 5.4: Probability measured using $\{0, 1\}$ -basis in one system, using $\{a, b\}$ -basis in the other system. $\phi_S = 0^\circ$ represents the product state and $\phi_S = 45^\circ$ the maximum entangled state.

FIG. 5.4 shows the probability results when one of the systems uses the $\{0, 1\}$ -basis and the other uses the $\{a, b\}$ -basis. The most important thing is that the two probability values, $P(0; a)$ and $P(a; 0)$, are extremely small. This indicates that it is possible to achieve $P(0; a) \approx P(a; 0) \approx 0$, causing a destructive interference effect by means of an adjustment method such that $N(0; 0) \approx N(0; 1)$. While in the past, one would have to reconcile statistics obtained in different measurement contexts to confirm the existence of quantum correlations, this result shows that one can control for quantum correlations using only results obtained in one measurement context, provided that only the relation between the contexts is known. This fact provides an important clue for the experimental study of quantum contextuality. TAB. 5.3 presents numerical data for $P(0; a)$ and $P(a; 0)$. Interestingly, $P(a; 0)$ is lower than $P(0; a)$. Since ϕ_M was determined so that $N(0; 0) \approx N(0; 1)$, one would intuitively expect $P(0; a)$ to be smaller than $P(a; 0)$. A discussion of under what conditions this could happen is given in Chapter 6. Another interesting point is

that the results for $P(1;a)$ or $P(a;1)$ and $P(1;b)$ or $P(b;1)$ do not coincide at $\phi_S = 22.5^\circ$. A visual reading from the graph suggests that the results of $P(1;a)$ or $P(a;1)$ and $P(1;b)$ or $P(b;1)$ have an intersection between $\phi_S = 20^\circ$ and $\phi_S = 22.5^\circ$. This is consistent with the result in FIG. 5.2 that the optimal ϕ_S value was slightly biased toward the product state.

TABLE 5.3: Numerical results of $P(0;a)$ and $P(a;0)$ for nine ϕ_S .

$\phi_S[\text{deg}]$	$P(0;a)$	$P(a;0)$
0	0.0072 ± 0.0008	0.0030 ± 0.0005
10	0.0078 ± 0.0008	0.0088 ± 0.0009
17.5	0.0110 ± 0.0010	0.0070 ± 0.0008
20	0.0100 ± 0.0009	0.0071 ± 0.0008
22.5	0.0104 ± 0.0010	0.0062 ± 0.0007
25	0.0125 ± 0.0010	0.0086 ± 0.0009
27.5	0.0111 ± 0.0010	0.0080 ± 0.0008
35	0.0137 ± 0.0011	0.0088 ± 0.0009
45	0.0104 ± 0.0009	0.0097 ± 0.0009

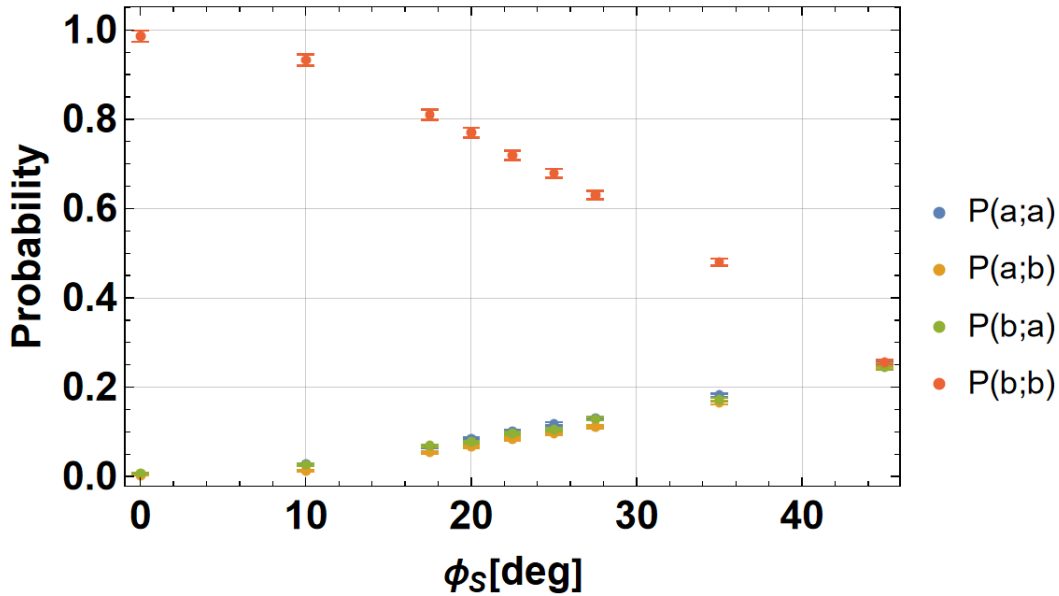


FIGURE 5.5: (a) Values of $P(1;1)$ for nine ϕ_S . (b) Fitting results with quadratic functions for five points near $\phi_S = 22.5^\circ$.

FIG. 5.5 shows the results of probabilities measured using the $\{a, b\}$ -basis for both systems A and B. The fact that all but $P(b;b)$ appear to show the same probabilities can be understood from the results of FIG. 5.4. Since $(b;b)$ can be considered to be the result of constructive interference between $(b;0)$ and $(b;1)$, $P(b;b)$ can be considered to be the sum of $P(b;0)$ and $P(b;1)$. TAB. 5.2 shows that when $\phi_S = 0^\circ$, the sum of the counts of $(b;0)$ and $(b;1)$ is indeed equal to the count of $(b;b)$. However, this way of thinking appears to break down significantly at $\phi_S = 45^\circ$. At $\phi_S = 45^\circ$, the sum of the counts of $(b;0)$ and $(b;1)$ does not equal the count of $(b;b)$. Interference is strongest only when two waves that can interfere are present with equal strength. Since the counts of $(b;1)$ are not large enough to interfere, $(b;b)$ is eventually detected at a frequency about the average of $(b;0)$ and $(b;1)$. Since the counts of $(a;1)$ and $(b;0)$ are almost equal in terms of counts, constructive interference would result in a large frequency of detection, but when the $\{a, b\}$ basis is used in both system A and B, there is no interference because it is possible to distinguish $(a;1)$ and $(b;0)$ with 100% accuracy. In the end, the $(a;1)$ and $(b;0)$ counts are equally distributed among the four measurement outcomes in the (a, b) basis.

$(a;a)$ is the result of destructive interference between $(a,0)$ and $(a;1)$, and $(a;b)$ is the result of constructive interference between $(a;0)$ and $(a;1)$, while $(a;0)$ is barely detected in all ϕ_S . As a result, $(a;0)$ and $(a;1)$ can hardly interfere, so the results of destructive and constructive interference are the almost same. For the same reason, the interference between $(a;0)$ and $(b;0)$ has almost the same destructive and constructive interference results. This is the reason why $P(a;a) \approx P(a;b) \approx P(b;a)$ is satisfied in FIG. 5.5.

Chapter 6

Discussion and consideration

6.1 On the joint probability distributions resulting in Bell's inequality violation observed from the joint measurements

In Chapter 4, we presented the features of the joint measurements and the joint statistical distribution obtained in the experiment to verify Bell's inequality, which introduced the joint measurements. We first discuss what physics can be read from the directly obtained joint statistical distributions. Since the experimentally controlled parameters are those that determine the balance of measurement errors of the complementary polarization physical properties, some relation should be found between the measurement outcomes and the counts. We then evaluate the flipping probabilities of the four physical properties using the spin-flip model (see Appendix E) based on the results of measurement visibilities, and discuss how the intrinsic joint probability distribution, which is a joint probability distribution excluding measurement errors, takes shape and how the expected values of the physical properties change, and we find an experimental evidence that the Cirel'son bound is an upper bound on the EPR correlation. We also discuss the consistency of quantum mechanics with experimental results.

6.1.1 Relation between the joint statistical distributions and the measurement visibilities

In this subsection, we discuss the relation between the measurement visibilities shown in Sec. 4.1 and the joint statistical distribution shown in Sec. 4.2. The change in the joint statistical distribution with changes in the joint measurement parameters can be illustrated by the competitive process between the four Bell correlations in FIG. 4.5.

Let's look at the process between $\theta_j = 0^\circ$ and $\theta_j = 20^\circ$. The rate of change of $\langle X_A Y'_B \rangle$ and $\langle Y_A Y'_B \rangle$ is roughly ± 0.2 , while the rate of change of $\langle X_A X'_B \rangle$ and $\langle Y_A X'_B \rangle$ have a rate of change of about ± 0.1 , roughly only half. Therefore, for the period between $\theta_j = 0^\circ$ and $\theta_j = 20^\circ$, $\langle X_A Y'_B \rangle$ and $\langle Y_A X'_B \rangle$ are the dominant factors that determine the changes in the joint statistical distribution. In FIG. 4.4, looking at the distribution of $\theta_j = 20^\circ$ with respect to the distribution of $\theta_j = 0^\circ$, the counts of the two measurement outcomes $(+, +; +, -)$ and $(-, -; -, +)$ are extremely reduced. What these two measurement outcomes have in common is that $x_A x'_B = +1$, $x_A y'_B = -1$, $y_A x'_B = +1$ and $y_A y'_B = -1$. Looking at the two Bell correlations that have a particularly dominant influence, the $\langle X_A Y'_B \rangle$ increases and $\langle Y_A X'_B \rangle$ decreases. The increase in Bell correlation means that the counts of measurement outcomes with $+1$ increases, and the counts of measurement outcomes with -1 decreases. Conversely, a decrease in Bell correlation gives the opposite result. From these things, an increase in $\langle X_A Y'_B \rangle$ decreases the count of measurement outcomes with $x_A y'_B = -1$, and a decrease in $\langle Y_A X'_B \rangle$ decreases the

count of measurement outcomes with $y_A x'_B = +1$. Thus, the counts of the two measurement outcomes, $(+, +; +, -)$ and $(-, -; -, +)$, decrease because the two Bell correlations, which have a dominant influence, both have a decreasing effect. Conversely, if we look for the measurement outcomes with a large increase in counts, the two outcomes $(+, -; +, +)$ and $(-, +; -, -)$ would fall into this category. Since both of these measurements have $x_A y'_B = +1$ and $y_A x'_B = -1$, they have opposite values to the $(+, +; +, -)$ and $(-, -; -, +)$ cases. This means that the two dominant Bell correlations influence the counts to increase, so the counts for $(+, -; +, +)$ and $(-, +; -, -)$ increased significantly.

Next, let's look at the process between $\theta_J = 20^\circ$ and $\theta_J = 45^\circ$. As can be seen in FIG. 4.5 and TAB. 4.6, the magnitude of the rate of change of $\langle X_A X'_B \rangle$ and $\langle Y_A Y'_B \rangle$ in this interval is larger than that of $\langle X_A Y'_B \rangle$ and $\langle Y_A X'_B \rangle$, so the influence of $\langle X_A X'_B \rangle$ and $\langle Y_A Y'_B \rangle$ becomes dominant. Looking at the joint probability distribution of $\theta_J = 20^\circ$ as a standard, there are two measurement outcomes with a large decrease in counts, $(-, +; +, +)$ and $(+, -; -, -)$. Both outcomes commonly satisfy $x_A x'_B = -1$ and $y_A y'_B = +1$. Between $\theta_J = 20^\circ$ and $\theta_J = 45^\circ$, $\langle X_A X'_B \rangle$ increases and $\langle Y_A Y'_B \rangle$ is decreasing, so the count of outcomes that result in $x_A x'_B = -1$ is decreasing, and the count of outcomes that result in $y_A y'_B = +1$ is also decreasing. Because the dominant influences $\langle X_A X'_B \rangle$ and $\langle Y_A Y'_B \rangle$ both influence the counts to decrease, the counts of $(-, +; +, +)$ and $(+, -; -, -)$ are greatly decreased.

By thinking in the same way, the behavior of all other outcomes in the range $\theta_J = 45^\circ$ to $\theta_J = 90^\circ$ is also consistent with the measurement results of the four Bell correlations. The measurement outcomes with extremely low counts can also be seen in $(-, +; +, +)$ and $(+, -; -, -)$ at $\theta_J = 70^\circ$. The four measurement outcomes with extremely low counts are discussed in more detail in the other section below.

Strictly speaking, the changes in the counts of the sixteen measurement outcomes are not determined solely by the influence of the two dominant Bell correlations, but must take into account the influence of the other two Bell correlations. The change in the counts of the sixteen measurement outcomes is determined by the competitive process of changes in the four Bell correlations.

The variation in the four Bell correlations themselves can be explained by the measurement visibility. As shown in FIG. 4.3, there is a clear trade-off between the measurement visibility given by

$$V_{X_A} = V_{X'_B} = \cos \theta_J \quad (6.1)$$

$$V_{Y_A} = V_{Y'_B} = \sin \theta_J. \quad (6.2)$$

Since the measurement visibility depends only on the measurement device, the measurement visibility of system A and B independently affect the Bell correlation. Therefore, $\langle X_A X'_B \rangle \propto \cos^2 \theta_J$, $\langle X_A Y'_B \rangle = -\langle Y_A X'_B \rangle \propto \sin \theta_J \cos \theta_J$, $\langle Y_A Y'_B \rangle \propto \sin^2 \theta_J$. Since $\cos^2 \theta_J$ and $\sin^2 \theta_J$ eventually change in the same way as $\cos 2\theta_J$, the magnitude of the rate of change of $\langle X_A X'_B \rangle$ and $\langle Y_A Y'_B \rangle$ is the same, the one of $\langle X_A Y'_B \rangle$ and $\langle Y_A X'_B \rangle$ is the same. Furthermore, when changing from $\theta_J = 0^\circ$ to $\theta_J = 90^\circ$, the measurement visibility for X_A and X'_B continues to decrease, while the measurement visibility for Y_A and Y'_B continues to increase. This is the reason why the absolute value of the $\langle X_A X'_B \rangle$ shows monotonically decreasing and the absolute value of the $\langle Y_A Y'_B \rangle$ monotonically increasing. On the other hand, $\langle X_A Y'_B \rangle$ and $\langle Y_A X'_B \rangle$ are proportional to $\sin 2\theta_J$ and therefore have extreme values at the point $\theta_J = 45^\circ$.

Thus, it can be seen that the joint statistical distribution, the change in the four Bell correlations, and the measurement visibility are closely related.

6.1.2 Flipping probability of the four polarization physical properties

The relation between the joint probabilities obtained by joint measurements, including measurement error, and the joint probabilities without the influence of measurement error can be related using measurement visibility (see Appendix E). The relation between the flipping probability of a physical property in a two-level system and the measurement visibility for that physical property is given by

$$P_{\Xi flip} = \frac{1}{2} (1 - V_{\Xi}), \quad (6.3)$$

where $\Xi = X_A, Y_A, X'_B, Y'_B$ is the physical property, V_{Ξ} is the measurement visibility of Ξ , which is defined by Eq. (2.1), $P_{\Xi flip}$ is the flipping probability of Ξ . Using Eq. (6.3) and the experimental results for the measurement visibility shown in TAB. 4.5, the flipping probabilities for the four physical properties are evaluated as shown in TAB. 6.1. The

TABLE 6.1: Numerical results of the flipping probability of X_A, Y_A, X'_B, Y'_B .

θ_j [deg]	$P_{X_A flip}$	$P_{Y_A flip}$	$P_{X'_B flip}$	$P_{Y'_B flip}$
0	0.0017 ± 0.0033	0.5000 ± 0.0014	0.0038 ± 0.0033	0.5000 ± 0.0014
10	0.0097 ± 0.0033	0.4161 ± 0.0015	0.0108 ± 0.0033	0.4143 ± 0.0015
20	0.0318 ± 0.0031	0.3306 ± 0.0017	0.0337 ± 0.0031	0.3284 ± 0.0017
30	0.0687 ± 0.0029	0.2488 ± 0.0021	0.0695 ± 0.0029	0.2509 ± 0.0021
40	0.1175 ± 0.0027	0.1796 ± 0.0024	0.1200 ± 0.0027	0.1784 ± 0.0024
45	0.1406 ± 0.0026	0.1506 ± 0.0025	0.1466 ± 0.0025	0.1470 ± 0.0025
50	0.1789 ± 0.0024	0.1179 ± 0.0027	0.1793 ± 0.0024	0.1152 ± 0.0027
60	0.2488 ± 0.0020	0.0680 ± 0.0030	0.2514 ± 0.0020	0.0645 ± 0.0030
70	0.3311 ± 0.0017	0.0306 ± 0.0032	0.3287 ± 0.0017	0.0281 ± 0.0032
80	0.4150 ± 0.0015	0.0089 ± 0.0033	0.4141 ± 0.0015	0.0037 ± 0.0033
90	0.5000 ± 0.0014	-0.0002 ± 0.0033	0.5000 ± 0.0014	-0.0027 ± 0.0034

flipping probabilities of X_A and X'_B are identical, and the flipping probabilities of Y_A and Y'_B are identical. As shown in FIG. 4.1, this is a natural result since the joint measurement parameters used in systems A and B are common. At $\theta_j = 0^\circ$ and $\theta = 90^\circ$, two of the four physical properties have a flipping probability of 0 and the other two have a flipping probability of 0.5. A flipping probability of 0 means that the measurement results are almost never inverted, which means that the statistics obtained in the joint measurement are almost identical to those obtained in the precise measurement. On the other hand, a flipping probability of 0.5 means that half of the time the measurement results are inverted, which means that the results obtained are completely random. Thus, the measurement visibility and the flipping probability are well consistent in a physical meaning.

6.1.3 Relation between the flipping probability of B and the joint probability distribution

In FIG. 4.4, the joint statistical distribution at $\theta_j = 45^\circ$ depends only on the value of b . Therefore, let us define the probability of a measurement outcome with $b = +2$ as $p(b = +2)$ and the probability of a measurement outcome with $b = -2$ as $p(b = -2)$, where the expression given by

$$8p(b = +2) + 8p(b = -2) = 1 \quad (6.4)$$

is hold. Since $\theta_J = 45^\circ$ means that the four polarization properties were measured with the same uncertainty, an intrinsic joint probability distribution, which is a distribution excluding measurement errors, has the same form as the experimentally obtained joint probability distribution, characterized by only two probabilities $p_{int}(b = +2)$ and $p_{int}(b = -2)$. Since the value of the B takes only two values of $b = \pm 2$, the bit-flip model (see Appendix E) results in the relations given by

$$p(b = +2) = (1 - P_{Bflip}) \cdot p_{int}(b = +2) + P_{Bflip} \cdot p_{int}(b = -2) \quad (6.5)$$

$$p(b = -2) = P_{Bflip} \cdot p_{int}(b = +2) + (1 - P_{Bflip}) \cdot p_{int}(b = -2), \quad (6.6)$$

where P_{Bflip} is a flipping probability of the b . In general, it is natural to assume that the flipping probability varies depending on the results of each of the sixteen measurement outcomes, but in the case of $\theta_J = 45^\circ$, it can be described by just one value because the measurements for the four polarization physical properties are made with the same accuracy. From this, applying operator \hat{B} to the expression for the measurement visibility defined in Eq. (2.1), Eq. (E.3) provides

$$P_{Bflip} = \frac{1}{2} \left(1 - \frac{\langle B \rangle_{joint}}{\langle B \rangle_{precise}} \right). \quad (6.7)$$

As shown in TAB. 4.6, the mean value for $\theta_J = 45^\circ$ is $\langle B \rangle_{joint} = -1.3782 \pm 0.0028$, so assuming $\langle B \rangle_{precise}$ is Cirel'son bound results in $P_{Bflip} = 0.2565 \pm 0.0005$. Assuming the intrinsic joint probability distributions, the average of the B and a normalization condition are given by

$$2 \cdot 8p_{int}(b = +2) - 2 \cdot 8p_{int}(b = -2) = \langle B \rangle_{precise} \quad (6.8)$$

$$8p_{int}(b = +2) + 8p_{int}(b = -2) = 1. \quad (6.9)$$

Using Eq. (6.8) and Eq. (6.9), the relation between an intrinsic joint probability and the average of B is given by

$$p_{int}(b = \pm 2) = \frac{1}{16} \left(1 \pm \frac{\langle B \rangle_{precise}}{2} \right). \quad (6.10)$$

A probability evaluated from experiments is definitely equal or greater than zero, thus, Eq. (6.5) gives

$$P_{Bflip} \geq \frac{\langle B \rangle_{precise} + 2}{2\langle B \rangle_{precise}}. \quad (6.11)$$

The reason for using Eq. (6.5) rather than Eq. (6.6) is that the probability of a measurement result with $b = +2$ has a value closer to zero. Eq. (6.11) shows that if there is a lower bound of the flipping probability for the value of B , it is possible to find the upper bound of the violation of Bell's inequality. Deviating from $\theta_J = 45^\circ$, the values of B are the same, but the probabilities are different due to the different measurement uncertainties for the four physical properties. This shows that, in general, $P_{Bflip}(m)$ depends on the measurement outcomes, so let us denote $P_{Bflip}(m)$, where m is the specific measurement outcome, in the following. The flipping probability of the B value of an individual measurement outcome obtained in an experiment can be derived by considering the simultaneous flipping probabilities of the four polarization physical properties. For example, the measurement outcome $(+, +; +, +)$ has $b = +2$ and the measurement outcome $(+, -; +, +)$ has $b = -2$. If x_A, x'_B and y'_B are not flipped and only y_A is flipped, the

photon pair that should have been measured as $(+, +; +, +)$ is detected as $(+, -; +, +)$. This would be considered as an error in the value of B . Thus, for example, when evaluating $P_{Bflip}(+, +; +, +)$, the probability that $(+, +; +, +)$ would be detected as the result of eight other measurement outcomes with $b = -2$ is calculated. The concrete expression is given by

$$\begin{aligned}
 p_{Bflip}(\pm, \pm; \pm, \pm) &= \frac{1}{16}(1 + V_{X_A})(1 - V_{Y_A})(1 + V_{X'_B})(1 + V_{Y'_B}) \\
 &+ \frac{1}{16}(1 - V_{X_A})(1 - V_{Y_A})(1 + V_{X'_B})(1 + V_{Y'_B}) \\
 &+ \frac{1}{16}(1 - V_{X_A})(1 + V_{Y_A})(1 + V_{X'_B})(1 - V_{Y'_B}) \\
 &+ \frac{1}{16}(1 - V_{X_A})(1 - V_{Y_A})(1 + V_{X'_B})(1 - V_{Y'_B}) \\
 &+ \frac{1}{16}(1 + V_{X_A})(1 + V_{Y_A})(1 - V_{X'_B})(1 + V_{Y'_B}) \\
 &+ \frac{1}{16}(1 + V_{X_A})(1 - V_{Y_A})(1 - V_{X'_B})(1 + V_{Y'_B}) \\
 &+ \frac{1}{16}(1 + V_{X_A})(1 + V_{Y_A})(1 - V_{X'_B})(1 - V_{Y'_B}) \\
 &+ \frac{1}{16}(1 - V_{X_A})(1 + V_{Y_A})(1 - V_{X'_B})(1 - V_{Y'_B}) \\
 &= \frac{1}{4}(2 - V_{X_A}(V_{X'_B} - V_{Y'_B}) - V_{Y_A}(V_{X'_B} + V_{Y'_B})). \quad (6.12)
 \end{aligned}$$

The flipping probabilities which the other outcomes have are similarly given by

$$p_{Bflip}(\pm, \mp; \pm, \pm) = \frac{1}{4}(2 + V_{X_A}(V_{X'_B} - V_{Y'_B}) - V_{Y_A}(V_{X'_B} + V_{Y'_B})) \quad (6.13)$$

$$p_{Bflip}(\mp, \pm; \pm, \pm) = \frac{1}{4}(2 + V_{X_A}(V_{X'_B} - V_{Y'_B}) - V_{Y_A}(V_{X'_B} + V_{Y'_B})) \quad (6.14)$$

$$p_{Bflip}(\mp, \mp; \pm, \pm) = \frac{1}{4}(2 - V_{X_A}(V_{X'_B} - V_{Y'_B}) - V_{Y_A}(V_{X'_B} + V_{Y'_B})) \quad (6.15)$$

$$p_{Bflip}(\pm, \pm; \pm, \mp) = \frac{1}{4}(2 - V_{X_A}(V_{X'_B} + V_{Y'_B}) - V_{Y_A}(V_{X'_B} - V_{Y'_B})) \quad (6.16)$$

$$p_{Bflip}(\pm, \mp; \pm, \mp) = \frac{1}{4}(2 - V_{X_A}(V_{X'_B} + V_{Y'_B}) + V_{Y_A}(V_{X'_B} - V_{Y'_B})) \quad (6.17)$$

$$p_{Bflip}(\mp, \pm; \pm, \mp) = \frac{1}{4}(2 - V_{X_A}(V_{X'_B} + V_{Y'_B}) + V_{Y_A}(V_{X'_B} - V_{Y'_B})) \quad (6.18)$$

$$p_{Bflip}(\mp, \mp; \pm, \mp) = \frac{1}{4}(2 - V_{X_A}(V_{X'_B} + V_{Y'_B}) - V_{Y_A}(V_{X'_B} - V_{Y'_B})). \quad (6.19)$$

These flipping probabilities are shown in FIG. 6.1 and the numerical data in TAB. 6.2. The eight flipping probabilities of $(\pm, \mp; \pm, \pm)$, $(\mp, \pm; \pm, \pm)$, $(\pm, \pm; \pm, \mp)$, $(\mp, \mp; \pm, \mp)$ depend on the θ_J , while the flipping probabilities for the other eight measurements are nearly constant. FIG. 4.4 shows that the diagonal and anti-diagonal components are almost unchanged with respect to θ_J . On the other hand, the other components are changing. These dependencies are manifested in the changes in the flipping probability of B . The most noteworthy of these are Eq. (6.14) and Eq. (6.16). These four results are the ones that show extremely low counts at $\theta_J = 20^\circ$ and $\theta_J = 70^\circ$, since the flipping probability of B is the smallest among all the results. Eq. (6.11) can tell us the relation between these four low probabilities and the $\langle B \rangle_{precise}$. The lowest flipping probability in TAB. 6.2 is 0.1473 ± 0.0028 that $(\pm, \mp; \pm, \pm)$ and $(\mp, \pm; \pm, \pm)$ have at $\theta_J = 70^\circ$. Substituting

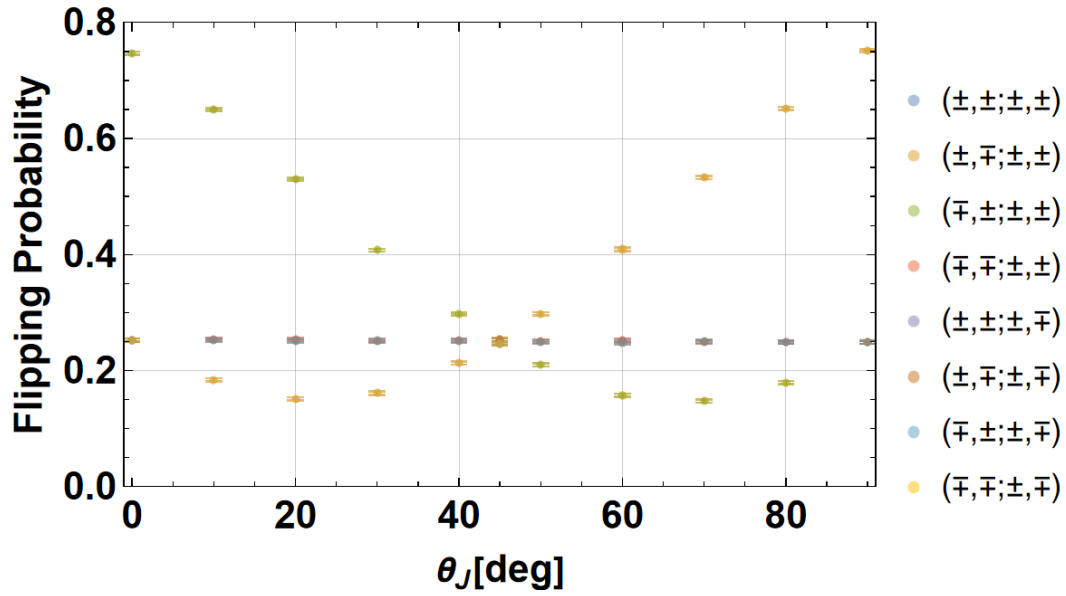


FIGURE 6.1: Value of flipping probability of B against the joint measurement parameter θ_J .

TABLE 6.2: Numerical results of the flipping probability of B that the sixteen outcomes have.

θ_J [deg]	$P_{\text{Bflip}}(\pm, \pm; \pm, \pm)$	$P_{\text{Bflip}}(\pm, \mp; \pm, \pm)$	$P_{\text{Bflip}}(\mp, \pm; \pm, \pm)$	$P_{\text{Bflip}}(\mp, \mp; \pm, \pm)$
0	0.2527 ± 0.0025	0.7473 ± 0.0025	0.7473 ± 0.0025	0.2527 ± 0.0025
10	0.2540 ± 0.0024	0.6496 ± 0.0024	0.6496 ± 0.0024	0.2540 ± 0.0024
20	0.2540 ± 0.0023	0.5300 ± 0.0023	0.5300 ± 0.0023	0.2540 ± 0.0023
30	0.2510 ± 0.0023	0.4076 ± 0.0023	0.4076 ± 0.0023	0.2510 ± 0.0023
40	0.2529 ± 0.0025	0.2975 ± 0.0025	0.2975 ± 0.0025	0.2529 ± 0.0025
45	0.2530 ± 0.0025	0.2533 ± 0.0025	0.2533 ± 0.0025	0.2530 ± 0.0025
50	0.2510 ± 0.0026	0.2099 ± 0.0026	0.2099 ± 0.0026	0.2510 ± 0.0026
60	0.2514 ± 0.0027	0.1575 ± 0.0027	0.1575 ± 0.0027	0.2514 ± 0.0027
70	0.2489 ± 0.0028	0.1473 ± 0.0028	0.1473 ± 0.0028	0.2489 ± 0.0028
80	0.2490 ± 0.0027	0.1792 ± 0.0027	0.1792 ± 0.0027	0.2490 ± 0.0027
90	0.2485 ± 0.0026	0.2485 ± 0.0026	0.2485 ± 0.0026	0.2485 ± 0.0026
θ_J [deg]	$P_{\text{Bflip}}(\pm, \pm; \pm, \mp)$	$P_{\text{Bflip}}(\pm, \mp; \pm, \mp)$	$P_{\text{Bflip}}(\mp, \pm; \pm, \mp)$	$P_{\text{Bflip}}(\mp, \mp; \pm, \mp)$
0	0.2527 ± 0.0025	0.2527 ± 0.0025	0.2527 ± 0.0025	0.2527 ± 0.0025
10	0.1843 ± 0.0027	0.2520 ± 0.0027	0.2520 ± 0.0027	0.1843 ± 0.0027
20	0.1514 ± 0.0028	0.2512 ± 0.0028	0.2512 ± 0.0028	0.1514 ± 0.0028
30	0.1613 ± 0.0029	0.2524 ± 0.0029	0.2524 ± 0.0029	0.1613 ± 0.0029
40	0.2129 ± 0.0029	0.2503 ± 0.0029	0.2503 ± 0.0029	0.2129 ± 0.0029
45	0.2460 ± 0.0028	0.2462 ± 0.0028	0.2462 ± 0.0028	0.2460 ± 0.0028
50	0.2980 ± 0.0028	0.2490 ± 0.0028	0.2490 ± 0.0028	0.2980 ± 0.0028
60	0.4089 ± 0.0027	0.2474 ± 0.0027	0.2474 ± 0.0027	0.4089 ± 0.0027
70	0.5325 ± 0.0026	0.2502 ± 0.0026	0.2502 ± 0.0026	0.5325 ± 0.0026
80	0.6521 ± 0.0026	0.2489 ± 0.0026	0.2489 ± 0.0026	0.6521 ± 0.0026
90	0.7515 ± 0.0026	0.2485 ± 0.0026	0.2485 ± 0.0026	0.7515 ± 0.0026

0.1473 ± 0.0028 for P_{Bflip} in Eq. (6.11), the upper bound of the absolute value of $\langle B \rangle_{precise}$ is given by

$$|\langle B \rangle_{precise}| \leq 2.835 \pm 0.023. \quad (6.20)$$

This result is consistent with Cirel'son bound $2\sqrt{2} \approx 2.8284$. The lowest flipping probability of \hat{B} should be determined by the measurement uncertainty limit, so that the maximal EPR correlation is limited by the measurement uncertainty.

To examine in more detail the measurement outcomes with small probabilities obtained by the joint measurement, we consider the relation between the probability obtained in the experiments and the flipping probability of B . Substituting Eq. (6.10) into Eq. (6.5), the linear relation between $p(b = +2)$ and $P_{Bflip}(m)$ is given by

$$p(b = +2) = \frac{1}{16} \left(-\langle B \rangle_{precise} P_{Bflip}(m) + \frac{2 + \langle B \rangle_{precise}}{2} \right). \quad (6.21)$$

Using the flipping probabilities of B shown in TAB. 6.2 and the joint probabilities obtained from FIG. 4.4, FIG. 6.2 shows the relation between the experimentally obtained probabilities and $P_{Bflip}(m)$ for the four measurement outcomes that showed extremely low counts in FIG. 4.4. All data points ride approximately on a straight line, and the result of linear fitting is

$$p(b = +2) = \frac{1}{16} \left((2.7526 \pm 0.0020) P_{Bflip}(m) + \frac{2 - (2.7526 \pm 0.0020)}{2} \right), \quad (6.22)$$

where $\langle B \rangle_{precise} = -2.7526 \pm 0.0020$. The ratio between the fitting result of $\langle B \rangle_{precise}$ and Cirel'son bound is given by

$$\frac{2.7526 \pm 0.0020}{2\sqrt{2}} = 0.9732 \pm 0.0007. \quad (6.23)$$

Note that this result is not obtained from the joint probabilities of probability distributions obtained at just one θ_J , but by averaging the joint probabilities obtained at different θ_J . The result in Eq. (6.1) is consistent with the interferometer visibilities shown in Eqs. (3.2)-(3.5). By extrapolation of the straight line obtained by fitting, the probability of a joint measurement such that $P_{Bflip}(m)$ is zero is

$$p_{int}(b = +2) = -0.02352 \pm 0.00006 \quad (6.24)$$

Thus, negative probabilities naturally appear as a result of the violation of Bell's inequality. In conventional experiments to verify Bell's inequality, only positive probabilities appeared because only one of the complementary physical properties was measured. The uncertainty limited joint measurement prevented the joint probabilities obtained in the actual experiment from being negative by providing the measurement with just enough uncertainty to barely hide the negative probabilities. If quantum correlations existed to the extent that the Cirel'son bound was exceeded, this would mean that the probabilities obtained in the actual experiment would be negative. This implies that the Cirel'son bound is the upper limit of Bell correlation.

6.1.4 Reconstruction of the intrinsic joint probabilities in one system

As stated in the definition for measurement visibility in Eq. (2.1), measurement visibility describes the relation between statistics with measurement error and statistics without

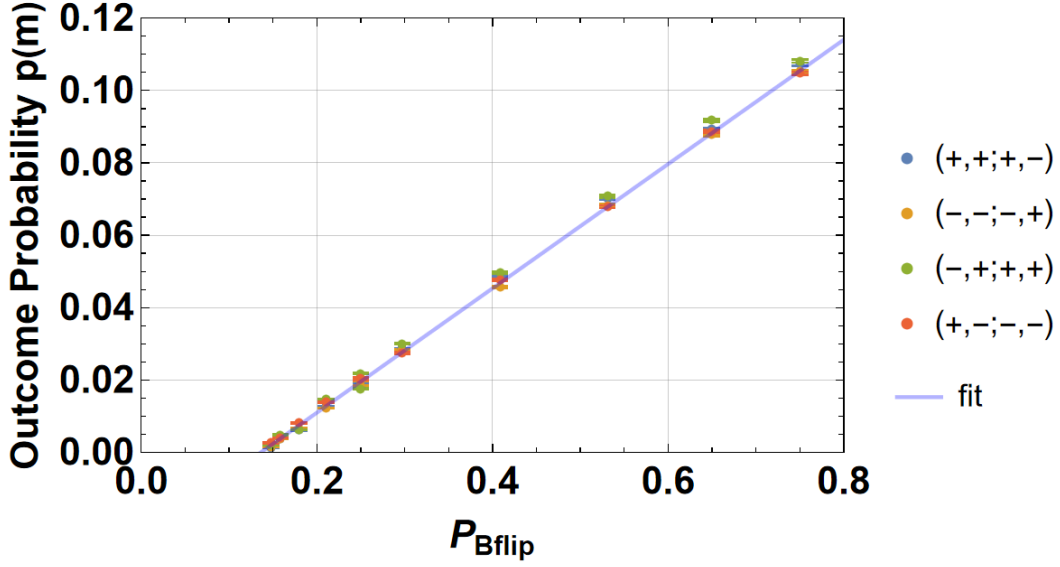


FIGURE 6.2: $(\mp, \pm; \pm, \pm), (\pm, \pm; \pm, \mp)$ for the flipping probability of B for each of the four measurements. The values on the horizontal axis are obtained by substituting Eq. (6.1) and Eq. (6.2) into Eq. (6.14) and Eq. (6.16), while the probabilities on the vertical axis are the joint probabilities derived from FIG. 4.4. Different $P_{Bflip}(m)$ corresponds to different θ_j . The fitting results were performed for all data points.

measurement error. Furthermore, since the measurement visibility is independent between system A and B, it is possible to reconstruct statistics without measurement error for either system A or B. By examining the effects of measurement error in System A and System B in this stepwise manner, we can examine in detail the relation between measurement visibility and statistics. In this subsection, we eliminate the effect of measurement error from the statistical distribution obtained for system A.

The measurement visibility defined by Eq. (2.1) provides

$$\begin{aligned} & P_{int}(+, +; x'_B, y'_B) + P_{int}(+, -; x'_B, y'_B) - P_{int}(-, +; x'_B, y'_B) - P_{int}(-, -; x'_B, y'_B) \\ &= \frac{1}{V_{X_A}} (P(+, +; x'_B, y'_B) + P(+, -; x'_B, y'_B) - P(-, +; x'_B, y'_B) - P(-, -; x'_B, y'_B)) \end{aligned} \quad (6.25)$$

$$\begin{aligned} & P_{int}(+, +; x'_B, y'_B) - P_{int}(+, -; x'_B, y'_B) + P_{int}(-, +; x'_B, y'_B) - P_{int}(-, -; x'_B, y'_B) \\ &= \frac{1}{V_{Y_A}} (P(+, +; x'_B, y'_B) - P(+, -; x'_B, y'_B) + P(-, +; x'_B, y'_B) - P(-, -; x'_B, y'_B)), \end{aligned} \quad (6.26)$$

where P_{int} is an intrinsic probability, which has no measurement errors. As shown in FIG. 4.6, the magnitude of the correlations of the complementary polarizations are less than 0.005, so they are very tiny values at least, so that they can be ignored. A correlation which the intrinsic joint probability distribution gives can be also regarded as zero because measurement uncertainty evenly increases or decreases the probability of the measurement outcomes; therefore, the correlation is given by

$$\begin{aligned} & P_{int}(+, +; x'_B, y'_B) - P_{int}(+, -; x'_B, y'_B) - P_{int}(-, +; x'_B, y'_B) + P_{int}(-, -; x'_B, y'_B) \\ &= 0. \end{aligned} \quad (6.27)$$

The normalization condition for the probability of system A provides

$$\begin{aligned} & P_{int}(+, +; x'_B, y'_B) + P_{int}(+, -; x'_B, y'_B) + P_{int}(-, +; x'_B, y'_B) + P_{int}(-, -; x'_B, y'_B) \\ &= P(+, +; x'_B, y'_B) + P(+, -; x'_B, y'_B) + P(-, +; x'_B, y'_B) + P(-, -; x'_B, y'_B). \end{aligned} \quad (6.28)$$

Summarized form of Eqs. (6.25)-(6.28) is given by

$$\begin{aligned} & \begin{pmatrix} 1 & 1 & -1 & -1 \\ 1 & -1 & 1 & -1 \\ 1 & -1 & -1 & 1 \\ 1 & 1 & 1 & 1 \end{pmatrix} \begin{pmatrix} P_{int}(+, +; x'_B, y'_B) \\ P_{int}(+, -; x'_B, y'_B) \\ P_{int}(-, +; x'_B, y'_B) \\ P_{int}(-, -; x'_B, y'_B) \end{pmatrix} \\ &= \begin{pmatrix} \frac{1}{V_{X_A}} & \frac{1}{V_{X_A}} & -\frac{1}{V_{X_A}} & -\frac{1}{V_{X_A}} \\ \frac{1}{V_{Y_A}} & -\frac{1}{V_{Y_A}} & \frac{1}{V_{Y_A}} & -\frac{1}{V_{Y_A}} \\ 0 & 0 & 0 & 0 \\ 1 & 1 & 1 & 1 \end{pmatrix} \begin{pmatrix} P(+, +; x'_B, y'_B) \\ P(+, -; x'_B, y'_B) \\ P(-, +; x'_B, y'_B) \\ P(-, -; x'_B, y'_B) \end{pmatrix} \end{aligned} \quad (6.29)$$

The inverse of the 4×4 matrix on the left side, acting on both sides from the left, gives

$$\begin{aligned} & \begin{pmatrix} P_{int}(+, +; x'_B, y'_B) \\ P_{int}(+, -; x'_B, y'_B) \\ P_{int}(-, +; x'_B, y'_B) \\ P_{int}(-, -; x'_B, y'_B) \end{pmatrix} \\ &= \frac{1}{4} \begin{pmatrix} \frac{1}{V_{X_A}} + \frac{1}{V_{Y_A}} + 1 & \frac{1}{V_{X_A}} - \frac{1}{V_{Y_A}} + 1 & -\frac{1}{V_{X_A}} + \frac{1}{V_{Y_A}} + 1 & -\frac{1}{V_{X_A}} - \frac{1}{V_{Y_A}} + 1 \\ \frac{1}{V_{X_A}} - \frac{1}{V_{Y_A}} + 1 & \frac{1}{V_{X_A}} + \frac{1}{V_{Y_A}} + 1 & -\frac{1}{V_{X_A}} - \frac{1}{V_{Y_A}} + 1 & -\frac{1}{V_{X_A}} + \frac{1}{V_{Y_A}} + 1 \\ -\frac{1}{V_{X_A}} + \frac{1}{V_{Y_A}} + 1 & -\frac{1}{V_{X_A}} - \frac{1}{V_{Y_A}} + 1 & \frac{1}{V_{X_A}} + \frac{1}{V_{Y_A}} + 1 & \frac{1}{V_{X_A}} - \frac{1}{V_{Y_A}} + 1 \\ -\frac{1}{V_{X_A}} - \frac{1}{V_{Y_A}} + 1 & -\frac{1}{V_{X_A}} + \frac{1}{V_{Y_A}} + 1 & \frac{1}{V_{X_A}} - \frac{1}{V_{Y_A}} + 1 & \frac{1}{V_{X_A}} + \frac{1}{V_{Y_A}} + 1 \end{pmatrix} \cdot \begin{pmatrix} P(+, +; x'_B, y'_B) \\ P(+, -; x'_B, y'_B) \\ P(-, +; x'_B, y'_B) \\ P(-, -; x'_B, y'_B) \end{pmatrix} \end{aligned} \quad (6.30)$$

By applying the 4×4 reconstruction matrix in the right hand side of Eq. (6.30) to the four joint probabilities composed of the combinations of x'_B and y'_B , the joint probability distribution of the four physical properties eliminating the influence of measurement uncertainty only from system A as shown in FIG. 6.3. Note that Eq. (6.25) cannot be reconstructed for the two cases $\theta_j = 0^\circ$ and $\theta_j = 90^\circ$ because the equations are valid only when the measurement visibility has a non-zero value. The most prominent feature is that negative probabilities are appeared in all joint probability distributions except for $\theta_j = 45^\circ$. The measurement outcomes with measurement errors approach a random result in the counts. Since there are a total of sixteen measurement outcomes in this case, the probability of a completely random measurement result is $1/16 = 0.0625$. Conversely, the probability of no measurement errors means that the absolute value of the difference from $1/16$ is larger than the probability of one with a measurement uncertainty. For example, looking at the probability distribution for $\theta_j = 10^\circ$ in FIG. 4.4, the number of $(+, +; +, +)$ and $(+, +; +, -)$ counts was not so large compared to the other measurement outcomes. The elimination of the measurement error from system A means that the probability changes so that the counts decreases further. The fact that the probability of some measurement outcomes goes down means that the probability of some other

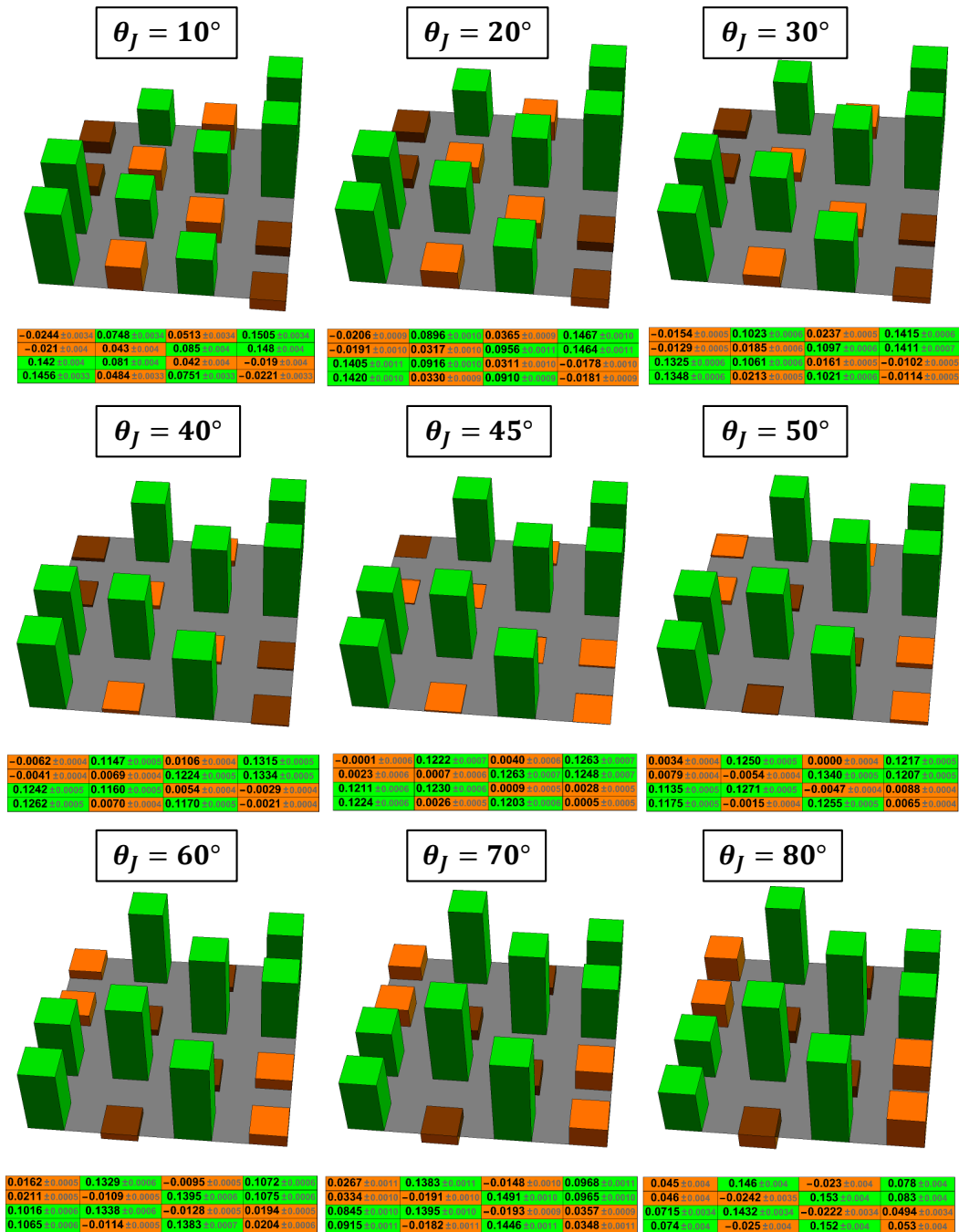


FIGURE 6.3: Reconstructed joint probability distribution by eliminating the measurement uncertainties from system A. Note that these probability distributions still have the measurement uncertainties in system B.

measurement outcomes increases to satisfy the condition that the sum of the probabilities is one. Thus, the probabilities of measurement outcomes whose probabilities were originally greater than $1/16$ will increase.

How did the negative probabilities come about in the first place? Since this is the result of eliminating the measurement errors, the cause is undoubtedly the quantum nature of the local system. Since the measurement uncertainty is derived from the relation between local complementary polarization physical properties, the negative probability is manifested by the quantum nature hidden in the uncertainty principle. However, the joint measurement assumes that the two complementary polarization physical properties both take only eigenvalues. Therefore, it is possible that the negative probability could be avoided by using a different theory in which the values of the physical properties could also take values other than eigenvalues.

Let us consider whether the joint probability distribution in FIG. 6.3 is a probability distribution that removes the measurement errors from system A. Removing the measurement errors from system A means that the two physical properties X_A and Y_A are measured precisely. Conversely, since the measurement error remains in the measurement outcomes obtained from system B, some characteristics should appear in the X'_B and Y'_B outcomes. For example, for $\theta_J = 10^\circ$, X'_B is measured almost precisely, but is almost ambiguous with respect to Y'_B . This feature can be seen, for example, in the two measurements $(+, +; +, +)$ and $(+, +; +, -)$. These probabilities do not change with respect to the reversal of y'_B . This means that the y'_B has no effect on the shape of the joint probability distribution. Similar characteristics appear in $(+, +; -, +)$ and $(+, +; -, -)$ or $(-, -; -, +)$ and $(-, -; -, -)$. Why are the probabilities for $(+, -; +, +)$ and $(+, -; +, -)$ not identical, even though only the value of y'_B is inverted? As you can see from the colors, $(+, -; +, +)$ has $b = -2$, while $(+, -; +, -)$ has $b = +2$. If the initial state is a singlet state, the measurement result with $b = -2$ must be larger, since $\langle B \rangle < 0$. Thus, a situation that the probabilities of two measurement outcomes with only the value of y'_B reversed are different can happen.

6.1.5 Reconstruction of the intrinsic joint probabilities in both systems

In subsec. 6.1.4, the measurement errors in system A are only eliminated. In this subsection, we also eliminate the measurement errors in system B and reconstruct the completely intrinsic joint probability distribution. Considering as in subsec. 6.1.4, the relation between the intrinsic joint probability in system B and the joint probability obtained through the joint measurement is given by

$$\begin{aligned}
 & \begin{pmatrix} P_{int}(x_A, y_A; +, +) \\ P_{int}(x_A, y_A; +, -) \\ P_{int}(x_A, y_A; -, +) \\ P_{int}(x_A, y_A; -, -) \end{pmatrix} \\
 = & \frac{1}{4} \begin{pmatrix} \frac{1}{V_{X'_B}} + \frac{1}{V_{Y'_B}} + 1 & \frac{1}{V_{X'_B}} - \frac{1}{V_{Y'_B}} + 1 & -\frac{1}{V_{X'_B}} + \frac{1}{V_{Y'_B}} + 1 & -\frac{1}{V_{X'_B}} - \frac{1}{V_{Y'_B}} + 1 \\ \frac{1}{V_{X'_B}} - \frac{1}{V_{Y'_B}} + 1 & \frac{1}{V_{X'_B}} + \frac{1}{V_{Y'_B}} + 1 & -\frac{1}{V_{X'_B}} - \frac{1}{V_{Y'_B}} + 1 & -\frac{1}{V_{X'_B}} + \frac{1}{V_{Y'_B}} + 1 \\ -\frac{1}{V_{X'_B}} + \frac{1}{V_{Y'_B}} + 1 & -\frac{1}{V_{X'_B}} - \frac{1}{V_{Y'_B}} + 1 & \frac{1}{V_{X'_B}} + \frac{1}{V_{Y'_B}} + 1 & \frac{1}{V_{X'_B}} - \frac{1}{V_{Y'_B}} + 1 \\ -\frac{1}{V_{X'_B}} - \frac{1}{V_{Y'_B}} + 1 & -\frac{1}{V_{X'_B}} + \frac{1}{V_{Y'_B}} + 1 & \frac{1}{V_{X'_B}} - \frac{1}{V_{Y'_B}} + 1 & \frac{1}{V_{X'_B}} + \frac{1}{V_{Y'_B}} + 1 \end{pmatrix} \cdot \begin{pmatrix} P(x_A, y_A; +, +) \\ P(x_A, y_A; +, -) \\ P(x_A, y_A; -, +) \\ P(x_A, y_A; -, -) \end{pmatrix} \quad (6.31)
 \end{aligned}$$

By applying the 4×4 reconstruction matrix in the right hand side of Eq. (6.31) to the four joint probabilities distinguished by the four values of the physical properties X_A and Y_A measured in system A, one can reconstruct the joint probability distribution without measurement error shown in FIG. 6.4.

The most noticeable feature is that the shape of the joint probability distribution appears to remain unchanged regardless of the value of θ_j . Originally, the joint measurement parameter θ_j was intended to control the balance of measurement accuracy between complementary polarization physical properties. All joint probability distributions in FIG. 6.4 should be independent of the value of the joint measurement parameter, since the measurement error has been eliminated from both systems. Therefore, returning a constant joint probability distribution for all θ_j is consistent with the physical meaning of measurement uncertainty.

Second, the probabilities of all measurement outcomes with $b = +2$ are negative; since there are only two possible values of B , $b = \pm 2$, the fact that $P(b = +2)$ is negative means that Bell's inequality is violated. This is consistent with the experimental fact that Bell's inequality is violated in the experiment to verify Bell's inequality using only precise measurements.

A third feature is that the probabilities of the eight measurements with $b = +2$ are almost identical, and the probabilities of the eight measurements with $b = -2$ are almost identical. Although they are truly in agreement, since they are not in agreement within the margin of error, let us discuss their consistency with the Cirel'son bound. If the relation between the four Bell correlations were to reach the Cirel'son bound, then $\langle B \rangle = -2\sqrt{2}$. The value of $P(b = \pm 2)$ such that Cirel'son bound is given can be derived from the two relations given by.

$$2P(b = +2) - 2P(b = -2) = -2\sqrt{2} \quad (6.32)$$

$$P(b = +2) + P(b = -2) = 1. \quad (6.33)$$

Eq. (6.32) is a relation giving Cirel'son bound, Eq. (6.33) is a condition that the sum of the all probabilities is 1. Solving the simultaneous equations of Eq. (6.32) and Eq. (6.33) results in

$$P(b = \pm 2) = \frac{1}{2} (1 \mp \sqrt{2}). \quad (6.34)$$

The signs are in the same order of the double sign. Assuming that these two probabilities are each equally distributed over the eight joint probabilities, the sixteen joint probabilities take

$$\frac{1}{8}P(b = +2) = \frac{1}{16}(1 - \sqrt{2}) \approx -0.00259 \quad (6.35)$$

$$\frac{1}{8}P(b = -2) = \frac{1}{16}(1 + \sqrt{2}) \approx 0.1509. \quad (6.36)$$

A comparison with the probabilities in FIG. 6.4 shows that more of them do not match within the margin of error, but they do match, at least with respect to the first digit.

6.1.6 Estimation of the initial state

As shown in Eqs. (3.2)-(3.5), the initial state that are prepared experimentally always contain imperfections. As a result of these imperfections, systematic errors occur, as shown in FIG. 4.6. In order to discuss what causes this systematic error, let us predict an initial state that can explain the experimental results. If the initial state is a perfect pure state,

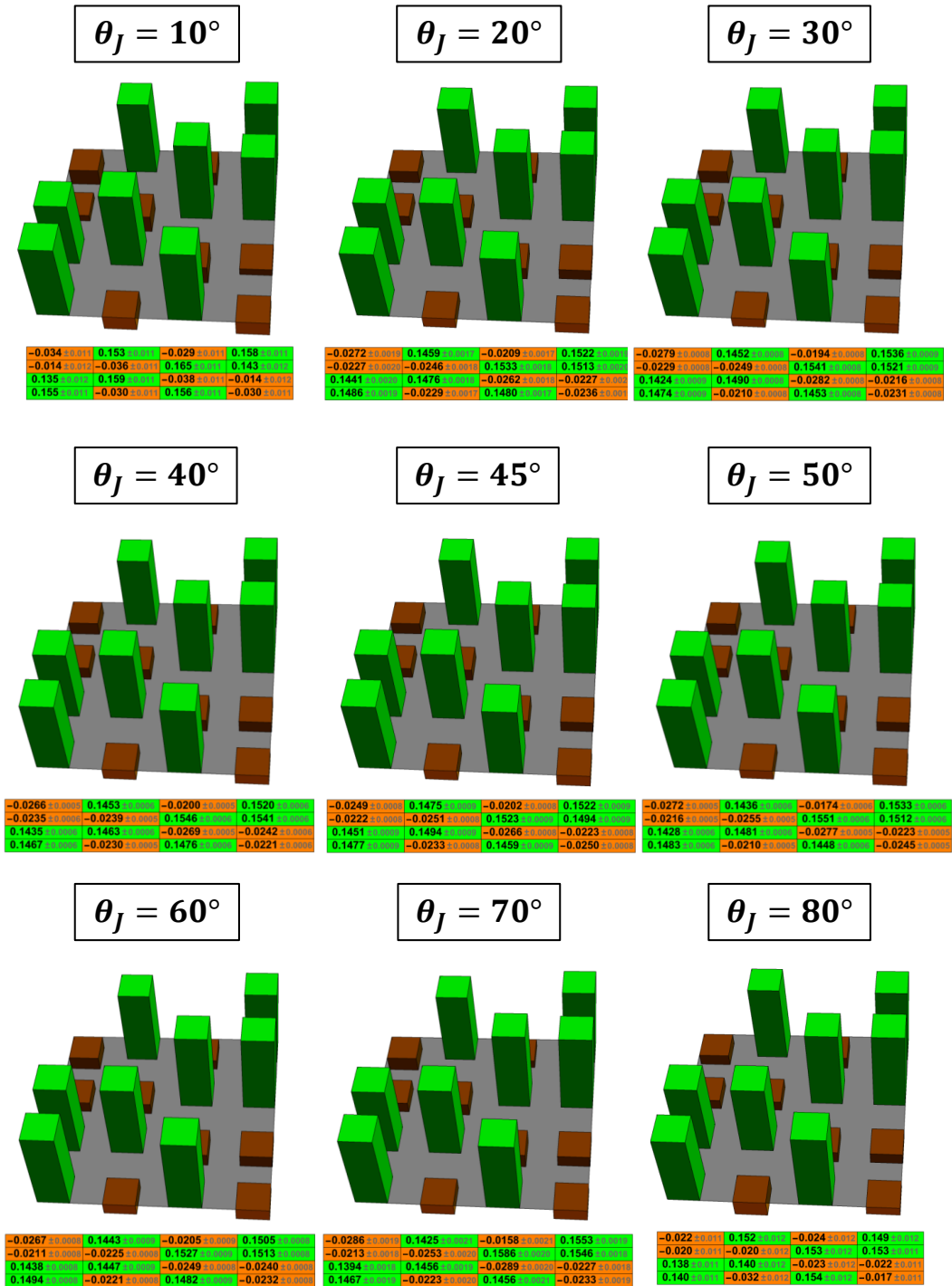


FIGURE 6.4: Reconstructed joint probability distribution by eliminating the measurement uncertainties from system A and B.

the density matrix is given by

$$\begin{aligned}\hat{\rho}_{singlet} &= \frac{1}{\sqrt{2}} (|H;V\rangle - |V;H\rangle) \cdot h.c. \\ &= \frac{1}{2} \begin{pmatrix} 0 & 0 & 0 & 0 \\ 0 & 1 & -1 & 0 \\ 0 & -1 & 1 & 0 \\ 0 & 0 & 0 & 0 \end{pmatrix}.\end{aligned}\quad (6.37)$$

A photon pair that loses coherence is no longer in a superposition. Taking this situation into account, the quantum state is given by

$$\hat{\rho}_0 = \alpha \hat{\rho}_{pure} + (1 - \alpha) \hat{\rho}_{mix}, \quad (6.38)$$

where α is the percentage of pure states in the total. The specific forms of the terms with and without coherence are given by

$$\hat{\rho}_{pure} = \begin{pmatrix} 0 & 0 & 0 & 0 \\ 0 & \cos^2 \gamma & -\sin \gamma \cos \gamma & 0 \\ 0 & -\sin \gamma \cos \gamma & \sin^2 \gamma & 0 \\ 0 & 0 & 0 & 0 \end{pmatrix} \quad (6.39)$$

$$\hat{\rho}_{mix} = \begin{pmatrix} 0 & 0 & 0 & 0 \\ 0 & \cos^2 \gamma & 0 & 0 \\ 0 & 0 & \sin^2 \gamma & 0 \\ 0 & 0 & 0 & 0 \end{pmatrix}, \quad (6.40)$$

where the γ is a parameter that determines the ratio of negative to positive correlation. Furthermore, even if there was no loss of coherence, the imperfections of the optical components in the experimental setup could generate positively correlated photon pairs. Given this situation, the term with coherence could be modified as

$$\begin{aligned}\hat{\rho}_{pure} &= \left(\frac{E^{i\phi}}{\sqrt{2}} \sin \gamma |H;H\rangle + \frac{1}{\sqrt{2}} \cos \gamma |H;V\rangle - \frac{1}{\sqrt{2}} \cos \gamma |V;H\rangle + \frac{E^{i\phi}}{\sqrt{2}} \sin \gamma |V;V\rangle \right) \cdot h.c. \\ &= \begin{pmatrix} \frac{1}{2} \sin^2 \gamma & \frac{1}{4} e^{i\phi} \sin 2\gamma & -\frac{1}{4} e^{i\phi} \sin 2\gamma & \frac{1}{2} \sin^2 \gamma \\ \frac{1}{4} e^{-i\phi} \sin 2\gamma & \frac{1}{2} \cos^2 \gamma & -\frac{1}{2} \cos^2 \gamma & \frac{1}{4} e^{-i\phi} \sin 2\gamma \\ -\frac{1}{4} e^{-i\phi} \sin 2\gamma & -\frac{1}{2} \cos^2 \gamma & \frac{1}{2} \cos^2 \gamma & -\frac{1}{4} e^{-i\phi} \sin 2\gamma \\ \frac{1}{2} \sin^2 \gamma & \frac{1}{4} e^{i\phi} \sin 2\gamma & -\frac{1}{4} e^{i\phi} \sin 2\gamma & \frac{1}{2} \sin^2 \gamma \end{pmatrix},\end{aligned}\quad (6.41)$$

where the ϕ is a parameter that also takes into account the inclusion of phase differences. The final predicted initial state eventually becomes

$$\hat{\rho} = \begin{pmatrix} \frac{1}{2} \alpha \sin^2 \gamma & \frac{1}{4} \alpha e^{i\phi} \sin 2\gamma & -\frac{1}{4} \alpha e^{i\phi} \sin 2\gamma & \frac{1}{2} \alpha \sin^2 \gamma \\ \frac{1}{4} \alpha e^{-i\phi} \sin 2\gamma & -\frac{1}{2} (\alpha - 2) \cos^2 \gamma & -\frac{1}{2} \alpha \cos^2 \gamma & \frac{1}{4} \alpha e^{-i\phi} \sin 2\gamma \\ -\frac{1}{4} \alpha e^{-i\phi} \sin 2\gamma & -\frac{1}{2} \alpha \cos^2 \gamma & \frac{1}{4} \alpha (3 \cos 2\gamma - 1) + \sin^2 \gamma & -\frac{1}{4} \alpha e^{-i\phi} \sin 2\gamma \\ \frac{1}{2} \alpha \sin^2 \gamma & \frac{1}{4} \alpha e^{i\phi} \sin 2\gamma & -\frac{1}{4} \alpha e^{i\phi} \sin 2\gamma & \frac{1}{2} \alpha \sin^2 \gamma \end{pmatrix} \quad (6.42)$$

The next items that need to be considered are the POVM elements in systems A and B. The POVM elements described in Eq. (2.11) are the results obtained under the assumption that the average value of the local correlation of the complementary physical properties is zero. Writing it as a general form without such an assumption, the POVM

elements in system A and B are given by

$$\hat{E}_A(+, +) = \frac{1}{4} (\hat{I}_A + V_{X_A} \hat{X}_A + V_{Y_A} \hat{Y}_A + C \hat{X}_A \hat{Y}_A) \quad (6.43)$$

$$\hat{E}_A(+, -) = \frac{1}{4} (\hat{I}_A + V_{X_A} \hat{X}_A - V_{Y_A} \hat{Y}_A - C \hat{X}_A \hat{Y}_A) \quad (6.44)$$

$$\hat{E}_A(-, +) = \frac{1}{4} (\hat{I}_A - V_{X_A} \hat{X}_A + V_{Y_A} \hat{Y}_A - C \hat{X}_A \hat{Y}_A) \quad (6.45)$$

$$\hat{E}_A(-, -) = \frac{1}{4} (\hat{I}_A - V_{X_A} \hat{X}_A - V_{Y_A} \hat{Y}_A + C \hat{X}_A \hat{Y}_A) \quad (6.46)$$

$$\hat{E}_B(+, +) = \frac{1}{4} (\hat{I}_B + V_{X'_B} \hat{X}'_B + V_{Y'_B} \hat{Y}'_B + C \hat{X}'_B \hat{Y}'_B) \quad (6.47)$$

$$\hat{E}_B(+, -) = \frac{1}{4} (\hat{I}_B + V_{X'_B} \hat{X}'_B - V_{Y'_B} \hat{Y}'_B - C \hat{X}'_B \hat{Y}'_B) \quad (6.48)$$

$$\hat{E}_B(-, +) = \frac{1}{4} (\hat{I}_B - V_{X'_B} \hat{X}'_B + V_{Y'_B} \hat{Y}'_B - C \hat{X}'_B \hat{Y}'_B) \quad (6.49)$$

$$\hat{E}_B(-, -) = \frac{1}{4} (\hat{I}_B - V_{X'_B} \hat{X}'_B - V_{Y'_B} \hat{Y}'_B + C \hat{X}'_B \hat{Y}'_B), \quad (6.50)$$

where C is the ratio of the average value obtained by the joint measurement to the average value obtained by the precise measurement. It is known from previous studies that this ratio is generally pure imaginary number[68]. Using Eqs. (6.42)-(6.50), average value of the local correlation becomes

$$\begin{aligned} \langle \hat{X}_A \hat{Y}_A \rangle_{joint} &= \text{Tr} [\hat{\rho} \cdot ((\hat{E}_A(+, +) - \hat{E}_A(+, -) - \hat{E}_A(-, +) + \hat{E}_A(-, -)) \otimes \hat{I}_B)] \\ &= i\alpha\beta C \sin \phi \sin 2\gamma \end{aligned} \quad (6.51)$$

$$\begin{aligned} \langle \hat{X}'_B \hat{Y}'_B \rangle_{joint} &= \text{Tr} [\hat{\rho} \cdot (\hat{I}_A \otimes (\hat{E}_B(+, +) - \hat{E}_B(+, -) - \hat{E}_B(-, +) + \hat{E}_B(-, -)))] \\ &= -i\alpha\beta C \sin \phi \sin 2\gamma. \end{aligned} \quad (6.52)$$

If C is pure imaginary number, these averages can take non-zero values; otherwise, they will be zero or complex. As a specific form of C , we assume a specific relation given by

$$C = iV_{X_A} V_{Y_A} = iV_{X'_B} V_{Y'_B}, \quad (6.53)$$

where i is imaginary unit. The rationale for writing such a measurement visibility for correlations between complementary polarization physical properties is highly intuitive.

FIG.6.5 shows the predicted values and experimental values of local correlation of complementary polarizations shown in FIG. 4.6. The three parameters for determining the predicted values α , γ , and ϕ were chosen such that the prediction of the local correlations are consistent with the experimental values. The α is the ratio of photon pairs with coherence to the total, and since this value should appear in the experimental values as the interferometric visibility, it is set to the same value as in Eq. (3.2). The $\gamma = 0.2^\circ$ results in $\cos 0.2^\circ = 0.999988$ as a probability. This number is consistent with the extinction ratio of G.T. used for polarization selection within FIG. 3.1. Intuitively, the value of γ seems to be determined by the extinction ratio of the DHWP in the interferometer, but if either one of the photon pairs is mistakenly transmitted or reflected by the DHWP, the DHWP cannot be a factor in mistakenly measuring positive correlations, since they are not measured as a coincidence count. It is therefore natural that the value $\gamma = 0.2^\circ$ is consistent with the extinction ratio of GT. Finally, for $\phi = 5^\circ$ to occur, there must be a phase difference somewhere. Most suspicious is the DHWP in the interferometer. The retardance corresponding to $\phi = 5^\circ$ is $5/360 = 0.01389$, which is the value that generally occurs when the wavelength of the photon pairs deviates from the design wavelength

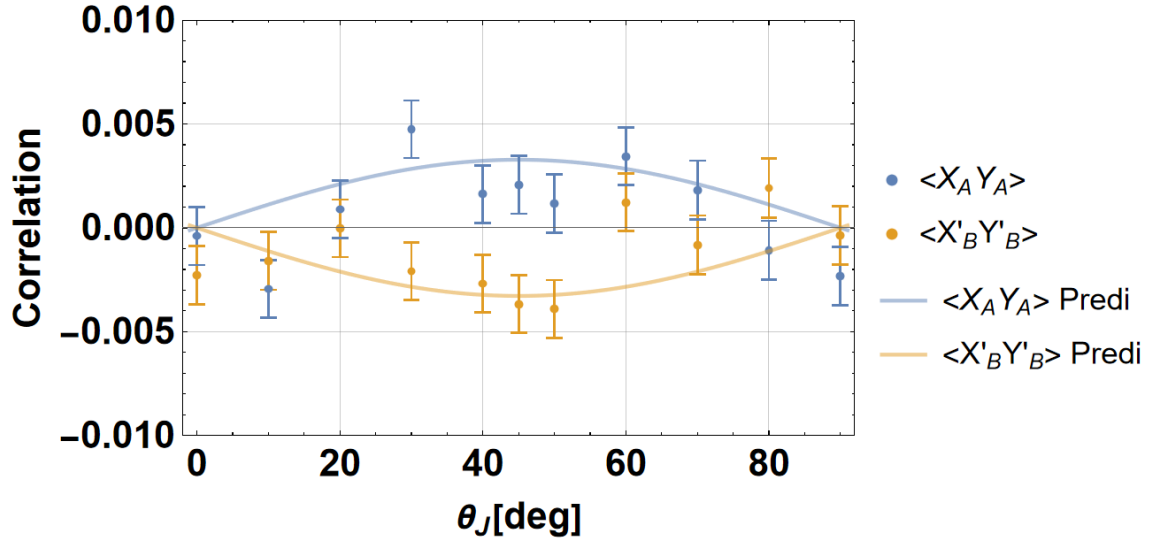


FIGURE 6.5: Experimental and predicted values of local correlations of complementary physical properties. The specific values of the parameters in Eq. (6.51) and Eq. (6.52) are $\alpha = 0.98$, $\gamma = 0.2^\circ$, and $\phi = 5^\circ$.

by $1 - 2[nm]$ in the case of HWP specifications. Since the wavelength of the pump light actually used is $404.5[nm]$, the wavelength of the photon pair produced is $809[nm]$, not $810[nm]$; therefore, a retardance can well occur. It is not clear as to the basis on which the measurement visibility can be written as in Eq. (6.53). Since the predicted and experimental values do not perfectly match, there is no guarantee that the assumptions that can be written in Eq. (6.53) are correct. There will be room for further discussion on this issue.

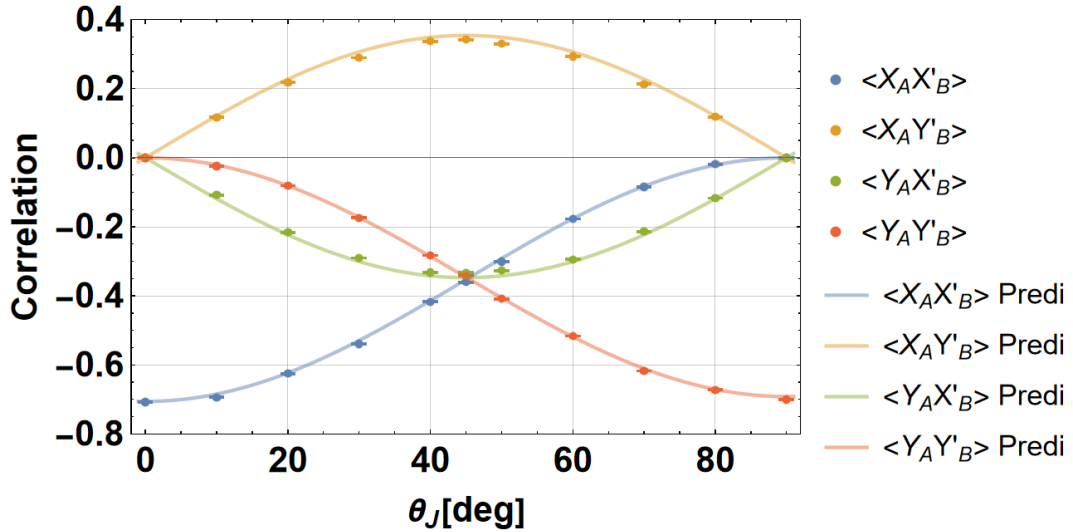


FIGURE 6.6: Experimental and predicted values of the four Bell correlations. The values of the parameters to be substituted into Eqs. (6.54)-(6.57) are $\alpha = 0.98$, $\gamma = 0.2^\circ$, and $\phi = 5^\circ$.

Using Eqs. (6.42)-(6.50), the predicted values of the four Bell correlations are given by the following equations.

$$\langle \hat{X}_A \hat{X}'_B \rangle_{joint} = \frac{\beta \cos^2 \theta (\alpha \cos \phi \sin 2\gamma + \alpha (-\cos 2\gamma) + \alpha - 1)}{\sqrt{2}} \quad (6.54)$$

$$\langle \hat{X}_A \hat{Y}'_B \rangle_{joint} = \frac{\beta \sin 2\theta (\alpha \cos \phi \sin 2\gamma + \alpha \cos 2\gamma - \alpha + 1)}{2\sqrt{2}} \quad (6.55)$$

$$\langle \hat{Y}_A \hat{X}'_B \rangle_{joint} = -\frac{\alpha \beta \sin 2\theta (\cos \phi \sin 2\gamma + \cos 2\gamma)}{2\sqrt{2}} \quad (6.56)$$

$$\langle \hat{Y}_A \hat{Y}'_B \rangle_{joint} = \frac{\alpha \beta \sin^2 \theta (\cos \phi \sin 2\gamma - \cos 2\gamma)}{\sqrt{2}} \quad (6.57)$$

FIG. 6.6 shows simultaneously the predicted values and the experimental values shown in FIG. 4.5 when $\alpha = 0.98$, $\gamma = 0.2^\circ$, and $\phi = 5^\circ$ are substituted into Eqs. (6.54)-(6.57). The experimental and predicted values agree very well. Thus, the experimental values of the correlations can be explained by assuming Eq. (6.42).

6.1.7 Evaluation of the properties of the estimated quantum state

There are many indicators for quantum states, such as purity, fidelity, and, in the case of many-body systems, negativity and entanglement-witness. Originally, quantum state tomography is used to evaluate experimentally obtained quantum states, but in this section, these indicators are evaluated for the predicted quantum states described in subsec. 6.1.6.

Purity is a measure of how close a quantum state is to a pure state, which is given by

$$\mathcal{P}(\hat{\rho}) = \text{Tr}[\hat{\rho}^2], \quad (6.58)$$

where $\hat{\rho}$ is a density matrix. The purity takes the value $1/d \leq \mathcal{P} \leq 1$ when the degree of freedom of the physical system is d . The closer to $1/d$, the closer the quantum state is to the mixed state, and the closer to 1, the closer to the pure state. Evaluating the purity of Eq. (6.42) and substituting the values $\alpha = 0.98$, $\gamma = 0.2^\circ$, and $\phi = 5^\circ$ for the parameters described in Subsec. 6.1.6, the result is 0.9804. This value is consistent with the result of measurement visibility in Eq. (3.2).

Fidelity is a measure of the distance between two different quantum states and is defined as

$$\mathcal{F}(\hat{\rho}_1, \hat{\rho}_2) = \left(\text{Tr} \left[\sqrt{\sqrt{\hat{\rho}_1} \hat{\rho}_2 \sqrt{\hat{\rho}_1}} \right] \right)^2, \quad (6.59)$$

where $\hat{\rho}_1$ and $\hat{\rho}_2$ represent two different quantum states. At first glance, fidelity appears to be asymmetric between $\hat{\rho}_1$ and $\hat{\rho}_2$, but in fact it is symmetric, so exchanging $\hat{\rho}_1$ and $\hat{\rho}_2$ does not change the value. From an experimental point of view, it is used to quantify how close a quantum state experimentally realized by a particular quantum operation is to the quantum state that would be expected to be realized by an ideal operation. Fidelity takes a value between 0 and 1, with the closer to 0 indicating that $\hat{\rho}_1$ and $\hat{\rho}_2$ are quantum states that do not resemble each other, and the closer to 1 indicating that $\hat{\rho}_1$ and $\hat{\rho}_2$ are similar to each other. The fidelity derived from the density matrix of Eq. (6.37) and the density matrix of Eq. (6.42) substituting $\alpha = 0.98$, $\gamma = 0.2^\circ$, and $\phi = 5^\circ$ was 0.9900. This result shows that our quantum operation is very close to the ideal operation.

Negativity represents a measure of the existence of an entanglement and is defined as

$$\mathcal{N}(\hat{\rho}) = \frac{\|\hat{\rho}^{TA}\| - 1}{2}, \quad (6.60)$$

where $\hat{\rho}^{TA}$ is the density matrix with partial transpose only for subsystem A and $\|\hat{\rho}^{TA}\|$ is the trace norm. The trace norm is defined as

$$\|\hat{\rho}^{TA}\| = \text{Tr} \left[\sqrt{(\hat{\rho}^{TA})^\dagger \hat{\rho}^{TA}} \right] \quad (6.61)$$

Negativity is an indicator to distinguish whether a quantum state is separable or entangled, and can be determined as separable if the negativity is zero, and entangled if it is positive. The negativity evaluated for the density matrix substituting $\alpha = 0.98$, $\gamma = 0.2^\circ$, and $\phi = 5^\circ$ into Eq. (6.42) is 0.489979. Although the value obtained by evaluating the negativity provides some assurance as to how strongly the property is manifested as quantum entanglement, it cannot be used as a quantitative degree to evaluate the degree of entanglement.

A quantitative indicator of the degree of entanglement is the entanglement witness. The specific expression of the entanglement witness changes its form depending on what kind of quantum state of the physical system it is. For a two-qubit system, as in this experiment, the entanglement witness may be described as

$$\mathcal{W}(\hat{\rho}) = -\text{Tr} [(\hat{X}_A \otimes \hat{X}_A) \hat{\rho}] - \text{Tr} [(\hat{Y}_A \otimes \hat{Y}_A) \hat{\rho}] - 1, \quad (6.62)$$

Eq. (6.62) takes values between 0 and 1, with the closer to 0, the closer to the product state, and the closer to 1, the closer to the maximum entanglement state. Evaluating Eq. (6.62) for a density matrix substituting $\alpha = 0.98$, $\gamma = 0.2^\circ$, and $\phi = 5^\circ$ into Eq. (6.42) yields 0.9800.

Although there are other quantitative measures of the distance between two quantum states and of entanglement, a simple and practical measure for experimental evaluation would be desirable.

6.1.8 Relation between the measurement uncertainties and the Bell correlations

As shown in FIG. 6.3 and FIG. 6.4, the joint probability distributions depend on whether there are the measurement uncertainties in the measurements, which means that the mean values evaluated from the different joint probability distributions also differ. In this subsection, we discuss how the Bell correlations and the mean value of B shown in FIG. 4.5 and TAB. 4.6 are affected by the measurement uncertainty. We also discuss whether the initial conditions described by Eq. (6.42) are valid for these averages.

The predicted value when the measurement error is eliminated is achieved by using the POVM elements with the measurement visibility within Eqs. (6.43)-(6.50) set to 1. The POVM elements describing the joint measurement without errors of complementary

physical properties is given by

$$\hat{E}_A(+,+) = \frac{1}{4} (\hat{I}_A + \hat{X}_A + \hat{Y}_A + i\hat{X}_A\hat{Y}_A) \quad (6.63)$$

$$\hat{E}_A(+,-) = \frac{1}{4} (\hat{I}_A + \hat{X}_A - \hat{Y}_A - i\hat{X}_A\hat{Y}_A) \quad (6.64)$$

$$\hat{E}_A(-,+) = \frac{1}{4} (\hat{I}_A - \hat{X}_A + \hat{Y}_A - i\hat{X}_A\hat{Y}_A) \quad (6.65)$$

$$\hat{E}_A(-,-) = \frac{1}{4} (\hat{I}_A - \hat{X}_A - \hat{Y}_A + i\hat{X}_A\hat{Y}_A) \quad (6.66)$$

$$\hat{E}_B(+,+) = \frac{1}{4} (\hat{I}_B + \hat{X}'_B + \hat{Y}'_B + i\hat{X}'_B\hat{Y}'_B) \quad (6.67)$$

$$\hat{E}_B(+,-) = \frac{1}{4} (\hat{I}_B + \hat{X}'_B - \hat{Y}'_B - i\hat{X}'_B\hat{Y}'_B) \quad (6.68)$$

$$\hat{E}_B(-,+) = \frac{1}{4} (\hat{I}_B - \hat{X}'_B + \hat{Y}'_B - i\hat{X}'_B\hat{Y}'_B) \quad (6.69)$$

$$\hat{E}_B(-,-) = \frac{1}{4} (\hat{I}_B - \hat{X}'_B - \hat{Y}'_B + i\hat{X}'_B\hat{Y}'_B), \quad (6.70)$$

where i is imaginary unit, coming from Eq. (6.53). FIG. 6.3 shows the experimentally obtained joint probability distributions, eliminating the measurement errors for system A. The predicted values of these joint probability distributions can be derived by using Eqs. (6.63)-(6.66) for system A and Eqs. (6.47)-(6.50) for system B. The joint probability distribution shown in FIG. 6.4, which is experimentally obtained by eliminating the measurement errors for both system A and system B, can be calculated by using Eqs. (6.63)-(6.70) for the predictions of this joint probability distribution.

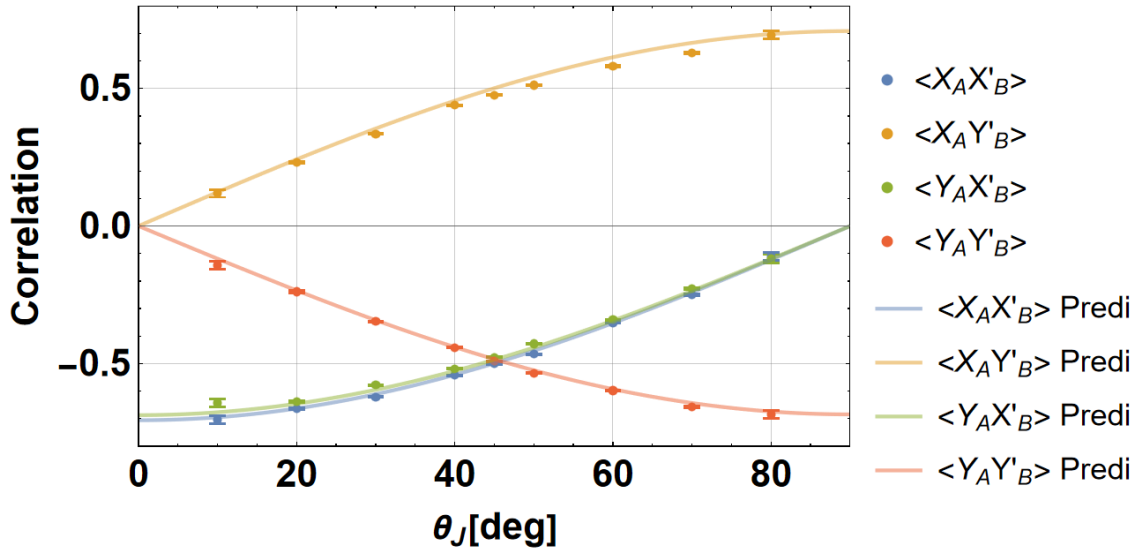


FIGURE 6.7: Predictions of the four Bell correlations derived using Eqs. (6.42), (6.63)-(6.66), and Eqs.(6.47)-(6.50), and experimental values derived from the results in FIG. 6.3. As described in the subsec. 6.1.6, the parameter values are set such that $\alpha = 0.98$, $\gamma = 0.2^\circ$, and $\phi = 5^\circ$.

FIG. 6.7 compares the results of the four Bell correlations evaluated from FIG. 6.3 and their respective predictions, while TAB. 6.3 shows the numerical data for the experimental values of the four Bell correlations. While $\langle X_A X'_B \rangle$ and $\langle Y_A X'_B \rangle$ show nearly identical values, $\langle X_A Y'_B \rangle$ and $\langle Y_A Y'_B \rangle$ are symmetrical about the axis of θ_J . The former shows a monotonically decreasing, while the latter shows a monotonically increasing. $\langle X_A X'_B \rangle$

TABLE 6.3: Numerical results of the four Bell correlations in FIG. 6.7.

θ_j [deg]	$\langle X_A X'_B \rangle$	$\langle X_A Y'_B \rangle$	$\langle Y_A X'_B \rangle$	$\langle Y_A Y'_B \rangle$
10	-0.704 ± 0.014	0.118 ± 0.014	-0.643 ± 0.014	-0.143 ± 0.014
20	-0.664 ± 0.004	0.232 ± 0.004	-0.638 ± 0.004	-0.239 ± 0.004
30	-0.6218 ± 0.0023	0.3341 ± 0.0023	-0.5779 ± 0.0023	-0.3470 ± 0.0023
40	-0.5428 ± 0.0018	0.4388 ± 0.0018	-0.5187 ± 0.0018	-0.4415 ± 0.0018
45	-0.5010 ± 0.0024	0.4759 ± 0.0024	-0.4775 ± 0.0024	-0.4910 ± 0.0024
50	-0.4660 ± 0.0018	0.5114 ± 0.0018	-0.4277 ± 0.0018	-0.5350 ± 0.0018
60	-0.3507 ± 0.0023	0.5808 ± 0.0023	-0.3409 ± 0.0023	-0.5977 ± 0.0023
70	-0.250 ± 0.004	0.628 ± 0.004	-0.228 ± 0.004	-0.658 ± 0.004
80	-0.110 ± 0.015	0.694 ± 0.015	-0.119 ± 0.015	-0.685 ± 0.015

and $\langle Y_A X'_B \rangle$ are two correlations involving X'_B , and $\langle X_A Y'_B \rangle$ and $\langle Y_A Y'_B \rangle$ are correlations that include Y'_B , so these increasing and decreasing trends are consistent with the changes in measurement visibility in System B. When the measurement error is also included in system A, the changes are complex, as seen in FIG. 4.5, but FIG. 6.7 clearly shows that they depend only on the measurement uncertainty in system B. This means that the joint probability distribution shown in FIG. 6.3 does not include the measurement error in the measurement of system A. Although there are positive and negative values, the change in the Bell correlation is exactly what is shown in FIG. 4.2(b), which represents the change in measurement visibility. A closer look reveals that $\langle Y_A X'_B \rangle$ is slightly higher than $\langle X_A X'_B \rangle$. This fine-tuned trend can also be seen in the predicted values, and in this sense, Eq. (6.42) is a good model.

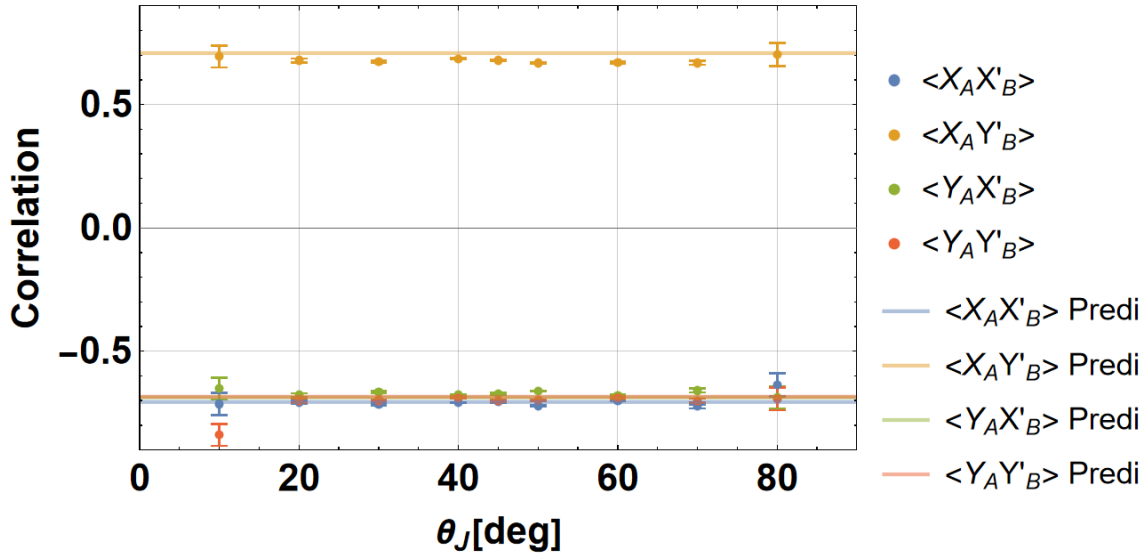


FIGURE 6.8: The predicted values of the four Bell correlations derived using Eq. (6.42), Eqs. (6.63)-(6.70), and the experimental values derived from the joint probability distribution in FIG. 6.4. As described in the subsec. 6.1.6, the parameter values are set such that $\alpha = 0.98$, $\gamma = 0.2^\circ$, and $\phi = 5^\circ$.

FIG. 6.8 shows a comparison of the experimental values of the four Bell correlations derived from FIG. 6.4 with those derived from Eq. (6.42) and Eqs. (6.63)-(6.70). The most prominent feature is that all four Bell correlations are constant, independent of θ_j . This is not surprising since the joint probability distributions shown in FIG. 6.4 also have almost the same shape regardless of θ_j . This result means that the measurement error has been completely removed from both system A and B. Furthermore, it can be seen that the closer one approaches $\theta_j = 0^\circ$ or $\theta_j = 90^\circ$, the larger the error range becomes.

TABLE 6.4: Numerical results of the four Bell correlations in FIG. 6.8.

θ_J [deg]	$\langle X_A X'_B \rangle$	$\langle X_A Y'_B \rangle$	$\langle Y_A X'_B \rangle$	$\langle Y_A Y'_B \rangle$
10	-0.71 ± 0.04	0.69 ± 0.04	-0.65 ± 0.04	-0.84 ± 0.04
20	-0.707 ± 0.007	0.679 ± 0.007	-0.679 ± 0.007	-0.700 ± 0.007
30	-0.7163 ± 0.0033	0.6742 ± 0.0033	-0.6658 ± 0.0033	-0.7001 ± 0.0033
40	-0.7085 ± 0.0023	0.6855 ± 0.0023	-0.6770 ± 0.0023	-0.6898 ± 0.0023
45	-0.7053 ± 0.0034	0.6794 ± 0.0034	-0.6722 ± 0.0034	-0.7010 ± 0.0034
50	-0.7207 ± 0.0023	0.6679 ± 0.0023	-0.6616 ± 0.0023	-0.6987 ± 0.0023
60	-0.6997 ± 0.0033	0.6702 ± 0.0033	-0.6802 ± 0.0033	-0.6896 ± 0.0033
70	-0.724 ± 0.008	0.669 ± 0.008	-0.660 ± 0.008	-0.701 ± 0.008
80	-0.64 ± 0.05	0.70 ± 0.05	-0.69 ± 0.05	-0.69 ± 0.05

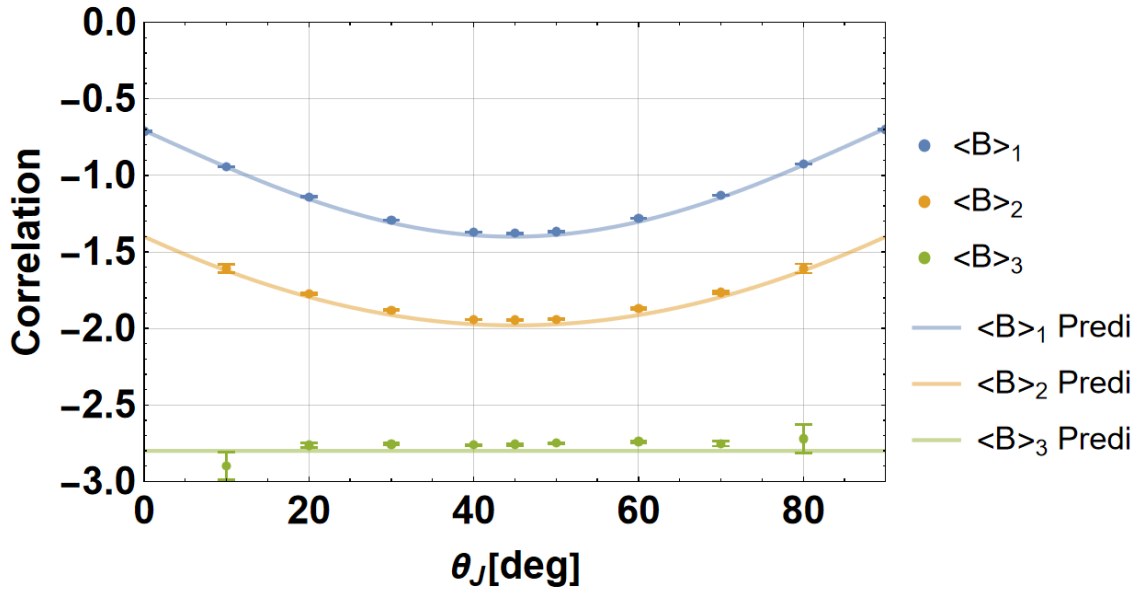


FIGURE 6.9: Mean values of B with and without measurement uncertainty. $\langle B \rangle_1$ is the average value obtained directly from FIG. 4.4, $\langle B \rangle_2$ is the average value obtained from (6.3), and $\langle B \rangle_3$ is the average value obtained from FIG. 6.4. The values of the parameters used to derive the predictions are $\alpha = 0.98$, $\gamma = 0.2^\circ$, and $\phi = 5^\circ$.

This is a remnant of the fact that the magnitude of the measurement error for X_A, X'_B or Y_A, Y'_B increases as $\theta_J = 0^\circ$ or $\theta_J = 90^\circ$. Since the experimental values shown in FIG. 6.8 were reconstructed from data obtained by joint measurements, the influence of θ_J remains with respect to the error range. The fact that only $\langle X_A Y'_B \rangle$ has a positive value is consistent with FIG. 4.5 and FIG. 6.7.

FIG. 6.9 shows the change in the mean value of B with and without the measurement error. The $\langle B \rangle_1$ is the mean value obtained directly from FIG. 4.4, so the magnitude of the mean is less than 2 and Bell's inequality cannot be violated. The smallest value at $\theta_J = 45^\circ$ is because the sum or difference of the four Bell correlations is the largest, and the four Bell correlations are the largest for the four physical properties because the measurement uncertainties are the same at $\theta_J = 45^\circ$. This trend is the same for the average value of $\langle B \rangle_2$, when only the measurement error for system A is eliminated. The difference between $\langle B \rangle_1$ and $\langle B \rangle_2$ is 0.575 ± 0.006 at $\theta_J = 45^\circ$, 0.666 ± 0.028 at $\theta_J = 10^\circ$, and 0.682 ± 0.028 at $\theta_J = 80^\circ$. It can be seen that the larger the difference between the visibility of the measurements of the two complementary physical properties, the larger the difference of the mean of B is. As can be seen in FIG. 4.2, the rate of change in the measurement visibility is greater closer to $\theta_J = 0^\circ$ and $\theta_J = 90^\circ$, so the more

TABLE 6.5: Numerical results of the four Bell correlations in FIG. 6.9.

θ_J [deg]	$\langle B \rangle_1$	$\langle B \rangle_2$	$\langle B \rangle_3$
10	-0.9422 ± 0.0028	-1.608 ± 0.028	-2.90 ± 0.09
20	-1.1402 ± 0.0028	-1.773 ± 0.008	-2.764 ± 0.015
30	-1.2934 ± 0.0028	-1.881 ± 0.005	-2.756 ± 0.007
40	-1.3698 ± 0.0028	-1.942 ± 0.004	-2.761 ± 0.005
45	-1.3782 ± 0.0028	-1.945 ± 0.005	-2.758 ± 0.007
50	-1.3664 ± 0.0028	-1.940 ± 0.004	-2.749 ± 0.005
60	-1.2809 ± 0.0028	-1.870 ± 0.005	-2.740 ± 0.007
70	-1.1292 ± 0.0028	-1.763 ± 0.008	-2.753 ± 0.015
80	-0.9265 ± 0.0028	-1.608 ± 0.029	-2.72 ± 0.09

susceptible to measurement uncertainty. Since the only difference between $\langle B \rangle_1$ and $\langle B \rangle_2$ is whether or not the measurement in system A includes the measurement error, the joint probabilities at $\theta_J = 10^\circ, 80^\circ$ compared to the joint probability at $\theta_J = 45^\circ$ probabilities are closer to a random result, resulting in an average of B approaching zero. Surprisingly, the results for $\langle B \rangle_2$ do not violate Bell's inequality for all θ_J . As seen in FIG. 6.3, there are some measurement outcomes whose probabilities are negative in the joint probability distribution, but for Bell's inequality to be violated, $P(b = +2)$ or $P(b = -2)$ must be negative. It is possible that Bell's inequality cannot be violated even if the probability of some measurement outcomes become negative. Furthermore, an interesting comparison between $\langle B \rangle_2$ and $\langle B \rangle_3$ can be made. TAB. 6.6 shows the ratios of $\langle B \rangle_1$ to $\langle B \rangle_2$ and of $\langle B \rangle_2$ to $\langle B \rangle_3$. Except for the case of $\theta_J = 10^\circ$, the two ratios agree within statistical error. This means that the effects of measurement uncertainties in the measurements of system A and system B are not only equivalent, but completely independent.

TABLE 6.6: Ratio of $\langle B \rangle_1$ and $\langle B \rangle_2$ to θ_J and ratio of $\langle B \rangle_2$ and $\langle B \rangle_3$.

θ_J [deg]	$\langle B \rangle_1 / \langle B \rangle_2$	$\langle B \rangle_2 / \langle B \rangle_3$
10	0.586 ± 0.010	0.555 ± 0.020
20	0.6432 ± 0.0033	0.641 ± 0.004
30	0.6877 ± 0.0022	0.6823 ± 0.0023
40	0.7055 ± 0.0019	0.7033 ± 0.0018
45	0.7085 ± 0.0023	0.7054 ± 0.0025
50	0.7043 ± 0.0020	0.7058 ± 0.0018
60	0.6849 ± 0.0022	0.6826 ± 0.0023
70	0.6403 ± 0.0034	0.641 ± 0.005
80	0.576 ± 0.011	0.591 ± 0.023

6.2 Adaptive and operation input state control using different measurement contexts

In Chapter 5, we demonstrated and presented a method for operationally imposing specific physical conditions on an entanglement source with variable degrees of entanglement; the purpose of the second experiment was to demonstrate a method for experimentally optimizing quantum correlations with input states, adaptive input state control, is to show that input state can be prepared such that they induce a paradox. In this section, the relation between the performance of the entanglement source and the four different contextual probabilities is discussed, as well as a discussion of the sources of error in the experimental results. The relation between the non-contextual inequality valid for non-contextual logic and the experimental results will be clarified to show that the

AISC demonstrated in this study is effective enough for the operational definition of an input state control that can lead to quantum contextuality.

6.2.1 Estimation of the input state and the evaluation of its properties

In order to show from which quantum state the experimental results presented in Chapter 5 are derived, let us confirm how close the quantum state gotten from the Sagnac interferometer is to the one described by Eq. (2.32). If the quantum state described by Eq. (2.32) is ideally realized, the description of the density matrix using correlations is given by

$$\hat{\rho}_{pure} = (\cos \phi_S |H; H\rangle - \sin \phi_S |V; V\rangle) h.c.. \quad (6.71)$$

How this density matrix can be described using correlations can be found by checking the components using the three polarization physical properties and the identity operator with dimension two, and the description of the density matrix using correlation is given by

$$\begin{aligned} \hat{\rho}_{initial} &= \frac{1}{4} (\hat{I} \otimes \hat{I} + C_X \hat{I} \otimes \hat{X} + C_X \hat{X} \otimes \hat{I} + V_X \hat{X} \otimes \hat{X} + V_Y \hat{Y} \otimes \hat{Y} - V_Y \hat{Z} \otimes \hat{Z}) \\ &= \begin{pmatrix} \frac{1}{4}(2V_X + C_X + 1) & 0 & 0 & \frac{C_Y}{2} \\ 0 & \frac{1-C_X}{4} & 0 & 0 \\ 0 & 0 & \frac{1-C_X}{4} & 0 \\ \frac{C_Y}{2} & 0 & 0 & \frac{1}{4}(-2V_X + C_X + 1) \end{pmatrix} \end{aligned} \quad (6.72)$$

where $C_X = \cos 2\phi_S$, $V_X = 1$, $V_Y = -\sin 2\phi_S$ are hold if the initial state is completely pure state. This is the case with the least experimental imperfection, and to account for experimental imperfection, we assume that the value of the correlations and the local polarization are

$$C_X = (0.968 \pm 0.013) \cos 2\phi_S \quad (6.73)$$

$$V_X = (0.968 \pm 0.013) \quad (6.74)$$

$$V_Y = (-0.935 \pm 0.011) \sin 2\phi_S \quad (6.75)$$

where (0.968 ± 0.013) and (-0.935 ± 0.011) correspond to Eq. (3.6) and Eq. (3.7), respectively. Eq. (6.74) and Eq.(3.6) are equivalent when $\phi_S = 45^\circ$, and Eq. (6.75) and Eq. (3.7) are also equivalent. A good reason for considering Eq. (6.73) and Eq. (6.74) identical when $\phi_S = 0^\circ$ is the equality of C_X and V_X in FIG. 3.8. Since photon pairs generated by nonlinear crystals are strongly correlated to the HV basis, changing the degree of entanglement does not change the magnitude of the correlation; the magnitude of local polarization represented by C_X should reflect the magnitude of polarization in the HV basis that the photon pairs have, so it is natural that the values are equal within the margin of error.

FIG. 6.10 shows the experimental values shown in FIG. 3.8 and the predictions derived from Eqs. (6.73)-(6.75) and Eq. (3.8). The range that the predicted values have reflects the statistical error that Eqs. (6.73)-(6.75) have. In Eqs. (6.73)-(6.75), two curves are drawn, one with a positive sign of standard deviation and the other with a negative sign, and the region between the two curves is colored. Almost all points are explained with respect to V_X and W_E , but for C_X , in the range of high degree of entanglement. We can see that there is a discrepancy between the experimental and predicted values. One possible cause could be the systematic error of the ϕ_S setting, which is assumed to be

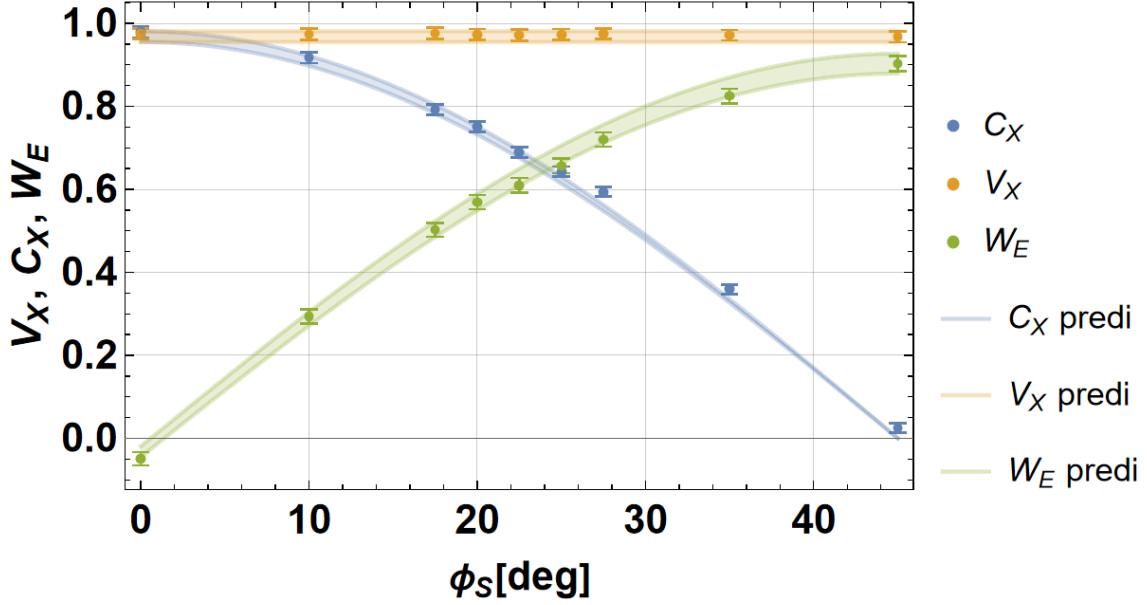


FIGURE 6.10: Experimental and predicted values for C_X , V_X , and W_E . The horizontal axis is ϕ_S [deg], which represents the degree of entanglement, with $\phi_S = 0^\circ$ representing the product state and $\phi_S = 45^\circ$ the end state. The predictions have some range because they reflect the range of statistical errors that Eqs. (6.73)-(6.75) have.

minimum at 0° and maximum at 45° because ϕ_S is a setting value, but systematic errors due to imperfections in HWP1 in FIG. 3.4 and differences in the actual wavelength of the pump light could cause the actual setting angle to be larger than the ideal setting angle. The angle may be larger than the ideal setting angle. Assuming that the experimental data points were shifted overall in the direction of smaller ϕ_S , C_X , V_X , and C_X would all fall within the range of predicted values.

Let us evaluate the various indices for the quantum state as shown in Subsec. 6.1.7 for the density matrix substituting Eqs. (6.73)-(6.75) into Eq. (6.72). TAB. 6.7 shows the results for purity defined by Eq. (6.58), fidelity defined by Eq. (6.59), and negativity defined by Eq. (6.60).

TABLE 6.7: Results of purity, fidelity, and negativity for the density matrix estimated from the experimental results. For a density matrix in Eq. (6.58) and Eq. (6.60) and for ρ_2 in Eq. (6.59), the density matrix in Eq. (6.72) is substituted for V_X , C_X , and V_Y derived from TAB. 3.3, and for ρ_1 in Eq. (6.59), $V_X = 1$, $V_Y = -\sin 2\phi_S$, and the density matrix substituting $C_X = \cos 2\phi_S$ was used.

ϕ_S [deg]	\mathcal{P}	\mathcal{F}	\mathcal{N}
0	0.967 ± 0.014	0.992 ± 0.006	0.006 ± 0.005
10	0.959 ± 0.015	0.9896 ± 0.0031	0.153 ± 0.005
17.5	0.941 ± 0.014	0.9847 ± 0.0029	0.257 ± 0.005
20	0.947 ± 0.014	0.9862 ± 0.0028	0.291 ± 0.005
22.5	0.927 ± 0.014	0.9809 ± 0.0028	0.312 ± 0.005
25	0.927 ± 0.014	0.9805 ± 0.0028	0.335 ± 0.005
27.5	0.941 ± 0.013	0.9844 ± 0.0027	0.366 ± 0.005
35	0.915 ± 0.013	0.9775 ± 0.0028	0.420 ± 0.005
45	0.922 ± 0.014	0.9796 ± 0.0034	0.460 ± 0.005

The purity results tend to become slightly smaller as the degree of entanglement increases. Since the purity represents how close the quantum state is to the pure state, a decrease in the pure state means a decrease in quantum coherence. Such a tendency is also shown in $\sqrt{C_X^2 + W_E^2}$ in TAB. 3.4, and the cause of the lowering is also considered to be the same. In other words, as the degree of entanglement increases, the degree of agreement between the two paths inside the interferometer becomes more important, and this imperfection shows up as a slight decreasing trend. Fidelity also has a decreasing trend, but is higher than 0.95 for all ϕ_S . Negativity is a measure of whether a quantum state is in an entangled state, and the further away from zero its magnitude is, the more strongly entangled it is, which means that it has an increasing trend.

6.2.2 Relation between $P(0;a), P(a;0)$ and the correlations

This subsection discusses the relation between the two probabilities $P(0;a), P(a;0)$ appearing in Eq. (2.25) and the three indices shown in FIG. 3.8. The unitary transformation in Eq. (2.33) and Eq. (2.34) is performed by the two HWP2s in FIG. 3.4. Since a HWP is optical elements that convert any linearly polarized light into other linearly polarized light, the relation between horizontal and vertical polarization and $\{0,1\}$ polarization can be given by

$$|0\rangle = \cos \phi_M |H\rangle - \sin \phi_M |V\rangle \quad (6.76)$$

$$|1\rangle = \sin \phi_M |H\rangle + \cos \phi_M |V\rangle. \quad (6.77)$$

Since the relation between the $\{0,1\}$ basis and the $\{a,b\}$ basis is Eq. (2.29) and Eq. (2.30), from Eqs. (6.76), (6.77) and (6.72), the value of $P(0;a) + P(a;0)$ becomes

$$\begin{aligned} P(0;a) + P(a;0) &= \langle 0| \otimes \langle a| \hat{\rho}_{initial} |0\rangle \otimes |a\rangle + \langle a| \otimes \langle 0| \hat{\rho}_{initial} |a\rangle \otimes |0\rangle \\ &= \frac{1}{2}(1 + C_X(\cos 2\phi_M - \sin 2\phi_M) \\ &\quad + (V_Y - V_X) \sin 2\phi_M \cos 2\phi_M). \end{aligned} \quad (6.78)$$

The results in TAB. 5.1 show that the range of set values of ϕ_M is roughly $40^\circ < 2\phi_M < 100^\circ$, so $\cos 2\phi_M - \sin 2\phi_M < 0$ always holds. Taking this into account, Eq. (6.78) becomes

$$\begin{aligned} P(0;a) + P(a;0) &= \frac{1}{2} \left(\frac{V_X - V_Y}{2} t^2 - C_X t + 1 - \frac{V_X - V_Y}{2} \right) \\ &= \frac{1}{2} \left(\frac{V_X - V_Y}{2} \left(t - \frac{C_X}{1 + W_E} \right)^2 + \frac{1 - W_E^2 - C_X^2}{2(1 + W_E)} \right), \end{aligned} \quad (6.79)$$

where $t = \sqrt{1 - 2 \sin 2\phi_M \cos 2\phi_M}$ and Eq. (3.8) is used in the middle. Regarding Eq. (6.79) as quadratic function with respect to t , the minimum value of $P(0;a) + P(a;0)$ is given by

$$P(0;a) + P(a;0) = \frac{1 - W_E^2 - C_X^2}{4(1 + W_E)} \quad (6.80)$$

when $t = C_X / (1 + W_E)$. To check whether the relation given by Eq. (6.80) can explain the actual experimental results, we consider Eq. (6.80) as a function of ϕ_S and substitute Eqs. (6.73)-(6.75). By moving (0.969 ± 0.013) and (0.935 ± 0.011) independently within the error, we can derive the maximum and minimum values of Eq. (6.80) at a particular ϕ_S .

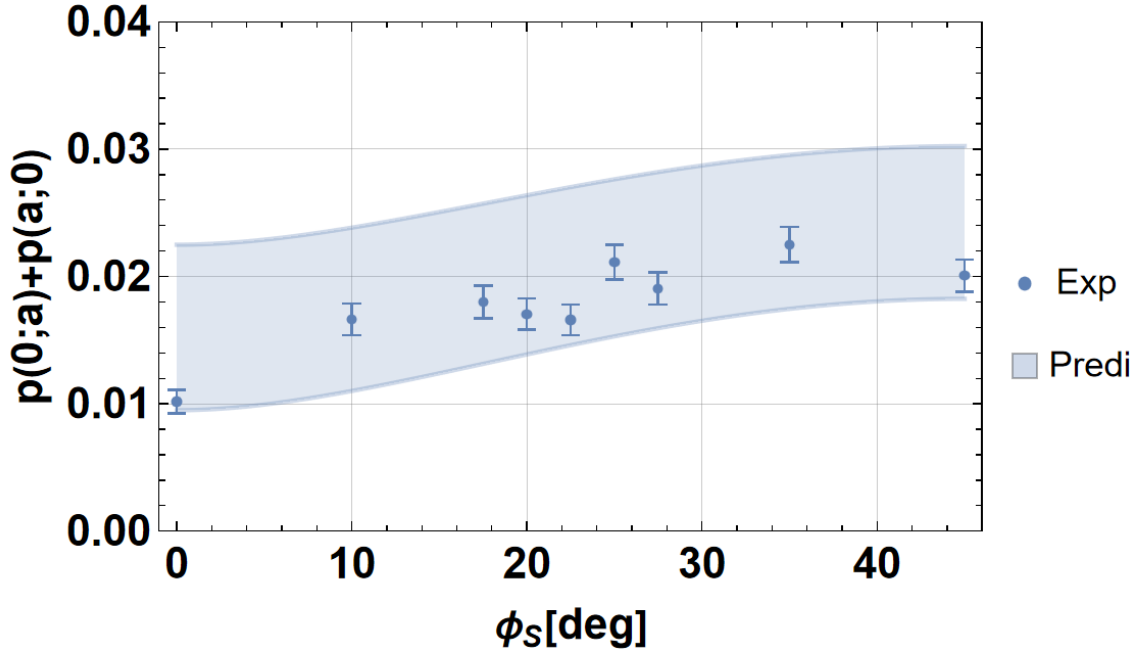


FIGURE 6.11: Comparison of experimental and predicted values for $P(0;a) + P(a;0)$. "Exp" is derived from the raw data shown in TAB. 5.2. "Predi" is the range of values that could change due to statistical errors when Eqs. (6.73)-(6.75) are substituted into Eq. (6.80).

FIG. 6.11 shows the $P(0;a) + P(a;0)$ shown in FIG. 5.4 and the predictions derived from Eq. (6.80). At first glance, the range of fluctuations propagating from (0.969 ± 0.013) and (0.935 ± 0.011) appears to be large, but in terms of probability it is about $\pm 0.5\%$. As ϕ_s increases, the experimental values appear to increase slightly, and the predictions also explain such a trend. Eq. (6.80) is obtained by minimizing Eq. (6.78). This mathematical condition is roughly corresponding to the operation such that $N(0;0) \approx N(0;1)$ is hold as explained in Sec. 5.1.

6.2.3 Relation between $P(1;1)$ and the correlations

In this subsection, we discuss the relation between $P(1;1)$ and the three indices shown in FIG. 3.8. Using Eq. (6.72) and Eq. (6.77), the predicted value of $P(1;1)$ is given by

$$P(1;1) = \frac{1}{8} (2 + V_X + V_Y - 4C_X \cos 2\phi_M + (V_X - V_Y) \cos 4\phi_M). \quad (6.81)$$

As in Subsec. 6.2.2, substituting $t = \sqrt{1 - 2 \sin 2\phi_M \cos 2\phi_M}$ and transforming the equation, noting that $40^\circ < 2\phi_M < 100^\circ$, we obtain

$$P(1;1) = \frac{1}{8} \left(2 + V_X + V_Y - 2C_X \left(\sqrt{2 - t^2} - t \right) + (V_X - V_Y) \sqrt{2t^2 - t^4} \right). \quad (6.82)$$

Using the condition that $P(0;a) + P(a;0)$ is minimized, $t = C_X / (1 + W_E)$, which was derived in Subsec. 6.2.2, Eq. (6.82) becomes

$$P(1;1) = \frac{1}{4} \left(1 + \frac{V_X + V_Y}{2} + \frac{C_X^2}{1 + W_E} - \frac{C_X}{2} \sqrt{2 - \frac{C_X^2}{(1 + W_E)^2}} \right). \quad (6.83)$$

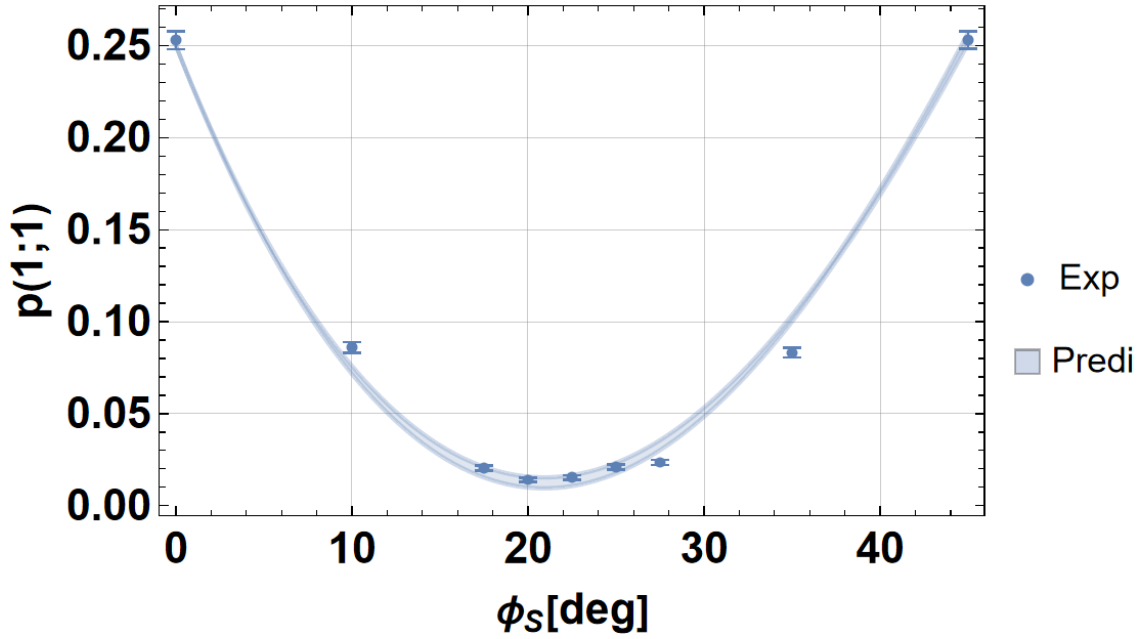


FIGURE 6.12: Comparison of experimental and predicted values of $P(1;1)$. The "Exp" is identical to that shown in FIG. 5.5, and the "Predi" is the value described by Eq. (6.83), with possible regions of variation in the range of (0.969 ± 0.013) and (0.935 ± 0.011) .

Substitute Eqs. (6.73)-(6.75), considering Eq. (6.83) as a function of ϕ_S . By moving (0.968 ± 0.013) and (0.935 ± 0.011) independently within the error, we can derive the maximum and minimum values of Eq. (6.83) at a particular ϕ_S .

FIG. 6.12 shows the experimental values of $P(1;1)$ shown in FIG. 5.3 and the predictions derived from Eq. (6.83). Because Eqs. (6.73)-(6.75) contain errors, the predictions have a certain range. For the three points $\phi_S = 10^\circ, 27.5^\circ$, and 35° , the experimental and predicted values do not agree. This indicates that we need to consider systematic errors such that the predictions are biased toward regions where ϕ_S is large overall. The density matrix described by Eq. (6.72) ignores the presence of correlations that have a value of zero, but in a real experiment there should be more or less influence. In FIG. 6.10, it seems that the effect of such correlations could be ignored, but in FIG. 5.3, the effect of such correlations was significant. The minimum of the experimental values is within the range of the predicted values. This indicates that the minimum value of the probability can be well explained by the magnitude of the correlation that the entangled photon pairs have.

6.2.4 Relation between $P(a;a)$ and the correlations

As in Subsec. 6.2.2 and Subsec. 6.2.3, the relation between $P(a;a)$ and correlation is discussed. Using Eq. (6.72) and Eqs. (2.29), (6.76), and (6.77), the predicted value of $P(a;a)$ is

$$P(a;a) = \frac{1}{8} (2 + V_X + V_Y - 4C_X \sin 2\phi_M - (V_X - V_Y) \cos 4\phi_M). \quad (6.84)$$

As in Subsec. 6.2.2, substituting $t = \sqrt{1 - 2 \sin 2\phi_M \cos 2\phi_M}$ and transforming the equation, noting that $40^\circ < 2\phi_M < 100^\circ$, we obtain

$$P(a;a) = \frac{1}{8} \left(2 + V_X + V_Y - 2C_X \left(\sqrt{2 - t^2} + t \right) + (V_X - V_Y)t\sqrt{2 - t^2} \right). \quad (6.85)$$

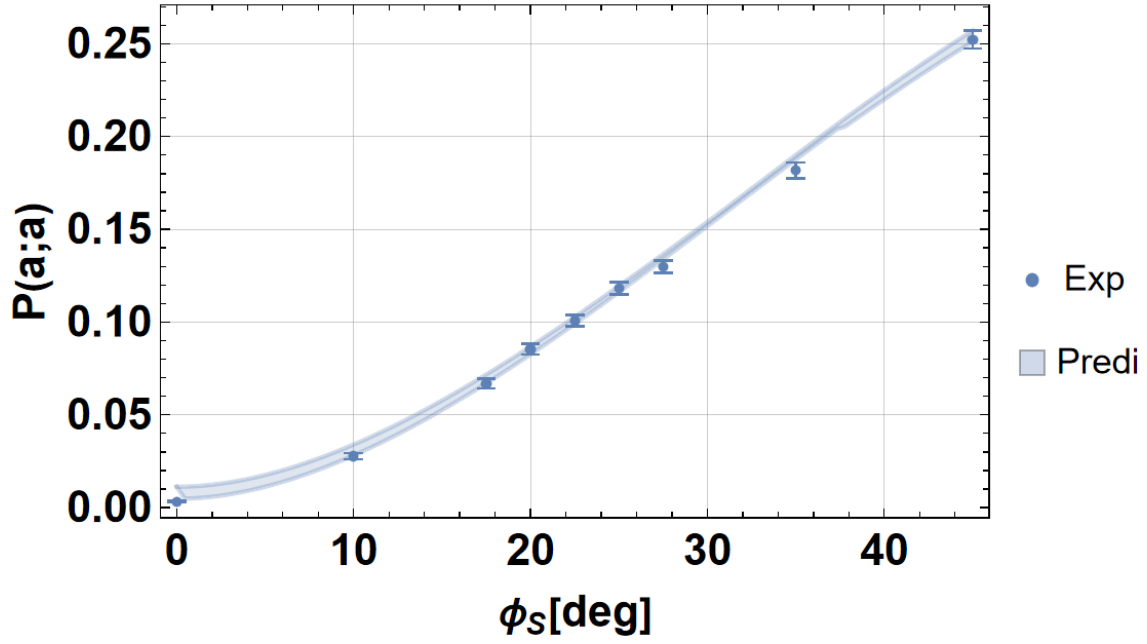


FIGURE 6.13: Comparison of experimental and predicted values of $P(a; a)$. "Exp" represents the experimental value of $P(a; a)$ derived from TAB. 5.2, and "Predi" represents the predicted value of $P(a; a)$ that can be taken when Eqs. (6.73)-(6.75) are substituted into Eq. (6.86).

Using the condition that $P(0; a) + P(a; 0)$ is minimal, $t = C_X / (V_X - V_Y)$, and Eq. (3.8), Eq. (6.85) becomes

$$P(a; a) = \frac{1}{4} \left(1 + \frac{V_X + V_Y}{2} - \frac{C_X^2}{1 + W_E} - \frac{C_X}{2} \sqrt{2 - \frac{C_X^2}{(1 + W_E)^2}} \right). \quad (6.86)$$

Substituting Eqs. (6.73)-(6.75) for Eq. (6.86) as a function of ϕ_s If (0.968 ± 0.013) and (0.935 ± 0.011) can vary in value independently within the error range, then the maximum and minimum values that $P(a; a)$ has for a particular ϕ_s are the errors of $P(a; a)$ derived by error propagation.

FIG. 6.13 shows the experimental values of $P(a; a)$ shown in FIG. 5.5 and the predictions derived from Eq. (6.86). Since all the experimental values are within the range of the predictions, the density matrix described by Eq. (6.72) is sufficient to understand the situation. In the range where ϕ_s is small, the error range is larger in the region where the rate of change of $P(a; a)$ is small. This trend is also observed in the FIG. 6.12. On the other hand, in the region where ϕ_s is large, there is a large error range and a small error range, even though the rate of change is almost unchanged. This means that the rate of change of $P(a; a)$ is smaller when (0.969 ± 0.013) and (0.935 ± 0.011) are allowed to vary freely; since it is not the rate of change relative to ϕ_s , it does not appear in the graph for ϕ_s .

6.2.5 Contrast of the four contextual probabilities

The purpose of the second experiment is to operationally define the initial state such that it exhibits quantum context dependence. How strongly it exhibits quantum context dependence can be determined by how strongly it violates the non-contextual inequality described by Eq. (2.20). The three deterministic conditions imposed on the initial state, Eqs. (2.17)-(2.19), have systematic errors of 1 – 2%, as shown in FIG. 5.3 and FIG. 5.4. It

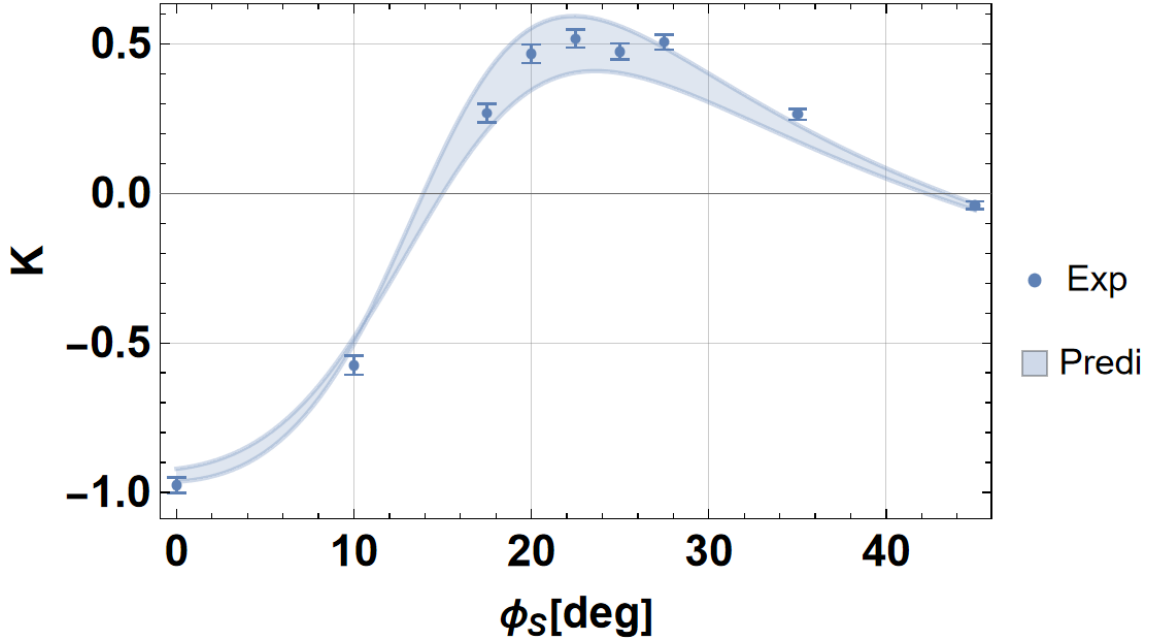


FIGURE 6.14: Comparison of experimental and predicted values of the contrast function. The horizontal axis is ϕ_S , which represents the degree of entanglement, and the vertical axis is the contrast function defined by Eq. (6.87).

would be useful to have a quantitative indicator that is sensitive to such small systematic errors to see how strongly the quantum context dependence is manifested. As such a quantitative indicator, we define the following contrast function.

$$K := \frac{P(a;a) - P(0;a) - P(a;0) - P(1;1)}{P(a;a) + P(0;a) + P(a;0) + P(1;1)}. \quad (6.87)$$

As can be seen from Eq. (2.20), it is consistent with non-contextual logic when $K \leq 0$, and quantum context dependence is manifested when $K > 0$. $K = -1$ is achieved only when $P(a;a) = 0$, and $K = 0$ is achieved when $P(0;a) + P(a;0) + P(a;a) = P(a;a)$, $K = 1$ is valid only when $P(0;a) + P(a;0) + P(a;a) = 0$.

The predicted value of the contrast function can be obtained by adding Eqs. (6.80), (6.83), and (6.86) to Eq. (6.87), which yields the equation given by

$$K = \frac{1 + C_X^2 - W_E^2}{C_X^2 - 2(2 + V_Y)(1 - W_E) + C_X \sqrt{2(1 + W_E)^2 - C_X^2}}. \quad (6.88)$$

Eqs. (6.73)-(6.75) are adopted here as the specific forms of C_X , V_X , and V_Y . The experimental values of the contrast function are obtained by substituting the experimental values shown in FIGs. 5.3 - 5.5 into Eq. (6.87).

FIG. 6.14 compares the experimental and predicted values of the contrast function expressed in Eq. (6.87), and TAB. 6.8 shows the specific values of the experimental values of the contrast function. The maximum value of the experimental value is roughly 0.5, which is the same at four points $\phi_S = 20^\circ$, 22.5° , 25° , and 27.5° . The range of degrees of entanglement where the non-contextual logic breaks down is wide, with non-contextual inequality breaking observed at least from $\phi_S = 17.5^\circ$ to $\phi_S = 35^\circ$. Interestingly, no non-contextual inequality breaking is observed at the maximum entanglement state of $\phi_S = 45^\circ$. Considering the relationship between FIG. 6.15 and FIG. 3.8, we can see that

TABLE 6.8: Numerical results for the contrast function. The contrast function is defined by Eq. (6.87) and all experimental values are derived from the numerical data in TAB. 5.2.

$\phi_S[\text{deg}]$	K
0	-0.975 ± 0.026
10	-0.575 ± 0.031
17.5	0.269 ± 0.031
20	0.467 ± 0.032
22.5	0.518 ± 0.030
25	0.475 ± 0.027
27.5	0.506 ± 0.026
35	0.265 ± 0.019
45	-0.040 ± 0.013

the breaking is largely observed where there are two types of correlations: non-local quantum correlations, expressed in terms of entanglement witness, and local correlations, expressed in terms of degree of local polarization. If the three deterministic conditions were perfectly prepared, the value of K would be 1, so the fact that it is reduced to 0.5 by systematic errors of less than 5% indicates that the contrast function is a sensitive indicator to systematic errors.

Although the predicted value of the contrast function is able to explain the tendency for the value of K to remain constant around its maximum value, it can be seen that at two points, $\phi_S = 10^\circ$ and $\phi_S = 35^\circ$, the experimental and predicted values are out of phase; at points slightly larger than $\phi_S = 10^\circ$ the range of change in the predicted value is smaller. The points (0.968 ± 0.013) and (0.935 ± 0.011) in Eqs. (6.73)-(6.75) represent the maximum value of coherence exhibited by the interferometer, so we can see that they are points that change little with respect to the change in coherence. Conversely, near $\phi_S = 22.5^\circ$, the maximum value of K is sensitive to changes in coherence because the change in K is large relative to the change in coherence.

6.2.6 Bell correlations in the consistency paradox

As shown in Eq. (2.25), the non-contextual inequality and Bell's inequality are mathematically equivalent. Therefore, it may be interesting to evaluate the experimental values of the four Bell correlations included in Eq. (2.25). We define the physical properties \hat{F} and \hat{W} as

$$\hat{F} = |1\rangle\langle 1| - |0\rangle\langle 0| \quad (6.89)$$

$$\hat{W} = |b\rangle\langle b| - |a\rangle\langle a|. \quad (6.90)$$

From these two equations, the four Bell correlations are given by

$$\langle FF \rangle = P(1;1) + P(0;0) - P(0;1) - P(1;0) \quad (6.91)$$

$$\langle FW \rangle = P(1;b) + P(0;a) - P(0;b) - P(1;a) \quad (6.92)$$

$$\langle WF \rangle = P(b;1) + P(a;0) - P(a;1) - P(b;0) \quad (6.93)$$

$$\langle WW \rangle = P(b;b) + P(a;a) - P(a;b) - P(b;a). \quad (6.94)$$

These four Bell correlations can be evaluated using the counts in TAB. 5.2. The predictions corresponding to each Bell correlation can be evaluated by using Eq. (6.72) and Eq. (6.89) and Eq. (6.90), where the $\{0,1\}$ -basis is given by Eq. (6.76) and Eq. (6.77) and the $\{a,b\}$

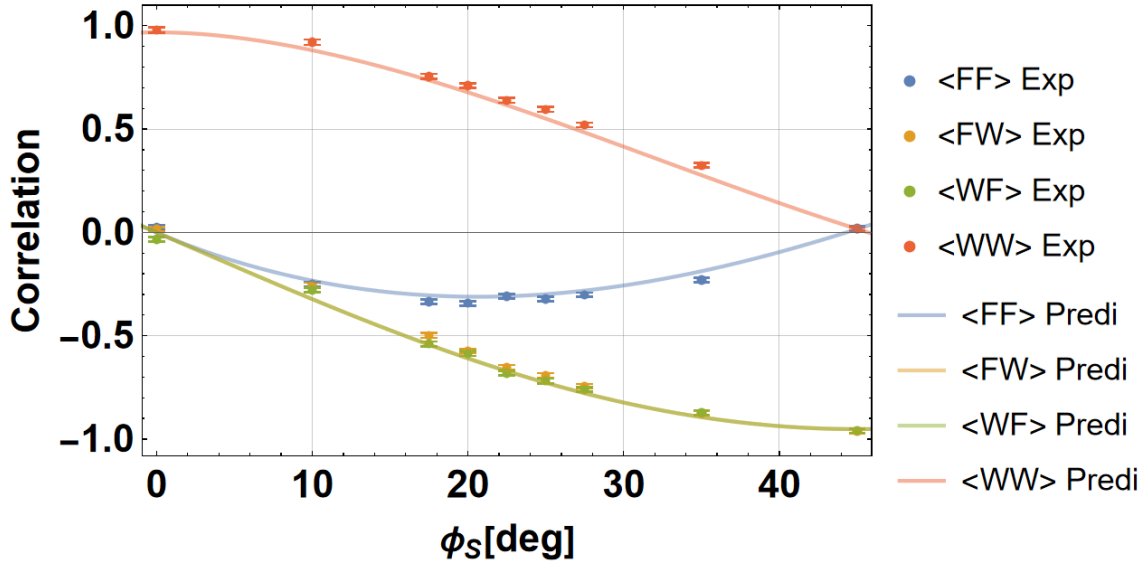


FIGURE 6.15: Experimental and predicted values of Bell correlation in the consistency paradox; "Exp" can be evaluated from the counts in TAB. 5.2; "Predi" represents the predicted values, substituting $C_X = 0.968 \cos 2\phi_S, V_X = 0.968, V_Y = -0.935 \sin 2\phi_S$ in Eqs. (6.99)-(6.102).

basis by Eq. (2.29) and Eq. (2.30). The four Bell correlations are given by

$$\langle \hat{F}\hat{F} \rangle = \frac{1}{2}((V_X - V_Y) \cos 4\phi_M + V_Y + V_X) \quad (6.95)$$

$$\langle \hat{F}\hat{W} \rangle = \frac{1}{2}(V_Y - V_X) \sin 4\phi_M \quad (6.96)$$

$$\langle \hat{W}\hat{F} \rangle = \frac{1}{2}(V_Y - V_X) \sin 4\phi_M \quad (6.97)$$

$$\langle \hat{W}\hat{W} \rangle = \frac{1}{2}((V_Y - V_X) \cos 4\phi_M + V_Y + V_X). \quad (6.98)$$

Using the same procedure as discussed in Subsec. 6.2.3, these four Bell correlations are expressed using $C_X, V_X,$ and V_Y like

$$\langle \hat{F}\hat{F} \rangle = \frac{1}{2} \left(-C_X \sqrt{2 - \frac{C_X^2}{(V_Y - V_X)^2}} + V_Y + V_X \right) \quad (6.99)$$

$$\langle \hat{F}\hat{W} \rangle = \frac{1}{2}(V_Y - V_X) \left(1 - \frac{C_X^2}{(V_Y - V_X)^2} \right) \quad (6.100)$$

$$\langle \hat{W}\hat{F} \rangle = \frac{1}{2}(V_Y - V_X) \left(1 - \frac{C_X^2}{(V_Y - V_X)^2} \right) \quad (6.101)$$

$$\langle \hat{W}\hat{W} \rangle = \frac{1}{2} \left(C_X \sqrt{2 - \frac{C_X^2}{(V_Y - V_X)^2}} + V_Y + V_X \right). \quad (6.102)$$

FIG. 6.15 compares the experimental values evaluated from Eqs. (6.91)-(6.94) with the predictions obtained by substituting $C_X = 0.968 \cos 2\phi_S, V_X = 0.968, V_Y = -0.935 \sin 2\phi_S$ in Eqs. (6.99)-(6.102). One interesting feature is that even though there was a strong positive correlation between W_A and W_B in the product state with $\phi_S = 0^\circ$, a strong negative correlation between F_A and W_B was created in the maximum entangle state with

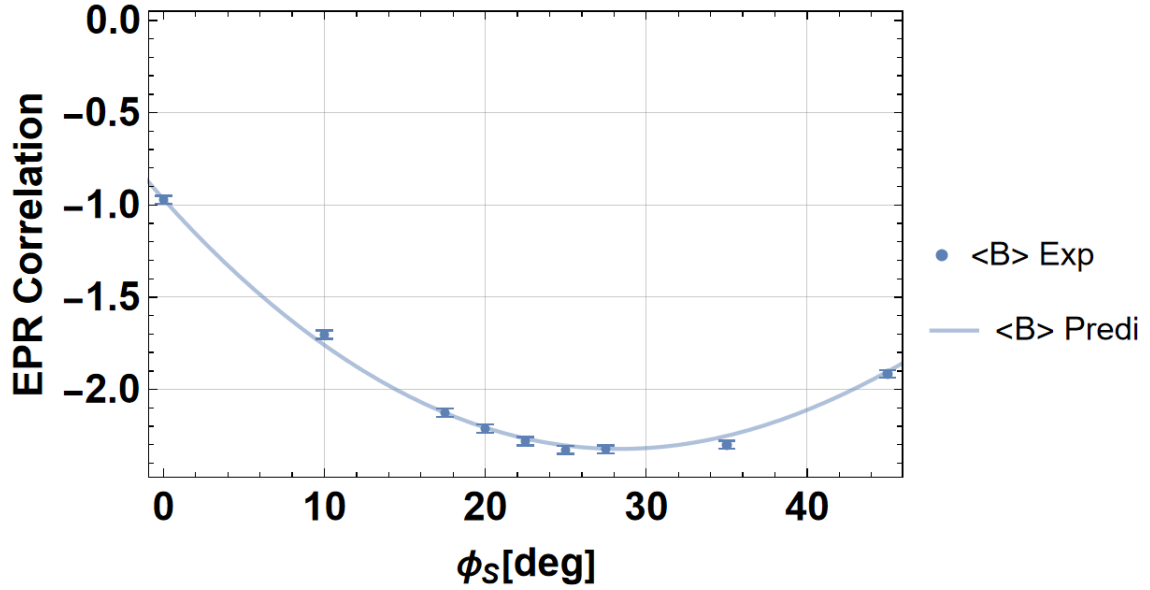


FIGURE 6.16: EPR correlation whose definition is given by Eq. (6.103). "Exp" is the experimental value evaluated using Eqs. (6.91)-(6.94), and "Predi" is the prediction obtained by substituting $C_X = 0.968 \cos 2\phi_S$, $V_X = 0.968$, $V_Y = -0.935 \sin 2\phi_S$ in Eqs. (6.99)-(6.102).

$\phi_S = 45^\circ$. The product state and the maximum entangle state have in common that the correlations between certain physical properties become larger, but usually the correlations between the same or different physical properties are maintained. On the other hand, the result that FIG. 6.15 shows is that when $\phi_S = 0^\circ$, there is correlation between the same physical property \hat{F} , yet when $\phi_S = 45^\circ$, there is correlation between different physical properties \hat{F} and \hat{W} . As the degree of entanglement changes, it means that the relation between physical properties with strong non-local correlations is also changing. Another interesting feature is the behavior of $\langle FF \rangle$. Why does only $\langle FF \rangle$ have an extreme value while the other three Bell correlations show monotonic variation? The reason is clear in FIG. 5.3. Even though the values of $P(0;0)$, $P(0;1)$ and $P(1;0)$ are almost identical, the value of $P(1;1)$ approaches 0 at the midpoint of the value of ϕ_S . This quantum interference causes an imbalance between the positive and negative correlations, and the extreme value of $\langle FF \rangle$ is created at the point where $P(1;1)$ is minimal.

Using the four Bell correlations, EPR correlation can be defined by

$$\langle B \rangle = \langle FF \rangle + \langle FW \rangle + \langle WF \rangle - \langle WW \rangle \quad (6.103)$$

FIG. 6.16 shows the experimental and predicted values of EPR correlation. The minimal value of the predicted value is $\langle B \rangle = -2.3221$ at $\phi_S = 28.342^\circ$. The quantum mechanical upper bound of EPR correlation is Cirel'son bound, $2\sqrt{2} \approx 2.828$, so that the experimental result seems to be far from the maximal EPR correlation, however the important point here is that the $\langle B \rangle$ is maximal where it is not a maximal entangled state. Such experimental results have also been reported by earlier research[54], but the physical properties they defined are not maximally complementary. Observing a violation of Bell's inequality that becomes extreme value in a place that is complementary and yet not in a maximally entangled state seems to be the first result in the world.

Chapter 7

Conclusion

7.1 Experiment to explore the cause of the upper bound of Bell's inequality

In the first experiment, to explore the upper bound of the CHSH-type Bell's inequality, we introduced a joint measurement, which is described as POVM measurement, subject to measurement uncertainty restrictions, to a Bell's inequality verification experiment to evaluate the joint statistical distribution of four polarization physical properties. First, to evaluate the performance of the joint measurement, the joint measurements were performed for eigenstates with a value of +1 for the polarization physical properties, and the measurement visibilities were evaluated. By varying the joint measurement parameter θ_J , the balance of measurement accuracy for the two complementary physical properties can be continuously changed. For some specific θ_J , we independently evaluated the measurement visibility in systems A and B and confirmed that both satisfy the measurement uncertainty limits. We then obtained the joint statistical distribution for a specific joint measurement parameter that can be changed independently in the two measurement systems. The Bell correlations derived from that joint probability distributions varied depending on the value of θ_J , and the statistics of a particular measurement outcome in the joint statistical distribution obtained at a particular θ_J showed extremely low counts that were not observed from the joint statistical distribution when only precise measurements were used. This is the first discovery in the world of the fact that joint measurements show such extremely low counts despite the inclusion of measurement error. By focusing on the measurement outcomes showing this specific outcomes with extremely low counts and considering the relation between the intrinsic joint probability distribution, which is a distribution excluding the measurement errors, and the joint probability distribution evaluated from the experiment, the specific outcomes with low counts need to be further reduced to explain the Cirel'son bounds, and the probabilities need to be negative when there is no measurement uncertainty and only eigenvalues of the physical property are allowed. Furthermore, the value of B defined by the four Bell correlations takes a value of either ± 2 for all sixteen possible measurement outcomes, and the error with respect to the value of B that each measurement outcome contains can be evaluated independently. Plotting the relation between the flip probability of B with respect to the measurement outcomes with extremely low counts and the experimentally obtained joint probabilities, we find that there is a lower bound on the error probability of B . If we assume that the flip probability of B exceeds that lower bound, it means not only that the probability obtained in the experiment must be negative, but also that the magnitude of EPR correlation exceeds the Cirel'son bound.

Using the spin-flip model, the measurement errors can be eliminated independently from the measurement outcomes in system A and in system B. The joint probability distribution without the measurement error exhibits negative probabilities, consistent with

the behavior of Bell correlations and measurement uncertainty limits. Furthermore, the marginal probabilities derived from the joint probability distribution are consistent with the joint probability distribution obtained by the precise measurement and can also explain the value of the Bell correlations.

The initial state, assumed to be a mixed state, is consistent with the results obtained from the experimentally obtained joint probability distributions and faithfully reflects the experimental imperfections. On the other hand, the behavior of the local correlation between the two complementary polarization physical properties is not completely explained, and there were data points where the predicted and experimental values seemed to be out of phase. However, there is a trend that seems to reflect the behavior of the experimental values, and since the correlation between the complementary polarization properties must be complex in order for such a trend to appear, the fact that the correlation obtained by the joint measurement takes a non-zero value indirectly indicates the existence of a pure imaginary correlation.

From the above, the upper bound of Bell's inequality, giving the Cirel'son bound, is caused by the local measurement uncertainty limit which gives a lower bound for the error, so that the probability that can be obtained experimentally is not negative. In other words, the upper bound of the quantum correlation is caused by the uncertainty relation between two complementary physical properties, and the non-locality of the entanglement is not intrinsically related to the violation of Bell's inequality[69].

7.2 Experiment to demonstrate the adaptive input state control

Based on the thought experiment proposed by Frauchiger and Renner, we introduced the concept of adaptive input state control(AISC) to demonstrate that quantum states can be prepared operationally such that quantum contextuality appears. In conventional input state preparation in basic research on quantum mechanics, the goal is to reproduce the quantum state described theoretically as faithfully as possible. However, not only is the quantum state itself physically poorly understood, but also there is always a gap between the unrealistic situation assumed in theory and the imperfection that always accompanies actual experiments, making it difficult to experimentally explore the quantum contextuality. AISC can be one way to overcome this situation. In a previous study, it was shown that the quantum state required in the thought experiment proposed by Frauchiger and Renner can be uniquely defined as a set of three specific deterministic conditions. It should be possible to prepare an input state based on physical properties by simultaneously adding the three deterministic conditions to the quantum state.

In the thought experiment proposed by Frauchiger and Renner, certain suitable entangled states are assumed. In order to experimentally impose the physical conditions on the quantum state, it is necessary to prepare a degree of entanglement variable entanglement source in order to determine the optimal degree of entanglement. In our experiments, we prepared entangled photon pairs of polarization with variable degrees of entanglement, and to confirm whether the degree of entanglement is indeed controllable, three indices of interferometric visibility, degree of local polarization, and entanglement witness were evaluated while changing the power ratio of pump beam between two paths in the Sagnac interferometer. The results showed that the correlation in $\{H, V\}$ -basis was not affected by the overlap of the Sagnac interferometers, and there is a trade-off between the degree local polarization and entanglement witness, and that the degree of entanglement can be controlled as an experimental parameter.

To impose two of the three physical conditions on the quantum state, the identical local polarization rotation was applied to the two physical system each, and the rotation

angle, ϕ_M , was set so that the counts of two particular measurement outcomes are the same. The two measurement outcomes whose counts should be equal can be determined from the local relation between the different measurement contexts. Two of the three physical conditions can be achieved simultaneously due to the symmetry of the physical system. Since symmetry is inherently an unrealistic factor, operations should be implemented that can be achieved without taking symmetry into account, but this is one of the issues to be addressed in the future. For the remaining one physical condition, we evaluated the probability of that physical condition for the experimentally evaluated ϕ_M while varying the degree of entanglement and searched for the degree of entanglement, ϕ_S , that would approach the most ideal value.

AISC resulted in errors of $< 2\%$ for the three physical conditions, and the values were found to be consistent with the magnitude of coherence given by the square root of the sum of the squares of the local degree of polarization and the entanglement witness. Therefore, by fine-tuning the interferometer, increasing the coherence of the state, and implementing a method of determining parameters that is independent of the symmetry of the physical system, it would be possible to achieve physical conditions that are more accurately free of systematic errors. To see how well the ideal physical conditions are achieved, we defined a contrast function with four probabilities for different measurement contexts that constitute a non-contextual inequality. The contrast function K represents that the statistical distribution is consistent with the non-contextual logic when $K \leq 0$, while $K > 0$ means that the statistical distribution is inconsistent with the non-contextual logic and quantum contextuality is manifested. In actual measurements, $K < 0$ was achieved over the range of weak entanglement and maximally entangled state, but $K > 0$ was achieved over a wide range from the point where the local degree of polarization and entanglement are included in just the right balance to the maximum entanglement state. The maximum value of K obtained experimentally is about 0.5, which is half of the maximum value of 1 that K can achieve. However, we were able to prepare input states in which quantum contextuality appeared over a wide range, demonstrating that it is possible to prepare input states operationally with AISC.

We were unable to identify a density matrix that would be roughly consistent with all experimental results. The assumed density matrix is composed of the degree of correlation/local polarization evaluated by the measurements, but ignores phase differences between potentially existing quantum states. Although we did not perform a rigorous quantum state estimation because it is not in line with the purpose of the second experiment, a rigorous evaluation of the statistical errors that non-local correlations and degrees of local polarization have allowed us to quantitatively evaluate at which degree of entanglement the experimentally obtained probabilities fluctuate more. Depending on the degree of entanglement, the measurement outcomes were found to have both sensitive and insensitive points to changes in coherence and to have a complex dependence on the correlation. A precise examination of the multiple interference terms by which the probability of the measurement result is affected may provide new insights into quantum contextuality and quantum correlations.

In summary, it is possible to operationally define input states that exhibit quantum features, and to explore quantum properties experimentally, independent of experiments to verify quantum mechanics. It will be important to conduct experiments with as few elements as possible that we assume and postulate in order to understand the complex quantum world as well as possible[70].

Appendix A

EPR paradox

The EPR paradox originates from a thought experiment proposed by A. Einstein, B. Podolsky, and N. Rozen in 1935[1]. Here is an overview of their argument, using as few mathematical formulas as possible. In the abstract of the EPR paper, they state:

A sufficient condition for the reality of a physical property is the possibility of predicting it with certainty, without disturbing the system.

In other words, the following two conditions are sufficient conditions for the reality of physical property \hat{A} .

- (a) A value of the physical property \hat{A} can be obtained with probability one.
- (b) The system is not disturbed.

Furthermore, the uncertainty principle precludes simultaneous precise measurement of the complementary physical properties, so that they state:

In quantum mechanics in the case of two physical quantities described by non-commuting operators, the knowledge of one precludes the knowledge of the other. Then either (1) the description of reality given by the wave function in quantum mechanics is not complete or (2) these two quantities cannot have simultaneous reality.

Writing their conclusion first, if the uncertainty principle is correct, it implies (1), not (2). The details of the basis on which we can conclude this are explained below. EPR believed that every theory must describe the relation between objective reality and physical concepts. This can be seen in:

Whatever the meaning assigned to the term complete, the following requirement for a complete theory seems to be a necessary one : every element of the physical reality must have a counterpart in the physical theory. We shall call this the condition of completeness.

Let us introduce two physical systems, I and II, and consider their composite system, and they assume

- (i) The two systems can interact from the time $t = 0$ to $t = T$.
- (ii) The quantum state of the composite system before $t = 0$ were known.

To rephrase these two conditions, (i) guarantees that after $t = T$, there is no causal relation between I and II, and (ii) is a necessary condition for assuming a maximally entangled state of position and momentum in the later discussion. Assigning a particle and an anti-particle generated by pair creation to systems I and II, the initial state is known, so that the momentum conservation law allows the measurement of the position/momentum of the particle to know the position/momentum of the anti-particle, which means that

the position/momentum of the anti-particle can satisfies the condition of realism, and if the momentum of the particles is measured, the momentum of the antiparticle satisfies the condition for the reality of a physical property (a) and (b). At times later than $t = T$, a measurement on the particle should not affect the anti-particle, so measuring the position/momentum on the particle and the momentum/position on the anti-particle can satisfy the simultaneous reality of complementary physical properties. This means that the uncertainty principle does not deduce (a). EPR said:

Thus the negation of (a) leads to the negation of the only other alternative (b). We are thus forced to conclude that the quantum-mechanical description of physical reality given by wave functions is not complete.

Furthermore, EPR anticipates the counterargument that only simultaneous measurements can claim simultaneous reality, arguing that:

Indeed, one would not arrive at our conclusion if one insisted that two or more physical quantities can be regarded as simultaneous elements of reality only when they can be simultaneously measured or predicted. On this point of view, since either one or the other, but not both simultaneously, of the quantities P and Q can be predicted, they are not simultaneously real. This makes the reality of P and Q depend upon the process of measurement carried out on the first system, which does not disturb the second system in any way. No reasonable definition of reality could be expected to permit this.

And finally, EPR concluded the paper with:

While we have thus shown that the wave function does not provide a complete description of the physical reality, we left open the question of whether or not such a description exists. We believe, however, that such a theory is possible.

Appendix B

Cirel'son bound

The Cirel'son bound is an upper bound on the quantum mechanical correlations in Bell's inequality violation. Here, instead of quoting the original paper exactly, I give a simplified proof for deriving the Cirel'son bound.

The quantum state of a two-level system can be generally described as follows.

$$|\psi\rangle = \cos\theta |H\rangle + e^{i\phi} \sin\theta |V\rangle, \quad (\text{B.1})$$

where $|H\rangle$ represents the horizontal polarization state, $|V\rangle$ represents the vertical polarization state, θ is the angle of linear polarization when counterclockwise is positive from horizontal polarization, and ϕ is the phase difference that the vertical polarization component has relative to horizontal polarization. Although described in terms of photon polarization in line with this paper, $|H\rangle$ and $|V\rangle$ are just labels, so they can be freely replaced by any physical property in the two-level system. The quantum state orthogonal to Eq. (B.1) is given by

$$|\psi_{\perp}\rangle = e^{-i\phi} \sin\theta |H\rangle + \cos\theta |V\rangle. \quad (\text{B.2})$$

Assuming a situation that one photon of an entangled photon pair is measured in system A and the other photon is measured in system B, two polarization physical properties, \hat{A}_1 and \hat{A}_2 , are measured in system A and two polarization physical properties, \hat{B}_1 and \hat{B}_2 , are measured in system B. The correlation between one polarization physical property in system A and one in system B can be written as

$$\langle \hat{A}_i \hat{B}_j \rangle = \sum_{i,j=1}^2 a_i b_j P(a_i, b_j), \quad (\text{B.3})$$

where a_i and b_j are the values of the corresponding polarization physical properties; according to Born's rule, the joint probability on the right-hand side is equal to the square of the probability amplitude. To determine the probability amplitude, a quantum state and a measurement basis must be defined. As an input state, I assume a maximally entangled states with negative correlation, which is given by

$$|\psi_0\rangle = \frac{1}{\sqrt{2}}(|H\rangle_A \otimes |V\rangle_B - |V\rangle_A \otimes |H\rangle_B), \quad (\text{B.4})$$

where the subscript denotes the system being measured. A measurement result with a value of +1 and a value of -1 is defined as

$$|+1\rangle = \cos\theta |H\rangle + e^{i\phi} \sin\theta |V\rangle \quad (\text{B.5})$$

$$|-1\rangle = e^{-i\phi} \sin\theta |H\rangle + \cos\theta |V\rangle. \quad (\text{B.6})$$

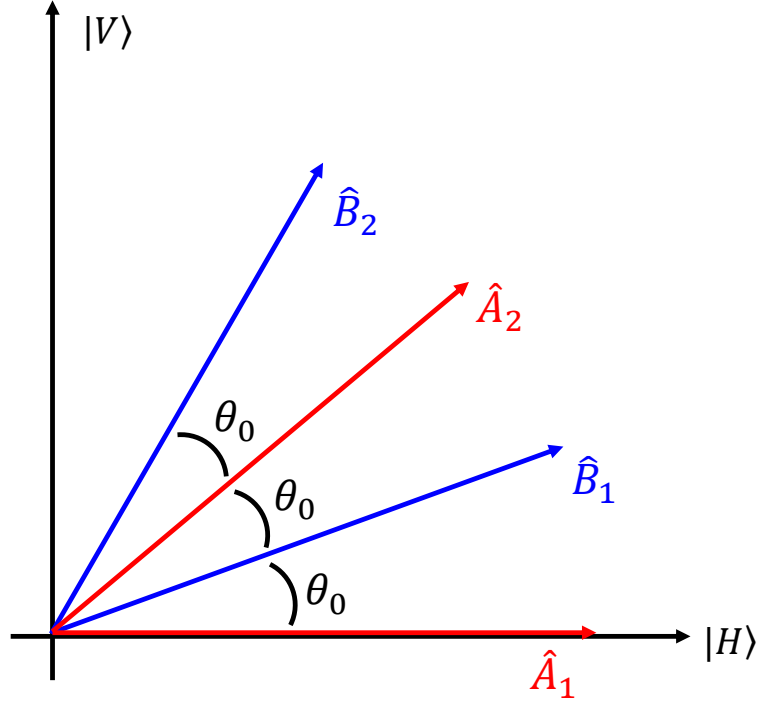


FIGURE B.1: Relation among the measured four polarization physical properties.

Depending on the combination of the two outcomes of the physical property measured in system A and the two outcomes of the physical property measured in system B, four different measurement outcomes are assumed. The two joint probabilities such that the value of the correlation is 1 are given by

$$P(a_i = +1, b_j = +1) = \frac{1}{2} \sin^2[\theta' - \theta] \quad (\text{B.7})$$

$$P(a_i = -1, b_j = -1) = \frac{1}{2} \sin^2[\theta - \theta'], \quad (\text{B.8})$$

where θ is the angle of polarization measured in system A and θ' is the angle of polarization measured in system B. Substituting these two equations for Eq. (B.7), the non-local correlation is given by

$$\begin{aligned} \langle \hat{A}_i \hat{B}_j \rangle &= P(a_i b_j = 1) - P(a_i b_j = -1) \\ &= 2P(a_i b_j = 1) - 1 \\ &= P(a_i = +1, b_j = +1) + P(a_i = -1, b_j = -1) - 1 \\ &= 2 \sin^2[\theta - \theta'] - 1. \end{aligned} \quad (\text{B.9})$$

This appears in the angular difference in the linearly polarized physical properties measured in system A and B.

Next, we define the specific polarization states of the four polarization physical properties to be measured. Assuming that the relationship between the four linearly polarized physical properties to be measured can be written in terms of a single parameter θ_0 , as in FIG. B.1, the relationship between the four Bell correlations is given by Eq. (B.9) as

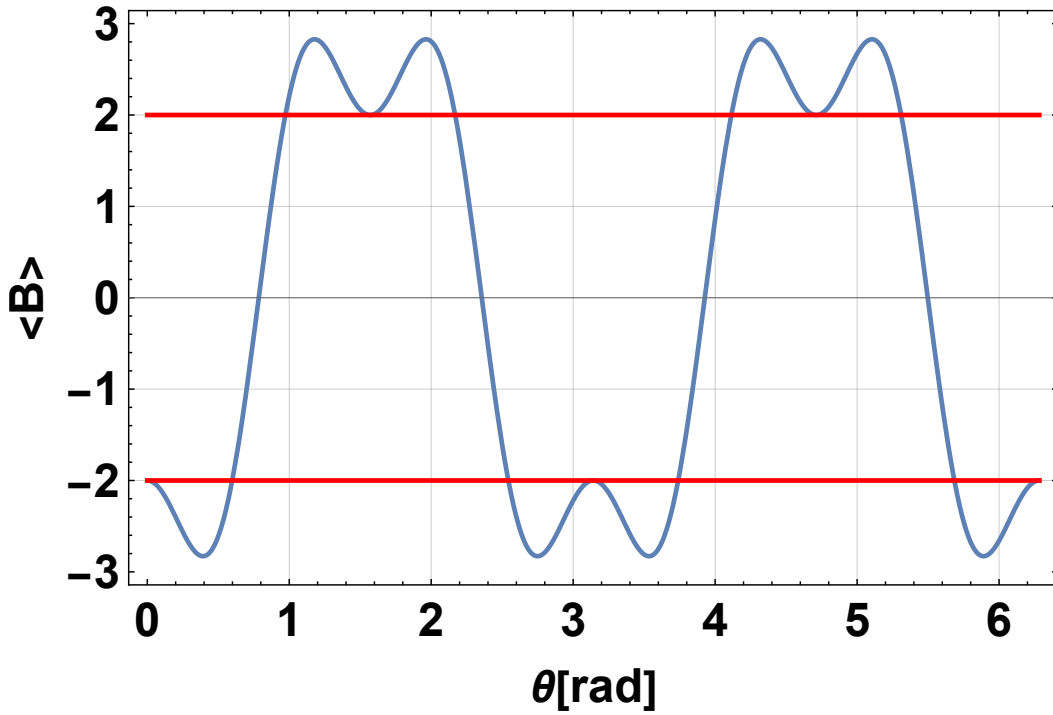


FIGURE B.2: Result of plotting θ_0 against Eq. (B.10). The blue curve represents the result of Eq. (B.10), the red line represents ± 2 .

follows.

$$\begin{aligned}
 \langle \hat{B} \rangle &= \langle \hat{A}_1 \hat{B}_1 \rangle - \langle \hat{A}_1 \hat{B}_2 \rangle + \langle \hat{A}_2 \hat{B}_1 \rangle + \langle \hat{A}_2 \hat{B}_2 \rangle \\
 &= 2 \sin^2[-\theta_0] - (2 \sin^2[-3\theta_0] - 1) + 2 \sin^2[2\theta_0 - \theta_0] - 1 + 2 \sin^2[2\theta_0 - 3\theta_0] - 1 \\
 &= \cos 6\theta - 3 \cos 2\theta
 \end{aligned} \tag{B.10}$$

FIG. B.10 plots the results of Eq. (B.10). It can be seen that for some θ_0 , Bell's inequality is violated and the maximum or minimum value is $\pm 2\sqrt{2}$, the Cirel'son bound.

Appendix C

PR-box

The notion of PR-box is based on the S. Popescu and D. Rohrlich paper[36], and PR stands for the initial of their names. They regarded quantum non-locality and relativistic causality as axioms. Referring the main text of their paper,

Relativistic causality is well defined, but quantum nonlocality appears in both non-local correlations and the AB effect.

And also they say

We discuss nonlocality with reference to nonlocal correlations, and without considering equation of motion. We apply our two axioms simply by asking which theories give rise to non-local correlations, in the sense of Bell's theorem, while preserving causality.

The quantum non-locality they mean is a little vague, however the relativistic causality is defined by

$$\begin{aligned} P(x_A = \pm 1) &= P(x_A = \pm 1; x'_B = +1) + P(x_A = \pm 1; x'_B = -1) \\ &= P(x_A = \pm 1; y'_B = +1) + P(x_A = \pm 1; y'_B = -1), \end{aligned} \quad (\text{C.1})$$

where the lower case letters show the physical system, the x, x' and y' are the values of physical properties \hat{X}, \hat{X}' and \hat{Y}' in two level system. The situation is the same as Bell's inequality test. Eq. (C.1) means that an outcome of a physical property measured in system A is independent of an outcome of physical property measured in the system B. Joint probability distribution always must satisfy this condition.

FIG. C.1 shows maximally achievable EPR correlation that Popescu and Rohrlich suggested. The joint probability distribution shown in FIG. C.1 results in

$$\langle \hat{X}_A \hat{X}'_B \rangle + \langle \hat{X}_A \hat{Y}'_B \rangle + \langle \hat{Y}_A \hat{X}'_B \rangle - \langle \hat{Y}_A \hat{Y}'_B \rangle = 4. \quad (\text{C.2})$$

This result is larger than Cirel'son bound, $2\sqrt{2}$, which is the quantum mechanical upper bound of the EPR correlations. Thus, it is possible to construct a joint probability distribution that satisfies the condition of the relativistic causality but exceeds the maximum quantum mechanical EPR correlation.

As a concrete illustration of the EPR correlation such that exceeds Cirel'son bound. FIG. C.2 shows a superquantum correlation function proposed by Popescu and Rohrlich, which is determined by an angle between two spin physical properties of two level system, one is measured in system A and the other is measured in system B. Rotational symmetry of the correlation function means that it satisfy the relativistic causality. With \hat{Y} as the reference, let us assume that \hat{X}' is the spin with $\pi/12$ rotation, \hat{X} is the spin with $\pi/6$ rotation, and \hat{Y}' is the spin with $\pi/4$ rotation. Calculating the EPR correlations

(a)			
	$x_A = +1$	$x_A = -1$	
$x'_B = +1$	$\frac{1}{2}$	0	
$x'_B = -1$	0	$\frac{1}{2}$	

(b)			
	$x_A = +1$	$x_A = -1$	
$y'_B = +1$	$\frac{1}{2}$	0	
$y'_B = -1$	0	$\frac{1}{2}$	

(c)			
	$y_A = +1$	$y_A = -1$	
$x'_B = +1$	$\frac{1}{2}$	0	
$x'_B = -1$	0	$\frac{1}{2}$	

(d)			
	$y_A = +1$	$y_A = -1$	
$y'_B = +1$	0	$\frac{1}{2}$	
$y'_B = -1$	$\frac{1}{2}$	0	

FIGURE C.1: Four kind of joint probability distribution in Bell's inequality experiment, which can achieve EPR correlation 4. (a) \hat{X}_A measured in system A and \hat{X}'_B measured in system B (b) \hat{X}_A measured in system A and \hat{Y}'_B measured in system B (c) \hat{Y}_A measured in system A and \hat{X}'_B measured in system B (d) \hat{Y}_A measured in system A and \hat{Y}'_B measured in system B. These joint probability distributions satisfy the condition of the relativistic causality shown in FIG. C.1.

according to the superquantum correlation function shown in FIG. C.2, we obtain

$$\begin{aligned}
& E(\hat{X}_A, \hat{X}'_B) + E(\hat{X}_A, \hat{Y}'_B) + E(\hat{Y}_A, \hat{X}'_B) - E(\hat{Y}_A, \hat{Y}'_B) \\
&= E\left(\frac{\pi}{12}\right) + E\left(\frac{\pi}{12}\right) + E\left(\frac{\pi}{12}\right) - E\left(\frac{\pi}{4}\right) = 4.
\end{aligned} \tag{C.3}$$

About the superquantum correlation function, Popescu and Rohrlich said

Of course, the correlation function $E(\theta)$ is contrived, but it illustrates how a correlation function could satisfy relativistic causality and still violate the CHSH inequality with the maximal value 4.

And then, they concluded their paper

Our analysis shows that stronger violations would not conflict with relativity theory. We emphasize that an experiment could test for such violations, which would disprove quantum mechanics without reference to any model.

The superquantum correlation function introduced are physically unclear in many respects. This ambiguous meaning of the function is considered a "black box" and is called a PR-box.

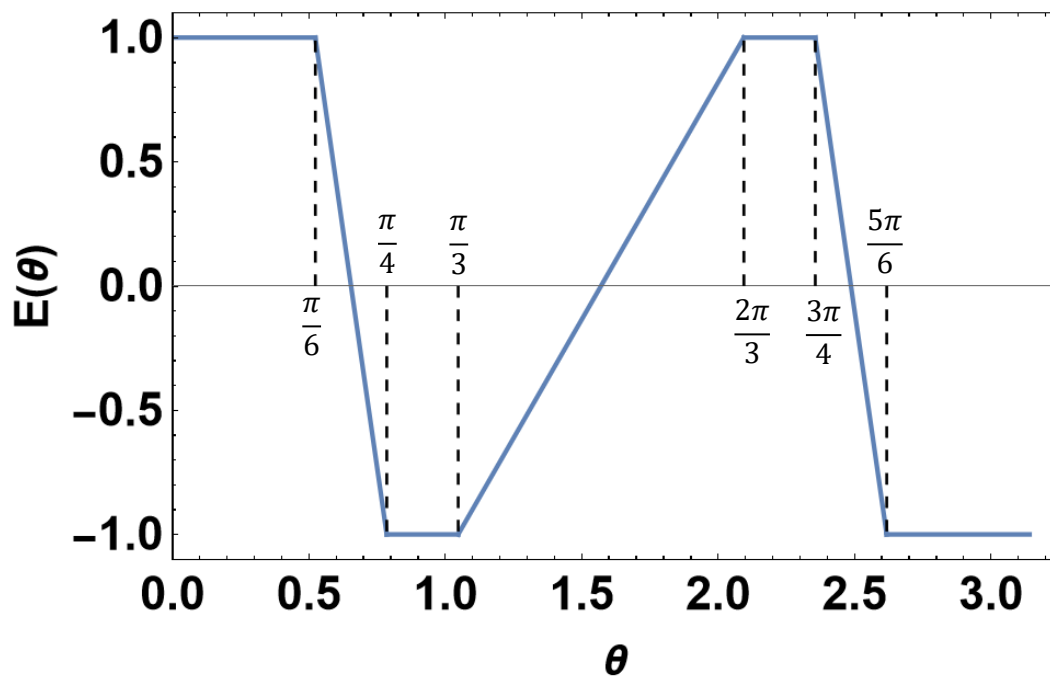


FIGURE C.2: Superquantum correlation function Popescu and Rhorlich proposed in their paper. θ is an angle between two spin vectors, one is measured in system A and the other is measured in system B. The vertical axis shows the value of correlation of the two spin physical properties.

Appendix D

POVM measurement

When considering the measurement of any physical property, whether that property is classical or quantum, it can be understood through the concept of the J. V. Neumann's indirect measurement model[71]. In general, measurements are classified into two categories: direct measurement and indirect measurement. Indirect measurements encompass direct measurements because direct measurements are a special case of indirect measurements. Direct measurement refers to a measurement in which the physical property to be measured is obtained by comparing a reference physical property with the same dimensions. As an example, a situation such as using a ruler to measure the length of an object is classified as a direct measurement. On the other hand, indirect measurement refers to a measurement in which the measured value is obtained indirectly using a relational equation between different physical properties. As an example, measuring the speed of a car using a speed gun is an indirect measurement. The wavelength of the microwaves hitting the car changes due to the Doppler effect. The speed of the car is calculated from the amount of that change of the wavelength. It can be seen that both direct and indirect measurements require two physical systems: the object to be measured and the measuring instrument. They are called a system and a probe, respectively. Conventional quantum mechanics assumes only measurements in which the values of physical property of the system corresponds one-to-one to the values of physical property of the probe. Such a measurement is mathematically called a projection valued measure measurement(PVM measurement). The positive operator valued measure measurement (POVM measurement) generalizes the PVM measurement by giving up a one-to-one correspondence between the values of physical properties of the system and the probe. To formulate the indirect measurement model, let the density matrix of the system be $\hat{\rho}_S$, the density matrix of the probe be $\hat{\rho}_P$, and the unitary operator representing time evolution be \hat{U} . The density matrix of the composite system after time evolution is given by

$$\hat{\rho} = \hat{U}\hat{\rho}_S \otimes \hat{\rho}_P\hat{U}^\dagger. \quad (\text{D.1})$$

The unitary time evolution of the composite system causes the interaction between the system and the probe, and information from the system is transferred to the probe. Thus, information about the system can be obtained from the information obtained by measuring the probe. Let $\{|\phi_m\rangle\}$ be the complete orthonormal basis of one of the probe, and the

probability of obtaining a measurement result m in one of them is given by

$$\begin{aligned}
P(m) &= \text{Tr} [\hat{\rho} |\phi_m\rangle \langle \phi_m|] \\
&= \text{Tr}_S [\text{Tr}_P [|\phi_m\rangle \langle \phi_m| \hat{\rho}]] \\
&= \text{Tr}_S \left[\sum_j p_j \langle \phi_m | \hat{U} |\psi_j\rangle \hat{\rho}_S \langle \psi_j | \hat{U}^\dagger | \phi_m \rangle \right] \\
&= \text{Tr}_S \left[\sum_j p_j \hat{M}_{mj} \hat{\rho}_S \hat{M}_{mj}^\dagger \right] \\
&= \text{Tr}_S [\hat{E}_m \hat{\rho}_S], \tag{D.2}
\end{aligned}$$

where, $\text{Tr}_P[\cdot]$ means a partial trace defined by

$$\text{Tr}_P[\hat{\rho}] := \sum_i (\langle i | \otimes \hat{I}_P) \hat{\rho} (|i\rangle \otimes \hat{I}_P). \tag{D.3}$$

The $\{|i\rangle\}$ is a complete orthogonal basis of the probe, and the following relation was used in the process.

$$\hat{\rho}_P = \sum_j p_j |\psi_j\rangle \langle \psi_j| \tag{D.4}$$

$$\hat{M}_{mj} = \langle \phi_m | \hat{U} |\psi_j\rangle \tag{D.5}$$

$$\hat{E}_m = \sum_j p_j \hat{M}_{mj}^\dagger \hat{M}_{mj}, \tag{D.6}$$

where Eq. (D.4) is the general expression of a density matrix, Eq. (D.5) is a Kraus operator, Eq. (D.6) is a POVM element of the measurement outcome m . At first glance, $\langle \phi_m | \hat{U} |\psi_j\rangle$ seems to be a constant rather than an operator, but the unitary transformation acts on the composite system, whereas $|\phi_m\rangle$ and $|\psi_j\rangle$ are the basis vectors of the probe, so the degrees of freedom do not equal 1. Looking at Eq. (D.6), \hat{E}_m clearly satisfies positivity given by

$$\langle \Psi | \hat{E}_m | \Psi \rangle \geq 0, \tag{D.7}$$

This positivity means an experimentally obtained probability is always positive. Furthermore, the sum of the all POVM elements is

$$\begin{aligned}
\sum_j \hat{E}_j &= \sum_{m,j} p_j \langle \psi_j | \hat{U}^\dagger | \phi_m \rangle \langle \phi_m | \hat{U} | \psi_j \rangle \\
&= \hat{I}. \tag{D.8}
\end{aligned}$$

This result shows that the sum of the probabilities of all measurement outcomes is 1. On the other hand, Eq. (D.5) and Eq. (D.6) says orthogonality is generally false. TAB. D.1 shows the difference of conditions between PVM and POVM measurements. PVM and

TABLE D.1: Comparison of the conditions between PVM and POVM measurement. \hat{P}_i is projection operator defined by $|\phi_m\rangle \langle \phi_m|$, \hat{E}_m is a POVM element. δ_{mn} is Kronecker delta.

Conditions	PVM measurement	POVM measurement
Completeness	$\sum_m \hat{P}_m = \hat{I}$	$\sum_m \hat{E}_m = \hat{I}$
Positivity	$\langle \Psi \hat{P}_m \Psi \rangle \geq 0$	$\langle \Psi \hat{E}_m \Psi \rangle \geq 0$
Orthogonality	$\hat{P}_m \hat{P}_n = \delta_{mn} \hat{I}$	$\hat{E}_m \hat{E}_n \neq \delta_{mn} \hat{I}$

POVM measurements differ in the actual orthogonal conditions. This condition physically indicates whether the measurement outcomes of the system and the probe correspond one-to-one. If the measurement outcomes do not correspond one-to-one, it means that one does not know to which value of the physical property of the system corresponds to the measurement outcomes obtained in the POVM measurement. This is the reason why it is believed that POVM measurement can not manifest the value of physical properties of system.

Appendix E

Bit flip model

How much more error is contained in either of the two physical properties measured by the joint measurement can be varied continuously by changing the joint measurement parameter θ_J . To illustrate it, I assign a specific polarization to the two complementary polarization physical properties as shown in FIG. E.1. Let \hat{X} be the physical property with H (+1) and V (-1) polarization in the measurement result and \hat{Y} be the physical property with P (+1) and M (-1) linear polarization. Defining the angle from the physical property \hat{X} as θ_J , it is possible to control how accurately one measures either \hat{X} or \hat{Y} by changing the value $0^\circ \leq \theta_J \leq 90^\circ$. The extent to which the statistics obtained through the joint measurements contain errors can be quantitatively evaluated by introducing the flipping probability of polarization, P_{flip} .

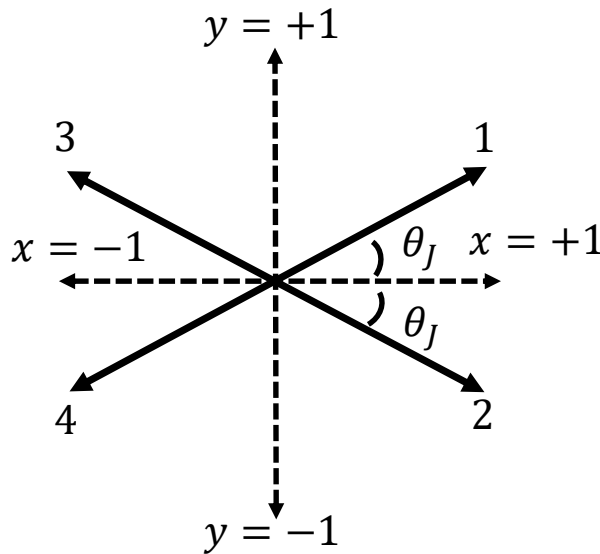


FIGURE E.1: Relation between two complementary polarization physical property in Bloch sphere. The x, y are the value of \hat{X}, \hat{Y} . The θ_J is the joint measurement parameter. Arrows labeled with i ($i = 1, 2, 3, 4$) are the four measurement outcomes in the joint measurements explained in Subsec. 2.1.1.

FIG. E.2 shows the change in the statistical distribution before and after the measurement. Writing "statistical distribution before the measurement" may involve complex realist arguments, but at the time of considering the dynamics of polarization flipping, it is natural to be concerned about the relation between the two statistical distributions before and after the flipping. The number of counts N_{int} that would have been obtained by a precise measurement actually approaches a random result because the measurement contains errors; the probability of a measurement outcome that was $x = +1$ being detected as $x = -1$ and the probability of a measurement outcome that was $x = -1$ being

detected as $x = +1$ are both commonly P_{flip} . Assuming that both probabilities can be described by P_{flip} , the following relationship holds.

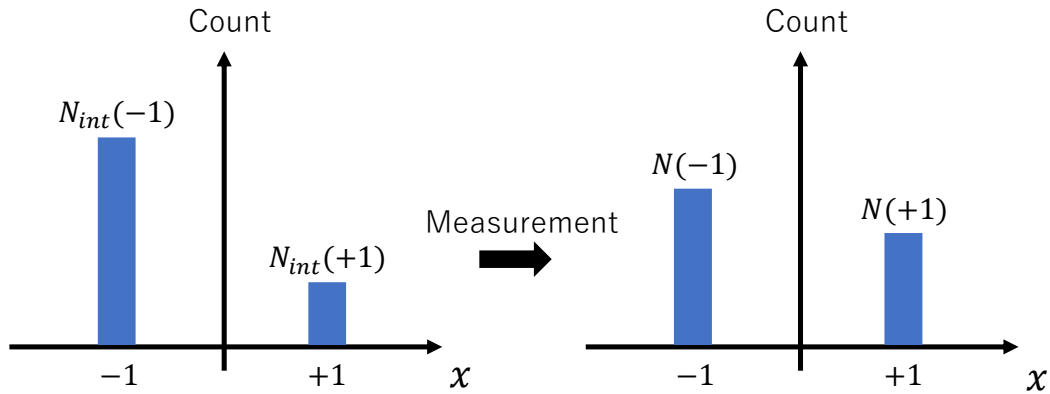


FIGURE E.2: Change in the statistical distribution of the polarization physical property \hat{X} due to performing a measurement with errors, where N_{int} is the number of counts that would have been obtained by a precise measurement and N is the number of counts obtained by a measurement with errors.

$$N(+1) = (1 - P_{flip})N_{int}(+1) + P_{flip}N_{int}(-1) \quad (\text{E.1})$$

$$N(-1) = P_{flip}N_{int}(+1) + (1 - P_{flip})N_{int}(-1), \quad (\text{E.2})$$

where P_{flip} is a probability that a measurement outcome flips, $1 - P_{flip}$ is a probability that a measurement outcome does not flip. Using Eq. (2.1), Eq. (E.1) and Eq. (E.2), the relation between the measurement visibility and the flipping probability is given by

$$V_X = 1 - 2P_{flip}. \quad (\text{E.3})$$

Since the measurement visibility is greater or equal to zero and less or equal to one, the flipping probability satisfies $0 \leq P_{flip} \leq 0.5$.

Appendix F

Three-box paradox

The three-box paradox was proposed by Aharonov and Vaidman in 1991. Here is an overview of the paradox.

As an initial state, let us assume a quantum state given by

$$|\psi_i\rangle = \frac{1}{\sqrt{3}} (|A\rangle + |B\rangle + |C\rangle). \quad (\text{F.1})$$

Eq. (F.1) represents a quantum state in which there are three boxes, A, B, and C, and a particle is contained somewhere in these three boxes with equal probability. Let us choose a final state given by

$$\langle\psi_f| = \frac{1}{\sqrt{3}} (\langle A| + \langle B| - \langle C|). \quad (\text{F.2})$$

An intermediate measurement is performed for the quantum state shown in Eq. (F.1). If we measure box A and find no particles, we obtain the quantum state that no particles were found in box A. If one measure box A and find no particles, one obtain the quantum state that no particles were found in box A, which is given by

$$(\hat{I} - |A\rangle\langle A|) |\psi_i\rangle \rightarrow \frac{1}{\sqrt{2}} (|B\rangle + |C\rangle). \quad (\text{F.3})$$

Since Eq. (F.2) and Eq. (F.3) are orthogonal, it follows that if no measurement was made in box A, then no particle is ultimately detected.

Next, if an intermediate measurement is made in Box B in the same way, the quantum state after the intermediate measurement is given by

$$(\hat{I} - |B\rangle\langle B|) |\psi_i\rangle \rightarrow \frac{1}{\sqrt{2}} (|A\rangle + |C\rangle). \quad (\text{F.4})$$

The quantum state in Eq. (F.4) is also orthogonal to the final state in Eq. (F.2), which means that if no particles are measured in box B, then no particles are measured in the other two boxes. Putting these results together, the next two arguments hold.

- If no particles are measured in box A, then no particles will ultimately be detected.
- If no particles are measured in Box B, then no particles will ultimately be detected.

It follows that if a proposition is true, then its counterpart is also true, so

- If a particle is eventually detected, it is measured in box A.
- If a particle is eventually detected, it is measured in box B.

are valid. The three-box paradox poses the problem that if these two propositions hold simultaneously, then there is more than one particle, and this problem becomes a paradox.

Appendix G

GHZ paradox

The GHZ paradox is one of the thought experiments used to verify Bell's theorem, which has the feature of being able to confirm the truth of local realism without using statistics such as averages or correlations[48]. Here is a brief description of the GHZ paradox. A quantum state, named GHZ state, is given by

$$|\psi\rangle_{GHZ} = \frac{1}{\sqrt{2}} (|\uparrow\uparrow\uparrow\rangle - |\downarrow\downarrow\downarrow\rangle). \quad (G.1)$$

The three particles are observed by A, B and C. The direction of the spin measured by these three observers is perpendicular to the direction of motion of the particles. The two spin physical properties, \hat{X} and \hat{Y} , are measured by the three observers. The A, B and C perform the following four kinds of measurements.

- (i) A measures \hat{X} , B and C measure \hat{Y}
- (ii) B measures \hat{X} , A and C measure \hat{Y}
- (iii) C measures \hat{X} , A and B measure \hat{Y}
- (iv) A, B and C measure \hat{X}

Assuming that the $|\uparrow\rangle$ and the $|\downarrow\rangle$ are eigenstates of the spin of Z axis, the \hat{X} and the \hat{Y} can be described as

$$\hat{X} = \begin{pmatrix} 0 & 1 \\ 1 & 0 \end{pmatrix} \quad (G.2)$$

$$\hat{Y} = \begin{pmatrix} 0 & -i \\ i & 0 \end{pmatrix}. \quad (G.3)$$

Under the quantum state of Eq. (G.1), the four measurements corresponding to (i)-(iv) are described as

$$\hat{X}_A \hat{Y}_B \hat{Y}_C |\psi\rangle_{GHZ} = +1 |\psi\rangle_{GHZ} \quad (G.4)$$

$$\hat{Y}_A \hat{X}_B \hat{Y}_C |\psi\rangle_{GHZ} = +1 |\psi\rangle_{GHZ} \quad (G.5)$$

$$\hat{Y}_A \hat{Y}_B \hat{X}_C |\psi\rangle_{GHZ} = +1 |\psi\rangle_{GHZ} \quad (G.6)$$

$$\hat{X}_A \hat{X}_B \hat{X}_C |\psi\rangle_{GHZ} = -1 |\psi\rangle_{GHZ}. \quad (G.7)$$

Thinking these situations from the point of view of local realism, an inconsistency is provided. Assuming that the three observers already know the results of the three measurements (i)-(iii), for example, in the situation of (i), A can predict the value of \hat{X}_A from

the results of \hat{Y}_B and \hat{Y}_C . Thinking the similar situations, (i)-(iii) results in

$$x_A y_B y_C = +1 \quad (\text{G.8})$$

$$y_A x_B y_C = +1 \quad (\text{G.9})$$

$$y_A y_B x_C = +1, \quad (\text{G.10})$$

where the lower case letters are the values of physical properties represented by upper-case letters. The product of these three expressions are given by

$$x_A x_B x_C y_A^2 y_B^2 y_C^2 = 1. \quad (\text{G.11})$$

The square of y is definitely 1, so that the relation among three x is given by

$$x_A x_B x_C = 1. \quad (\text{G.12})$$

This result is contradict with the prediction of quantum mechanics shown in Eq. (G.7). Experimental verification agreed with the prediction of quantum mechanics[55].

Appendix H

Hardy's paradox

Hardy's paradox is based on the paper written by L. Hardy in 1992[72]. The original motivation of the paper was to show a contradiction between quantum mechanics and local realism without using an inequality in a 2×2 level system. FIG. H.1 shows the setup of the thought experiment of the Hardy's paradox. The setup of the thought experiment consists of two Mach-Zehnder interferometers, with an electron and a positron incident on each interferometer simultaneously. If each interferometer were independent, the two paths of each interferometer would be adjusted so that the the electron and the positron are always detected at detector C^\pm . If the two interferometers are aligned as shown in FIG. H.1, the electron and positron have a probability 1/4 of annihilating each other at point P. The γ -rays produced are not detected. The $BS1^\pm$ make a quantum state given by

$$|e^\pm\rangle \rightarrow \frac{1}{\sqrt{2}} (i|u^\pm\rangle + |v^\pm\rangle), \quad (\text{H.1})$$

where $|u^\pm\rangle$ and $|v^\pm\rangle$ are the path physical properties of electrons and positrons. The $BS2^\pm$ make a quantum state given by

$$\begin{aligned} |u^\pm\rangle &\rightarrow \frac{1}{\sqrt{2}} (|C^\pm\rangle + i|D^\pm\rangle) \\ |v^\pm\rangle &\rightarrow \frac{1}{\sqrt{2}} (i|C^\pm\rangle + |D^\pm\rangle), \end{aligned} \quad (\text{H.2})$$

where $|D^\pm\rangle$ and $|C^\pm\rangle$ means the detection of the electron and positron. If the $BS2^\pm$ are removed, then the quantum state becomes

$$\begin{aligned} |u^\pm\rangle &\rightarrow |C^\pm\rangle \\ |v^\pm\rangle &\rightarrow |D^\pm\rangle. \end{aligned} \quad (\text{H.3})$$

The quantum state immediately after passing through $BS1^\pm$ is

$$|e^+\rangle |e^-\rangle \rightarrow \frac{1}{2} (i|u^+\rangle + |v^-\rangle) (i|u^-\rangle + |v^-\rangle). \quad (\text{H.4})$$

After passing through point P, this quantum state becomes

$$\frac{1}{\sqrt{3}} (|v^+\rangle |v^-\rangle + i|v^+\rangle |u^-\rangle + i|u^+\rangle |v^-\rangle). \quad (\text{H.5})$$

From here, we consider four different situations as follows.

- (i) Both the $BS2^\pm$ are placed.
- (ii) The $BS2^+$ is placed but the $BS2^-$ is removed.

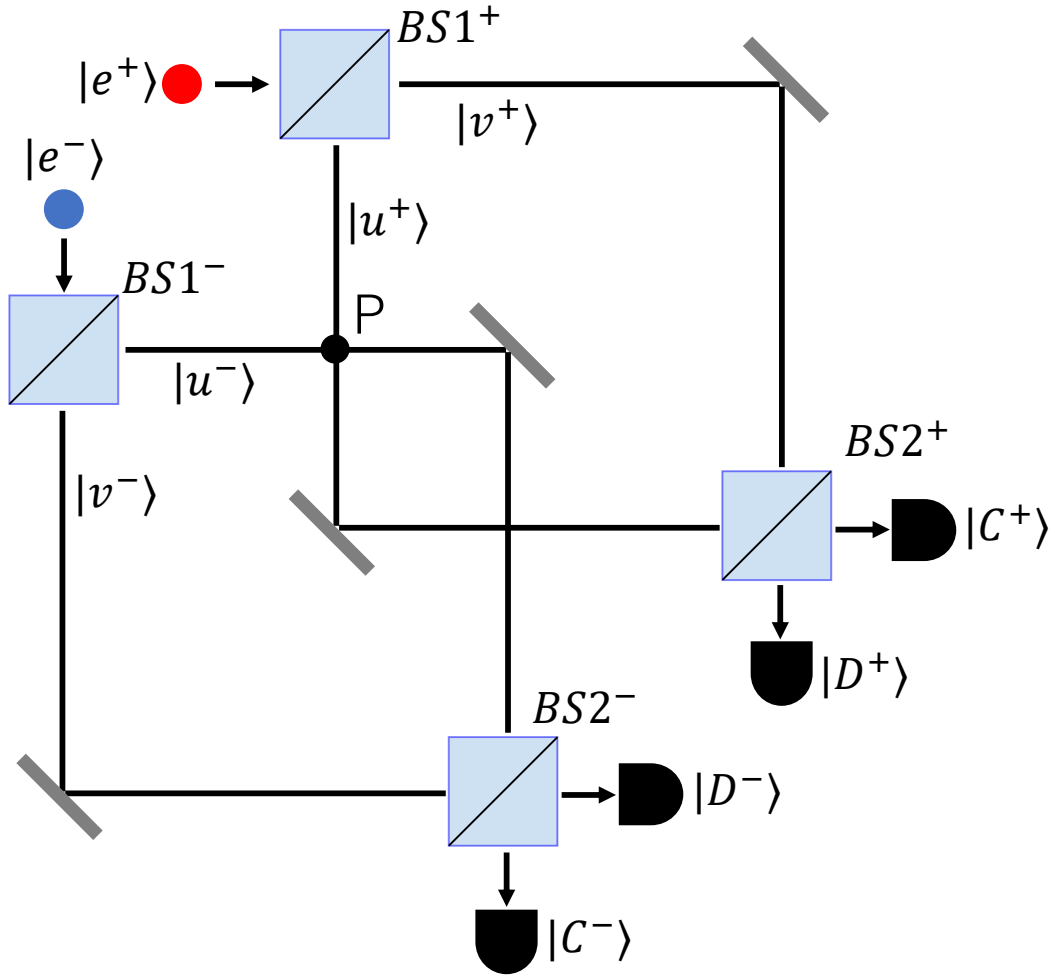


FIGURE H.1: Thought experiment of Hardy's paradox. The $|e^\pm \rangle$ is the quantum state showing the existence of the electron and positron, the $|u^\pm \rangle$ and $|v^\pm \rangle$ are the path physical properties, the $|D^\pm \rangle$ and $|C^\pm \rangle$ means the detection of the particles.

(iii) The $BS2^-$ is placed but the $BS2^+$ is removed,

(iv) Both the $BS2^\pm$ are removed.

Each case leads to the quantum states given by

$$(i) \Rightarrow \frac{1}{\sqrt{12}} (-3 |C^+ \rangle |C^- \rangle + i |C^+ \rangle |D^- \rangle + i |D^+ \rangle |C^- \rangle - |D^+ \rangle |D^- \rangle) \quad (H.6)$$

$$(ii) \Rightarrow \frac{1}{\sqrt{6}} (- |C^+ \rangle |C^- \rangle + i2 |C^+ \rangle |D^- \rangle + i |D^+ \rangle |C^- \rangle) \quad (H.7)$$

$$(iii) \Rightarrow \frac{1}{\sqrt{6}} (- |C^+ \rangle |C^- \rangle + i |C^+ \rangle |D^- \rangle + i2 |D^+ \rangle |C^- \rangle) \quad (H.8)$$

$$(iv) \Rightarrow \frac{1}{\sqrt{3}} (i |C^+ \rangle |D^- \rangle + i |D^+ \rangle |C^- \rangle + |D^+ \rangle |D^- \rangle). \quad (H.9)$$

If local realism is correct, it should be possible to consider all four of these quantum states to be true simultaneously, since the measurement outcome in one system does not depend on the measurement outcome in the other system, and the values are considered to be determined before the measurement is made. Eq. (H.9) predicts the simultaneous

detection at $|C^\pm\rangle$, $P(C^+;C^-) = 0$. Eq. (H.8) says that if $P(D^-) = 1$ then $P(C^+) = 1$, and Eq. (H.7) says that if $P(D^+) = 1$ then $P(C^-) = 1$. Now, let us consider the experiment for which $P(D^+;D^-) = 1$. Eq. (H.6) implies that $P(D^+;D^-) = 1/12$, so that the simultaneous detection at D^\pm is predicted even in quantum mechanics. Simultaneous reality of Eq. (H.7) and Eq. (H.8) requires $P(C^+;C^-) = 1$ however this result contradicts with the prediction of Eq. (H.7), $P(C^+;C^-) = 0$. This is the contradiction in Hardy's paradox.

Appendix I

Bloch sphere

A Bloch sphere is a tool used to visually identify the quantum state of a two-level physical system. The Bloch sphere is highly practical not only for basic research in quantum mechanics using two-level physical systems, but also for visual understanding of the quantum state of a qubit in the recent field of quantum information technology. In this section, we will explain the fundamentals necessary to understand the quantum states of two-level systems using the Bloch sphere. The quantum pure state of a two-level physical system is generally described as

$$|\psi\rangle = \cos \frac{\theta}{2} |\uparrow\rangle + e^{i\phi} \sin \frac{\theta}{2} |\downarrow\rangle, \quad (\text{I.1})$$

where the θ is a parameter that determines the ratio between the $|\uparrow\rangle$ and the $|\downarrow\rangle$, and the ϕ is the phase difference of the $|\downarrow\rangle$ relative to the $|\uparrow\rangle$, i is imaginary unit. If $|\uparrow\rangle$ is an eigenstate with eigenvalue $+1$ and $|\downarrow\rangle$ is an eigenstate with eigenvalue -1 , then the physical property defined by the basis of $\{|\uparrow\rangle, |\downarrow\rangle\}$ is described by the Pauli operator $\hat{\sigma}_Z$. Similarly, the physical property with $\{(|\uparrow\rangle + |\downarrow\rangle)/2, (|\uparrow\rangle - |\downarrow\rangle)/2\}$ as an eigenstate corresponds to $\hat{\sigma}_X$ and the physical property with $\{(|\uparrow\rangle + i|\downarrow\rangle)/2, (|\uparrow\rangle - i|\downarrow\rangle)/2\}$ as an eigenstate corresponds to $\hat{\sigma}_Y$, where $(|\uparrow\rangle + |\downarrow\rangle)/2$ and $(|\uparrow\rangle - |\downarrow\rangle)/2$ are eigenstates belonging to eigenvalue $+1$, and $(|\uparrow\rangle - |\downarrow\rangle)/2$ and $(|\uparrow\rangle + i|\downarrow\rangle)/2$ are eigenstates belonging to eigenvalue -1 . Using Eq. (I.1), the expectation values of these three physical properties are given by

$$\langle \psi | \hat{\sigma}_Z | \psi \rangle = \cos \theta \quad (\text{I.2})$$

$$\langle \psi | \hat{\sigma}_X | \psi \rangle = \sin \theta \cos \phi \quad (\text{I.3})$$

$$\langle \psi | \hat{\sigma}_Y | \psi \rangle = \sin \theta \sin \phi. \quad (\text{I.4})$$

As can be seen from Eqs. (I.2)-(I.4), once the two parameters θ and ϕ are determined, one point on the sphere of radius 1 is uniquely determined. This sphere is called Bloch sphere as shown in FIG. I.1. Each of the three axes corresponds to the expected value of three physical properties, one quantum state is determined by the expectation of three physical properties. If the quantum state is a pure state, the Bloch vector points to a point on the Bloch sphere, and the relation among the three expectation values are given by

$$\langle \psi | \hat{\sigma}_Z | \psi \rangle^2 + \langle \psi | \hat{\sigma}_X | \psi \rangle^2 + \langle \psi | \hat{\sigma}_Y | \psi \rangle^2 = 1. \quad (\text{I.5})$$

If the quantum state is a mixed state, the length of the Bloch vector is less than 1. Since a mixed state is a statistical superposition of some pure states, it can be described using

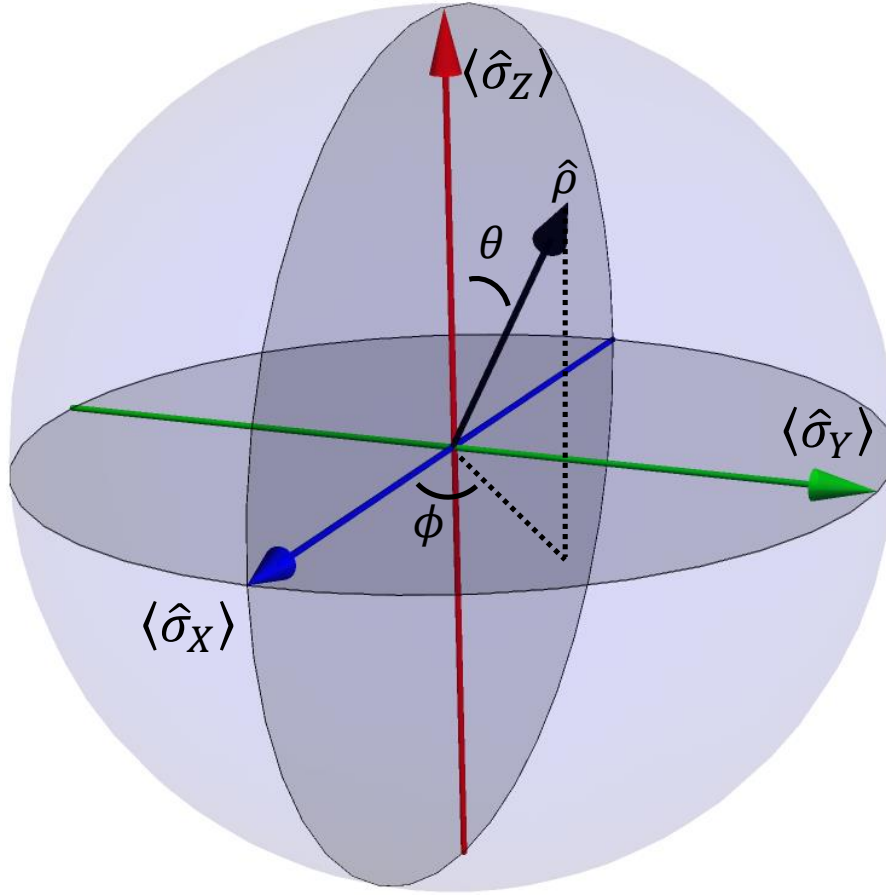


FIGURE I.1: Bloch sphere and a quantum state. The red arrow shows the expectation value of $\hat{\sigma}_Z$, the blue arrow is the expectation value of $\hat{\sigma}_X$ and the green arrow is corresponding to the one of $\hat{\sigma}_Y$. A quantum state described by $\hat{\rho}$ is corresponding to one arrow whose starting point is the origin in the Bloch sphere. This black arrow is called Bloch vector.

Eq. (I.1) as

$$\begin{aligned} \hat{\rho} &= \sum_i p_i |\psi_i\rangle \langle \psi_i| \\ &= \begin{pmatrix} \sum_i p_i \cos^2 \theta_i & \sum_i e^{-i\phi_i} p_i \cos \theta_i \sin \theta_i \\ \sum_i e^{i\phi_i} p_i \cos \theta_i \sin \theta_i & \sum_i p_i \sin^2 \theta_i \end{pmatrix}, \end{aligned} \quad (\text{I.6})$$

where $|\psi_i\rangle = \cos \frac{\theta_i}{2} |\uparrow\rangle + e^{i\phi_i} \sin \frac{\theta_i}{2} |\downarrow\rangle$, p_i is classical statistical ratio of a pure state labeled with i in the total quantum state. Under this mixed state, the expected values of the three physical quantities are given by

$$\langle \hat{\sigma}_Z \rangle = \text{Tr} [\hat{\rho} \hat{\sigma}_Z] = \sum_i p_i \langle \psi_i | \hat{\sigma}_Z | \psi_i \rangle \quad (\text{I.7})$$

$$\langle \hat{\sigma}_X \rangle = \text{Tr} [\hat{\rho} \hat{\sigma}_X] = \sum_i p_i \langle \psi_i | \hat{\sigma}_X | \psi_i \rangle \quad (\text{I.8})$$

$$\langle \hat{\sigma}_Y \rangle = \text{Tr} [\hat{\rho} \hat{\sigma}_Y] = \sum_i p_i \langle \psi_i | \hat{\sigma}_Y | \psi_i \rangle. \quad (\text{I.9})$$

Therefore, the Bloch vector representing the mixed state can be understood as a weighted addition to the Bloch vector representing the all pure states. Since Bloch space is a convex

space, the weighted addition of Bloch vectors representing pure states always points to the interior of the Bloch sphere. A quantum state such that all expectations are zero is called a maximally mixed state. A quantum time evolution described by unitary transformation implies a rotation of the Bloch vector around an axis.

Appendix J

Verification of the Bell's inequality violation

Prior to the first experiment, we conducted an experiment to verify Bell's inequality with precise measurements using an experimental setup shown in FIG. 3.1. In this Appendix, I describe the results of the verification. Two polarization physical properties, \hat{X}_A and \hat{Y}_A , are measured in system A, and two polarization physical properties, \hat{X}'_B and \hat{Y}'_B , in system B. FIG. J.1 shows the joint statistical distributions obtained in the experiment. In the case of precise measurements, $2 \times 2 = 4$ independent joint statistical distributions are evaluated because one of the two polarization physical properties is measured randomly. In each joint statistical distribution, the probabilities are normalized and the four joint probability distributions result in the four Bell correlations given by

$$\langle \hat{X}_A \hat{X}'_B \rangle = -0.634 \pm 0.003 \quad (\text{J.1})$$

$$\langle \hat{X}_A \hat{Y}'_B \rangle = 0.811 \pm 0.004 \quad (\text{J.2})$$

$$\langle \hat{X}_A \hat{X}'_B \rangle = -0.735 \pm 0.004 \quad (\text{J.3})$$

$$\langle \hat{X}_A \hat{X}'_B \rangle = -0.511 \pm 0.003. \quad (\text{J.4})$$

Eqs. (J.1)-(J.4) provides the average of \hat{B} defined by Eq. (2.14),

$$\langle \hat{B} \rangle = -2.691 \pm 0.007 \quad (\text{J.5})$$

This is roughly a 98σ violation compared to $\langle \hat{B} \rangle = -2$. Similar to the results confirmed by numerous experiments, Bell's inequality was confirmed to be violated. Since the relation among all four physical properties are normally equal, the four Bell correlations should show the same value, but there are differences among the correlation values due to imperfections in the initial state and the setting angles of polarization selection. It is believed that this uneven result could be alleviated by adjusting the interferometer and determining the setting angle of polarization selection more precisely.

	$x_A = +1$	$x_A = -1$
$x'_B = +1$	11413	49579
$x'_B = -1$	48971	10630

	$x_A = +1$	$x_A = -1$
$y'_B = +1$	52016	7795
$y'_B = -1$	3581	56793

	$y_A = +1$	$y_A = -1$
$x'_B = +1$	8030	53404
$x'_B = -1$	52206	8128

	$y_A = +1$	$y_A = -1$
$y'_B = +1$	11494	48215
$y'_B = -1$	42967	17989

FIGURE J.1: Experimental results of statistical distributions obtained in an experiment to verify Bell's inequality using precision measurements. All values were obtained from a 10-second measurement. (a) \hat{X}_A was measured in system A and \hat{X}'_B in system B. (b) \hat{X}_A was measured in system A and \hat{Y}'_B in system B. (c) \hat{Y}_A was measured in system A and \hat{X}'_B in system B. (d) \hat{Y}_A was measured in system A and \hat{Y}'_B in system B.

Appendix K

Derivation of Bell's inequalities

This appendix gives the derivation of two types of historically important Bell inequalities. The first is the inequality given by Bell himself in 1964[3], and the second is a CHSH-type inequality[7].

K.1 Original Bell's inequality

Bell assumed the following situation. Two observers, Alice and Bob, measure the spin of entangled 1/2 spin particles. The three spin to be measured are \hat{A} , \hat{B} and \hat{C} . When one of the three physical properties is measured, the value obtained is ± 1 , so that the value of the spin obtained by Alice or Bob is given by

$$S_{A,B}(\hat{X}, \lambda) = \pm 1, \quad (\text{K.1})$$

where the A, B are the label of the two observers, the \hat{X} is one of the three spin physical properties, the λ is a hidden variable. Eq. (K.1) assumes locality, viz, the value of spin doesn't depend the other value of spin. Assuming hidden variables or pre-assigning spin values implies an assumption of reality. If one assumes initial conditions such that the spin values measured by Alice and Bob are always opposite, the relation between the two spin values is given by

$$S_A(\hat{X}, \lambda) = -S_B(\hat{X}, \lambda). \quad (\text{K.2})$$

Let us define the correlation of non-local spin physical properties given by

$$C(\hat{X}_A; \hat{X}_B) := \int S_A(\hat{X}_1, \lambda) S_B(\hat{X}_2, \lambda) d\lambda, \quad (\text{K.3})$$

where the \hat{X}_A and the \hat{X}_B are spin physical properties measured by Alice and Bob, $\int d\lambda = 1$ is hold. Even if we assume a situation where the hidden variables are unevenly distributed, we can easily generalize an argument. Given the difference between the two types of correlations,

$$\begin{aligned} C(\hat{A}; \hat{B}) - C(\hat{A}; \hat{C}) &= \int S_A(\hat{A}, \lambda) S_B(\hat{B}, \lambda) - S_A(\hat{A}, \lambda) S_B(\hat{C}, \lambda) d\lambda \\ &= - \int S_A(\hat{A}, \lambda) S_A(\hat{B}, \lambda) (1 - S_A(\hat{B}, \lambda) S_A(\hat{C}, \lambda)) d\lambda, \end{aligned} \quad (\text{K.4})$$

where Eq. (K.2) and $S_A(\hat{B}, \lambda)^2 = 1$ were used during the transformation of the equation. Absolute value of the $S_A(\hat{A}, \lambda) S_A(\hat{B}, \lambda)$ is definitely less than $+1$, so that the relation

between left hand side and right hand side is given by

$$\begin{aligned} |C(\hat{A}; \hat{B}) - C(\hat{A}; \hat{C})| &\leq \left| \int 1 - S_A(\hat{B}, \lambda) S_A(\hat{C}, \lambda) d\lambda \right| \\ &= |1 + C(\hat{B}; \hat{C})|, \end{aligned} \quad (\text{K.5})$$

due to Eq. (K.2). The $1 + C(\hat{B}; \hat{C})$ is definitely positive, so that the Bell's inequality is given by

$$|C(\hat{A}; \hat{B}) - C(\hat{A}; \hat{C})| \leq 1 + C(\hat{B}; \hat{C}). \quad (\text{K.6})$$

Suppose \hat{A} and \hat{B} are orthogonal spin physical properties and \hat{C} is a physical property exactly between the two spins, the three correlations in the inequality become

$$C(\hat{A}; \hat{B}) = 0 \quad (\text{K.7})$$

$$C(\hat{A}; \hat{C}) = -\frac{1}{\sqrt{2}} \quad (\text{K.8})$$

$$C(\hat{B}; \hat{C}) = -\frac{1}{\sqrt{2}}, \quad (\text{K.9})$$

thus, Eq. (K.6) is violated in quantum mechanics.

K.2 CHSH-type Bell's inequality

The assumed physical situation is the same as the derivation of Bell's inequality above. Alice measures \hat{X}_A and \hat{B} . Bob measures \hat{X}'_B and \hat{Y}'_B . The value of these four spin physical properties are x_A, y_A, x'_B and y'_B , and they can take +1 or -1. The assumption of reality allows us to assign the value of these four spin physical properties simultaneously, so that we can consider the relation given by

$$b := x_A(x'_B - y'_B) + y_A(x'_B + y'_B). \quad (\text{K.10})$$

No matter how the values of the four spins are assigned, the absolute value of b cannot exceed 2 because $x'_B - y'_B$ or $x'_B + y'_B$ become 0. This value of b is defined for just one pair of particles, but if we consider the mean value of b in the population, the mean value of b must satisfy the inequality given by

$$-2 \leq \langle \hat{X}_A \hat{X}'_B \rangle - \langle \hat{X}_A \hat{Y}'_B \rangle + \langle \hat{Y}_A \hat{X}'_B \rangle + \langle \hat{Y}_A \hat{Y}'_B \rangle \leq 2. \quad (\text{K.11})$$

This is just CHSH-type Bell's inequality.

Appendix L

Semiconductor laser

Laser is an acronym for light Amplification by Stimulated Emission of Radiation, and originally meant amplifier. Therefore, when one simply say "laser", it means laser device, and the light produced by a laser device is called laser light. This section does not go into the historical background of laser or their applied use, but rather explains the minimum necessary to understand the semiconductor lasers used in our experiment. The elements necessary to realize a laser are the inverted distribution and the optical resonator. These will be explained, followed by an explanation of how the semiconductor laser achieves these conditions.

L.1 Inverted distribution

There are only three types of light-matter interactions that occur within matter: absorption, induced emission, and spontaneous emission. An electron absorbing a photon and having an energy of E_1 transitions to a state having an energy of E_2 . The relation between these two energy levels is given by

$$\hbar\omega = E_2 - E_1, \quad (\text{L.1})$$

where \hbar is the Dirac constant and ω is the angular frequency of light; Eq. (L.1) is called the Bohr's frequency condition. The energy of light incident on a material is reduced by the energy of the absorbed photons; an electron with energy E_2 can be shaken by an oscillating electromagnetic wave and return to the E_1 energy level again, or it can return to the E_1 energy level without interaction with light. The former is induced emission and the latter is spontaneous emission. After induced emission occurs, the energy of the light increases by the energy of the photons emitted when the energy level of the electrons falls. The probability of photon absorption and induced emission occurring is characterized by the fact that they are proportional to the intensity of the light incident on the material. For a population of photons, the above three phenomena occur simultaneously. The model for dealing with these phenomena simultaneously is given by

$$p_{emi} = A + B\rho_\omega \quad (\text{L.2})$$

$$p_{abs} = B\rho_\omega, \quad (\text{L.3})$$

where ρ_ω is energy density of light with angular frequency ω , A is called the natural emission coefficient and B is called the induced emission coefficient. If the number of electrons at the energy level of E_1 is N_1 and the number of electrons at the energy level of E_2 is N_2 , the energy of absorbed light per unit time is given by

$$I_{abs} = \hbar\omega N_1 p_{abs} = \hbar\omega N_2 B\rho_\omega. \quad (\text{L.4})$$

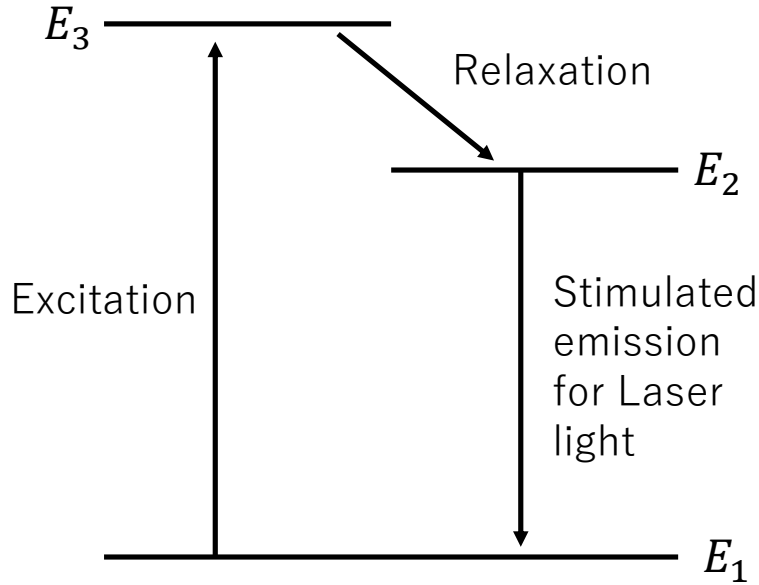


FIGURE L.1: Energy level diagram for inverted distribution. When electrons are excited from the E_1 level to the E_3 level, some fall directly to the E_1 level, but some relax to the E_2 level; if a material is used that stays in the E_2 level for a long time, the number of electrons in E_2 is larger than the number in E_1 , and an inverted distribution is realized between E_1 and E_2 .

The energy of light emitted per unit time is given by

$$I_{emi} = \hbar\omega N_2 p_{emi} = \hbar\omega N_2 (A + B\rho_\omega). \quad (\text{L.5})$$

When matter is in thermal equilibrium, Eq. (L.4) and Eq. (L.5) should be equal because absorption and emission of light apparently do not occur. This relation provides

$$\rho_{ther} = \frac{A}{B} \cdot \frac{N_2}{N_1 - N_2}, \quad (\text{L.6})$$

where ρ_{ther} is energy density of radiation when in thermal equilibrium. The relation between the number of electrons occupying different energy levels when a substance and light are in thermal equilibrium is given by the Boltzmann factor as

$$N_2 = N_1 e^{-\frac{\hbar\omega}{k_B T}}, \quad (\text{L.7})$$

where k_B is Boltzmann's constant and T is the temperature of the substance. Substituting Eq. (L.7) for Eq. (L.6) yields

$$\rho_{ther} = \frac{A}{B} \cdot \frac{1}{e^{\frac{\hbar\omega}{k_B T}} - 1}. \quad (\text{L.8})$$

Considering the case where light with an angular frequency of ω is incident on a material in thermal equilibrium, Eqs. (L.4), (L.5), and (L.8) provide the net absorbed light energy given by

$$\Delta\rho = \hbar\omega B(\rho_\omega - \rho_{ther})(N_1 - N_2). \quad (\text{L.9})$$

If light with an energy higher than the thermal radiation emitted by a material in thermal

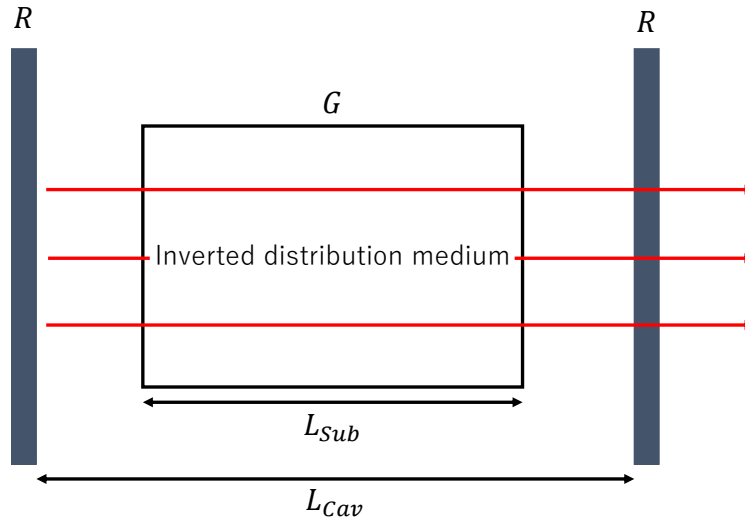


FIGURE L.2: Principle of laser oscillation. An inverted distribution medium of length L_{sub} and gain constant the G is placed in an optical resonator. The R is the reflectance of the mirror and the L_{cav} is the length of the optical resonator. Red arrows show laser light.

equilibrium is incident on the material, the light should be absorbed. Under this condition, $\rho_{ther} < \rho_{\omega}$ is satisfied. Eq. (L.7) shows that the number of electrons in higher energy level is never larger than the one of in lower energy level. However, if one can somehow create a situation where the number of electrons at the energy level of E_2 is greater than the number of electrons at the energy level of E_1 , then Eq.(L.9) will be negative and the energy of the light will be amplified. Such a situation is called an inverted distribution. Until 1960, when lasers were actually realized, it was thought to be impossible to achieve an inverted distribution.

If only two energy levels are used to amplify light, it is not possible to create an inverted distribution. This is because induced emission occurs with the same probability of absorbing light, and N_2 and N_1 will soon become the same. Therefore, to amplify light, three or more levels are used, as shown in FIG. L.1. The world's first laser was realized using rubies as the inverted distribution medium. Rubies have a long lifetime (roughly 3[ms]) for electrons to remain in E_2 and have a broad absorption spectrum but a narrow fluorescence spectrum, making them suitable for realizing lasers.

L.2 Optical resonator

Simply achieving an inverted distribution not only does not efficiently amplify the light, but also does not provide the monochromatic, directional, and other properties of laser light. To solve these problems, an optical resonator is necessary. FIG. L.2 shows the principle of laser oscillation. The inverted distribution medium is sandwiched between mirrors with reflectance R . During one passage of light through this inverted distribution medium, the intensity of the light is multiplied by $e^{GL_{sub}}$. Even if R were less than 1, the light intensity would continue to increase because the light is amplified each time it passes through the inverted distribution medium. To be amplified, $Re^{GL_{sub}} > 1$ is necessary. Since the gain constant is proportional to the difference between the number of electrons in E_2 and the number of electrons in E_1 , the light is amplified to some extent and the number of electrons in E_2 decreases to satisfy $Re^{GL_{sub}} = 1$, at which point the light is not amplified any further.

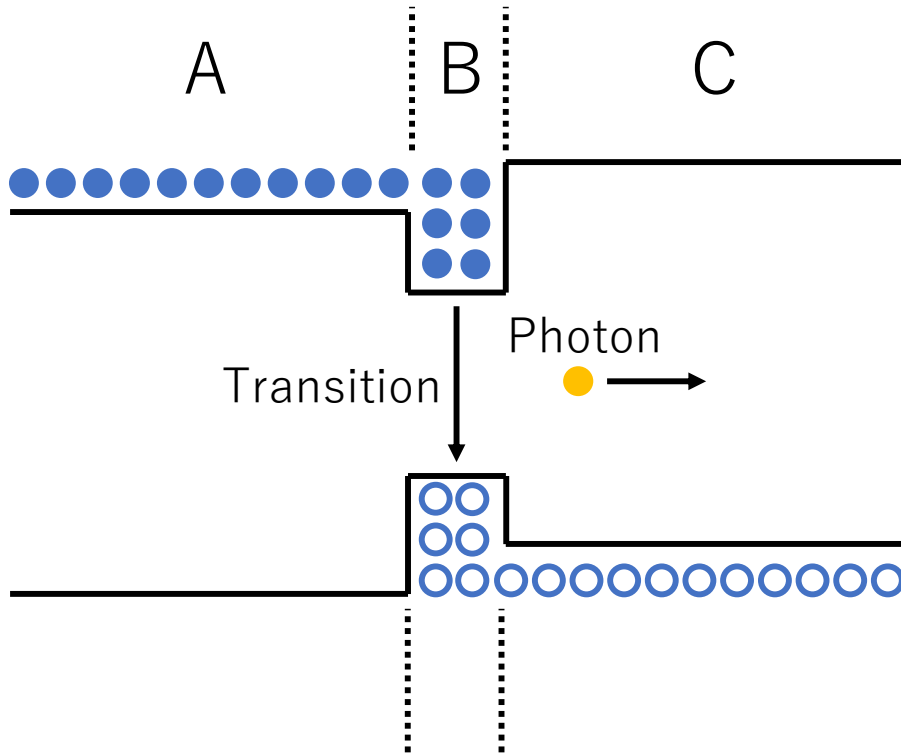


FIGURE L.3: Energy band diagram of a double heterostructure, where A represents the n-type clad layer, B represents the active layer, and C represents the p-type clad layer. n-type clad layers contain many electrons, while p-type clad layers contain many holes. The band-junction energy of the active layer is smaller than that of the p- and n-type semiconductors, allowing electrons and holes to accumulate more efficiently. The transitions of electrons produced in this active layer generate photons.

The light amplified in an optical resonator is limited to only that which has a resonant frequency which satisfy a condition given by

$$\omega_{res} = \frac{n\pi c}{L_{cav}}, \quad (\text{L.10})$$

where ω_{res} is resonance angular frequency, $n \in \mathbb{N}$, c is the speed of light. This condition is derived from the fact that the length of the optical resonator is equal to the product of half the wavelength of the light and a natural number.

L.3 Semiconductor laser

A semiconductor laser is a laser that uses light emission from a semiconductor. This section describes how semiconductor lasers achieve an inverted distribution and an optical resonator. In Sec. L.1, we assumed electrons taking discrete energy levels, but energy levels in semiconductors can be considered to take on nearly continuous values. However, due to the periodicity of the crystal, it is not possible to take an energy level in a certain region. This region is called the forbidden band. The energy band below the forbidden band is called the valence band, and the energy band above the forbidden band is called the conduction band. Electrons in the conduction band can move freely and thus contribute to electrical conduction, while electrons in the valence band can move only within a localized area and thus do not contribute to electrical conduction. When

electrons in the conduction band transition to the valence band, it emits photon corresponding to the band gap energy of the forbidden band. Semiconductor lasers use this radiation. Even if electrons are present in the conduction band, they cannot transition to the valence band if there is no seat for the electrons to move to the valence band. A p-n junction is used to create a situation where there are electrons in the conduction band and a seat for the transfer of electrons, or so-called holes, in the valence band. By doping semiconductors with impurity elements, it is possible to create n-type semiconductors, which have electrons in the conduction band, and p-type semiconductors, which have holes in the valence band. Which type of semiconductor is created depends on the valence electron number of the doped element. When a p-type and n-type semiconductors are p-n junctioned and a positive voltage is applied to the p-type semiconductor, an electron in the conduction band of the n-type semiconductor transitions to the position of a hole in the p-type semiconductor, thus emitting a single photon. In order for laser oscillation to occur, the probability of an electron in the conduction band must be greater than the probability of an electron in the valence band, namely an inverted distribution must be achieved. A mere p-n junction requires a large current density ($100kA/cm^2$) and could not efficiently achieve an inverted distribution. Therefore, a double heterostructure was considered, as shown in FIG. L.3. The active layer inserted between the p-type and the n-type clad layer has a smaller band gap energy than them. Therefore, electrons and holes are accumulated efficiently in the active layer, and electron transitions occur in the active layer. The double heterostructure can create an inverted distribution more efficient than a p-n junction.

In general, the band gap energy and the refractive index are in the trade-off relation. Therefore, the refractive index of the active layer is greater than that of the p-type and n-type clad layers. This fact means that light repeatedly undergoes total reflection within the active layer and light is confined within the active layer. FIG. L.3 is written as if the generated photons propagate through the p-type clad layer, but in reality they propagate through the active layer. The optical resonator necessary for laser oscillation is realized by the cleavage plane of the crystals in the active layer. The two facing cleavage planes act as mirrors to amplify the laser light in the active layer. This is the principle of a semiconductor laser.

Appendix M

Single mode fiber

Optical fiber is an optics that enables long-distance transmission of light, and single-mode fiber is a type of optical fiber. The only physical phenomenon used to transmit light is total reflection of light. As shown in FIG. M.1, when light is incident from a medium with a large refractive index into a medium with a small refractive index, light incident at an angle greater than a certain angle of incidence, which is given by $\theta = \arcsin n_2/n_1$, is totally reflected and propagates through the medium called the core of the optical fiber. Thus, the refractive index of the core is designed to be greater than that of the cladding, but the difference between them is roughly on the order of 10^{-3} , then $n_1 - n_2 \ll 1$. Single mode fiber means an optical fiber whose core diameter is about 10 times or less than the wavelength of the light propagating inside. Typically, the core diameter of a single-mode fiber is about $9 - 10[\mu m]$, the diameter of the cladding is defined by international standards to be $125[\mu m]$. As can be seen from the structure of the optical fiber, it is convenient to solve Maxwell's equations in a cylindrical coordinate system to predict the electromagnetic field inside the optical fiber. Considering that the materials inside the optical fiber are all dielectric, Maxwell's equation is given by

$$\vec{\nabla} \times \vec{E}(\vec{r}, t) = -\partial_t \vec{B}(\vec{r}, t) \quad (\text{M.1})$$

$$\vec{\nabla} \cdot \vec{D}(\vec{r}, t) = 0 \quad (\text{M.2})$$

$$\vec{\nabla} \times \vec{H}(\vec{r}, t) = \partial_t \vec{D}(\vec{r}, t) \quad (\text{M.3})$$

$$\vec{\nabla} \cdot \vec{B}(\vec{r}, t) = 0, \quad (\text{M.4})$$

where ∂_t is equivalent to $\partial/\partial t$, \vec{r} is position. These four equations derive wave equation given by

$$\left(\Delta - \frac{n^2 k_0^2}{\omega^2} \partial_t^2 \right) \begin{bmatrix} \vec{E}(\vec{r}, t) \\ \vec{H}(\vec{r}, t) \end{bmatrix} = 0, \quad (\text{M.5})$$

where n is the refractive index distribution shown in FIG. M.1, k_0 is the magnitude of wave number vector in air, ω is angular frequency of incident electromagnetic wave. Considering the propagation of light in the z -axis direction, if we assume that the magnitude of the electromagnetic field depends only on the distance from the central axis of the optical fiber r and the angle of rotation ϕ , the shape of the electromagnetic field can be expressed by

$$\begin{bmatrix} \vec{E}(\vec{r}, t) \\ \vec{H}(\vec{r}, t) \end{bmatrix} = \begin{bmatrix} \vec{E}(r, \phi) \\ \vec{H}(r, \phi) \end{bmatrix} e^{i(k_z z - \omega t)}, \quad (\text{M.6})$$

where k_z is z -component of the wave number vector. Representing Eq. (M.1) and Eq. (M.3) in cylindrical coordinate system and substituting Eq. (M.6) for Eq. (M.1) and Eq.

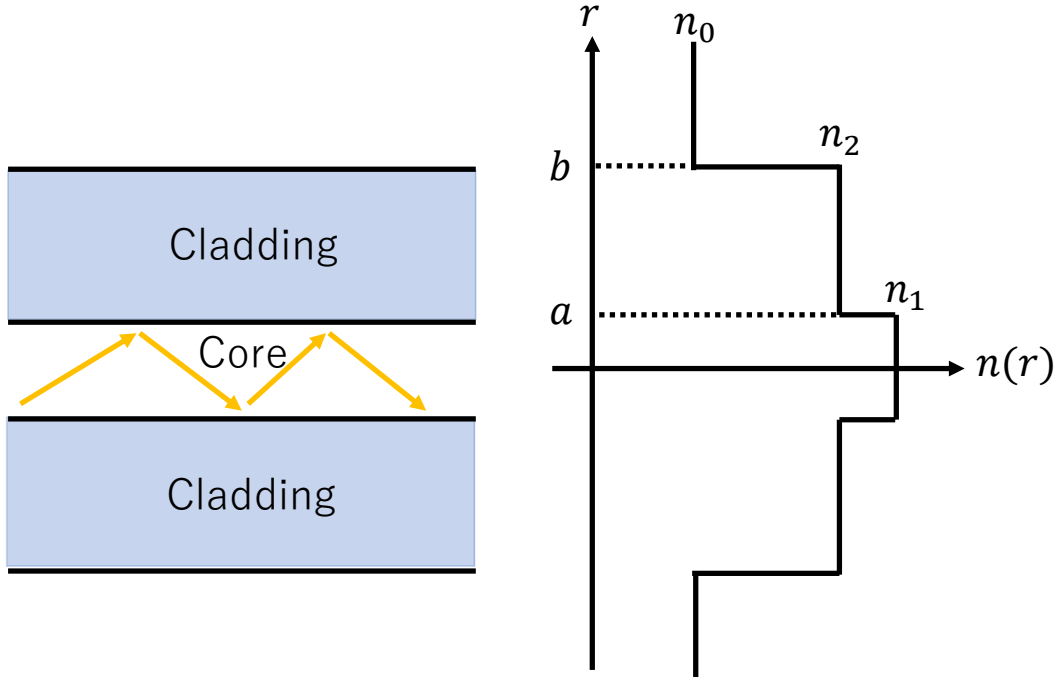


FIGURE M.1: Schematic of an optical fiber and the refractive index distribution. n_1 is the refractive index of the core with radius a , n_2 is the refractive index of the cladding with radius b . n_0 is the refractive index of air, which is approximately equal to that of a vacuum.

(M.3), the six equations are given by

$$i\omega\varepsilon E_r = ik_z H_\phi - \frac{1}{r} \partial_\phi H_z \quad (\text{M.7})$$

$$i\omega\varepsilon E_\phi = -ik_z H_r + \partial_r H_z \quad (\text{M.8})$$

$$i\omega\varepsilon E_z = \frac{1}{r} \partial_\phi H_r - \frac{1}{r} \partial_r r H_\phi \quad (\text{M.9})$$

$$i\omega\mu H_r = -ik_z E_\phi + \frac{1}{r} \partial_\phi E_z \quad (\text{M.10})$$

$$i\omega\mu H_\phi = ik_z E_r - \partial_r E_z \quad (\text{M.11})$$

$$i\omega\mu H_z = -\frac{1}{r} \partial_\phi E_r + \frac{1}{r} \partial_r r E_\phi, \quad (\text{M.12})$$

where ε is the dielectric constant and μ is the magnetic permeability. The wave equation for the z-component is not different from its form in the Cartesian coordinate system and can be solved easily. In other words, finding E_z and H_z is not so complicated. Considering that the z-component is used to express the components of r and ϕ , Eq. (M.5)

- (M.6) leads to expressions given by

$$E_r = \frac{ik_z}{\omega^2 \varepsilon \mu - k_z^2} \left(\partial_r E_z + \frac{\omega \mu}{k_z} \frac{1}{r} \partial_\phi H_z \right) \quad (\text{M.13})$$

$$E_\phi = \frac{ik_z}{\omega^2 \varepsilon \mu - k_z^2} \left(\frac{1}{r} \partial_\phi E_z - \frac{\omega \mu}{k_z} \partial_r H_z \right) \quad (\text{M.14})$$

$$H_r = \frac{ik_z}{\omega^2 \varepsilon \mu - k_z^2} \left(\partial_r H_z - \frac{\omega \mu}{k_z} \frac{1}{r} \partial_\phi E_z \right) \quad (\text{M.15})$$

$$H_\phi = \frac{ik_z}{\omega^2 \varepsilon \mu - k_z^2} \left(\frac{1}{r} \partial_\phi H_z + \frac{\omega \mu}{k_z} \partial_r E_z \right). \quad (\text{M.16})$$

In other words, all components of the electromagnetic field can be derived by obtaining the z-component of the electromagnetic field from these relations. Using the Laplacian in cylindrical coordinates, the z-component of Eq. M.5 becomes

$$\left(\partial_r^2 + \frac{1}{r} \partial_r + \frac{1}{r^2} \partial_\phi^2 + (k^2 - k_z^2) \right) \begin{bmatrix} E_z \\ H_z \end{bmatrix} = 0. \quad (\text{M.17})$$

Since this equation is in a form in which the method of separation of variables can be used, the z-component of the electromagnetic field are given by

$$\begin{bmatrix} E_z \\ H_z \end{bmatrix} = \begin{bmatrix} E_{z0}(r) \\ H_{z0}(r) \end{bmatrix} e^{\pm il\phi}, \quad (\text{M.18})$$

where $U(r)$ is the magnitude of E_z or H_z . Since the electromagnetic field should be a single-values function, l must be a natural number or 0. Substituting this relation for Eq. (M.17), the equation for r is given by

$$d_r^2 + \frac{1}{r} d_r + \left(k^2 - k_z^2 - \frac{l^2}{r^2} \right) \begin{bmatrix} E_{z0}(r) \\ H_{z0}(r) \end{bmatrix} = 0. \quad (\text{M.19})$$

This equation is the Bessel equation and there are two cases given by

$$\begin{bmatrix} E_{z0}(r) \\ H_{z0}(r) \end{bmatrix} = \begin{cases} c_1 J_l(hr) + c_2 Y_l(hr) & (k^2 - k_z^2 > 0) \\ c_1 I_l(qr) + c_2 K_l(qr) & (k^2 - k_z^2 < 0) \end{cases} \quad (\text{M.20})$$

where c_1 and c_2 are constant, J_l is Bessel functions of the first kind of order l , Y_l is Bessel functions of the second kind of order l , I_l is Modified Bessel functions of the first kind of order l , K_l is Bessel functions of the first kind of order l , h and q are defined by $h \equiv \sqrt{k^2 - k_z^2} = \sqrt{n_1^2 k_0^2 - k_z^2}$, $q \equiv \sqrt{k_z^2 - k^2} = \sqrt{k_z^2 - n_2^2 k_0^2}$, respectively. The four types of Bessel functions have the form given by

$$J_l(x) \equiv \sum_{m=0}^{\infty} \frac{(-1)^m}{m! \Gamma(m+l+1)} \left(\frac{x}{2} \right)^{2m+l} \quad (\text{M.21})$$

$$Y_l(x) \equiv \lim_{n \rightarrow l} \frac{J_n(x) \cos n\pi - J_{-n}(x)}{\sin n\pi} \quad (\text{M.22})$$

$$I_l(x) \equiv \sum_{m=0}^{\infty} \frac{1}{m! \Gamma(m+l+1)} \left(\frac{x}{2} \right)^{2m+l} \quad (\text{M.23})$$

$$K_l(x) \equiv \lim_{n \rightarrow l} \frac{\pi}{2} \frac{I_{-n}(x) - I_n(x)}{\sin n\pi}, \quad (\text{M.24})$$

where $\Gamma(z)$ is gamma function defined by

$$\Gamma(z) \equiv \lim_{n \rightarrow \infty} \frac{n^z n!}{\prod_{m=0}^n (z+m)}. \quad (\text{M.25})$$

The coefficients within Eq. (M.20) can be determined from physical intuition and boundary conditions at the core-cladding boundary.

The electromagnetic field inside the core should have an oscillating form, and it is J_l and Y_l that exhibit such behavior. Thus, $k^2 - k_z^2 > 0$ is satisfied inside the core. In the limit where r is 0, $Y_l(hr)$ diverges. Since the electromagnetic field must take a finite value, c_2 must be zero for the effect of $Y_l(hr)$ to disappear. Therefore, when $r < a$ is satisfied, the z-component of the electromagnetic field inside the core is as follows

$$E_z(r, t) = AJ_l(hr) e^{i(k_z z - \omega t \pm l\phi)} \quad (\text{M.26})$$

$$H_z(r, t) = BJ_l(hr) e^{i(k_z z - \omega t \pm l\phi)}, \quad (\text{M.27})$$

A, B are arbitrary constants. Substituting these relations into Eq. (M.13)-(M.16), all components of the electromagnetic field can be determined as follows.

$$E_r = \frac{ik_z}{h^2} \left(Ahd_{hr}J_l(hr) \pm \frac{i\omega\mu l}{k_z r} BJ_l(hr) \right) e^{i(k_z z - \omega t \pm l\phi)} \quad (\text{M.28})$$

$$E_\phi = \frac{ik_z}{h^2} \left(\pm \frac{il}{r} AJ_e(hr) - \frac{\omega\mu}{k_z} Bhd_{hr}J_l(hr) \right) e^{i(k_z z - \omega t \pm l\phi)} \quad (\text{M.29})$$

$$H_r = -\frac{ik_z}{h^2} \left(Bhd_{hr}J_l(hr) \mp \frac{in\varepsilon_1 l}{k_z r} AJ_l(hr) \right) e^{i(k_z z - \omega t \pm l\phi)} \quad (\text{M.30})$$

$$H_\phi = -\frac{ik_z}{h^2} \left(\pm \frac{il}{r} BJ_l(hr) + \frac{\omega\varepsilon_1}{k_z} Ahd_{hr}J_l(hr) \right) e^{i(k_z z - \omega t \pm l\phi)}, \quad (\text{M.31})$$

where $h \equiv \sqrt{k^2 - k_z^2} = \sqrt{n_1^2 k_0^2 - k_z^2}$, $d_{hr} = d/d(hr)$, $\varepsilon_1 = \varepsilon_0 n_1^2$.

Next, let us consider the electromagnetic field in the cladding. At the boundary between the core and the cladding ($r = a$), the direction of ϕ of the electromagnetic field must be continuous. This is a requirement obtained from Maxwell's equations. The electromagnetic field seeps into the cladding as evanescent light, but its amplitude is immediately attenuated. It is the modified Bessel function, $I_l(qr)$ and $K_l(qr)$, that can describe such behavior. However, $I_l(qr)$ diverges in the limit where r is infinite. In order for the electromagnetic field not to diverge, c_1 in Eq. (M.20) must be zero. Eventually, the electromagnetic waves at the cladding ($r > a$) are given by

$$E_z(r, t) = CK_l(qr) e^{i(k_z z - \omega t \pm l\phi)} \quad (\text{M.32})$$

$$H_z(r, t) = DK_l(qr) e^{i(k_z z - \omega t \pm l\phi)}, \quad (\text{M.33})$$

where C, D are arbitrary constants. Substituting these relations into Eq. (M.13)-(M.16), all components of the electromagnetic field can be given by

$$E_r = -\frac{ik_z}{q^2} \left(Ckd_{qr}K_l(qr) \pm \frac{i\omega\mu l}{k_z r} DK_l(qr) \right) e^{i(k_z z - \omega t \pm l\phi)} \quad (\text{M.34})$$

$$E_\phi = -\frac{ik_z}{q^2} \left(\pm \frac{il}{r} CK_l(qr) - \frac{\omega\mu}{k_z} Dqd_{qr}K_l(qr) \right) e^{i(k_z z - \omega t \pm l\phi)} \quad (\text{M.35})$$

$$H_r = \frac{ik_z}{q^2} \left(Dqd_{qr}K_l(qr) \mp \frac{in\varepsilon_2 l}{k_z r} CK_l(qr) \right) e^{i(k_z z - \omega t \pm l\phi)} \quad (\text{M.36})$$

$$H_\phi = \frac{ik_z}{q^2} \left(\pm \frac{il}{r} DK_l(qr) + \frac{\omega\varepsilon_2}{k_z} Cqd_{qr}K_l(qr) \right) e^{i(k_z z - \omega t \pm l\phi)}, \quad (\text{M.37})$$

where $q \equiv \sqrt{k_z^2 - k^2} = \sqrt{k_z^2 - n_2^2 k_0^2}$, $d_{qr} = d/d(qr)$, $\varepsilon_2 = \varepsilon_0 n_2^2$.

Since the components of the electromagnetic field horizontal to the core-cladding boundary must be continuous, the E_ϕ, E_z, H_ϕ and H_z must be continuous at $r = a$. This requirement results in the simultaneous equations given by

$$\begin{pmatrix} J_l(ha) & 0 & -K_l(qa) & 0 \\ \pm \frac{ik_z l}{ah^2} J_l(ha) & -\frac{\omega\mu}{h} d_{ha} J_l(ha) & \pm \frac{ik_z l}{aq^2} K_l(qa) & -\frac{\omega\mu}{q} d_{qa} K_l(qa) \\ 0 & J_l(ha) & 0 & -K_l(qa) \\ \frac{\omega\varepsilon_1}{h} d_{ha} J_l(ha) & \pm \frac{ik_z l}{ah^2} J_l(ha) & \frac{\omega\varepsilon_2}{q} d_{qa} K_l(qa) & \pm \frac{ik_z l}{aq^2} K_l(qa) \end{pmatrix} \begin{pmatrix} A \\ B \\ C \\ D \end{pmatrix} = 0. \quad (\text{M.38})$$

In order for the equation to be satisfied without the arbitrary counts from A to D being zero, the condition that the determinant of the four times four matrix on the left-hand side be zero is satisfied by

$$\begin{aligned} \varepsilon_0 \left(\frac{d_{ah} J_l(ah)}{ah J_l(ha)} + \frac{d_{aq} K_l(aq)}{aq K_l(aq)} \right) \left(\frac{n_1^2 d_{ah} J_l(ah)}{ah J_l(ah)} + \frac{n_2^2 d_{aq} K_l(aq)}{aq K_l(aq)} \right) \\ = l^2 \left(\pm \left(\frac{1}{ah} \right)^2 \pm \left(\frac{1}{aq} \right)^2 \right)^2 k_z^2. \end{aligned} \quad (\text{M.39})$$

By solving this equation, the z-component of the wavenumber vector can be obtained.

Appendix N

Polarization beam splitter

A polarizing beam splitter (PBS) is an optical element used to separate the horizontal (H) and vertical (V) components of incident light. To understand the principle and optical properties of PBS, it is necessary to understand the behavior of light at the interface between two media with different refractive indices and the thin film technology that exploits these properties. This appendix will explain the minimum knowledge required to understand the principles of PBS.

N.1 Boundary conditions and relation between electric and magnetic fields

In this section, the boundary conditions that the electric and magnetic fields must satisfy at the boundary surfaces with different refractive indices and the relation between the electric and magnetic fields are derived from Maxwell's equations. Maxwell's equations in dielectric are given by Eqs. (M.1)-(M.4). Considering a single mode plane wave, Eq. (M.1) the relation between the magnitude of the electric and magnetic fields, which is given by

$$|\vec{E}| = \sqrt{\frac{\mu}{\epsilon}} |\vec{H}|, \quad (\text{N.1})$$

where $|\vec{E}|$, $|\vec{H}|$ is the magnitude of the electric and magnetic field, μ is a magnetic permeability, ϵ is a dielectric constant. Eq. (N.1) is often used to simplify the description of the electromagnetic field at the boundary.

Next, let us derive the boundary conditions for the electric field. Integrating Eq. (M.1) in the region shown in FIG. N.1 and applying Stokes' theorem, we obtain

$$\int_l \vec{E} \cdot d\vec{l} = - \int_s \partial_t \vec{B} \cdot d\vec{s}. \quad (\text{N.2})$$

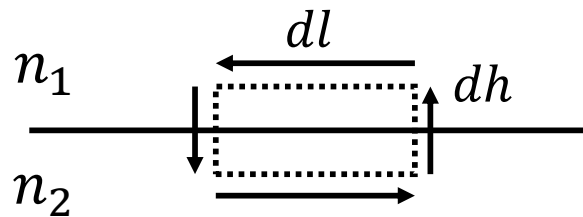


FIGURE N.1: A virtual micro-rectangle on the boundary surface of a medium with different refractive indices, where dh is the micro-height and dl is the micro-width.

In the limit $dh \rightarrow 0$, the area of the rectangle in FIG. N.1 is zero, so the value on the right side of Eq. (N.2) is zero. Since only the components of the electric field parallel to the edge of length dl are relevant to the calculation of the left-hand integral, Eq. N.2 becomes

$$\begin{aligned} -E_{1t}dl + E_{2t}dl &= 0 \\ E_{1t} &= E_{2t}, \end{aligned} \quad (\text{N.3})$$

where E_{1t} is the component of the electric field in a medium with refractive index n_1 , parallel to the boundary plane, and E_{2t} is the component of the electric field in a medium with refractive index n_2 , parallel to the boundary plane. Therefore, at the boundary surface of a medium with different refractive indices, the components of the electric field parallel to the boundary surface become continuous.

Next, let us derive the boundary conditions of the magnetic field. Integrating Eq. (M.3) in the region shown in FIG. N.1, and applying Stokes' theorem, the following relational equation is derived

$$\int_l \vec{H} \cdot d\vec{l} = \int_S \partial_t \vec{D} \cdot d\vec{s}. \quad (\text{N.4})$$

By following the same procedure as when the boundary conditions for the electric field was derived, the boundary condition of the magnetic field is given by

$$\begin{aligned} H_{1t}ds - H_{2t}dl &= 0 \\ H_{1t} &= H_{2t}, \end{aligned} \quad (\text{N.5})$$

where H_{1t} is the component of the magnetic field in a medium with refractive index n_1 , parallel to the boundary plane, and B_{2t} is the component of the magnetic field in a medium with refractive index n_2 , parallel to the boundary plane. Thus, under conditions where there is no current density at the boundary, the components of the magnetic field parallel to the boundary plane must be continuous.

N.2 Fresnel equations and Brewster angle

The physical phenomena necessary to understand thin film technology are summarized in Fresnel equations. Fresnel equations describe the reflectance and transmittance of light at the interface between two media with different refractive indices. FIG. N.2 shows an electromagnetic wave incident from a medium with a refractive index of n_1 into a medium with a refractive index of n_2 . The plane containing the incident and reflected electromagnetic wave is called the entrance plane. Polarization perpendicular to the entrance plane is called s-polarization, and parallel polarization is called p-polarization¹. The polarization of an electromagnetic wave is usually defined as the orientation of oscillation of the electric field because near the wavelength region of light, the electric field has a greater effect on the electrons that consist of the medium than the magnetic field. In FIG. N.2, we assume a situation where the polarization of the incoming electromagnetic wave is s-polarized, i.e., the oscillation orientation of the electric field is perpendicular to the incident plane, but let us consider the case of p-polarized wave later.

If the incident electromagnetic wave is s-polarized, the electric field is always oscillating perpendicular to the entrance plane and is therefore always parallel to the boundary

¹The names p-polarization and s-polarization have come from the German words "parallel" and "senkrecht", meaning "parallel" and "perpendicular".

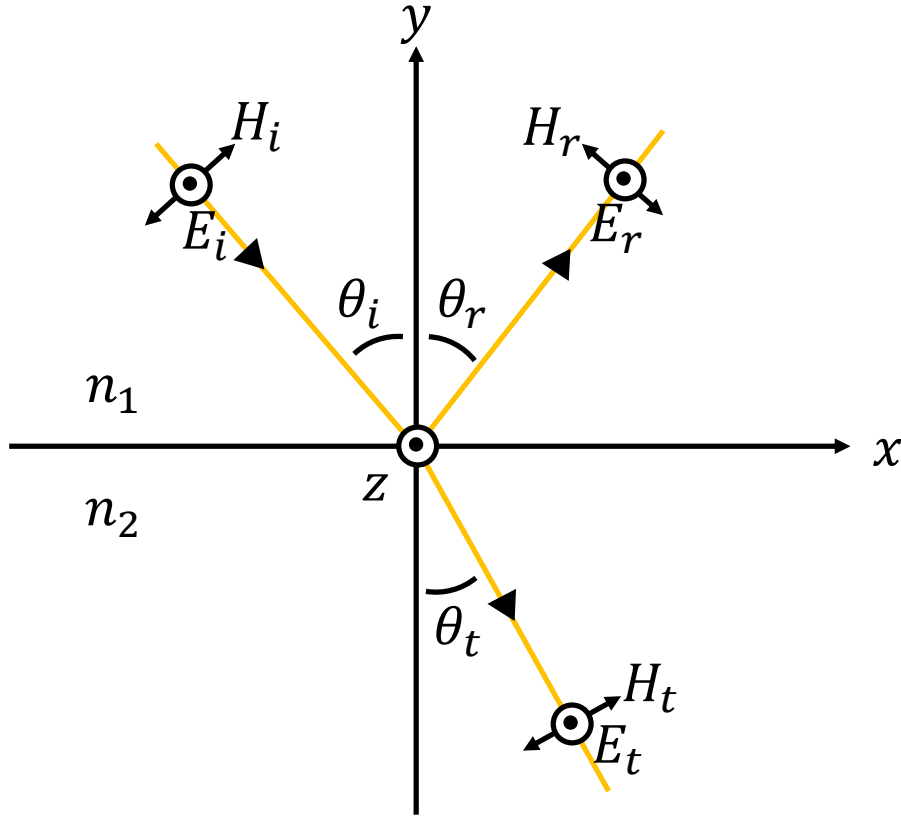


FIGURE N.2: The relation among incident, reflected, and transmitted light at the interface between two media with different refractive indices. In this figure, the electric field is assumed to oscillate perpendicular to the incident plane. The direction of oscillation of the magnetic field perpendicular to the electric field is parallel to the plane of incidence, where θ_i , θ_r , and θ_t are the angle of incidence, reflection, and refraction, respectively.

of the medium, viz, Eq. (N.3) requires

$$E_i + E_r = E_t. \quad (\text{N.6})$$

On the other hand, Eq. (N.5) requires that the components of the magnetic field oscillating parallel to the boundary plane be continuous, so the incident, reflected, and refracted angles must be considered in the situation shown in FIG. N.2, i.e., Eq. (N.1) and Eq. (N.5) requires

$$E_i \sqrt{\frac{\varepsilon_1}{\mu_1}} \cos \theta_i - E_r \sqrt{\frac{\varepsilon_1}{\mu_1}} \cos \theta_r = E_t \sqrt{\frac{\varepsilon_2}{\mu_2}} \cos \theta_t. \quad (\text{N.7})$$

In general dielectric materials, the permeability, which expresses the ease of magnetization, is almost the same as the permeability value in a vacuum. Therefore, if $\mu_0 \approx \mu_1 \approx \mu_2$ holds, the boundary condition becomes

$$E_i n_1 \cos \theta_i - E_r n_1 \cos \theta_r = E_t n_2 \cos \theta_t, \quad (\text{N.8})$$

where the relations $\sqrt{\varepsilon_j} = n_j \sqrt{\varepsilon_0}$, $n_j = \sqrt{\varepsilon_j \mu_j} / \sqrt{\varepsilon_0 \mu_0}$ ($j = 1, 2$) were considered. Solving the simultaneous equations of Eq. (N.6) and Eq. (N.8), the amplitude reflectance and

amplitude transmittance are given by

$$r_s := \frac{E_r}{E_i} = \frac{n_1 \cos \theta_i - n_2 \cos \theta_t}{n_1 \cos \theta_i + n_2 \cos \theta_t} \quad (\text{N.9})$$

$$t_s := \frac{E_t}{E_i} = \frac{2n_1 \cos \theta_i}{n_1 \cos \theta_i + n_2 \cos \theta_t}, \quad (\text{N.10})$$

where $\theta_i = \theta_r$ was used because of Snell's law.

In the situation shown in FIG. N.2, the amplitude reflectance and transmittance can be derived in the same way when the incident polarization is p-polarization, and they are given by

$$r_p := \frac{E_r}{E_i} = \frac{n_2 \cos \theta_i - n_1 \cos \theta_t}{n_2 \cos \theta_i + n_1 \cos \theta_t} \quad (\text{N.11})$$

$$t_p := \frac{E_t}{E_i} = \frac{2n_1 \cos \theta_i}{n_2 \cos \theta_i + n_1 \cos \theta_t}, \quad (\text{N.12})$$

where $\theta_i = \theta_r$ was used because of Snell's law as well.

Looking at the form of the Eqs. (N.9)-(N.12), the only situations in which the value is likely to be zero are Eq. (N.12) and Eq. (eqn:appendix amplitude reflectance for p-polarization), but the only situation in which Eq. (N.9) is zero is when $n_1 = n_2$. On the other hand, Eq. (N.11) can be zero when the incidence angle satisfies a specific angle given by

$$\theta_B = \arctan \frac{n_2}{n_1}. \quad (\text{N.13})$$

This angle is called Brewster angle, and in this case, the sum of the reflection angle and the refraction angle is 90° .

N.3 Reflectance and Transmittance of the light intensity

The Fresnel equation gives the amplitude reflectance and amplitude transmittance, but it is useful to derive the equations for reflectance and transmittance, since most experimental cases measure the intensity or energy of electromagnetic waves. In this section, the Fresnel equation gives the transmittance and reflectance of the intensity.

The intensity of an electromagnetic wave propagating in a medium with a refractive index of n is given by

$$I = \frac{\epsilon_0 n c}{2} |\vec{E}|^2, \quad (\text{N.14})$$

where ϵ is dielectric constant in vacuum, c is speed of light in vacuum, n is refractive index in the medium. The intensity of the electromagnetic wave is proportional to the square of the electric field, but not equal to the square of the electric field. Note that the refractive index must be taken into account to determine the transmission and reflection coefficients.

As shown in FIG. N.2, the incident and reflected light are in a medium with the same refractive index. Therefore, the reflectance for s-polarized and p-polarized light is equal

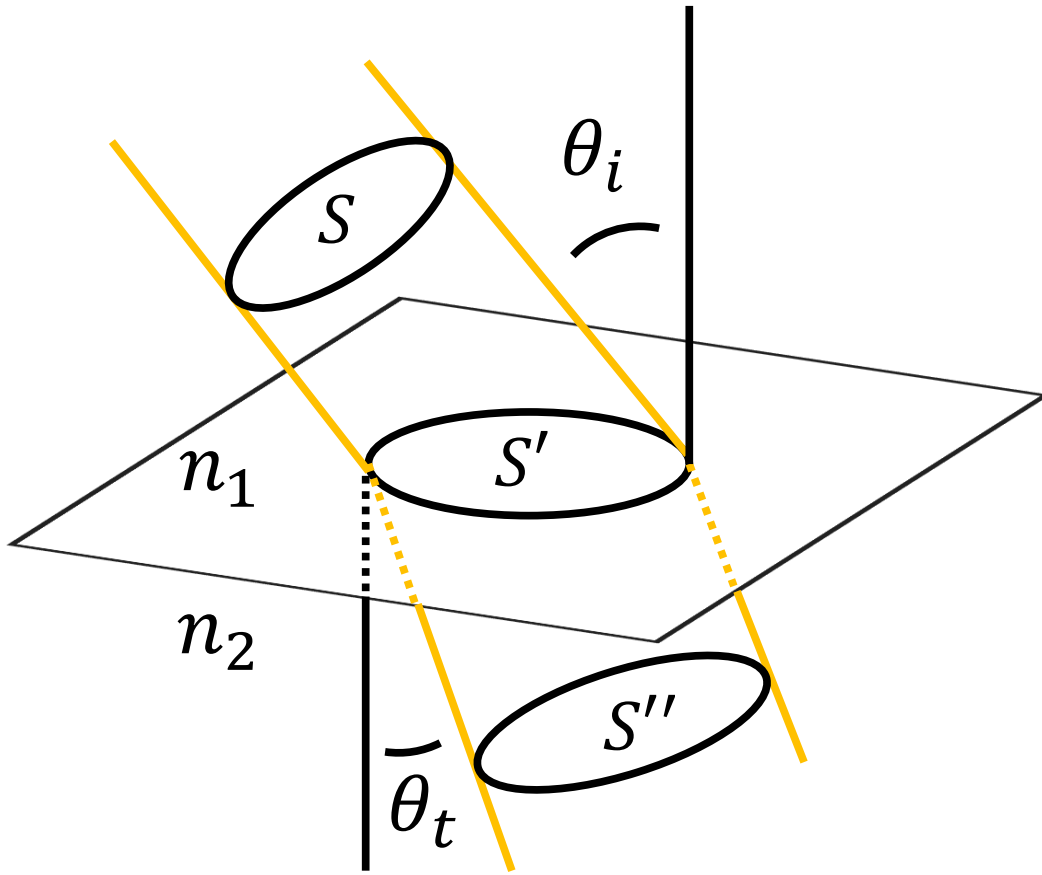


FIGURE N.3: An electromagnetic wave with cross-section area S incident on a medium with refractive index n_1 into a medium with refractive index n_2 . the area at the boundary between the two media is S' . θ_i is the angle of incidence and θ_t is the angle of refraction. S'' is the cross-section area of transmitted light.

to the square of Eq. (N.9) and Eq. (N.11). Thus, they are given by

$$\begin{aligned}
 R_s &:= \frac{I_r}{I_i} \\
 &= r_s^2 \\
 &= \left(\frac{\eta_{1s} - \eta_{2s}}{\eta_{1s} + \eta_{2s}} \right)^2
 \end{aligned} \tag{N.15}$$

$$\begin{aligned}
 R_p &= r_p^2 \\
 &= \left(\frac{\eta_{1p} - \eta_{2p}}{\eta_{1p} + \eta_{2p}} \right)^2,
 \end{aligned} \tag{N.16}$$

where $\eta_{1s} = n_1 \cos \theta_i$, $\eta_{2s} = n_2 \cos \theta_t$, $\eta_{1p} = n_1 / \cos \theta_i$ and $\eta_{2p} = n_2 / \cos \theta_t$ hold. By using Snell's law, the reflectance can be summarized in these simple form.

When determining transmittance, the derivation of transmittance is slightly more complicated because the incident and transmitted light propagate in media with different refractive indices. The sum of reflectance and transmittance must be one because of the law of conservation of energy. To obtain the energy per unit time from the intensity, the area through which the electromagnetic wave passes must be multiplied to the intensity.

As shown in FIG. N.3, consider the situation where an electromagnetic wave is incident from a medium with a refractive index of n_1 to a medium with a refractive index of n_2 . The cross-section area of the incident light is S . Assuming that the light is cleanly circular, the cross-section area S can be written as $S = \pi r^2$, using an appropriate radius r . The area S' on the boundary surface becomes an ellipse, with the minor axis remaining r , but the major axis changing to r' given by

$$r' = \frac{r}{\cos \theta_i}. \quad (\text{N.17})$$

Therefore, the cross-section area of transmitted light is also an ellipse whose cross-section area is given by

$$S'' = \pi r^2 \frac{\cos \theta_t}{\cos \theta_i}. \quad (\text{N.18})$$

Finally, the transmittance for s-polarized and p-polarized light are given by

$$\begin{aligned} T_s &:= \frac{I_t}{I_i} \\ &= |t_s|^2 \frac{n_2 \cos \theta_t}{n_1 \cos \theta_i} \\ &= \frac{4\eta_{1s}\eta_{2s}}{(\eta_{1s} + \eta_{2s})^2} \end{aligned} \quad (\text{N.19})$$

$$\begin{aligned} T_p &= |t_p|^2 \frac{n_2 \cos \theta_t}{n_1 \cos \theta_i} \\ &= \frac{4\eta_{1p}\eta_{2p}}{(\eta_{1p} + \eta_{2p})^2}, \end{aligned} \quad (\text{N.20})$$

where $\eta_{1s} = n_1 \cos \theta_i$, $\eta_{2s} = n_2 \cos \theta_t$, $\eta_{1p} = n_1 / \cos \theta_i$ and $\eta_{2p} = n_2 / \cos \theta_t$ hold.

N.4 Characteristic matrix

A characteristic matrix is a tool used to predict the optical properties by dielectric multi-layers. Understanding the reflection and transmittance of electromagnetic waves by the characteristic matrix let us understand what phenomena are occurring inside the PBS. To understand the interaction of light with multi-layers, let us first discuss the interaction of light with monolayers. Before proceeding to the discussion, the concept of optical admittance should be introduced. Optical admittance is defined as

$$Y := \frac{|\vec{H}|}{|\vec{E}|} = \sqrt{\frac{\epsilon}{\mu}}, \quad (\text{N.21})$$

where Eq. (N.1) was used for the last transformation. The unit of optical admittance is the reciprocal of ohm, which represents resistance, and is called siemens. Optical admittance is useful in describing the optical properties of a material.

Consider the situation shown in FIG. N.4, where electromagnetic waves are incident on a monolayer film. The situation of oblique incidence will be discussed later because it is accomplished by simply replacing certain letters in the vertical incidence results. The boundary conditions for the electric field, Eq. (N.3), at the boundary surfaces a and b are

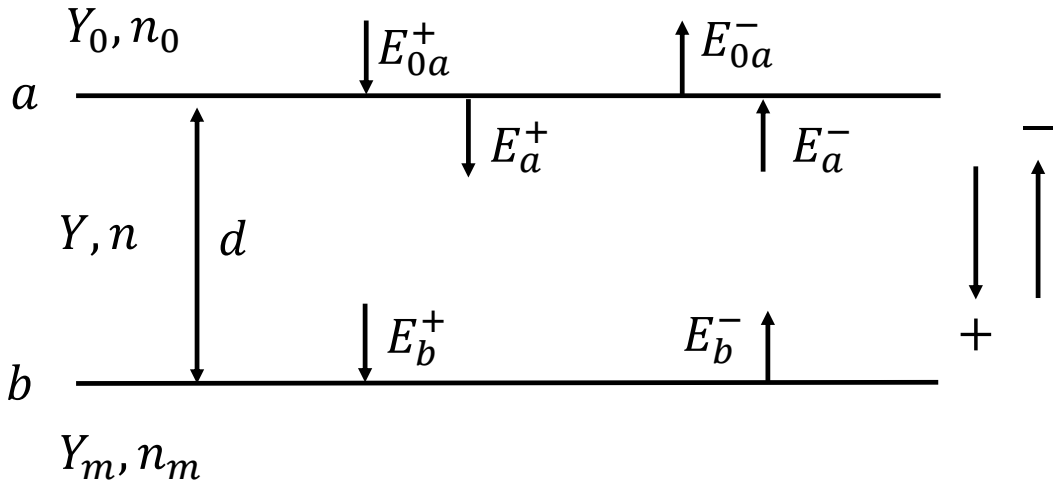


FIGURE N.4: A situation in which an electromagnetic wave is incident perpendicularly from a medium with a refractive index of n_0 to a thin film with a refractive index of n and reaches a substrate with a refractive index of n_m . Vector of $+$ and $-$ define two directions. a and b are labels of boundary surfaces. Y is optical admittance, d is the width of thin film. Arrows near the electric field indicate the propagation direction of electromagnetic wave, not the direction of oscillation of the electric field. The direction of oscillation of the magnetic field is perpendicular to the direction of electromagnetic oscillation.

given by

$$E_a \equiv E_{0a}^+ + E_{0a}^- = E_a^+ + E_a^- \quad (\text{N.22})$$

$$E_b \equiv E_b^+ + E_b^- \quad (\text{N.23})$$

Similarly, the boundary condition for the magnetic field, Eq. (N.5) requires the relation given by

$$H_a \equiv Y_0 E_{0a}^+ - Y_0 E_{0a}^- = Y E_a^+ - Y E_a^- \quad (\text{N.24})$$

$$H_b \equiv Y E_b^+ - Y E_b^- \quad (\text{N.25})$$

where Eq. (N.21) was used. The electromagnetic fields at the boundary surfaces a and b should be linked by a phase difference characterized by the thickness d of the thin film. They are given by

$$E_a^+ = E_b^+ e^{i\delta} \quad (\text{N.26})$$

$$E_a^- = E_b^- e^{-i\delta}, \quad (\text{N.27})$$

where δ means the phase difference. Using these two relations, the simultaneous equations of Eqs. (N.22)-(N.25) provides

$$\begin{pmatrix} E_a \\ H_a \end{pmatrix} = \begin{pmatrix} \cos \delta & \frac{i \sin \delta}{Y} \\ iY \sin \delta & \cos \delta \end{pmatrix} \begin{pmatrix} E_b \\ H_b \end{pmatrix}, \quad (\text{N.28})$$

where Y can be represented as $Y = n\sqrt{\epsilon_0}/\sqrt{\mu_0} \approx n \cdot 0.002654417$ too. The matrix on the right-hand side is called the characteristic matrix and is defined as

$$M \equiv \begin{pmatrix} \cos \delta & \frac{i \sin \delta}{Y} \\ iY \sin \delta & \cos \delta \end{pmatrix} \equiv \begin{pmatrix} m_{11} & im_{12} \\ im_{21} & m_{22} \end{pmatrix}. \quad (\text{N.29})$$

The characteristic matrix describes the physical interactions of the thin films. Within the actual thin film, some of the light will travel back and forth between the boundary surfaces a and b , but all of their contributions will be included in this matrix. The characteristic matrix in the absence of absorption has the property that the determinant becomes one.

Let us consider how the characteristic matrix represented by Eq. (N.29) relates to the reflectance and refractive index. Since both incident and reflected light exist in a medium with a refractive index of n_0 , the reflectance is simply obtained by squaring the ratio of the electric field, which is given by

$$\begin{aligned} R &= \frac{|E_{0a}^-|^2}{|E_{0a}^+|^2} \\ &= \frac{(n_0 m_{11} - n_m m_{22})^2 + (n_0 n_m m_{12} - m_{21})^2}{(n_0 m_{11} + n_m m_{22})^2 + (n_0 n_m m_{12} + m_{21})^2}. \end{aligned} \quad (\text{N.30})$$

The transmittance is determined by the ratio of the electric field propagating through a medium with a refractive index of n_0 to that propagating through a medium with a refractive index of n_m . The transmittance can be calculated using the electric field in the n medium instead of the electric field in the n_m medium since the electric field is continuous before and after the boundary surface b . Noting that the intensity of light depends on the refractive index as shown in Eq. (N.14), the transmittance is given by

$$\begin{aligned} T &= \frac{n_m}{n_0} \cdot \frac{|E_b|^2}{|E_{0a}^+|^2} \\ &= \frac{4n_0 n_m}{(n_0 m_{11} + n_m m_{22})^2 + (n_0 n_m m_{12} + m_{21})^2}. \end{aligned} \quad (\text{N.31})$$

When light is incident vertically to the boundary surface, the reflectance and transmittance are independent of the polarization of the incident light, as seen in Eq. (N.30) and Eq. (N.31).

Consider the case where light is incident from an oblique angle. In such situations, reflectance and transmittance depend on the polarization state of the incoming light. A generalization to the case where light enters the thin film from an oblique angle is achieved by replacing the refractive index in Eq. (N.30) and Eq. (N.31) with a gradient admittance given by

$$\eta_{0s} \equiv n_0 \cos \theta_i \quad (\text{N.32})$$

$$\eta_{0p} \equiv \frac{n_0}{\cos \theta_i} \quad (\text{N.33})$$

$$\eta_s \equiv n \cos \theta \quad (\text{N.34})$$

$$\eta_p \equiv \frac{n}{\cos \theta} \quad (\text{N.35})$$

$$\eta_{ms} \equiv n_m \cos \theta_t \quad (\text{N.36})$$

$$\eta_{mp} \equiv \frac{n_m}{\cos \theta_t'} \quad (\text{N.37})$$

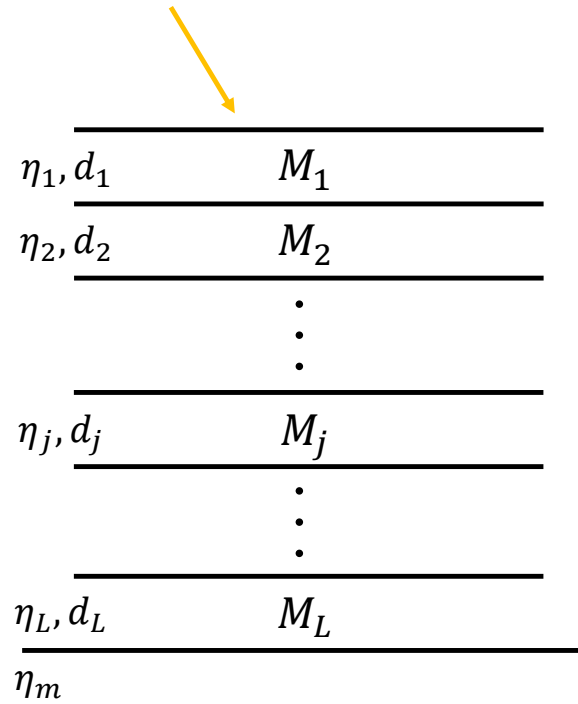


FIGURE N.5: Schematic diagram of the concept of expansion into a multi-layer membrane. First, the incident light enters the thin film of the characteristic matrix M_1 , then interacts with the thin film of the characteristic matrix M_2 . Finally, some of the light reaches the substrate with a gradient admittance of η_m .

where the θ_i is an incidence angle, the θ is the refraction angle to θ_i , the θ_t is the refraction angle to θ when the θ is regarded as the incidence angle to the substrate. The "s" and "p" in the subscripts must be distinguished according to the polarization or component of the incident light. In addition to these substitutions, the phase difference δ in Eq. (N.29) is written as

$$\delta = nk_0d \cos \theta, \quad (\text{N.38})$$

where the k_0 is the wave number in the incident medium, the n is refractive index in the thin film, the d is the thickness of the thin film.

Next, consider the case where light is incident on the multi-layer. The extension to the multi-layer case is accomplished simply by sequential multiplication of the characteristic matrices. As shown in FIG. N.5, the incident light interacts continuously with the thin film whose characteristic matrix is M_1 to the thin film of M_L . The multi-layer interaction is described as the multiplication of the characteristic matrix of each thin film. The overall characteristics matrix can be given by

$$M = M_1 \cdot M_2 \cdots M_j \cdots M_L = \begin{pmatrix} m_{11} & im_{12} \\ im_{21} & m_{22} \end{pmatrix}. \quad (\text{N.39})$$

As can be seen from Eq. (N.28), the order of multiplication should be noted because the characteristic matrix acts on the electric field near the final boundary surface. Since Eq. (N.39) has exactly the same form as Eq. (N.29), the reflectance and transmittance in multi-layers are described in the same form as Eq. (N.30) and Eq. (N.31). The physical phenomena occurring inside a multilayer film are complex because they include multiple

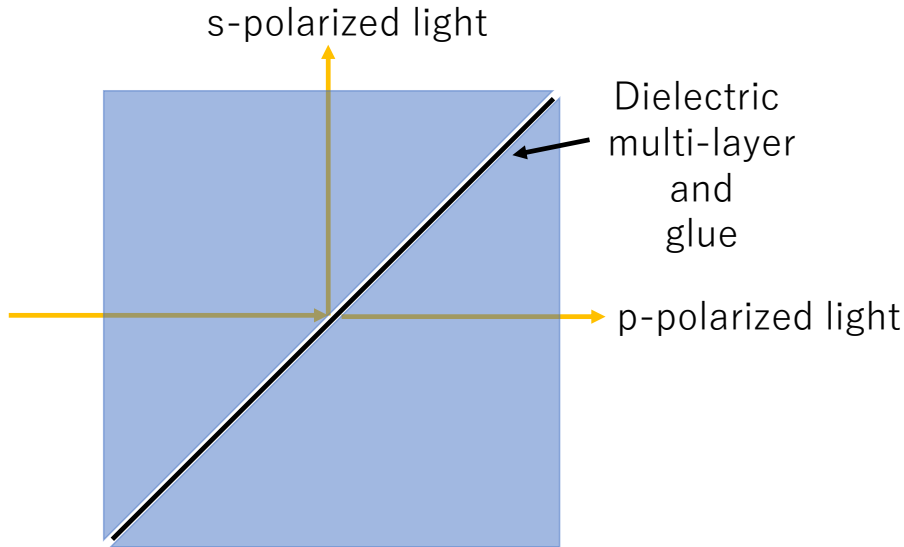


FIGURE N.6: Schematic diagram of the structure of PBS. Dielectric multi-layers and glue are applied to the oblique side of the right-angle prism. The p-polarized component of the incident light is transmitted and the s-polarized component is reflected.

reflections, but a characteristic matrix can be used to represent such complex physical phenomena in a simple manner.

N.5 Structure of a PBS

There are two types of PBS: plate type and cube type. The cube type used in this experiment is explained in this appendix. As shown in FIG. N.6, the cube-shaped PBS consists of a dielectric multi-layer film and adhesive applied to the oblique side of a right-angle prism and laminated to the other right-angle prism. Dielectric multi-layer have a structure consisting of alternating layers with a high refractive index n_H and layers with a low refractive index n_L . PBS is an optical element that separates s-polarized and p-polarized components, so that it is necessary to create a situation where the p-polarized component does not interact with the dielectric multi-layer film and the s-polarized component is reflected. Using the Brewster angle shown in Eq. (N.13), the transmission of p-polarized light can be made almost 100%, so the relation between the refractive index n_H of the one layer with low refractive index and the refractive index n_H of one layer with the high refractive index is given by

$$\tan \theta_H = \frac{n_L}{n_H}, \quad (\text{N.40})$$

where θ_H is the angle of incidence of light when it enters the layer with low refractive index from the layer with high refractive index. If the refractive index of a right angle prism is n_0 and the angle of incidence of the prism on the slope is 45° , so Snell's law provides

$$\sin \theta_H = \frac{n_0}{\sqrt{2}n_H}. \quad (\text{N.41})$$

Combining the above two equations, the relation between the three refractive indices is given by

$$n_0^2 = \frac{2n_H^2 n_L^2}{n_H^2 + n_L^2}. \quad (\text{N.42})$$

If the right-angle prism and dielectric multilayer film satisfy this relation, the transmittance for p-polarized light approaches 100%. The high reflectance for s-polarized light is determined by the number of layers in the dielectric multilayer. The greater the number of layers, the higher the reflectance, but the more expensive PBS becomes.

Appendix O

Wave Plate

A waveplate is an optical component to give a specific phase difference to any orthogonal component in a plane perpendicular to the wavenumber vector of the transmitted electromagnetic wave. The physical principles and mathematical description of waveplates are explained in this appendix. Birefringence is a property of an anisotropic crystal such that the refractive index perceived by an electromagnetic wave differs depending on the direction of vibration of the electromagnetic wave incident on the crystal. When the refractive indices perceived by an electromagnetic waves parallel to the three orthogonal axes of a crystal are different no matter how the three-dimensional Cartesian coordinates are defined, the crystal is called a biaxial crystal. On the other hand, an uniaxial crystal is a crystal which has a three-dimensional Cartesian coordinates such that the two of the three components of an electromagnetic wave perceives the same refractive index. Let the two axes that have the same refractive index be axes A and B, and the remaining one axis be axis C, the oscillation component perpendicular to the plane formed by the axis C and the wavenumber vector is called ordinary light and the oscillation component parallel to the plane is called extraordinary light. When the angle between the axis C and the wavenumber vector is θ , the refractive index perceived by ordinary light is independent of θ , while the refractive index perceived by extraordinary light depends on θ because ordinary light is always parallel to the AB plane. When we consider the plane perpendicular to the wavenumber vector, which is created by the two orthogonal S-axis and F-axis, we can give an appropriate phase difference between the component of electromagnetic wave parallel to the S-axis and the component of electromagnetic wave parallel to the F-axis by designing the crystal well. FIG. O.1 shows the relation between the Slow (S-axis) and Fast (F-axis) axes for horizontally and vertically polarized light. n_S, n_F are the refractive indices of the components of electromagnetic waves parallel to the Slow, Fast axes, and the phase differences immediately before and after the incident on the waveplate are $n_S|\vec{k}|L, n_F|\vec{k}|L$. This means that there will be a phase difference between the S-axis component and the F-axis component given by

$$\phi = (n_S - n_F)|\vec{k}|L, \quad (\text{O.1})$$

where, L is the thickness of the waveplate, and $n_S > n_F$ is hold because the phase velocity of the S-axis component is smaller than that of the F-axis component. As shown in FIG. O.1, consider the situation where a photon with H polarization component A_{Hin} and V polarization component A_{Vin} enters a waveplate such that the S-axis is tilted by θ_S with respect to the H polarization. The polarization state of a photon immediately after

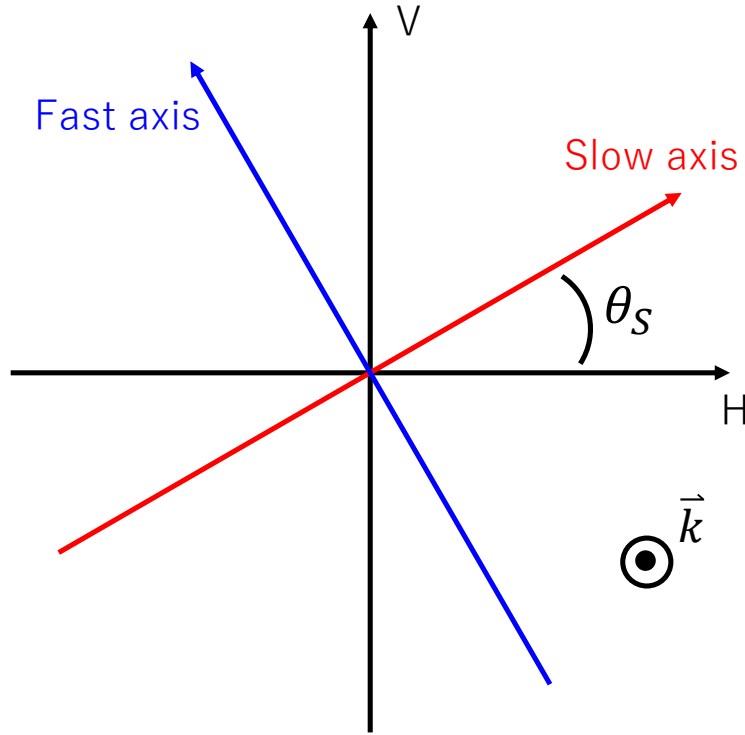


FIGURE O.1: Relation between the Slow and Fast axes with respect to the $\{H, V\}$ -basis. θ_S is the angle between the direction of H polarization and the Slow axis, and \vec{k} is the wavenumber vector of the electromagnetic wave incident on the waveplate.

passing through the waveplate is given by

$$\begin{aligned}
 & \begin{pmatrix} A_{Hout} \\ A_{Vout} \end{pmatrix} = \\
 & \begin{pmatrix} \cos \theta_S & -\sin \theta_S \\ \sin \theta_S & \cos \theta_S \end{pmatrix} \begin{pmatrix} e^{-i\frac{\phi}{2}} & 0 \\ 0 & e^{i\frac{\phi}{2}} \end{pmatrix} \begin{pmatrix} \cos \theta_S & \sin \theta_S \\ -\sin \theta_S & \cos \theta_S \end{pmatrix} \begin{pmatrix} A_{Hin} \\ A_{Vin} \end{pmatrix} \\
 & = \begin{pmatrix} e^{-i\frac{\phi}{2}} (\cos^2 \theta_S + e^{i\phi} \sin^2 \theta_S) & -i \sin \frac{\phi}{2} \sin 2\theta_S \\ -i \sin \frac{\phi}{2} \sin 2\theta_S & e^{-i\frac{\phi}{2}} (\sin^2 \theta_S + e^{i\phi} \cos^2 \theta_S) \end{pmatrix} \quad (O.2)
 \end{aligned}$$

The first matrix in the right hand side acting on the polarization state of the incident photon is a rotation matrix that gives the transformation from the $\{H, V\}$ -basis to the $\{S, F\}$ -basis; the second matrix gives the phase difference between the S and F axes, described by Eq. (O.2); the third matrix is a rotation matrix that transforms from the $\{S, F\}$ -basis to the $\{H, V\}$ -basis.

A half-wavelength plate is a wavelength plate designed so that $\phi = n\pi$ ($n \in \mathbb{Z}$). Substituting $\phi = \pi$ into Eq. (O.2), the unitary operator for a half waveplate is given by

$$\hat{U}_{HWP} = \begin{pmatrix} \cos 2\theta_S & \sin 2\theta_S \\ \sin 2\theta_S & -\cos 2\theta_S \end{pmatrix}. \quad (O.3)$$

By changing the direction of the S-axis θ_S , any linear polarization can be converted to another arbitrary linear polarization. If we consider the conversion of polarization visually using the Bloch sphere, the unitary transformation by the half waveplate can be thought of as a π rotation when the vector representing the direction of the S-axis is considered to

be a right-handed screw.

Technically, there are three main types for waveplates, depending on how $\phi = (2n + 1)\pi$ ($n = 0$ or $n \in \mathbb{N}$) is realized.

- True zero order half waveplate: A waveplate designed so that $\phi = \pi$. Quartz and mica, which are commonly used as materials for waveplates, are very easily damaged and difficult to handle because the thickness of the waveplate is several tens of micrometers. However, since the expansion of the waveplate due to temperature and the incident angle dependence of the waveplate are small, the polarization state can be manipulated most accurately.
- Multi order half waveplates: Waveplates with thicker waveplates by setting $\phi = (2n + 1)\pi$ ($n \in \mathbb{N}$) for better technical handling. Although this improves the technical tractability, temperature dependence and incident angle dependence appear, so the temperature and incident angle must be precisely controlled.
- Zero order half waveplates: Waveplates designed to reduce the disadvantages of Multi order waveplates. By combining two multi-order half waveplates so that their optical axes of the crystals are orthogonal, the change in phase difference due to temperature change is canceled out. However, the incident angle dependence still remains.

A quarter-wave plate, designed as $\phi = \pi/2$, is also often used. Substituting $\phi = \pi/2$ into Eq. (O.2), the unitary operator of a quarter-wave plate becomes

$$\hat{U}_{QWP} = \frac{1}{\sqrt{2}} \begin{pmatrix} i + \cos 2\theta_S & \sin 2\theta_S \\ \sin 2\theta_S & i - \cos 2\theta_S \end{pmatrix}, \quad (\text{O.4})$$

where a global phase is properly chosen. A quarter-wave plate is used to generate or measure a circular polarization, and if we consider the transformation of polarization visually using a Bloch sphere, the unitary transformation by a quarter waveplate can be thought of as a $\pi/2$ rotation when the vector representing the direction of the S-axis is considered to be a right-handed screw.

For most optical experiments, a half-wave plate and a quarter-wave plate are sufficient to create or measure arbitrary polarization states. To illustrate this generality, consider the polarization state on the Bloch sphere as represented by the black arrow in FIG. O.2. The colored plane is the plane containing the Bloch vector representing the polarization state and the axis (green arrow) representing the expected value of *RL* polarization. As shown in FIG. O.3, if the S-axis of the QWP is directed to the intersection of this plane and the plane containing the red and blue arrows, the polarization state is converted to the linear polarization (thin black arrow). Next, as shown in FIG. O.4, if the S-axis of a HWP is directed to the orientation between the Bloch vector converted in FIG. O.3 and the Bloch vector representing *H* polarization, the polarization state is converted to *H* polarization. The series of processes from FIG. O.2 to FIG. O.4 are quantum operations performed when one wants to measure a certain polarization state, and conversely, when one wants to prepare a certain polarization state by considering the reverse process.

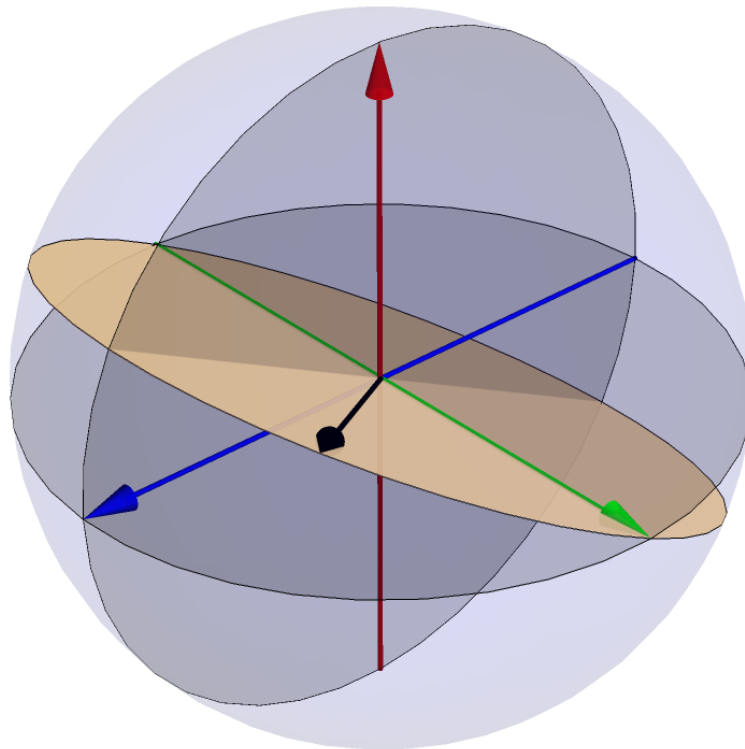


FIGURE O.2: Specific polarization state on the Bloch sphere (black arrows). The red arrow represents the expected value of HV polarization, the blue arrow represents the expected value of PM polarization, and the green arrow represents the expected value of RL polarization. The colored plane is the plane containing the Bloch vector representing the polarization state and the axis representing the expected value of RL polarization (green arrow).

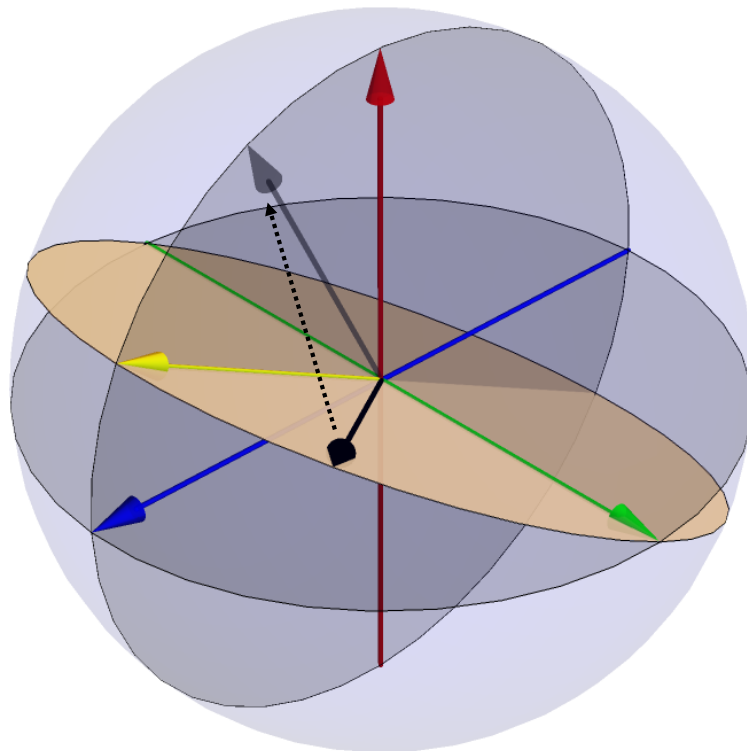


FIGURE O.3: Relation between a given polarization state (dark black arrows) and the polarization state after transformation by the QWP (thin black arrow). The yellow arrow represents the direction of the S-axis of the QWP, the black dashed arrow represents the unitary transformation of the QWP.

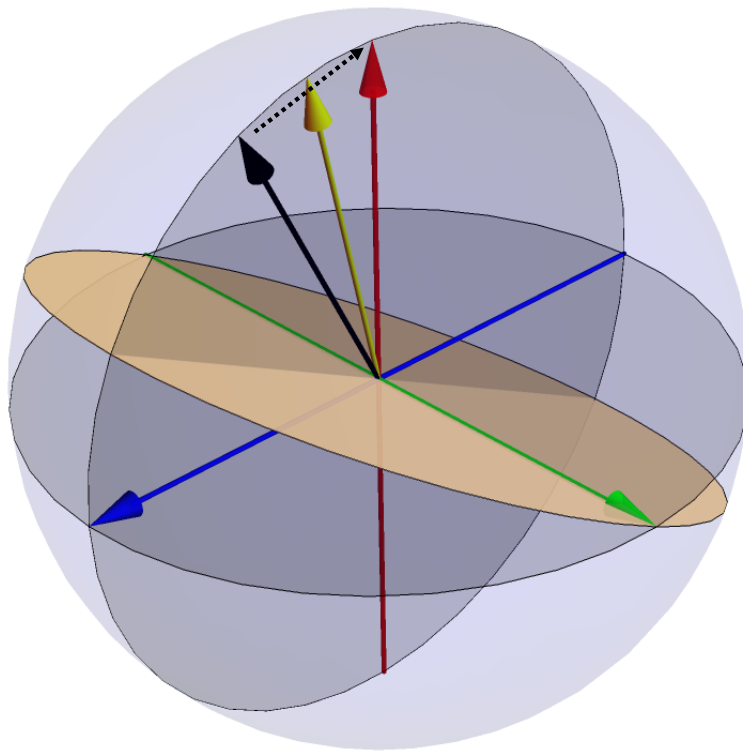


FIGURE O.4: Relation between a given polarization state (black arrows) and the polarization state after conversion by HWP. The yellow arrows represent the orientation of the S-axis of the HWP, and the black dashed arrows represent the unitary transformation of the HWP; the polarization state after transformation by the HWP is consistent with the H polarization state.

Appendix P

Dichroic mirror

A dichroic mirror is a mirror that has high reflectivity for a specific wavelength range of light and high transmittance for other wavelength ranges. The wavelength region that is transmitted is called the transmission band and the wavelength region that is reflected is called the reflection band. The dichroic mirror is realized by the dielectric multi-layer technology described in Sec. N.4. This appendix describes the conditions necessary to form dielectric multi-layer realizing dichroic mirrors.

P.1 Symmetric multi-layer system

A symmetric multi-layer system is a multi-layer such that the composition of the multi-layer is symmetric when viewed from the center film of the multi-layer. For example, in the situation shown in FIG. N.5, a multi-layer that is in the situation of $M_1 \cdot M_2 \cdots M_j \cdots M_2 M_1$ can be regarded as a symmetric multi-layer system. The two most basic symmetric multi-layer systems are $(H/2, L, H/2)^s$ and $(L/2, H, L/2)^s$, where the H means a layer with a high refractive index, L means a layer with a low refractive index, and $1/2$ means half the thickness of the layer, s means how many times the same structure is repeated. The dichroic mirror used in the experiment reflects light with short wavelengths and transmits light with longer wavelengths, the same as a short-pass filter (SPF) in the absence of absorption. The $(L/2, H, L/2)^s$ is important to realize a SPF. If the characteristic matrix shown in Eq. (N.29) of the thin film at both ends is M_A and the characteristic matrix of the thin film in the center is M_B , the whole characteristic matrix of the multi-layer is given by

$$\begin{aligned} & \begin{pmatrix} \cos \delta_A & \frac{i \sin \delta_A}{Y} \\ iY \sin \delta_A & \cos \delta_A \end{pmatrix} \begin{pmatrix} \cos \delta_B & \frac{i \sin \delta_B}{Y} \\ iY \sin \delta_B & \cos \delta_B \end{pmatrix} \begin{pmatrix} \cos \delta_A & \frac{i \sin \delta_A}{Y} \\ iY \sin \delta_A & \cos \delta_A \end{pmatrix} \\ & = \begin{pmatrix} m_{11} & im_{12} \\ im_{21} & m_{22} \end{pmatrix}, \end{aligned} \quad (\text{P.1})$$

where

$$\begin{aligned} m_{11} &= m_{12} = \cos 2\delta_A \cos \delta_B - \frac{1}{2} \left(\frac{n_B}{n_A} + \frac{n_A}{n_B} \right) \sin 2\delta_A \sin \delta_B \\ m_{12} &= \frac{1}{2n_A^2 n_B Y_0} (\cos \delta_A \cos \delta_B (n_A^2 n_B^2 + 4n_A n_B \sin \delta_B) - (n_A^2 - n_B^2) \sin \delta_B) \\ m_{21} &= \frac{Y_0}{2n_B} (\cos \delta_A \cos \delta_B (n_A^2 n_B^2 + 4n_A n_B \sin \delta_B) + (n_A^2 - n_B^2) \sin \delta_B), \end{aligned} \quad (\text{P.2})$$

where n_A, B are the refractive index in the layer A, B , Y_0 is the optical admittance in vacuum, Since Eq. (P.1) has the same form as Eq. (N.29), the multi-layer film can be

regarded as a monolayer film. Therefore, Y_E and δ_E in the

$$\begin{aligned} m_{11} &= m_{22} = \cos \delta_E \\ m_{12} &= \frac{\sin \delta_E}{Y_E} \\ m_{21} &= Y_E \sin \delta_E. \end{aligned} \quad (\text{P.3})$$

are called equivalent admittance and equivalent phase thickness. When $|m_{11}| > 1$, Y_E and δ_E become imaginary numbers, and the wavelength region satisfying this condition is the reflection. In other words, reflectance becomes high. On the other hand, when $|m_{11}| < 1$, Y_E and δ_E are real numbers, and this wavelength region becomes a transmission band. The $m_{11} = -1$ corresponds to the edge of the transmission and reflection bands.

P.2 Transmittance in a reflection band and transmission band

If the multi-layer is stacked s times with an equivalent phase thickness of $(\lambda_0/8, \lambda_0/4, \lambda_0/8)^s$ where λ_0 is the wavelength in incident medium, the Eq. (N.31) becomes

$$T = \frac{16\eta_0\eta_m}{\left(\frac{\eta_H}{\eta_L}\right)^{2s} \left((\eta_0 + \eta_m)^2 + \left(\frac{\eta_0\eta_m}{\eta_A} - \eta_A\right)^2 \right)}, \quad (\text{P.4})$$

where η_A is the gradient admittance of the non-centered medium, η_H is the gradient admittance of the higher medium, η_L is the gradient admittance of the lower refractive index, η_0 is the gradient admittance of the incident medium, and η_m is the gradient admittance of the base. If the number of layers s is sufficiently large,

$$\left(\frac{\eta_H}{\eta_L}\right)^s \gg \left(\frac{\eta_L}{\eta_H}\right)^s \quad (\text{P.5})$$

holds. Once all gradient admittances are determined, the number of layers can be determined to achieve desirable transmittance.

The approximation shown in Eq. (P.5) is still valid for the estimation of the transmittance in a transmission band. In the transmission band, the equivalent admittance and equivalent phase thickness are real numbers, the Eq. (N.31) becomes

$$T = \frac{4E^2\eta_0\eta_m}{(E^2 + \eta_0\eta_m)^2}. \quad (\text{P.6})$$

If one wants to create a SPF, it should be based on $(L/2, H, L/2)^s$ to create a SPF with good performance.

Appendix Q

Glan-Taylor prism

The Glan-Taylor prism (GT) is an optical element for extracting only one linearly polarized light component. GT takes out one linearly polarized component using a completely different principle than the PBS described in Appendix N. GT has a structure similar to the PBS shown in FIG. N.6, but glue and dielectric multilayer film are not used. The layer between the two right angle prisms is filled with air. Since the refractive index in air is almost the same as that of a vacuum, it can be regarded as a vacuum. The physical properties that are the principles of GT are birefringence, as described in Appendix O, and total reflection, as described in Appendix N. Birefringence is the property that the refractive index perceived by electromagnetic waves differs depending on the direction in which electromagnetic wave vibrates. The different refractive index means that the total reflection angle given by $\theta = \arcsin n_2/n_1$ differs depending on the direction of vibration. If the angle of the slope of the right angle prism is adjusted so that the p-polarized component is transmitted and the s-polarized component is totally reflected, the p-polarized component can be extracted with a high extinction ratio which is approximately $10^5 : 1$. The transmittance of GT is about 95% at best, and the remaining p-polarized component is contained in the reflected light. Therefore, it is mostly used when pure linearly polarized light is desired to be prepared. Since the reflected light contains both *s* and *p* polarization, GT is not suitable for applications that separate two orthogonal components, such as PBS.

Appendix R

Band pass filter

A band-pass filter (BPF) is an optical element that transmits only light of a certain wavelength. If the wavelength band of light to be transmitted is wide, a dielectric multi-layer film alone is sufficient to achieve the purpose but for narrow bandwidths, BPFs are realized based on a completely different principle. A common method is to create a Fabry-Perot resonator by making a thin metal film with high reflectivity inside the filter. This appendix describes the physical principles and features of narrow band BPF realization. As shown in FIG. R.1, the BPF consists of two multi-layers A and B and a spacer layer between them. As explained in Sec. N.4, the multi-layers can be mathematically treated as a single thin film. Thus, multi-layer A and multi-layer B work as a coupled mirror with high reflectivity. The layer corresponding to the interior of the Fabry-Perot resonator is called spacer layer. Predicting transmittance based on the method described in Sec. N.4 yields

$$T = \frac{T_A T_B}{(1 - \sqrt{R_A R_B})^2} \left(\frac{1}{1 + F \sin^2 \left[\frac{\phi_A + \phi_B}{2} - \frac{2\pi nd}{\lambda} \right]} \right), \quad (\text{R.1})$$

where R_A, T_A, R_B and T_B are the reflectance and transmittance of multi-layers A and B, d is the thickness of the spacer layer, λ is the wave length in vacuum, and ϕ_A and ϕ_B are the phase differences between the amplitude reflectance of multi-layers A and B. In other words, they have the relation given by

$$\begin{aligned} R_A &= |r_A| e^{i\phi_A} \cdot |r_A| e^{-i\phi_A} \\ R_B &= |r_B| e^{i\phi_B} \cdot |r_B| e^{-i\phi_B} \end{aligned} \quad (\text{R.2})$$

F shows finesse given by

$$F = \frac{4\sqrt{R_A R_B}}{(1 - \sqrt{R_A R_B})^2}. \quad (\text{R.3})$$

Finesse is the sharpness of the narrow band of transmitted light.

The central wavelength of the transmission band can be derived as the wavelength such that the sine argument in Eq. (R.1) is an integer multiple of π , which is obtained as

$$\lambda = \frac{2nd}{m + \frac{\phi_A + \phi_B}{2\pi}} \quad (m \in \mathbb{Z}). \quad (\text{R.4})$$

Thus, this result means that some transmission bands centered on wavelengths corresponding to different integer m appear.

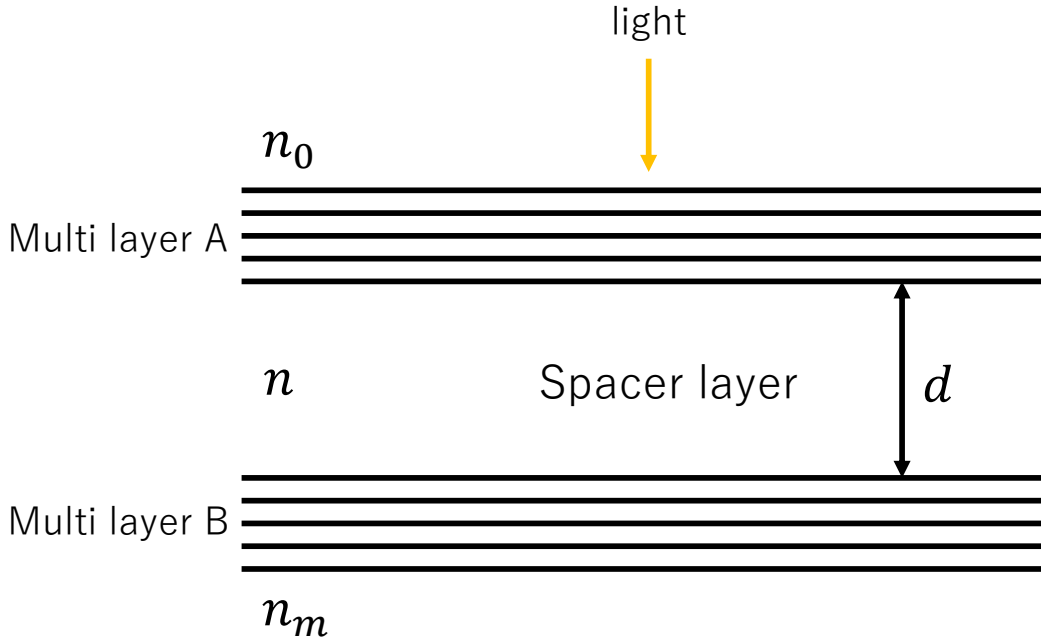


FIGURE R.1: A model of multi-layers to realize narrow band BPF. It consists of two multi-layers A and B composed of a dielectric and a thin metal film, and a spacer layer sandwiched between them. n_0 is the refractive index of the medium into which light is incident, n_m is the refractive index of the substrate, and n is the refractive index of the spacer layer.

Next, let's discuss the half-width of the transmission band. The half-width is the width of the wavelength such that the transmittance is half of the maximum value, which is given by

$$T = \frac{1}{2} T_{max}. \quad (\text{R.5})$$

Let ϕ be the argument of the sine in Eq. (R.1). Assuming that the half-width of transmittance when this ϕ is taken on the horizontal axis is from $\phi = \phi_c - \varepsilon$ to $\phi = \phi_c + \varepsilon$, the Eq. (R.5) becomes

$$\varepsilon = \arcsin \sqrt{\frac{1}{F}}. \quad (\text{R.6})$$

Therefore, when phase is considered as the abscissa, the half-width becomes

$$\Delta\phi = 2\varepsilon = 2 \arcsin \left[\frac{1}{F} \right]. \quad (\text{R.7})$$

The half-width, with wavelength as the abscissa, is obtained by differentiating

$$\phi = \frac{\phi_A + \phi_B}{2} - \frac{2\pi nd}{\lambda} \quad (\text{R.8})$$

and substituting Eq. (eqn:appendix bpf half-value of phase), which results in

$$\Delta\lambda = \frac{\lambda^2}{\pi nd} \arcsin \left[\frac{1}{F} \right]. \quad (\text{R.9})$$

This result indicates that to narrow the full width at half maximum (FWHM) of the transmission band, either the thickness of the SPACER layer must be increased or the reflectivity of the mirrors that make up the Fabry-Perot resonator must be increased.

Appendix S

Single photon counting module

The single photon counting module (SPCM) is a single photon detector using the property of an avalanche photodiode. This appendix explains the principle of an avalanche photodiode. To understand avalanche photodiodes, it is necessary to review the principles of ordinary photodiodes. As shown in FIG. S.1, applying a positive voltage to a p-n junctioned p-type semiconductor is called forward bias, while applying a positive voltage to an n-type semiconductor is called reverse bias. A p-n junction diode to which a forward bias is applied continues to emit light and allow current to flow because electron-hole pairs are generated at the p-n junction. This property is used as an LED. On the other hand, a p-n junction diode to which a reverse bias is applied does not produce an electron-hole pair at the p-n junction, so no current flows, but current flows only when the p-n junction diode absorbs light. This is the basic principle of photodiode operation.

An avalanche photodiode is a photodiode with a large reverse bias voltage applied to a p-n junction diode. When light strikes the p-n junction diode to which a large reverse bias voltage is applied, the generated electron-hole pairs gain large acceleration. When the accelerated charged particle collides with another electron, it may transition to the conduction band, depending on the kinetic energy gained by the colliding electron. The transition of an electron to the conduction band means that a new electron-hole pair is created, and the created charged particle is accelerated and collides with another electron. This sequence of events causes a large current to flow in the p-n junction diode. This phenomenon is called electron avalanche multiplication. Therefore, when a certain voltage is applied, the current multiplication factor increases significantly. A photodiode in this state is an avalanche photodiode.

Avalanche photodiodes require fairly uniform formation of the p-n junction because the multiplication factor changes rapidly with a small change in the applied voltage. This is a major difference from ordinary photodiodes. When light of high intensity hits an avalanche photodiode, the electrical circuit is damaged by the large current flowing through the circuit. Therefore, when counting photon using avalanche photodiodes, great care must be taken to eliminate unwanted background and to prevent the signal from becoming too intense.

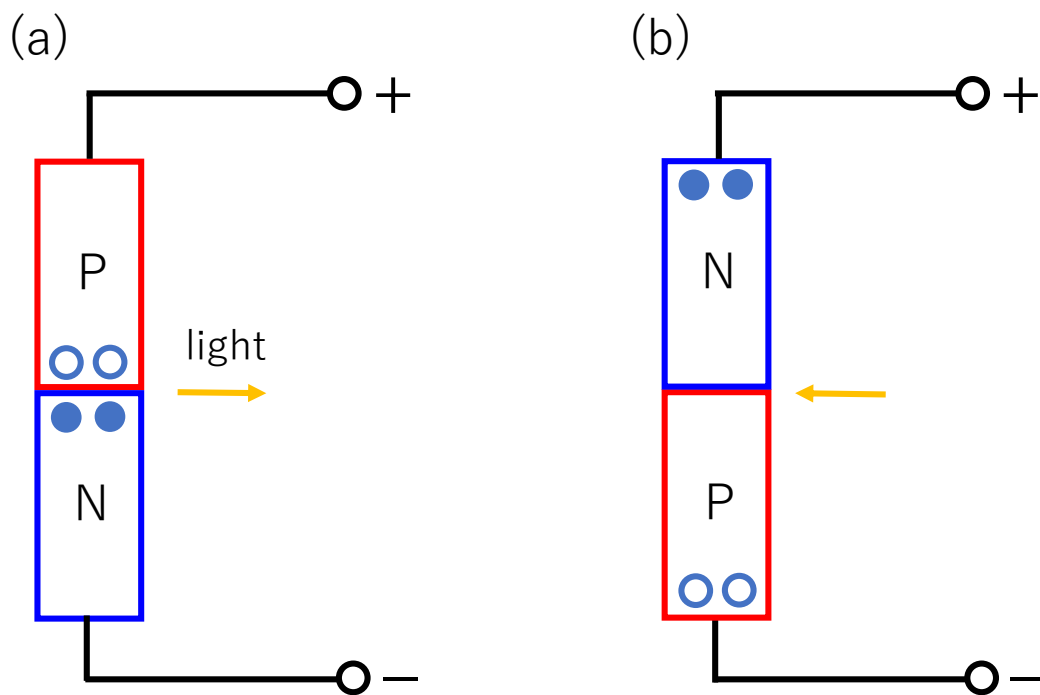


FIGURE S.1: Forward and reverse bias voltages applied to the p-n junction. (a) A p-n junction diode with a forward bias voltage applied. This diode works as a light emitting diode (LED) (b) p-n junction diode with reverse bias voltage applied. This diode works as a photodiode.

Appendix T

Spontaneous parametric down conversion

This appendix describes the physical phenomena that produces the two-photon necessary to generate polarization entanglement. That physical phenomenon is called spontaneous parametric down conversion (SPDC) and is widely used in experimental studies of quantum information science and quantum mechanical foundations. SPDC was predicted theoretically in the early 1960s[73–75] and first demonstrated in 1967[76]. SPDC is classified as a second-order nonlinear optical phenomenon related to polarization. The beginning of this appendix describes the properties of materials that can cause second-order nonlinear optical effects, followed by a description of the interaction between materials and light.

T.1 Crystals which can cause nonlinear optical effect

When an electromagnetic wave strikes a material, it causes the charged particles that make up the material to vibrate. The total bias in the charge distribution caused by this vibration is called polarization and is given by

$$P_j = \varepsilon_0 \left(\sum_k \chi_{jk}^{(1)} E_k + \sum_{k,l} \chi_{jkl}^{(2)} E_k E_l + \dots \right) \quad \{j, k, l\} = \{x, y, z\}, \quad (\text{T.1})$$

where ε_0 is the dielectric constant of the vacuum, $\chi^{(1)}$ is the linear dielectric susceptibility, $\chi^{(2)}$ is the second-order nonlinear dielectric susceptibility, and E is the electric field of the incident electromagnetic wave, x, y, z are the coordinates of the position. The nonlinear dielectric susceptibility is very small compared to the linear dielectric susceptibility, but as the electric field increases, the nonlinear term becomes non-negligible because it takes effect as a power of the electric field. This Physically means that the frequency of the charged particle no longer matches the frequency of the electromagnetic wave. Ignoring nonlinear terms of third order or higher, the nonlinear polarization is given by

$$P_j^{(NL)} \equiv \varepsilon_0 \sum_{k,l} \chi_{jkl}^{(2)} E_k E_l. \quad (\text{T.2})$$

The second-order nonlinear dielectric susceptibility is a third rank tensor, so it typically has twenty seven independent elements, but consideration of physical requirements reduces the number of independent elements. If the substance has space-reversal symmetry, the sign of the nonlinear dielectric susceptibility should not be inverted with respect to the inversion of the coordinates, but the direction of the polarization and electric field

should be inverted, so that Eq. (T.2) becomes

$$-P_j^{(NL)} = \varepsilon_0 \sum_{k,l} \chi_{jkl}^{(2)} (-E_k)(-E_l) = \varepsilon_0 \sum_{k,l} \chi_{jkl}^{(2)} E_k E_l. \quad (\text{T.3})$$

To resolve the contradiction between this equation and Eq. (T.2), the second-order nonlinear dielectric susceptibility must be zero. Conversely, for second-order nonlinear optical effects to appear, the material must have no space-reversal symmetry. Materials without inversion symmetry are empirically known to have piezoelectricity¹. To simplify the situation, if one define coordinates such that k and l are indistinguishable, $\chi_{jkl}^{(2)} = \chi_{jlk}^{(2)}$ holds, so there are eighteen independent elements. Thus, the relation between nonlinear polarization and voltage is given by

$$\begin{pmatrix} P_x^{(NL)} \\ P_y^{(NL)} \\ P_z^{(NL)} \end{pmatrix} = \varepsilon_0 \begin{pmatrix} \chi_{11}^{(2)} & \chi_{12}^{(2)} & \chi_{13}^{(2)} & \chi_{14}^{(2)} & \chi_{15}^{(2)} & \chi_{16}^{(2)} \\ \chi_{21}^{(2)} & \chi_{22}^{(2)} & \chi_{23}^{(2)} & \chi_{24}^{(2)} & \chi_{25}^{(2)} & \chi_{26}^{(2)} \\ \chi_{31}^{(2)} & \chi_{32}^{(2)} & \chi_{33}^{(2)} & \chi_{34}^{(2)} & \chi_{35}^{(2)} & \chi_{36}^{(2)} \end{pmatrix} \begin{pmatrix} E_x^2 \\ E_y^2 \\ E_z^2 \\ 2E_y E_z \\ 2E_x E_z \\ 2E_x E_y \end{pmatrix}, \quad (\text{T.4})$$

where $kl = \{xx, yy, zz, yz, zx, xy\} = \{1, 2, 3, 4, 5, 6\}$. It is customary to show a third rank tensor as a second rank tensor in this way. In general, the second-order nonlinear dielectric susceptibility has permutation symmetry, so the following relation holds

$$\chi_{jkl}^{(2)} = \chi_{kjl}^{(2)} = \chi_{ljk}^{(2)}. \quad (\text{T.5})$$

This means that there is no difference between the x, y and z axes if they are fixed to the right-hand system. Furthermore, if there is no absorption or dispersion of light, the second dielectric susceptibility also satisfies Kleinman's symmetry condition given by

$$\chi_{jkl}^{(2)} = \chi_{kjl}^{(2)} = \chi_{ljk}^{(2)}. \quad (\text{T.6})$$

The number of independent elements can be reduced by applying permutation symmetry and Kleinman's symmetry condition.

T.2 Electromagnetic waves propagating in nonlinear crystals

When nonlinear polarization is taken into account, an electric flux density is given by

$$\begin{aligned} \vec{D} &= \varepsilon_0 \vec{E} + \vec{P} \\ &= \varepsilon_0 \left(1 + \chi^{(1)}\right) \vec{E} + \vec{P}^{(NL)} \\ &= \varepsilon \vec{E} + \vec{p}^{(NL)}, \end{aligned} \quad (\text{T.7})$$

where ε is dielectric constant in a matter. A term representing nonlinear polarization is added to the wave equation, which is given by

$$\Delta E - \mu_0 \varepsilon \partial_t^2 E = \mu_0 \partial_t^2 P^{(NL)}. \quad (\text{T.8})$$

¹The property of a voltage produced when pressure is applied.

If a ferromagnetic material is not assumed, the magnetic permeability in the material may be regarded as the magnetic permeability in a vacuum. Considering the possibility of attenuation of electromagnetic waves as they propagate through the material, the electric field and polarization can be given by

$$E(z, t) = A(z)e^{i(k'z - \omega t)} \quad (\text{T.9})$$

$$P^{(NL)}(z, t) = P_0^{(NL)}e^{i(kz - \omega t)}. \quad (\text{T.10})$$

where k' is the wavenumber of the electric field and k is the wavenumber of the polarization. Since the direction of propagation of the electric field and polarization are generally different, situations with different wavenumbers should be assumed. Substituting Eq. (T.9) and Eq. (eqn:appendix spdc polarization) into Eq. (T.8) and applying slowly varying amplitude (SVA) approximation expressed in

$$|d_z^2 A(z)| \ll |kd_z A(z)|, \quad (\text{T.11})$$

where d_z means d/dz , Eq. (T.8) becomes

$$d_z A(z) = \frac{i\mu_0\omega^2}{2k'} P_0^{(NL)}(z)e^{i(k-k')z}. \quad (\text{T.12})$$

SVA approximation represents a situation where the amplitude hardly changes at lengths of about a wavelength. When light of two different frequencies, ω_1 and ω_2 , are present in the matter, the nonlinear polarization can be given by

$$P_{0j}^{(NL)}(z, t) = \varepsilon_0 \sum_{k,l} \chi_{jkl}^{(2)} E_k(\omega_1) E_l(\omega_2). \quad (\text{T.13})$$

It can be seen that there can be polarizations in the matter that oscillate at angular frequencies corresponding to the sum or difference of ω_1 and ω_2 in the matter. Considering the situation where $\omega_1 = \omega_2 \equiv \omega$ holds and the polarization of the electromagnetic wave incident on the matter has only j component, which means linear polarization, the nonlinear polarization shown in Eq. (T.13) takes the form given by

$$P_{0j}^{(NL)}(z, t) = \varepsilon_0 \sum_k \chi_{jkk}^{(2)} A_j^2(z) e^{i(2k_1z - 2\omega t)}, \quad (\text{T.14})$$

where $A_j(z)$ is the amplitude of the incident electromagnetic wave, k_1 is the wavenumber, and ω is the angular frequency. This nonlinear polarization induces electromagnetic waves with a frequency of 2ω , so that the new electric field can cause in the matter, which is given by

$$E_{2j}(z, t) = A_{2j}(z) e^{i(k_2z - 2\omega t)}, \quad (\text{T.15})$$

Here, the subscript "2" is a label to distinguish between the incident electric field and the electric field generated inside the matter. The wave equation that this electric field must satisfy can be derived as in Eq. (T.12) as

$$d_z A_2(z) = \frac{i2\mu_0\omega^2}{k_2} P_0^{(NL)}(z) e^{i(\Delta k)z}, \quad (\text{T.16})$$

where $P_0^{(NL)}(z)$ and Δk are given by

$$P_0^{(NL)}(z) = \varepsilon_0 \sum_k \chi_{jkk}^{(2)} A_{1k}^2 \quad (\text{T.17})$$

$$\Delta k = 2k - k_2. \quad (\text{T.18})$$

Assuming that the intensity of the incident electromagnetic wave is sufficiently large and that the decrease in intensity when propagated over a distance z is negligible, the amplitude of the incident electromagnetic wave can be regarded as having no dependence on z . Integrating Eq. (T.16) from $z = 0$ to $z = z'$ gives

$$A_{2j}(z) - A_{2j}(0) = \int_0^{z'} i \frac{2\mu_0\omega^2}{k_2} P_0^{(NL)}(z) e^{i\Delta k z} dz \quad (\text{T.19})$$

$$= i \frac{2\omega^2}{k_2 c^2} \sum_k \chi_{jkk}^{(2)} A_{1k}^2 \int_0^{z'} \frac{2}{\Delta k} \sin \left[\frac{\Delta k}{2} z \right] e^{i\frac{\Delta k}{2} z} dz \quad (\text{T.20})$$

$$= i \frac{2\omega^2}{k_2 c^2} \sum_k \chi_{jkk}^{(2)} A_{1k}^2 \frac{\sin \left[\frac{\Delta k}{2} z' \right]}{\frac{\Delta k}{2}} e^{i\frac{\Delta k}{2} z'}, \quad (\text{T.21})$$

where c is the speed of light. If the coordinates are set so that the electromagnetic wave is incident on the material at the point $z = 0$, then $A_{2j}(0) = 0$ because there is no nonlinear polarization at the point $z = 0$. Thus, the intensity of electromagnetic waves with an angular frequency of 2ω is

$$I_{2j} \propto \frac{\sin^2 \left[\frac{\Delta k}{2} z' \right]}{\left(\frac{\Delta k}{2} \right)^2}. \quad (\text{T.22})$$

This result implies that the intensity of electromagnetic waves with a doubled angular frequency of the incident beam generated inside a nonlinear crystal oscillates with a period of $\pi/\Delta k$ called coherent length.

The propagation of electromagnetic waves in nonlinear crystals discussed so far has described the transformation of electromagnetic waves with an angular frequency of ω into electromagnetic waves with an angular frequency of 2ω . Such a phenomenon is called second harmonic generation (SHG); SPDC can be understood as the inverse process of SHG. That is, an electromagnetic wave with an angular frequency of 2ω is injected into a nonlinear crystal, which generates light with an angular frequency of ω . However, the critical difference between SPDC and SHG is that SPDC requires spontaneous emission of light during the parametric fermentation process. Hence, light of various wavelengths will be produced in the nonlinear crystal while satisfying the energy conservation law.

There are three different types of SPDC. In type-0 SPDC, the pump photon and the converted two photons, the signal photon and idler photon, are all in the same polarization state; in type-1 SPDC, the signal and idler photon are in the same polarization state, but the pump photon is orthogonal. In type-2 SPDC, either the signal photon or the idler photon will be in the same polarization state as the pump photon, but the other is orthogonal.

Appendix U

Phase matching

This appendix illustrates phase matching. Phase matching is a physical requirement that must be met in order to efficiently extract electromagnetic waves generated by nonlinear optical effects. First, normal phase matching will be explained, followed by the current mainstream quasi phase matching.

In Appendix T, the intensity of the electromagnetic wave generated in the nonlinear crystal at an angular frequency different from that of the incident electromagnetic wave is proportional to the function expressed by Eq. (T.22). This is a periodic function such that the electromagnetic wave has the same intensity every time it travels by $\pi/\Delta k$. However, if the situation is realized such that $\Delta k = 0$, the magnitude of the intensity would be proportional to a quadratic function. Phase matching is to define the relation between the incident electromagnetic wave and the nonlinear crystal so that $\Delta k = 0$ is realized, and the condition that $\Delta k = 0$ is called the phase matching condition. At first glance it seems impossible to achieve phase matching conditions because, in general, the greater the angular frequency, the greater the difference in the refractive index perceived by the light, which causes it to propagate with different phase speeds. However, by using the birefringence described at the beginning of Appendix O, it is possible to achieve phase matching conditions, as shown in FIG. U.1. The use of birefringence to satisfy phase matching conditions is called angular phase matching. Once the angular phase matching is achieved, the light generated inside the nonlinear crystal increases in proportion to the quadratic function, but the crystal length cannot be increased because the ordinary and extra-ordinary light propagate in non-parallel directions. The angle between the Poynting vectors of ordinary and extra-ordinary light is called the walk-off angle. For ordinary light, the normal vector of the wavefront and the direction of the Poynting vector are parallel, but it is not true for extra-ordinary light. This is the cause of birefringence. A phase matching method called quasi-phase matching was devised to solve this problem. As shown in FIG. U.2, quasi-phase matching is a phase matching method that increases the intensity of down converted light by using a crystal in which the direction of the crystal's nonlinear susceptibility is reversed at the length where the down converted light begins to decrease. Quasi-phase matching has the disadvantage that the polarization reversal period and crystal temperature must be optimized according to the wavelength of the pump light used in the experiment, but in principle the length of the crystal can be as long as desired, since there is no need to worry about walk-off. At first glance, FIG. U.2 seems to suggest that quasi-phase matching is less efficient than angular phase matching, which is correct when the same material is used as the nonlinear crystal. In fact, crystals with larger nonlinear optical constants can be selected because one does not have to pay attention to the angle at which the pump light is incident on the crystal. to achieve angular phase matching.

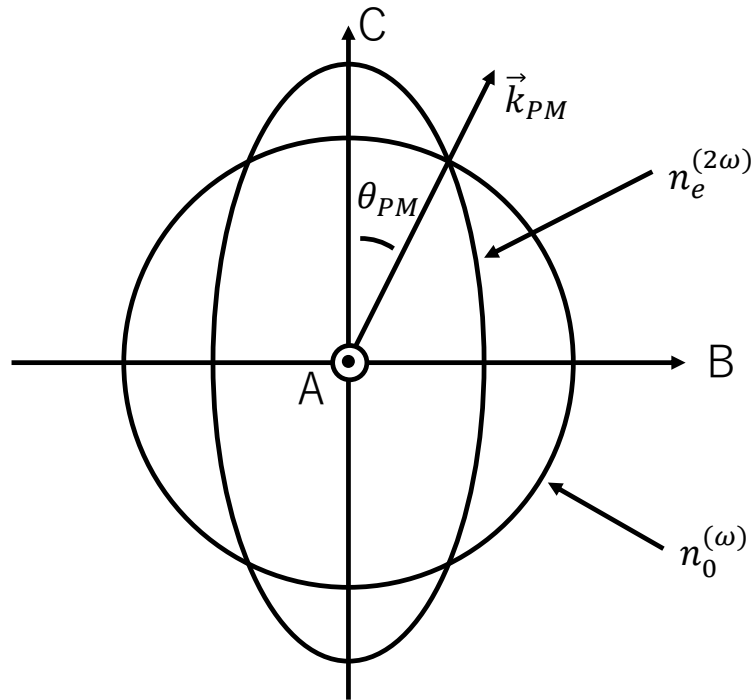


FIGURE U.1: Geometric relation between the phase matching angle and the refractive index distribution such that angular phase matching is satisfied. The A, B, and C axes make Cartesian coordinate defined in a uniaxial crystal. This Cartesian coordinate is defined so that polarization components parallel to the A and B axes perceive the same refractive index but polarization components parallel to the C axis perceive different refractive indices. $n_0^{(\omega)}$ is the refractive index for electromagnetic waves with an angular frequency of ω , and $n_e^{(2\omega)}$ is the refractive index for electromagnetic waves with an angular frequency of 2ω . The distance from the center of the coordinates to the circle or ellipse corresponds to the value of the refractive index. The subscripts "o" and "e" correspond to ordinary and extraordinary light, where ordinary light has an oscillating component parallel to the AB plane and extra-ordinary light oscillates in a direction perpendicular to both the wavenumber vector and ordinary light. It can be seen that when the electromagnetic wave propagates at an angle θ_{PM} deviating from the C axis, the values of the refractive index perceived by ordinary light and extra-ordinary light are equal. Such an angle is called the phase matching angle.

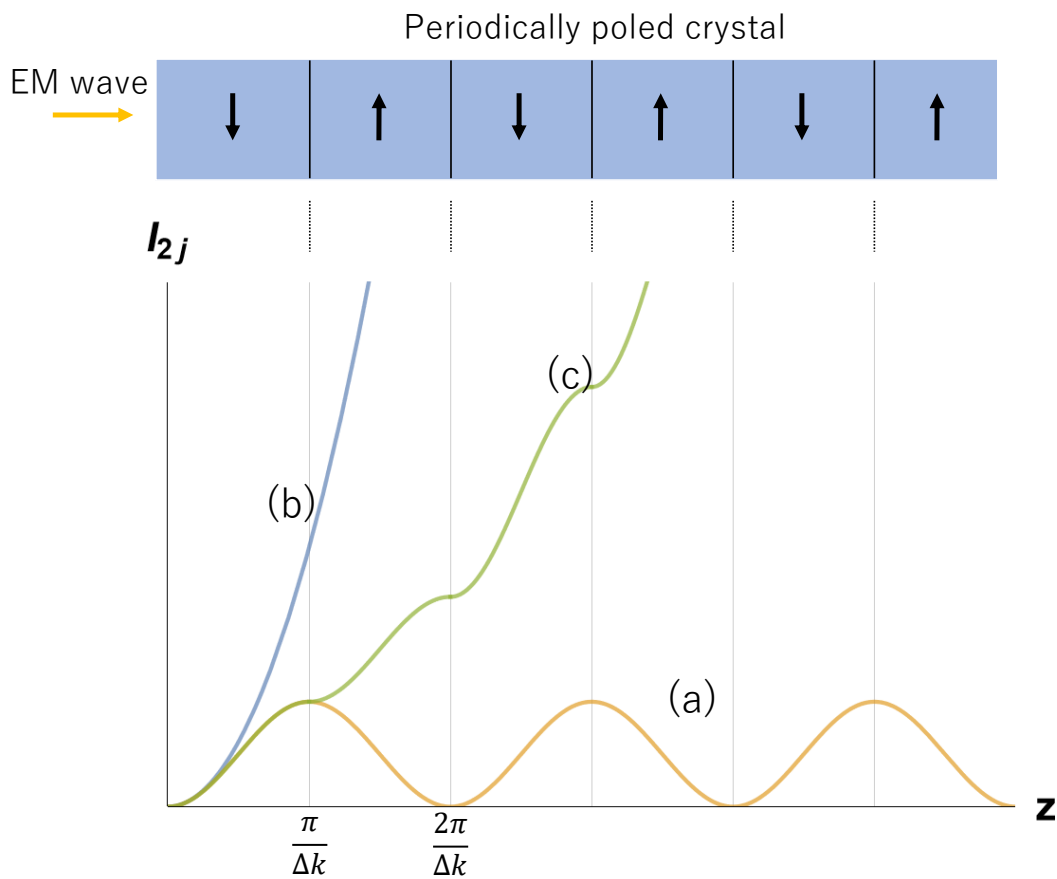


FIGURE U.2: Intensity changes of light generated in a nonlinear crystal in the case of (a) non-phase matching, (b) quasi phase matching and (c) angular phase matching. If the phase matching condition is not achieved, the intensity of the light produced inside the crystal will start to decrease as the pump light propagates $\pi/\Delta k$. If a crystal is used in which the direction of polarization reverses when the light propagates for a decreasing length, the intensity of the generated light will continue to increase. Such a crystal is called a periodically poled crystal.

Appendix V

Gaussian beam

A Gaussian beam is a beam in which the transverse modes of electromagnetic waves propagating through space has Gaussian distribution. In this appendix, a theoretical description of Gaussian beams will be explained. The wave equation that holds in free space is given by

$$(\Delta - \epsilon\mu\partial_t^2) E(\vec{r}, t) = 0, \quad (\text{V.1})$$

where ϵ is the dielectric constant of the space, μ is the magnetic permeability and ∂_t means $\partial/\partial t$. If the time dependence of the electric field is described as $e^{-i\omega t}$, the equation above can be described

$$(\Delta + k^2) U(r, z) = 0, \quad (\text{V.2})$$

where $k = n\omega/c$ is the wavenumber parallel to the z-axis, c is speed of light in vacuum, ω is angular frequency, n is the refractive index in the medium, $E(\vec{r}, t) = U(r, z)e^{-i\omega t}$ holds, and the coordinate system is assumed to be a cylindrical coordinate system, which means $r = \sqrt{x^2 + y^2}$ holds. Let us assume that the electric field in the wave equation above has the form of

$$U(r, z) = \exp\left[-i\left(P(z) + \frac{k}{2q(z)}r^2\right)\right] e^{ikz}, \quad (\text{V.3})$$

where $P(z)$ and $q(z)$ are complex functions that depend on z . Substituting this expression for the electric field into Eq. (V.2) and assuming slowly varying amplitude (SVA) approximation given by

$$|d_z^2 U(r, z)| \ll |kd_z U(r, z)|, \quad (\text{V.4})$$

where d_z means d/dz , we obtain

$$\left(\left(\frac{1}{q(z)}\right)^2 + d_z\left(\frac{1}{q(z)}\right)\right) k^2 r^2 - 2\left(d_z P(z) + \frac{i}{q(z)}\right) k = 0. \quad (\text{V.5})$$

The SVA approximation represented by Eq. (V.4) represents a situation where the amplitude hardly changes at lengths of about a wavelength. For Eq. (V.5) to hold, the contents of the two brackets should be zero, so solving the two equations given by

$$\left(\frac{1}{q(z)}\right)^2 + d_z\left(\frac{1}{q(z)}\right) = 0 \quad (\text{V.6})$$

$$d_z P(z) + \frac{i}{q(z)} = 0 \quad (\text{V.7})$$

is necessary. The solutions to these two equations have the form given by

$$P(z) = -i \ln \left[1 + \frac{z}{q_0} \right] \quad (\text{V.8})$$

$$q(z) = z + q_0, \quad (\text{V.9})$$

where q_0 is some complex constant. To find out what value this complex constant takes, substituting these two results into Eq. (V.3) results in

$$U(r, z) = \frac{1}{1 + \frac{z}{q_0}} \exp \left[-i \frac{k}{2(z + q_0)} t^2 \right] e^{ikz}. \quad (\text{V.10})$$

In general, q_0 can be written as $\alpha + i\beta$, because q_0 is a complex constant. But as can be seen in this equation, α represents a parallel shift of position, so the physical situation is invariant even if α is regarded as zero. Therefore, transforming Eq. (V.10) by regarding q_0 as iz_R , we obtain

$$U(r, z) = \frac{\omega_0}{\omega} \exp \left[-\frac{r^2}{\omega^2(z)} + \frac{k}{2R(z)} \right] e^{i(kz + \eta(z))}, \quad (\text{V.11})$$

where $\omega(z)$, $R(z)$ and $\eta(z)$ are given by

$$\omega(z) = \omega_0 \sqrt{1 + \left(\frac{z}{z_R} \right)^2} \quad (\text{V.12})$$

$$R(z) = z \left(1 + \frac{z_R^2}{z^2} \right) \quad (\text{V.13})$$

$$\eta(z) = \arctan \left[\frac{z}{z_R} \right]. \quad (\text{V.14})$$

Therefore, the final form of the electric field is given by

$$E(r, z, t) = E_0 \frac{\omega_0}{\omega} \exp \left[-\frac{r^2}{\omega^2(z)} + \frac{k}{2R(z)} \right] e^{i(kz + \eta(z) - \omega t)}, \quad (\text{V.15})$$

where E_0 is the magnitude of the electric field at $z = 0$. A beam in which the electric field of electromagnetic waves propagating through space is represented in this equation is called a fundamental Gaussian beam. The "fundamental" means that the amplitude of the electric field has no angular dependence around the z -axis, and of course there are modes that have angular dependence.

To understand the geometry of the fundamental Gaussian beam, the relationship between the key parameters and the physical situation will be explained. As shown in FIG. V.1, the fundamental Gaussian beam has an intensity distribution in the form of a Gaussian function around the z -axis, the intensity is greatest on the z -axis. As Eq. (V.15) shows, the distance from the z -axis at which the intensity is $1/e^2$ times of its maximum value represents the beam radius $\omega(z)$ shown in Eq. (V.12). The distance at which the beam radius is twice the root of the minimum beam radius ω_0 is called the Rayleigh length, which is defined as

$$z_R := \frac{n\pi\omega_0^2}{\lambda}, \quad (\text{V.16})$$

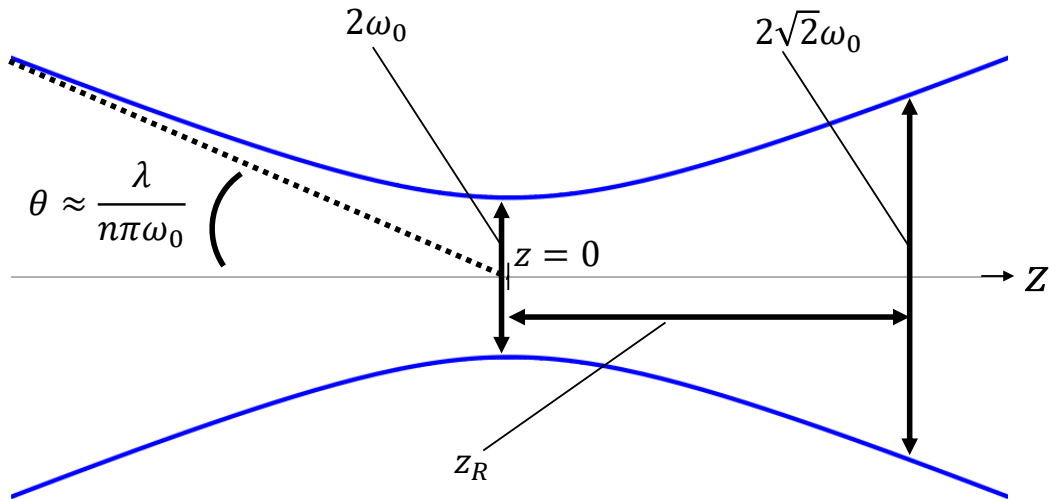


FIGURE V.1: The envelope of the fundamental Gaussian beam propagating in the z -axis direction in space. ω_0 is the beam radius at the beam waist, z_R is the Rayleigh length, and θ is the beam spread angle.

where n is the refractive index in a space, λ is the wave length in vacuum. Rayleigh length is a measure of how close the Gaussian beam is to a parallel beam. Eq. (V.13) shows the radius of curvature of the beam's wavefronts at z . It can be seen that the radius of curvature is infinite at $z = 0$. At this point, the fundamental Gaussian beam is a perfectly parallel ray. $\eta(z)$ in Eq. (V.14) is the Gouy phase at z , an extra phase term attributable to the phase velocity of light.

Appendix W

Construction of polarization entangled photon paris source

This appendix describes the procedure for generating entanglement photon pairs of polarized light. This appendix will focus on what to watch out for. Experimental techniques and specific methods will be described in Appendix Y. The procedure can be broadly divided into the following steps.

1. Determination of the dimensions of the entire experimental setup.
2. Shaping of the spatial modes of the light emitted from the optical fiber.
3. Fixing the position of the optical elements and checking the photon pair generation.
4. Fine tuning of the interferometer.

The following sections describe what adjustments are made in each of these steps.

W.1 Determination of the dimensions of the entire experimental setup

First of all, it is important to make sure that all necessary optical components can be placed on the optical table and that they can be fixed. FIG. W.1 is a photograph of the actual experimental setup corresponding to FIG. 3.4. The optical components in the picture are not yet fixed, but just placed. After tentatively placing them in this manner, it is important to roughly know the distance between the optical components. Of particular importance will be the distance from the three fiber couplers to the DPBS and the distance from the DPBS to the PPKTP. The smaller the size of the Sagnac interferometer, the better, because it provides greater precision and stability in the adjustment of the two mirrors. The setup we made roughly had 200[mm] from FC2,3 to DPBS, 250[mm] from FC1 to DPBS, 125[mm] from DPBS to PPKTP, where the location of the FCs was defined as the rough location of the optical fiber's exit, and for DPBS and PPKTP, the location of the center of them were defined as their location. Knowing how much the distance from the three fiber couplers to the DPBS can be varied is very important for shaping the spatial modes explained in the next section.

W.2 Shaping of the spatial modes of the light emitted from the optical fiber

The smaller the diameter of the pump light that should be realized inside the PPKTP, the more efficient the generation of photon pairs will be, but the adjustment will be more

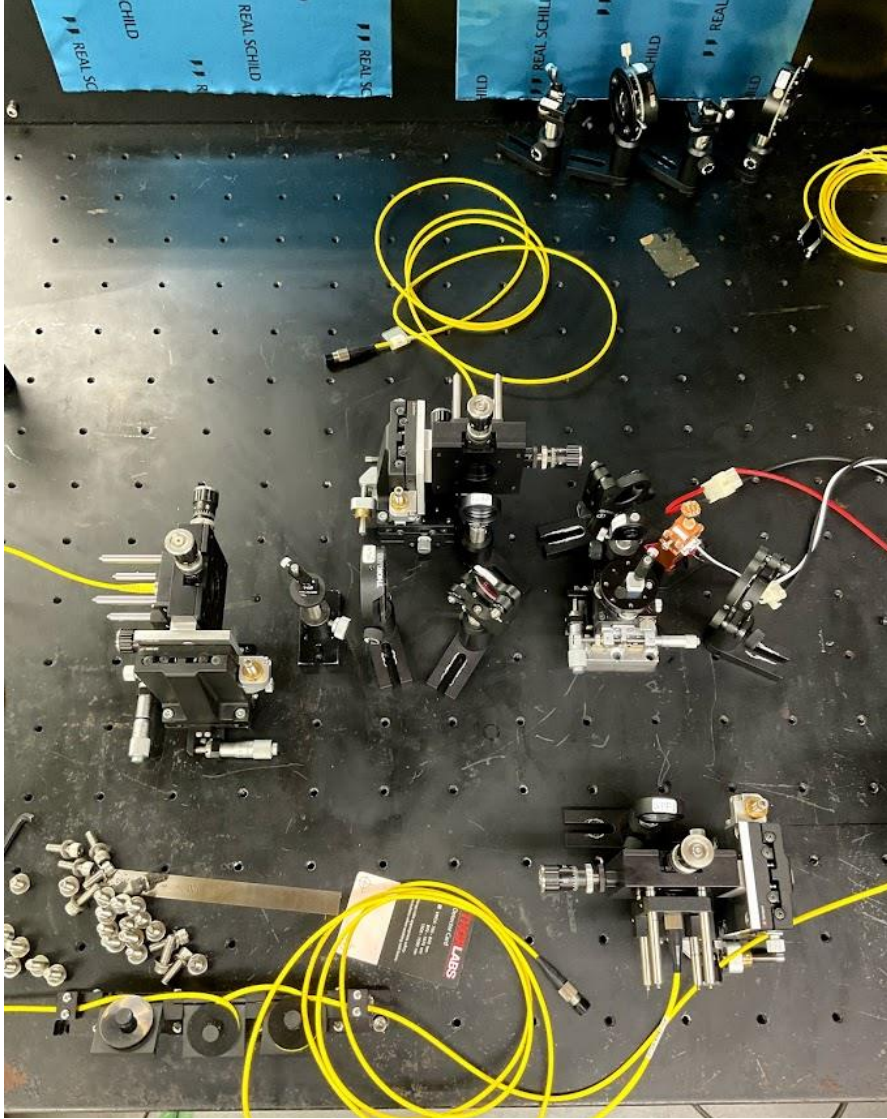


FIGURE W.1: Photo of presetting of all optics. This setup is corresponding to the one shown in FIG. 3.4. There are no HWP2 and GT in front of the FC1 and FC2.

difficult because the spatial modes will deviate from parallel rays. Therefore, the transverse diameter of the pump light should be large enough to fit well inside the PPKTP. The position of the beam waist of the pump light is adjusted so that it is just at the center of the PPKTP. This is to maximize the efficiency of photon pair generation and to achieve spatial mode matching. Spatial mode matching is to unify the spatial modes of the pump light emitted from FC1 and the light emitted from FC2 and FC3. Quantitatively, spatial mode matching refers to unifying the Rayleigh lengths described by Eq. (V.16). Since the wavelength of the photon pair that is finally detected is equal to twice the wavelength of the pump light, the wavelength of the light emitted from FC2 and FC3 is twice the wavelength of the light emitted from FC1. This relation is given by

$$\begin{aligned} \frac{n\pi\omega_R^2}{2\lambda} &= \frac{n\pi\omega_B^2}{\lambda} \\ \omega_R &= \sqrt{2}\omega_B, \end{aligned} \quad (\text{W.1})$$

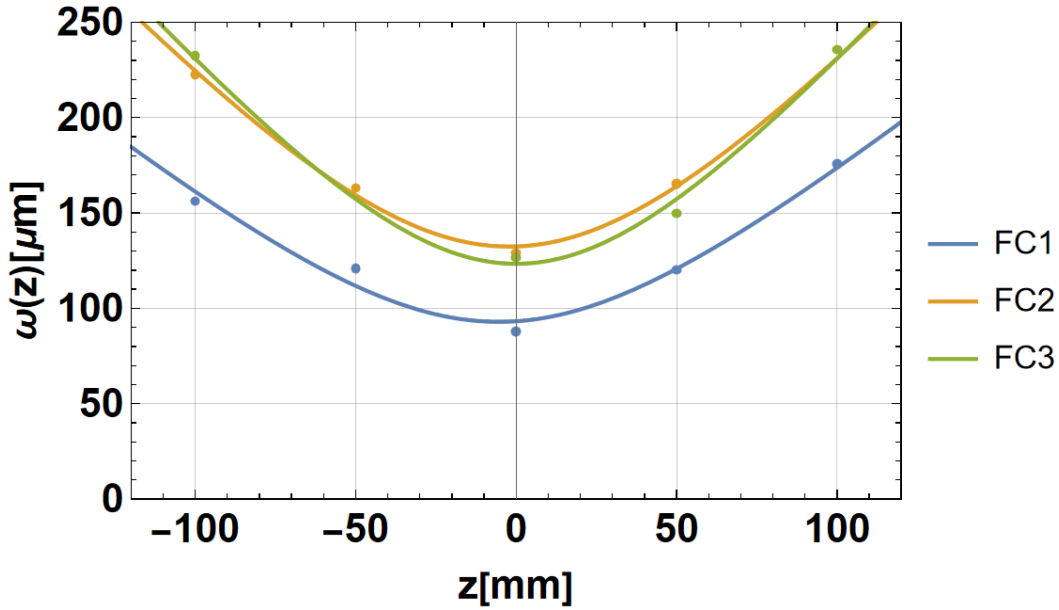


FIGURE W.2: Results of spacial mode matching. The horizontal axis is defined as the position of the PPKTP at $z = 0$, with the upstream side being negative and the downstream side being positive. The vertical axis represents the beam radius at position z . The beam radius is defined as the distance that is $1/e^2$ times the maximum beam intensity. All points are experimental data and curves are the result of fitting to experimental data. The experimental data are given as the average of the cross-section of the intensity distribution in the direction of horizontal polarization and in the direction of vertical polarization.

where n is the refractive index in a medium, λ is wave length of pump beam, ω_B is the minimum beam radius for light with a wavelength of 810[nm] and ω_R is the minimum beam radius for light with a wavelength of 405[nm] in our experiment. Plus, the 810[nm] laser beam emitted from FC2 and FC3 and the 405[nm] laser beam emitted from FC1 must create a beam waist at the center of the PPKTP simultaneously. If the distance from each FC to the center of the PPKTP and the beam radius to be realized are known, the focal length of the built-in collimation lens of the FCs is uniquely determined. In principle, this can be determined by ray tracing, but the FCs we used was not designed to measure the distance between the optical fibers and the collimation lens, so we had to prepare several collimation lenses with different focal lengths and repeat trial and error to find the optimum collimation lens. In the stage of actually emitting the beam from the FC2,3, optical components such as BPF and LPF should be included in the FCs. The radius of the beam is usually measured by a beam profiler. Care must be taken to ensure that the beam is perpendicular to the beam profiler. In other words, the optical axis of the laser beam emitted from the FCs is parallel to the optical table and the optical axis passes through the center of the collimation lens in the FCs before the laser beam radius is measured.

FIG. W.2 shows the results of the mode matching. The fitting function is given by

$$\omega(z) = \omega_0 \sqrt{1 + \alpha(z - z_0)^2}, \quad (\text{W.2})$$

where ω_0, α and z_0 are fitting parameters, α is corresponding to

$$\alpha = \frac{M^4}{z_R^2}. \quad (\text{W.3})$$

M^2 is called beam quality factor which means how ideal the beam represents a pledge to the basic Gaussian beam, z_R is Rayleigh length introduced in Eq. (V.16). FIG. W.2 shows that the minimum beam radius of the pump beam emitted from FC1 is roughly $90[\mu\text{m}]$, and the minimum beam radius of the beams emitted from FC2 and 3 is roughly $125[\mu\text{m}]$, so the conditions of Eq. (W.1) are satisfied. Plus, The PPKTP has the dimensions of $1[\text{mm}] \times 1[\text{mm}] \times 1[\text{cm}]$, so the full intensity of the pump light can be incident inside the PPKTP.

W.3 Fixing the position of the optical components and checking the photon pair generation

Before arranging the optical components that make up the experimental setup, it must be confirmed that the optical axes of the $405[\text{nm}]$ laser beam emitted from FC1 and the $810[\text{nm}]$ laser beams emitted from FC2,3 are parallel to the optical table and that the optical axis passes through the center of the collimation lens. After checking them, the FC should not be touched until all optical components are fixed (See Appendix Y for adjustment method). When FC1 is regarded as the upstream side and FC2,3 as the downstream side, the optical components, shown in FIG. 3.4, should be aligned from the upstream side.

The GT immediately after FC1 translates the optical axis slightly in the transverse direction, but even after the translation, there is no problem if the GT is fixed so that the transmitted light passes through the same transverse position at two different points. It is also important to check that the GT is fixed horizontally to the holder using a level gauge because the GT immediately after FC1 defines the direction of horizontal polarization of the pump beam.

Although the HWP hardly changes the optical axis of the transmitted light, care must be taken to ensure that the beam enters perpendicular to the HWP because of the incident angle dependence, as explained in Appendix O. Since the HWP hardly changes the optical axis of the transmitted light, it is difficult to fix the position of the HWP with reference to the transmitted light. Fix the beam so that it enters as perpendicularly as possible by visual measurement from the top of HWP. If it is necessary to fix the position strictly, it can be adjusted by using an IR viewer and looking at the surface reflected light of the HWP. The HWP1 and DHWP should be calibrated at this stage. See Appendix Y for specific configuration methods.

The position and angle of the DM is fixed so that the reflected light of the beam emitted from FC2 and the transmitted light of the pump beam emitted from FC1 have the same optical axis. At this time, GT and HWP2 should not be placed immediately after FC2 (See Appendix Y for a method to check whether the optical axes have the same optical axis). Although the use of an X stage simplifies adjustment, we did not use an X stage because it increases the overall height of the optical axis in the experimental setup.

When determining the angle of the DPBS, the reflected light should be referenced because the rate of change of the optical axis of the transmitted light is small in relation to the change of the angle of the DPBS, the accuracy of the adjustment will be poor. Therefore, the reflected light of the beam emitted from FC1 and the transmitted light of the beam emitted from FC3 should be referenced to fix the position of the DPBS so that their optical axes are aligned. At this time, GT and HWP2 should not be placed immediately after FC3. Since the actual DPBS is not a perfect cube, the optical axis of the transmitted light of the beam from FC1 may not be horizontal to the optical table, but this is not a concern here because the final adjustment is made by the two mirrors that make up the Sagnac interferometer.

Silver mirrors are used for the two mirrors that make up the Sagnac interferometer because high reflectivity is guaranteed for both pump light and down-converted photon pairs. First, the two mirrors are adjusted so that their reflective surfaces are perpendicular to the optical table. The condition to be achieved in the adjustment of the two metal mirrors is that the clockwise and counterclockwise optical paths are perfectly aligned. There is no need to place DHWP at this time (See Appendix Y for the adjustment method). The degree of congruence of the paths has a dominant influence on the final interferometric clarity.

Adjustment of the PPKTP position is done by eye. Fix the position so that the pump light coming from both the counterclockwise and clockwise paths enter the PPKTP simultaneously.

Normally, connecting FC2 and FC3 to two SPCM at this stage, photon pairs should be detectable. To determine whether photon pairs can be detected, one can observe the delay curve, as shown in FIG. 3.6. Since the photon pair generation efficiency of PPKTP highly depends on the temperature of the crystal, it is important to know which temperature setting will maximize the number of photon pair counts.

W.4 Fine tuning of the interferometer

This section describes how to do fine tuning of Sagnac interferometer to prepare for maximally entangled states. The 810[nm] light is injected from FC3 and the GT and HWP2 are fixed so that the optical axis passes through their center. Since the GT translates the optical axis, it is better to fix the GT as close as possible to the exit of FC3 to make it easier to detect photon pairs. The GT near FC3 and DPBS can be used to calibrate the two HWP2 in advance. After calibrating two HWP2, one should be transferred near FC2, and GT should be placed in the same manner in front of FC2. Plus, DHWP should also be placed in Sagnac interferometer such that DHWP transform H polarizations into V polarizations.

Adjust HWP1 so that the pump light becomes P polarization, connect FC2 and FC3 to two SPCMs respectively, and fine-tune FC2 and FC3 so that their respective single counts are maximized. At this time, the coincident counts should be increased along with the single counts. Be careful not to change the distance between the optical fiber and the collimation lens for the adjustment.

Fine adjustment of the two silver mirrors is needed to improve the agreement between the two optical paths in the Sagnac interferometer. As Figure of merit, the interferometer visibility is used, which is defined by

$$V := \frac{N(+; -) + N(-; +) - N(+; +) - N(-; -)}{N(+; -) + N(-; +) + N(+; +) + N(-; -)}, \quad (\text{W.4})$$

where + and – corresponds to the two measurement outcomes which consist of a measurement basis. $N(+; -)$ is the coincidence count such that SPCM1 detects the polarization corresponding to + and SPCM2 detects the polarization corresponding to – simultaneously. In this time, + is defined as corresponding to the P polarization state and – to the M polarization state because the photon pairs produced by PPKTP are in the H and V polarization states, the coherence can be most strongly measured by observing the visibility in the PM basis. After that, the angle of the two mirrors is moved slightly while measuring the interferometer visibility in PM basis. If the interferometer clarity value improves, the direction in which the mirrors were tilted is known to be correct. Once the adjustment of the two mirrors have been completed, the DHWP and HWP1 should also be fine-tuned because they will also affect the interferometer visibility.

Appendix X

Hanbury Brown-Twiss experiment

The Hanbury Brown-Twiss experiment demonstrated that light is a population of photons[77]. Strictly speaking, the experiments conducted by J. F. Clauser, P. Grangier, G. Roger and A. Aspect were conclusive evidence[78, 79]. Although It is possible to cite and explain the results of these researches, we will report the results of a similar experiment conducted in our laboratory. As shown in FIG. X.1, the experimental setup is quite simple. Light incident on the Non-polarization Beam Splitter (NPBS) enters FC1 with 50% and FC2 with 50%. The output to the PC is the counts output by each of SPCM1 and SPCM2 and their coincident counts. If a photon is split by the NPBS, then the coincidence count should be zero. Therefore, the ratio of single photon defined as

$$R_S := 1 - \frac{N_C}{N_1 + N_2 - N_C} \quad (\text{X.1})$$

should be zero. However, this equation does not take into account the case where a photon in a multiphoton state is detected by only one of the two detectors. The following sections report two results when weak coherent light is used as the light source and when photon pairs generated by SPDC are used as the light source.

X.1 Ratio of single photon with weak coherent light

First, we will explain how to prepare the weak coherent light of the light source. In preparation for using an attenuated laser source, the upper limit of the intensity of the source is estimated by calculation. The counting limit of the SPCM is approximately $10^6[1/s]$, so that the intensity limit calculated from the wavelength of the laser source to be used, 808 [nm], is given by

$$10^6 \times h\nu \approx 2.469 \times 10^{-13}[W]. \quad (\text{X.2})$$

The intensity of the laser light immediately after emission was 38.48[mW]. By passing this laser beam through four ND filters whose transmittance was measured beforehand, the intensity of the laser beam immediately after transmission through the ND filters can be estimated as

$$38.48 \times 10^{-3} \times 1.835 \times 10^{-12} = 7.061 \times 10^{-14}[W] \quad (\text{X.3})$$

This power is sufficiently smaller than the result for Eq. (X.2). To eliminate background effects, measurements shall be taken in both situations, with and without the laser switched on, and the counts with the laser switched on shall be subtracted from the counts without the laser switched on, and the result shall be used to calculate the anti-correlation parameter.

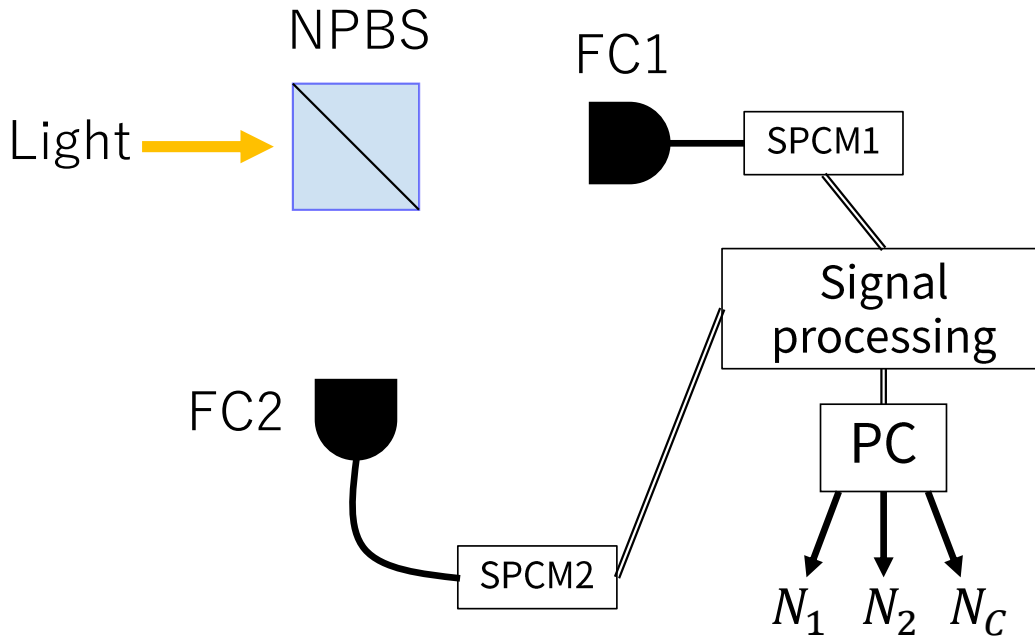


FIGURE X.1: Schematic of the experimental setup for evaluating the ratio of single photon; light incident on the NPBS enters FC1 with a 50% probability and FC2 with a 50% probability. What is done in signal processing is the same as what is described in Subsec. 3.1.1. $N_{1,2}$ are the number of photon counts measured in SPCM1,2, and N_C is the number of coincidence counts.

TABLE X.1: Experimental results with weak coherent light. The measurement time was 100 seconds, and measurements were taken both with and without the laser turned on.

Label of counts	Laser On[1/100s]	Laser Off[1/100s]
N_1	5882677	64397
N_2	5613249	756422
N_C	23240	506

TAB. X.1 shows the experimental results of them. The results shown in TAB. X.1 and Eq. (X.1) provides

$$R_S = 0.997866 \pm 0.000014. \quad (\text{X.4})$$

This result indicates that the weak coherent light is mostly a population of single photons.

X.2 Ratio of single photon with down-converted photons

Of the two photons produced by SPDC, one can be used as signal photon and the other as reference photon, so a high percentage of single photons is expected. As shown in FIG. X.2, when using SPDC photon pairs, one of the photons can be used as a reference photon, which significantly reduces background. N_1 represents the coincidence of SPCM1 and SPCM3, N_2 represents the coincidence of SPCM2 and SPCM3, and N_C represents the coincidence of N_1 and N_2 .

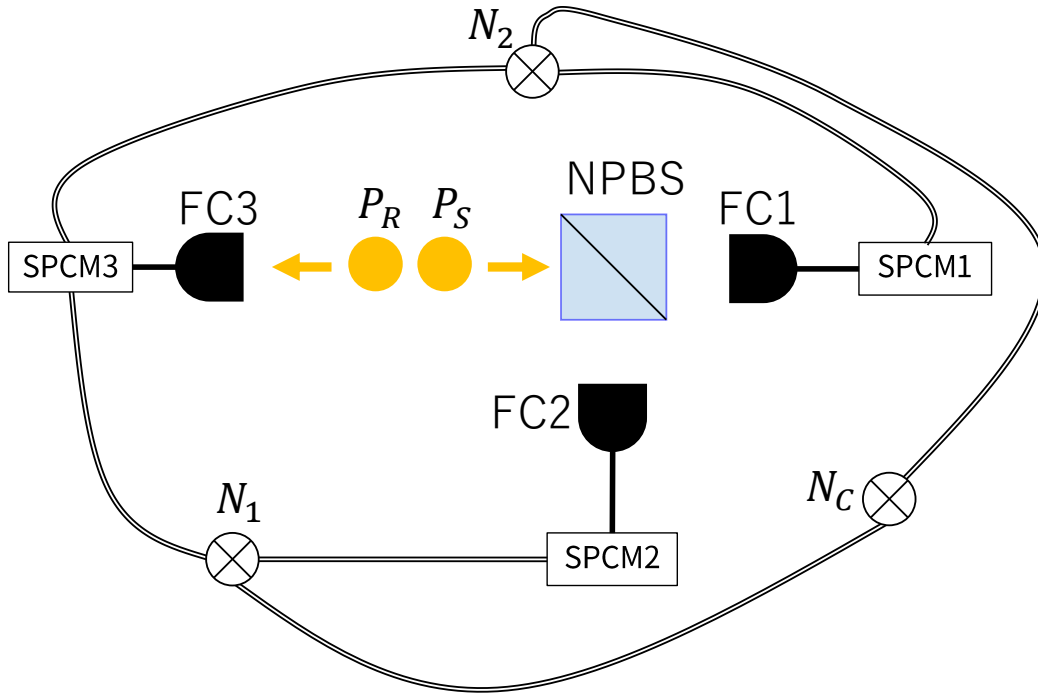


FIGURE X.2: Experimental setup for measuring the ratio of single photons using a down-converted photon pair as a source. The symbol \otimes means that the output is a coincidence counts. Thus, N_1 represents the coincidence of SPCM1 and SPCM3, N_2 represents the coincidence of SPCM2 and SPCM3, and N_C represents the coincidence of N_1 and N_2 . FC3 corresponds to FC2 in FIG. 3.4. Signal photon P_S uses photons incident on FC1 in FIG. 3.4. When detecting single photons, GT and HWP2 immediately before FC1 and FC2 in FIG. 3.4 were removed.

The results of the experiment are shown in TAB. X.2. This result and Eq. (X.1) provides

$$R_S = 0.99824 \pm 0.00007. \quad (\text{X.5})$$

The difference between Eq. (X.4) and Eq. (X.5) are less than 1%, however, the photon pairs produced by SPDC are guaranteed to be closer to single photons.

TABLE X.2: Experimental results with down-converted photons. The measurement time was 100 seconds.

Label of counts	Counts[1/100s]
N_1	186526
N_2	175904
N_C	656

Appendix Y

Technical know-how for the optical experiment

This appendix describes specific coordination techniques to achieve the physical conditions required for the experimental setup. The experimental setup is a set of numerous adjustments. Understanding what to look for and what to optimize will lead to a true understanding of the characteristics of the experimental setup.

Y.1 Adjustment of an optical axis

The optical axis is a hypothetical axis through the center of the beam. Proper adjustment of the optical axis is very important for accurate observation of photon interference phenomena. There are three tools used to adjust the optical axis. FIG. Y.1(a) measures the height of the optical axis from the optical table. By using this height ruler to measure the height of the optical axis at two different points, it is possible to determine whether the optical axis is parallel to the optical table. The two different points should be as far apart as possible to increase the accuracy of the measurement. FIG. Y.1(b) is used to measure the position of transverse direction of the optical axis. The distance between the two different screw holes on the optical table and the thickness of the rod are precisely defined, so the position of the ruler is highly reproducible. By placing this "torii" at two different points on the optical axis, it is possible to measure how much the optical axis has moved laterally. The third tool is a digital microscope. This is a tool used to accurately read the position of the optical axis reflected on a ruler. A digital microscope can magnify the surface of a ruler. In recent years, it could be replaced by a smartphone.

In sec. W.3, on the adjustment of DC, if the reflected light coming from FC2 and transmitted light coming from FC1 hit the same position on the two kinds of ruler at the different two points, it means that those two light have the same optical axis. There could be situations where there is no space for a "torii" or where it is not possible to install a "torii" at two different points. In such cases, the method of using two pinholes is useful. This is exactly the method used to align the two silver mirrors in the Sagnac interferometer. Two pinholes are placed on the input and output sides of the DPBS as shown in FIG. Y.2. The tilt of the two mirrors is adjusted so that the intensity of light transmitted through pinhole 1 is the same as the intensity of light transmitted through pinhole 2. Of course, the reflectance of the two silver mirrors is not 100%, so this must be taken into account. If the counterclockwise and clockwise optical paths are perfectly matched, the same situation should be realized for both the 405[nm] beam put in from FC1 and the 810[nm] beam from FC3.

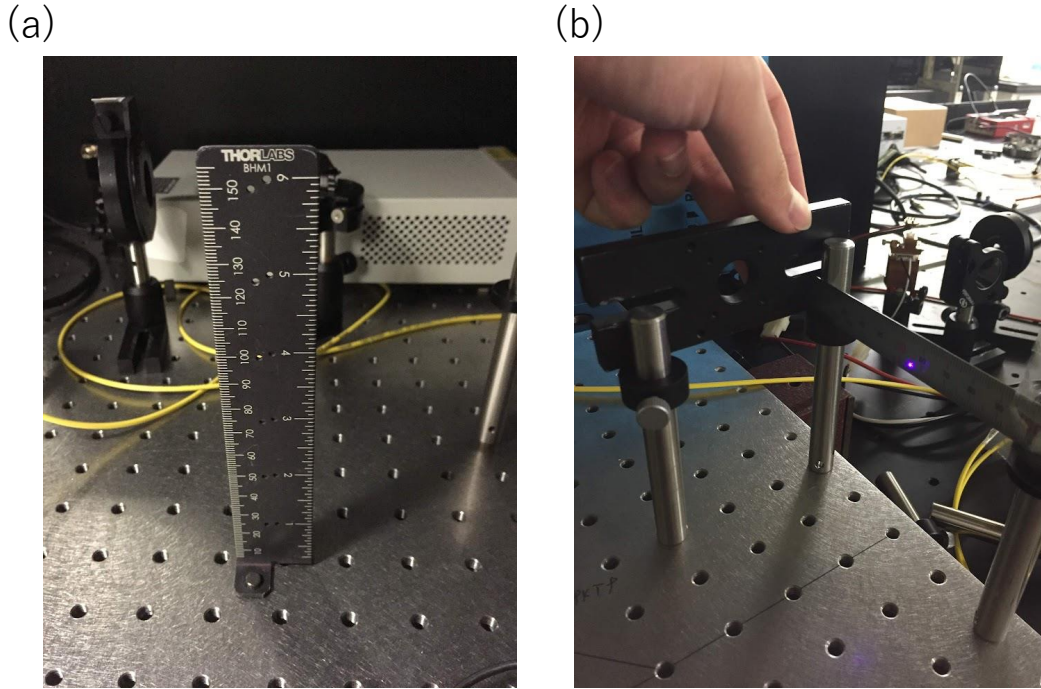


FIGURE Y.1: (a) Height ruler for an optical axis. (b) Transverse ruler for an optical axis.

Y.2 Calibration of a HWP

Calibration of a HWP requires two polarizing plates and a HWP. Polarizing plate can be substituted with PBS or GT. From the upstream side, the polarizing plate, HWP, and polarizing plate are placed in this order. It is useful to set the two polarizing plates in such an orientation that they transmit light of the same polarization. The orientation in which the HWP is installed must be defined so that it is uniquely determined. Since there is always a memory attached to the holder of the HWP, it is convenient to install the HWP so that the light enters the HWP from the opposite side of the side where the memory is written, so that counterclockwise is the positive direction of rotation. For accurate calibration, it is recommended to use an auto-rotating stage for the HWP holder and to select two polarizing plates with a high extinction ratio. Rotating the HWP while measuring the intensity of the beam behind the second polarizing plate will provide the data needed to calibrate. It is convenient for the calibration to use the fitting function given by

$$I = I_0(V \sin \theta - \theta_0 + 1), \quad (\text{Y.1})$$

where the fitting parameters are I_0 , V , and θ_0 , where A is the offset, V is the visibility, and θ_0 is the phase translation. The angle of maximal intensity means that the slow axis of the HWP is aligned with the direction of polarization of the two polarizing plates. It should be noted that the set angle and the angle of polarization realized by the HWP differ by a factor of 2.

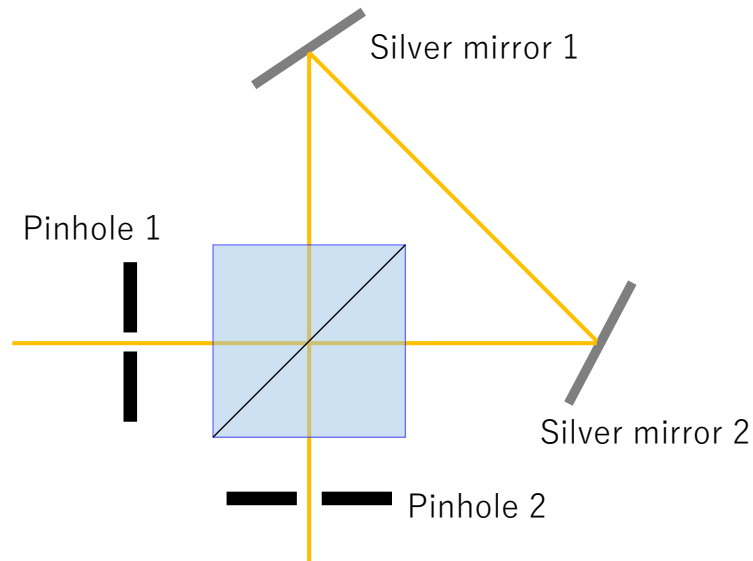


FIGURE Y.2: Schematic of optical axis adjustment using two pinholes in the Sagnac interferometer.

Y.3 Adjustment of a collimation lens

Usually, collimation lenses are used to create parallel beams, however this section describes a method to extend this application to achieve a Gaussian beam with the required longitudinal modes. If the distance between the exit of the optical fiber and the collimation lens can be measured, the focal length of the lens can be determined theoretically by ray tracing, but if it cannot be measured, it must be determined operationally. For the fundamental Gaussian beam, once the position of the beam waist and the minimum beam radius are determined, the propagation before and after the beam waist is uniquely determined. Another feature is that it is plane symmetric with respect to the cross-section at the position of the beam waist. This feature can be used to create a beam waist at a specific location. The height of the optical axis of the beam from the optical table and the lateral position of the beam can be achieved by using the method described in Sec. Y.1. The following procedure is used to optimize the adjustment of the longitudinal mode. Measure the beam radius at a location 5[cm] before and after the position of the beam waist. Adjust the distance between the edge of the optical fiber and the collimation lens so that the beam radii at the two points before and after the beam waist are the same. Once the two beam radii are the same, one can measure the beam radii at several other points and perform the fitting as explained in Sec. W.2.

Y.4 Measurement of polarization physical properties

This section gives tips for accurately measuring photon polarization physical properties. The measurement of polarization needs a polarizing plate or a combination of PBS and HWP. PBS can be replaced by a crystal polarizer using total reflection. The combination of HWP and a polarizing plate can also be used to measure polarization, but in this case the polarizing plate must not be rotated. Whichever method is used, the higher the extinction ratio, the better it is able to distinguish between different polarization.

The use of polarizing plate alone has the advantages of requiring less space and being effective for lasers with a wide spectral band of wavelengths, but it has the disadvantage

that the optical axis of the transmitted beam through the polarizing plate changes depending on the angle of the polarizing plate. Therefore, it is not recommended for use in setups where light propagating in free space is coupled with an optical fiber. The use of an HWP in combination with a polarizer has the advantage that the optical axis of the transmitted light hardly changes when the selected polarization is changed, but it has the disadvantage that it requires a relatively large space and is effective only for light at the design wavelength of the HWP. However, it requires a relatively large space and is effective only for light at the design wavelength of the HWP. In situations where light includes different bands of some wave length, it may be necessary to use a BPF to select necessary signal. When using a power meter as a measuring instrument, it is better to install the power meter some distance away from the polarizer. Scattered light generated inside the polarizer will be mixed into the power meter and can become background.

Appendix Z

Data analysis and rest

This section introduces the knowledge required for statistical analysis of experimental data and the applications/websites that are useful for research in general.

Z.1 Errors that experimental data includes

Z.1.1 Residuals, deviations and errors

The purpose of obtaining experimental data is to understand the true nature. However, experimental data are invariably subject to complex physical influences that we do not anticipate. This manifests itself numerically as error. We believe that the physical property associated with the object being measured has a true mean before conducting an experiment. This true mean can be determined by making exactly the same independent measurement an infinite number of times in exactly the same physical situation. This is called the central limit theorem. The central limit theorem is based on the two assumption; each measurement is independent and the random variables follow exactly the same distribution. Why do we need to make an infinite number of measurements? It is because the experimental data contain statistical errors. The cause of statistical error is the inherent fluctuation of nature. This fluctuation does not disappear even if the temperature of the system reaches absolute zero, and cannot be avoided in principle, but if the number of measurements is infinite, the error in the average value will disappear. In actual experiments, the number of measurements is finite, and the obtained average value is called the sample mean. The difference between the sample mean and the measurement outcome of each measurement is called the residual. When the number of measurements is infinite, the mean value is precisely called the population mean, and the difference between the population mean and the measurement outcome of each and every measurement is called the deviation. The reason why it is necessary to use different names for the true mean and the population mean is that there is an error called systematic error, which is different from statistical error. Systematic errors can have various causes, such as an unintentional error by the observer or unexpected physical effects. Systematic errors disrupt the assumption that random variables follow exactly the same distribution, so that the sample mean and the true mean no longer agree. The difference between the true value and the measurement outcome of each measurement is the error, which is the inherent meaning of "error". By the way, should we distinguish between the terms "true value" and "true mean"? Quantitatively, the true value and the true mean should be exactly the same number, but the biggest difference is that the true mean requires an infinite number of measurements, while the true value may be obtained by chance with a finite number of measurements. It is possible that if one were to make an infinite number of measurements, some of those measurements would have yielded measurement outcomes consistent with the true mean.

Z.1.2 Propagation of errors

The physical property we want to know is not always the value directly obtained experimentally. It is often expressed by a combination of several independent observables. For example, the volume of a rectangular body is expressed as the product of its length, width, and height. In general, all observable are functions of multiple directly obtainable physical properties as variables. Since directly observed physical properties always contain errors, it is important to consider how they relate to errors in physical properties expressed as functions. Let's first consider univariate functions and then extend to multivariate functions. Suppose that a physical property z is a function of a directly obtained property x , then

$$z = f(x), \quad (\text{Z.1})$$

where we assume that the function $f(x)$ is differentiable with respect to x any number of times. If x_i ($i = 1, 2, \dots, n$) is the result of n times measurements of x , then Eq. (Z.1) becomes

$$\begin{aligned} z_i &= f(x_i) \\ &= f(X_n + \Delta x_i) \\ &= f(X_n) + \Delta x_i d_x f(X_n) + \frac{\Delta x_i^2}{2} d_x^2 f(X_n) + \dots \end{aligned} \quad (\text{Z.2})$$

where X_n is the mean value of x , Δx is the deviation of x , and d_x is the differential operator with respect to x . Thus, the average value of z is given by

$$\begin{aligned} Z_n &= \frac{1}{n} \sum_{i=1}^n z_i \\ &= f(X_n) + \frac{\sigma_x^2}{2} d_x^2 f(X_n), \end{aligned} \quad (\text{Z.3})$$

where σ_x is the standard deviation of x . From Eq. (Z.2) and Eq. (Z.3), the variance becomes

$$\begin{aligned} \sigma_z^2 &= \frac{1}{n} \sum_{i=1}^n (z_i - Z_n)^2 \\ &\approx \sum_{i=1}^n \frac{\Delta x_i^2}{n} (d_x f(X_n))^2 \\ &= \sigma_x^2 (d_x f(X_n))^2, \end{aligned} \quad (\text{Z.4})$$

where in the first equality, it was assumed that $(d_x f(X_n))^2$ is much greater than the other terms.

Such an analysis can be easily extended to multivariate functions. If the physical property z is a function of the directly obtained physical properties $\alpha, \beta, \gamma, \dots$, then the variance of the physical property z is

$$\sigma_z^2 = \sigma_\alpha^2 (\partial_\alpha f(\alpha, \beta, r, \dots))^2 + \sigma_\beta^2 (\partial_\beta f(\alpha, \beta, r, \dots))^2 + \dots, \quad (\text{Z.5})$$

where *partial* denotes the partial derivative with respect to the subscript. This equation is called the error propagation formula.

Using error propagation formulas for actual experimental data may seem tedious, but

"Around" function in Mathematica deals with it easily. For example, assuming a rectangle with length, width, and height of 5[cm], 7[cm], and 10[cm], respectively, and that each side has a standard deviation of 5%, the standard deviation of the volume derived by error propagation Shown in Eq. (Z.5) can be calculated as shown in List. Z.1.

LISTING Z.1: Example of error propagation in volume

```

1 In [1] := Quantity[Around[5, 5*0.05], "Centimeters"]*
2 Quantity[Around[7, 7*0.05], "Centimeters"]*
3 Quantity[Around[10, 10*0.05], "Centimeters"]
4
5 Out [1] = (350. ± 30.)cm3

```

The calculation results show that the volume of the rectangle is 350[cm³] with a standard deviation of 30[cm³].

Z.2 Poisson distribution

There are three distributions that are particularly important for understanding the scatter of values of physical properties, and they are called the Bernoulli¹, Gaussian, and Poisson distributions. In this section, Poisson distribution, which is of greater relevance to experiments in which particles are measured, is explained.

If the probability of an event occurring during a certain time Δt is p , the probability of the event not occurring is $1 - p$. If some finite time T is divided into n equal parts, each interval corresponding to Δt , then the probability that an event will occur r times during time T is given by

$$P(r; n, p) = \frac{n!}{r!(n-r)!} p^r (1-p)^{n-r}, \quad (\text{Z.6})$$

where r is random variable, n, p are parameters. This distribution is called Bernoulli distribution. The argument so far has only one flaw. It does not take into account the possibility that the event may occur more than once during the interval Δt . To avoid having to consider this situation, it would be solved by assuming that the probability p of the event occurring is sufficiently small and n is sufficiently large. It should be possible to ignore the probability of the event occurring more than once during Δt . As can be seen from this situation, the probability p of the event occurring and the number of divisions n would be inversely proportional, which is given by

$$p = \frac{\lambda}{n}, \quad (\text{Z.7})$$

where λ is the proportionality coefficient. Assuming that n is sufficiently large, Eq. (Z.6) can be transformed as

$$\begin{aligned}
\log P(t; n, p) &= r \log \frac{p}{1-p} + n \log (1-p) + \log n! - \log (n-r)! - \log r! \\
&\approx r \log \lambda - t \log \left[1 - \frac{\lambda}{n} \right] - n \log \left[1 - \frac{r}{n} \right] - r + r \log \left[1 - \frac{r}{n} \right] \\
&+ n \log \left[1 - \frac{\lambda}{n} \right] - \frac{1}{2} \log \left[1 - \frac{r}{n} \right] - \log r!
\end{aligned} \quad (\text{Z.8})$$

¹Also called binomial distribution

Here, Stirling's approximation was used, the approximation is given by

$$n! \approx \sqrt{2\pi n} \left(\frac{n}{e}\right)^n. \quad (\text{Z.9})$$

If we expand the logarithmic function around λ/n or r/n and take the limit of $n \rightarrow \infty$, the equation ends up with

$$\begin{aligned} \lim_{n \rightarrow \infty} P(r; n, p) &\rightarrow \log P(r; \lambda) \\ &= -\lambda + r \log \lambda - \log r! \\ P(r; \lambda) &= \frac{\lambda^r e^{-\lambda}}{r!}. \end{aligned} \quad (\text{Z.10})$$

As is well known, both the mean and variance of the Poisson distribution are λ as shown in

$$\langle r \rangle = \sum_{r=0}^{\infty} r P(r; \lambda) = \lambda \quad (\text{Z.11})$$

$$\sigma_r^2 = \sum_{r=0}^{\infty} (r - \langle r \rangle)^2 P(r; \lambda) = \lambda. \quad (\text{Z.12})$$

Finally, let us list the differences between the Poisson and Gaussian distributions.

1. The random variables of the Poisson distribution are non-negative integers, while those of the Gaussian distribution are real numbers. Therefore, the Poisson distribution is discrete, while the Gaussian distribution is continuous.
2. With respect to the mean value, the Poisson distribution is asymmetric, while the Gaussian distribution is symmetric. The Poisson distribution can be considered symmetric as the value of λ increases.
3. Poisson distribution has only one parameter λ , and once λ is determined, the shape of the distribution is determined.

Z.3 Frequently used functions and knowledge of Mathematica to analysis the experimental data

In this section, we present some features of Mathematica and tidbits that we frequently used to analyze experimental data. Let's divide it into subsections according to the type of object to be analyzed. First, as it pertains to notebook editing in general, the following is a list of frequently used shortcut keys.

- "Alt" + Number key : Change to a different format depending on the number key. The number keys used in particular are 1, 2, 7 and 9. 1 and 2 were used to indicate a break in the analysis, 7 was used to enter long sentences, and 9 was used to return to the normal input format.
- "Alt" + "/" : Selected sections and letters can be commented out. It is also possible to comment out multiple selected cells on the right, and the same shortcut key can be used to undo the comment out.
- "Ctrl" + "2" : Enter the square root.
- "Ctrl" + "6" : Enter superscripts or exponents.

- "Ctrl" + "-" : Enter subscripts.
- "Ctrl" + "/" : Enter fractions

Z.3.1 Analytical calculations

This subsection presents frequently used shortcut keys, functions and useful knowledge for analytical calculations.

- FullSimplify [] : A well-known and useful function that also allows you to add conditions to variables, as shown in List. Z.2. The shortcut key to enter \in is "Esc" + "elem" + "Esc".
- N[Expr] : Give the numerical value of "Expr".
- D[Expr] : Differentiate "Expr".
- Series[Expr] : Series expansion of "Expr".
- NonlinearModelFit[], FindFit[] : Both are functions for fitting to data, but former gives detailed statistical information such as residuals and confidence intervals for the population, but may not allow for fitting. FindFit[], on the other hand, does not compute detailed information, but allows for simple fitting. List. Z.3 shows an example of fitting for the calibration of HWP.
- Solve[Equa] : Solve the equation "Equa".
- Manipulate[] : Variables inside [] can be moved within a specified range. It can be used for both analytical calculations and graphics.

LISTING Z.2: Conditional calculation using FullSimplify function

```

1 In[1]:= FullSimplify[(a + I*b)*Conjugate[(a - I*b)]]
2
3 Out[1]= (a + I b) (Conjugate[a] + I Conjugate[b])
4
5 In[2]:= FullSimplify[(a + I*b)*
6 Conjugate[(a - I*b)], {a, b} ∈ Reals]
7
8 Out[2]= (a + I b)^2

```

LISTING Z.3: Example of fitting for the calibration of HWP

```

1 Define a list of angles.
2
3 In[1]:= angle = Table[10*a, {a, 0, 19, 1}]
4
5 Out[1]= {0, 10, 20, 30, 40, 50, 60, 70, 80, 90, 100, 110, 120,
6 130, 140, 150, 160, \
7 170, 180, 190}
8
9 Next, the intensity for the set angle of HWPO is transferred from
10 the experimental notes.
11
12 In[2]:= HWP0power = {10.05, 7.748, 4.196, 1.184, 0.04935, 1.389,
13 4.581, 8.025, 10.23,
14 10.08, 7.682, 4.153, 1.131, 0.05146, 1.3930, 4.54, 8.044,
15 10.16, 9.9};

```

```

12
13 Create a list of errors for each strength value
14
15 In[2]:= HWP0err = {0.002, 0.0006, 0.0008, 0.0002, 0.00004,
16             0.00007, 0.000008, 0.0012,
17             0.002, 0.0008, 0.0012, 0.0004, 0.0003, 0.00003, 0.0002, 0.002,
18             0.001,
19             0.001, 0.003};
20
21 Next, define the list for fitting.
22
23 In[3]:= HWP0list = Table[{angle[[i]], HWP0power[[i]]}, {i, 1,
24             19}]
25
26 Out[3]= {{0, 10.05}, {10, 7.748}, {20, 4.196}, {30, 1.184}, {40,
27             0.04935}, {50,
28             1.389}, {60, 4.581}, {70, 8.025}, {80, 10.23}, {90, 10.08},
29             {100,
30             7.682}, {110, 4.153}, {120, 1.131}, {130, 0.05146}, {140,
31             1.393}, {150,
32             4.54}, {160, 8.044}, {170, 10.16}, {180, 9.9}}
33
34 Define the fitting function.
35
36 In[4]:= model = p1*Sin[p2 ( $\theta$  - p3) Degree] + p4;
37
38 Create a list of weights first for fitting
39
40 In[5]:= weight = Table[1/HWP0err[[i]]^2, {i, 1, 19}]
41
42 Out[5]= {250000., 2.77778*10^6, 1.5625*10^6, 2.5*10^7, 6.25*10^8,
43             2.04082*10^8,
44             1.5625*10^10, 694444., 250000., 1.5625*10^6, 694444., 6.25*10^6,
45             1.11111*10^7, 1.11111*10^9, 2.5*10^7, 250000., 1.*10^6, 1.*10^6,
46             111111.}
47
48 The Manipulate function is used to find out how the initial
49 values of parameters should be defined.
50
51 In[6]:= Manipulate[
52 Show[ListPlot[HWP0list, Frame -> True, GridLines -> Automatic],
53 Plot[p1*Sin[p2 ( $\theta$  - p3) Degree] + p4, { $\theta$ , 0, 180}]], {p1, 0,
54 10, 0.1}, {p2, 0, 5, 0.1}, {p3, 0, 180, 1}, {p4, 0, 10, 0.1}]
55
56 Out[6]= Manipulate[Show[ListPlot[HWP0list, Frame -> True,
57 GridLines -> Automatic],
58 Plot[p1*Sin[(p2*( $\theta$  - p3))*Degree] + p4, { $\theta$ , 0, 180}]], {p1, \
59 0, 10, 0.1},
60 {p2, 0, 5, 0.1}, {p3, 0, 180, 1}, {p4, 0, 10, 0.1}]
61
62 The results of the Manipulate function above give some idea of
63 the range of parameters.
64
65 In[7]:= nlm = NonlinearModelFit[
66 HWP0list, {model, {5 < p1 < 5.5, 3.9 < p2 < 4.1, 55 < p3 < 65,
67 5 < p4 < 6}}, {p1, p2, p3, p4},  $\theta$ , Weights -> weight];
68
69

```

```

58 The fitting parameters obtained are as follows
59
60 In[8]:= fit = nlm["BestFitParameters"]
61
62 Out[8]= {p1 -> 5.25468, p2 -> 4.003, p3 -> 61.9668, p4 ->
        5.30063}
63
64 Parameter errors are as follows
65
66 In[9]:= nlm["ParameterTable"]
67
68 Out[9]= \!\(\(*
69 StyleBox[
70 TagBox[GridBox[{
71 {"\<\>", "\<\>Estimate\>", "\<\>Standard Error\>", \
72 "\<\>t-Statistic\>", "\<\>P-Value\>"},
73 {"p1", "5.25467850531482'", "0.009588899897451238'", "
        547.9959704982979'",
74 "1.110535298910244'*^-33"},
75 {"p2", "4.003001501108563'", "0.0027187195848814008'", "
        1472.3848400434376'",
76 "4.045802678183333'*^-40"},
77 {"p3", "61.96678501614212'", "0.023395305312575537'", "
        2648.6846052328924'",
78 "6.0518158219651'*^-44"},
79 {"p4", "5.300634167764399'", "0.009781093711607288'", "
        541.9265292872209'",
80 "1.3124513583315877'*^-33"}
81 },
82 AutoDelete->False,
83 GridBoxAlignment->{"Columns" -> {{Left}}, "Rows" -> {{Automatic
        }}},
84 GridBoxDividers->{"ColumnsIndexed" -> {2 -> GrayLevel[0.7]},
85 "RowsIndexed" -> {2 -> GrayLevel[0.7]}},
86 GridBoxItemSize->{"Columns" -> {{Automatic}}, "Rows" -> {{
        Automatic}}},
87 GridBoxSpacings->{"ColumnsIndexed" -> {2 -> 1}, "RowsIndexed" ->
        {2 -> 0.75}}],
88 "Grid", "DialogStyle",
89 StripOnInput->False]\)
90
91 In[10]:= 5.300634167764399' +
92 5.25467850531482' Sin[0.06986555615661987' (-61.96678501614212'
        +  $\theta$ )]
93
94 Out[10]= 5.30063 + 5.25468 Sin[0.0698656 (-61.9668 +  $\theta$ )]
95
96 Find out at what setting angle the desired polarization state can
        be obtained.
97
98 In[11]:= Solve[0.06986555615661987' (-61.96678501614212' +  $\theta$ ) ==
        +1  $\pi/2$ ]
99
100 Out[11]= {{ $\theta$  -> 84.4499}}
101
102 At this angle, it means that the Slow axis is oriented in the
        direction of H polarization.

```

```

103
104 In [12]:= Solve[0.06986555615661987' (-61.96678501614212' +  $\theta$ ) ==
      +3  $\pi/2$ ]
105
106 Out [12]= {{ $\theta$  -> 129.416}}
107
108 At this angle, the Slow axis is oriented toward D polarization.
109
110 In [13]:= N[(129.4161726631935' + 84.4499142318259')/2]
111
112 Out [13]= 106.933
113
114 At this angle, the Slow axis is halfway between H and D
      polarization.
115
116 In [14]:= Solve[0.06986555615661987' (-61.96678501614212' +  $\theta$ ) ==
      +5  $\pi/2$ ]
117
118 Out [14]= {{ $\theta$  -> 174.382}}
119
120 In [15]:= N[(129.4161726631935' + 174.38243109456107')/2]
121
122 Out [15]= 151.899
123
124 At this angle, the Slow axis is halfway between VD and V
      polarization.

```

Z.3.2 Algebraic calculations

This subsection presents frequently used shortcut keys, functions and useful knowledge for algebraic calculations.

- "Ctrl" + "Enter" : Add a row. After entering the parentheses and bringing the cursor inside them, this shortcut key can be used to enter a two-dimensional column vector.
- "Ctrl" + "," : Add a column. After entering the parentheses and bringing the cursor inside them, this shortcut key can be used to enter a two-dimensional row vector.
- "Esc" + "c" + "*" + "Esc" : Enter the symbol for Kronecker product. Since the symbol for Kronecker product alone does not function as a Kronecker product, it is best to define the symbol as follows. "a_ \otimes b_:=KroneckerProduct[a,b]". One example is shown in List. [Z.4](#)
- Transpose[M] : Gives the transpose matrix of the matrix M. It can also transform row vectors and column vectors.
- ConjugateTranspose[M] : Gives the conjugate transpose matrix of the matrix M.
- Eigenvalues[M] : Gives the eigenvalues of the square matrix M.
- Eigenvectors[M] : Gives a list of eigenvectors of a square matrix M.
- Tr[L] : Give the trace of a matrix or tensor list.
- Det[M] : Give the determinant of the square matrix M.

- Flatten[T] : Make the tensor T a one-dimensional vector.
- Partition[] : Split elements in a list into multiple sub-lists.
- Length[L] : Give the number of elements in list L .
- Table[Rule] : Give a list according to certain rules.

LISTING Z.4: Example of Kronecker product

```

1 In[1]:= a_⊗ b_ := KroneckerProduct[a, b]
2 MatrixForm[ $\begin{pmatrix} 1 & 0 \\ 0 & -1 \end{pmatrix} \otimes \begin{pmatrix} 0 & 1 \\ 1 & 0 \end{pmatrix}$ ]
3
4 Out[1]//MatrixForm=
5  $\begin{pmatrix} 0 & 1 & 0 & 0 \\ 1 & 0 & 0 & 0 \\ 0 & 0 & 0 & -1 \\ 0 & 0 & -1 & 0 \end{pmatrix}$ 

```

Z.3.3 Illustration of tables and graphs

This subsection presents functions that were frequently used when creating graphs.

- Plot[] : Function used to graph theoretical equations. List. Z.5 is the code that was entered when outputting FIG. C.2.
- ListPlot[] : Function used primarily to graph experimental data.
- Graphics3D[] : Function used to create 3D graphics, where List. Z.6 is the input code to obtain FIG. 4.4.
- Manipulate[] : Introduced in Subsec. Z.3.1, this function is used when you want to vary parameters while viewing a graph.
- Plot3D[] : This function is used when you want to see how a bivariate function changes. List. Z.7 is an example.

LISTING Z.5: Input code to get FIG. C.2

```

1 Show[Plot[1, {θ, 0, π/6}, Frame -> True,
2 FrameStyle -> Directive[Black, Bold, 16],
3 FrameLabel -> {"θ", "E(θ)"},
4 PlotRange -> {{0, π + 0.1}, {-1.1, 1.1}},
5 Epilog -> {Black, Dashed, Line[{{π/6, 0}, {π/6, 1}}],
6 Black, Dashed, Line[{{π/4, 0}, {π/4, -1}}],
7 Black, Dashed, Line[{{π/3, 0}, {π/3, -1}}],
8 Black, Dashed, Line[{{(2 π)/3, 0}, {(2 π)/3, 1}}],
9 Black, Dashed, Line[{{(3 π)/4, 0}, {(3 π)/4, 1}}],
10 Black, Dashed, Line[{{(5 π)/6, 0}, {(5 π)/6,
-1}}]}],
11 Plot[(-1 - 1)/(π/4 - π/6) (θ - π/6) +
12 1, {θ, π/6, π/4}],
13 Plot[-1, {θ, π/4, π/3}],
14 Plot[(1 + 1)/((2 π)/3 - π/3) (θ - (2 π)/3) +
15 1, {θ, π/3, (2 π)/3}],
16 Plot[1, {θ, (2 π)/3, (3 π)/4}],

```

```

17 Plot[(-1 - 1)/((5 π)/6 - (3 π)/4) (θ - (3 π)/4) +
18 1, {θ, (3 π)/4, (5 π)/6}],
19 Plot[-1, {θ, (5 π)/6, π}]

```

LISTING Z.6: Input code to get FIG. 4.4

```

1  jointraw = {{{9850, 10064, 60444, 60540}, {10101, 10146, 60977,
2  61003}, {58608, 58662, 10380, 10277}, {58637, 58553, 10399,
3  10391}}, {{9965, 18996, 51685, 61401}, {3461, 9824, 62244,
4  67861}, {65233, 59868, 9948, 3692}, {58803, 49972, 19977,
5  10438}}, {{10204, 30914, 40239, 61936}, {745, 10280, 61836,
6  71854}, {68780, 59444, 10366, 878}, {59168, 38590, 32255,
7  10863}}, {{9909, 42681, 28316, 63076}, {2147, 10353, 62096,
8  71901}, {67385, 60101, 10028, 2198}, {59566, 27170, 43509,
9  10787}}, {{10228, 54292, 17255, 62126}, {7318, 11089, 62893,
10 67235}, {62552, 59623, 10159, 7015}, {59489, 15787, 55548,
11 11615}}, {{10822, 59071, 12350, 60926}, {11039, 10422, 61610,
12 61017}, {59539, 59761, 10001, 11242}, {58932, 11627, 58160,
13 10658}}, {{9689, 61277, 8218, 60337}, {15970, 10380, 61445,
14 55728}, {52558, 58280, 9918, 15741}, {58524, 7745, 61340,
15 10706}}, {{10028, 67052, 2729, 59680}, {27475, 11414, 60841,
16 45665}, {42702, 58382, 10012, 25765}, {60357, 2286, 68914,
17 11903}}, {{9133, 66314, 1140, 58864}, {38520, 11200, 59769,
18 33036}, {28456, 56836, 9189, 37430}, {57940, 1448, 67816,
19 11331}}, {{9541, 64078, 3416, 57526}, {48724, 11453, 58856,
20 21336}, {18266, 56498, 9368, 47904}, {57707, 4460, 65092,
21 11630}}, {{9204, 57982, 9588, 57595}, {58521, 11220, 58268,
22 10862}, {9419, 57580, 9620, 57425}, {58333, 10987, 58205,
23 10822}}};
24 G1 = Manipulate[
25 Graphics3D[{{Green,
26 Cuboid[{0, 0, 0}, {1, 1, 1/30000*jointraw[[i, 4, 1]]}], {Orange,
27 Cuboid[{2, 0, 0}, {3, 1, 1/30000*jointraw[[i, 4, 2]]}], {Green,
28 Cuboid[{4, 0, 0}, {5, 1, 1/30000*jointraw[[i, 4, 3]]}]}, {
29 Orange,
30 Cuboid[{6, 0, 0}, {7, 1, 1/30000*jointraw[[i, 4, 4]]}], {Green,
31 Cuboid[{0, 2, 0}, {1, 3, 1/30000*jointraw[[i, 3, 1]]}], {Green,
32 Cuboid[{2, 2, 0}, {3, 3, 1/30000*jointraw[[i, 3, 2]]}], {Orange,
33 Cuboid[{4, 2, 0}, {5, 3, 1/30000*jointraw[[i, 3, 3]]}], {Orange,
34 Cuboid[{6, 2, 0}, {7, 3, 1/30000*jointraw[[i, 3, 4]]}], {Orange,
35 Cuboid[{0, 4, 0}, {1, 5, 1/30000*jointraw[[i, 2, 1]]}], {Orange,
36 Cuboid[{2, 4, 0}, {3, 5, 1/30000*jointraw[[i, 2, 2]]}], {Green,
37 Cuboid[{4, 4, 0}, {5, 5, 1/30000*jointraw[[i, 2, 3]]}], {Green,
38 Cuboid[{6, 4, 0}, {7, 5, 1/30000*jointraw[[i, 2, 4]]}], {Orange,
39 Cuboid[{0, 6, 0}, {1, 7, 1/30000*jointraw[[i, 1, 1]]}], {Green,
40 Cuboid[{2, 6, 0}, {3, 7, 1/30000*jointraw[[i, 1, 2]]}], {Orange,
41 Cuboid[{4, 6, 0}, {5, 7, 1/30000*jointraw[[i, 1, 3]]}], {Green,
42 Cuboid[{6, 6, 0}, {7, 7, 1/30000*jointraw[[i, 1, 4]]}], {Black,
43 Opacity[0.5], InfinitePlane[{{0, 0, 0}, {1, 0, 0}, {0, 1, 0}}]},
44 Inset[Grid[jointraw[[i]], Frame -> All,
45 Background -> {None,
46 None, {{1, 1} -> Orange, {1, 2} -> Green, {2, 1} -> Orange,
47 {2, 3} ->
48 Green, {3, 2} -> Green, {3, 4} -> Orange, {4, 3} -> Green,
49 {4, 4} ->
50 Orange, {1, 3} -> Orange, {1, 4} -> Green, {2, 2} ->
51 Orange, {2, 4} -> Green, {3, 1} -> Green, {3, 3} ->

```

```

49      Orange, {4, 1} -> Green, {4, 2} -> Orange}},
50  ItemStyle -> {Automatic,
51      Automatic, {{1, 1} -> Directive[Bold, FontSize -> 16], {1, 2}
      ->
52      Directive[Bold, FontSize -> 16], {2, 1} ->
53      Directive[Bold, FontSize -> 16], {2, 3} ->
54      Directive[Bold, FontSize -> 16], {3, 2} ->
55      Directive[Bold, FontSize -> 16], {3, 4} ->
56      Directive[Bold, FontSize -> 16], {4, 3} ->
57      Directive[Bold, FontSize -> 16], {4, 4} ->
58      Directive[Bold, FontSize -> 16], {1, 3} ->
59      Directive[Bold, FontSize -> 16], {1, 4} ->
60      Directive[Bold, FontSize -> 16], {2, 2} ->
61      Directive[Bold, FontSize -> 16], {2, 4} ->
62      Directive[Bold, FontSize -> 16], {3, 1} ->
63      Directive[Bold, FontSize -> 16], {3, 3} ->
64      Directive[Bold, FontSize -> 16], {4, 1} ->
65      Directive[Bold, FontSize -> 16], {4, 2} ->
66      Directive[Bold, FontSize -> 16]}}], {3, 0, -5}], Boxed ->
      False,
67 PlotRange -> {{0, 7}, {0, 7}, {-5, 5}}, {i, 1, 11, 1}]

```

LISTING Z.7: Example to use Plot3D function

```

1  Manipulate[
2  Plot3D[1/(2 π*σx*σy) E^(-(x^2/(2 σx)))*
3  E^(-(y^2/(2 σy))), {x, -10, 10}, {y, -10, 10},
4  AxesLabel -> {"x", "y", "P(x,y;σx,σy)"},
5  AxesStyle -> Directive[Black, Bold, 16],
6  ColorFunction -> Function[{x, y, z}, Hue[.65 (1 - z)]],
7  PlotRange -> {{-5, 5}, {-5, 5}, {0, 0.15}}, {σx, 1, 10,
8  1}, {σy, 1, 10, 1}]

```

Z.3.4 Useful websites, applications and tools

In this subsection, websites, apps, and tools that have been helpful in overall research activities will be presented.

- Visual Studio Code (VS code) : Editor for programming and writing LaTeX. In recent years, Overleaf (<https://www.overleaf.com/>), which enables writing LaTeX in the cloud, has become popular, but the advantages of using a local editor are its multi-cursor feature, and although it is rarely a problem these days, it is convenient to be able to program and write LaTeX even in no Internet environment.
- Blender : If you know how to use it, you can not only create beautiful 3D graphics, but also perform simple physics simulations. It is also possible to create beautiful optical illustrations.
- Google Scholar (<https://scholar.google.com/>) : Tools to search for references. By entering the title of an article, you can obtain Citation. Naturally, work must be done to verify that the output results are correct.
- Whiteboard Fox (<https://r9.whiteboardfox.com/>) : Online whiteboards are easy for anyone to use. You can discuss with colleagues in remote locations while talking on the phone. Multiple people can write on it at the same time, and the written content can be saved as an image.

- SPDCalc (<https://spdcalc.org/>) : Various simulations related to SPDC can be performed.
- MyScript (<https://webdemo.myscript.com/>) : Mathematical expressions written on the screen can be output in LaTeX or MathML format, which is useful for writing in LaTeX or creating documents using Microsoft Word, as it allows you to quickly write mathematical expressions. If the PC you are using does not support a touch screen, you can purchase an external pen tablets to easily write mathematical expressions on the screen.
- DeepL (<https://www.deepl.com/en/translator>) : A translation site that is said to have the highest translation accuracy.
- Irasutoya (<https://www.irasutoya.com/>) : If certain rules are adhered to, illustrations may be used free of charge. This was useful when creating presentation slides. It is quite famous in Japan.
- ChatGPT (<https://chat.openai.com/auth/login>) : A website that answers all kinds of questions. Of course, it is dangerous to believe the output as it is. You can use the website in various ways, such as regarding them as a discussion partner, or asking for references related to the keywords you want to look up.
- Bluetooth and Wireless Keyboards : This is useful when typing quickly on a smartphone or tablet device. With Overleaf, you can edit LaTeX from a tablet device, and with MyScript, you will have no trouble entering mathematical expressions.
- Quick Access Toolbar : The Quick Access Toolbar is one of the features in Microsoft Office products. It is useful when creating slides for a presentation because it eliminates the need to switch between different tabs.
- Multi Button Mouse : Assigning a variety of shortcut keys to many buttons increases the efficiency of desk work.
- Custom Office Templates : You can create templates for your own use in Word and PowerPoint. This is convenient because it eliminates the need to change the settings of every document and slide.

Reference

1. Einstein, A., Podolsky, B. & Rosen, N. Can Quantum-Mechanical Description of Physical Reality Be Considered Complete? *Phys. Rev.* **47**, 777–780 (10 1935) (cit. on pp. **1**, **79**).
2. Bohm, D. & Aharonov, Y. Discussion of Experimental Proof for the Paradox of Einstein, Rosen, and Podolsky. *Phys. Rev.* **108**, 1070–1076 (4 1957) (cit. on p. **1**).
3. Bell, J. S. On the Einstein Podolsky Rosen paradox. *Physics Physique Fizika* **1**, 195–200 (3 1964) (cit. on pp. **1**, **109**).
4. De Broglie, L. *An introduction to the study of wave mechanics* in () (cit. on p. **1**).
5. Bohm, D. A Suggested Interpretation of the Quantum Theory in Terms of "Hidden" Variables. I. *Phys. Rev.* **85**, 166–179 (2 1952) (cit. on p. **1**).
6. Bohm, D. A Suggested Interpretation of the Quantum Theory in Terms of "Hidden" Variables. II. *Phys. Rev.* **85**, 180–193 (2 1952) (cit. on p. **1**).
7. Clauser, J. F., Horne, M. A., Shimony, A. & Holt, R. A. Proposed Experiment to Test Local Hidden-Variable Theories. *Phys. Rev. Lett.* **23**, 880–884 (15 1969) (cit. on pp. **1**, **109**).
8. Freedman, S. J. & Clauser, J. F. Experimental Test of Local Hidden-Variable Theories. *Phys. Rev. Lett.* **28**, 938–941 (14 1972) (cit. on p. **1**).
9. Aspect, A., Grangier, P. & Roger, G. Experimental Tests of Realistic Local Theories via Bell's Theorem. *Phys. Rev. Lett.* **47**, 460–463 (7 1981) (cit. on p. **1**).
10. Aspect, A., Dalibard, J. & Roger, G. Experimental Test of Bell's Inequalities Using Time-Varying Analyzers. *Phys. Rev. Lett.* **49**, 1804–1807 (25 1982) (cit. on p. **1**).
11. Aspect, A., Grangier, P. & Roger, G. Experimental Realization of Einstein-Podolsky-Rosen-Bohm Gedankenexperiment: A New Violation of Bell's Inequalities. *Phys. Rev. Lett.* **49**, 91–94 (2 1982) (cit. on p. **2**).
12. Ou, Z. & Mandel, L. Violation of Bell's inequality and classical probability in a two-photon correlation experiment. *Phys. Rev. Lett.* **61**, 50 (1988) (cit. on p. **2**).
13. Weihs, G., Jennewein, T., Simon, C., Weinfurter, H. & Zeilinger, A. Violation of Bell's Inequality under Strict Einstein Locality Conditions. *Phys. Rev. Lett.* **81**, 5039–5043 (23 1998) (cit. on p. **2**).
14. Takesue, H. & Inoue, K. Generation of polarization-entangled photon pairs and violation of Bell's inequality using spontaneous four-wave mixing in a fiber loop. *Physical Review A* **70**, 031802 (2004) (cit. on p. **2**).
15. Sakai, H, Saito, T, Ikeda, T, *et al.* Spin correlations of strongly interacting massive fermion pairs as a test of Bell's inequality. *Physical review letters* **97**, 150405 (2006) (cit. on p. **2**).
16. Ansmann, M., Wang, H, Bialczak, R. C., *et al.* Violation of Bell's inequality in Josephson phase qubits. *Nature* **461**, 504–506 (2009) (cit. on p. **2**).

17. Kuroda, T., Mano, T., Ha, N., *et al.* Symmetric quantum dots as efficient sources of highly entangled photons: Violation of Bell's inequality without spectral and temporal filtering. *Physical Review B* **88**, 041306 (2013) (cit. on p. 2).
18. Hensen, B., Bernien, H., Dréau, A. E., *et al.* Loophole-free Bell inequality violation using electron spins separated by 1.3 kilometres. *Nature* **526**, 682–686 (2015) (cit. on pp. 2, 4).
19. Ballance, C., Schäfer, V., Home, J. P., *et al.* Hybrid quantum logic and a test of Bell's inequality using two different atomic isotopes. *Nature* **528**, 384–386 (2015) (cit. on p. 2).
20. Giustina, M., Versteegh, M. A., Wengerowsky, S., *et al.* Significant-loophole-free test of Bell's theorem with entangled photons. *Phys. Rev. Lett.* **115**, 250401 (2015) (cit. on pp. 2, 4).
21. Shalm, L. K., Meyer-Scott, E., Christensen, B. G., *et al.* Strong loophole-free test of local realism. *Phys. Rev. Lett.* **115**, 250402 (2015) (cit. on pp. 2, 4).
22. Hensen, B., Kalb, N., Blok, M., *et al.* Loophole-free Bell test using electron spins in diamond: second experiment and additional analysis. *Sci. Rep* **6**, 30289 (2016) (cit. on pp. 2, 4).
23. Kofler, J., Giustina, M., Larsson, J.-Å. & Mitchell, M. W. Requirements for a loophole-free photonic Bell test using imperfect setting generators. *Phys. Rev. A* **93**, 032115 (2016) (cit. on pp. 2, 4).
24. Dehollain, J. P., Simmons, S., Muhonen, J. T., *et al.* Bell's inequality violation with spins in silicon. *Nature nanotechnology* **11**, 242–246 (2016) (cit. on p. 2).
25. Jöns, K. D., Schweickert, L., Versteegh, M. A., *et al.* Bright nanoscale source of deterministic entangled photon pairs violating Bell's inequality. *Scientific reports* **7**, 1700 (2017) (cit. on p. 2).
26. Rosenfeld, W., Burchardt, D., Garthoff, R., *et al.* Event-ready Bell test using entangled atoms simultaneously closing detection and locality loopholes. *Phys. Rev. Lett.* **119**, 010402 (2017) (cit. on pp. 2, 4).
27. Collaboration, B. B. T. *et al.* Challenging local realism with human choices. *Nature* **557**, 212 (2018) (cit. on p. 2).
28. Zopf, M., Keil, R., Chen, Y., *et al.* Entanglement swapping with semiconductor-generated photons violates Bell's inequality. *Physical review letters* **123**, 160502 (2019) (cit. on p. 2).
29. Zhong, Y., Chang, H.-S., Satzinger, K., *et al.* Violating Bell's inequality with remotely connected superconducting qubits. *Nature Physics* **15**, 741–744 (2019) (cit. on p. 2).
30. Liu, Z.-H., Meng, H.-X., Xu, Z.-P., *et al.* Experimental observation of quantum contextuality beyond Bell nonlocality. *Physical Review A* **100**, 042118 (2019) (cit. on p. 2).
31. Proietti, M., Pickston, A., Graffitti, F., *et al.* Experimental test of local observer independence. *Science advances* **5**, eaaw9832 (2019) (cit. on pp. 2, 3).
32. Paneru, D., Te'eni, A., Peled, B. Y., *et al.* Experimental tests of multiplicative Bell inequalities and the fundamental role of local correlations. *Phys. Rev. Res* **3**, L012025 (2021) (cit. on p. 2).
33. Qu, D., Wang, K., Xiao, L., Zhan, X. & Xue, P. State-independent test of quantum contextuality with either single photons or coherent light. *npj Quantum Information* **7**, 154 (2021) (cit. on p. 2).

34. Ru, S., Tang, W., Wang, Y., *et al.* Verification of Kochen-Specker-type quantum contextuality with a single photon. *Physical Review A* **105**, 012428 (2022) (cit. on p. 2).
35. Cirel'son, B. S. Quantum generalizations of Bell's inequality. *Letters in Mathematical Physics* **4**, 93–100 (1980) (cit. on p. 2).
36. Popescu, S. & Rohrlich, D. Quantum nonlocality as an axiom. *Foundations of Physics* **24**, 379–385 (1994) (cit. on pp. 2, 85).
37. De Muynck, W. M. & Martens, H. Joint measurement of incompatible observables and the bell inequalities. *Physics Letters A* **142**, 187–190 (1989) (cit. on p. 2).
38. Andersson, E., Barnett, S. M. & Aspect, A. Joint measurements of spin, operational locality, and uncertainty. *Phys. Rev. A* **72**, 042104 (4 2005) (cit. on p. 2).
39. Banik, M., Gazi, M. R., Ghosh, S. & Kar, G. Degree of complementarity determines the nonlocality in quantum mechanics. *Phys. Rev. A* **87**, 052125 (5 2013) (cit. on p. 2).
40. Bene, E. & Vértesi, T. Measurement incompatibility does not give rise to Bell violation in general. *New Journal of Physics* **20**, 013021 (2018) (cit. on p. 2).
41. Hofmann, H. F. Local measurement uncertainties impose a limit on nonlocal quantum correlations. *Phys. Rev. A* **100**, 012123 (1 2019) (cit. on p. 2).
42. Shi, B.-S. & Tomita, A. Generation of a pulsed polarization entangled photon pair using a Sagnac interferometer. *Phys. Rev. A* **69**, 013803 (1 2004) (cit. on pp. 2, 11).
43. Kim, T., Fiorentino, M. & Wong, F. N. Phase-stable source of polarization-entangled photons using a polarization Sagnac interferometer. *Physical Review A* **73**, 012316 (2006) (cit. on pp. 2, 11).
44. Wong, F., Shapiro, J. & Kim, T. Efficient generation of polarization-entangled photons in a nonlinear crystal. *Laser physics* **16**, 1517–1524 (2006) (cit. on pp. 2, 11).
45. Lee, S. M., Kim, H., Cha, M. & Moon, H. S. Polarization-entangled photon-pair source obtained via type-II non-collinear SPDC process with PPKTP crystal. *Optics express* **24**, 2941–2953 (2016) (cit. on pp. 2, 11).
46. Aharonov, Y & Vaidman, L. Complete description of a quantum system at a given time. *Journal of Physics A: Mathematical and General* **24**, 2315 (1991) (cit. on p. 3).
47. Ravon, T. & Vaidman, L. The three-box paradox revisited. *Journal of Physics A: Mathematical and Theoretical* **40**, 2873 (2007) (cit. on p. 3).
48. Greenberger, D. M., Horne, M. A., Shimony, A. & Zeilinger, A. Bell's theorem without inequalities. *American Journal of Physics* **58**, 1131–1143 (1990) (cit. on pp. 3, 97).
49. Hardy, L. Quantum mechanics, local realistic theories, and Lorentz-invariant realistic theories. *Phys. Rev. Lett.* **68**, 2981–2984 (20 1992) (cit. on p. 3).
50. Hardy, L. Nonlocality for two particles without inequalities for almost all entangled states. *Phys. Rev. Lett.* **71**, 1665–1668 (11 1993) (cit. on p. 3).
51. Irvine, W. T. M., Hodelin, J. F., Simon, C. & Bouwmeester, D. Realization of Hardy's Thought Experiment with Photons. *Phys. Rev. Lett.* **95**, 030401 (3 2005) (cit. on p. 3).
52. Torgerson, J. R., Branning, D., Monken, C. H. & Mandel, L. Experimental demonstration of the violation of local realism without Bell inequalities. *Physics Letters A* **204**, 323–328 (1995) (cit. on p. 3).
53. Boschi, D, De Martini, F & Di Giuseppe, G. Test of the violation of local realism in quantum mechanics without Bell inequalities. *Physics Letters A* **228**, 208–214 (1997) (cit. on p. 3).

54. Boschi, D., Branca, S, De Martini, F. & Hardy, L. Ladder proof of nonlocality without inequalities: Theoretical and experimental results. *Physical review letters* **79**, 2755 (1997) (cit. on pp. [3](#), [74](#)).
55. Pan, J.-W., Bouwmeester, D., Daniell, M., Weinfurter, H. & Zeilinger, A. Experimental test of quantum nonlocality in three-photon Greenberger–Horne–Zeilinger entanglement. *Nature* **403**, 515–519 (2000) (cit. on pp. [3](#), [98](#)).
56. Frauchiger, D. & Renner, R. Quantum theory cannot consistently describe the use of itself. *Nature communications* **9**, 1–10 (2018) (cit. on pp. [3](#), [9](#)).
57. Wigner, E. P. in *Philosophical reflections and syntheses* 247–260 (Springer, 1995) (cit. on p. [3](#)).
58. Deutsch, D. Quantum theory as a universal physical theory. *International Journal as a universal physical theory*, 1–41 (1 1985) (cit. on p. [3](#)).
59. Bell, J. S. On the problem of hidden variables in quantum mechanics. *Reviews of Modern physics* **38**, 447 (1966) (cit. on p. [3](#)).
60. Kochen, S. & Specker, E. P. in *The logico-algebraic approach to quantum mechanics* 293–328 (Springer, 1975) (cit. on p. [3](#)).
61. Ji, M. & Hofmann, H. F. Characterization of the nonclassical relation between measurement outcomes represented by nonorthogonal quantum states. *Phys. Rev. A* **107**, 022208 (2 2023) (cit. on pp. [4](#), [10](#)).
62. Englert, B.-G. Fringe visibility and which-way information: An inequality. *Phys. Rev. Lett.* **77**, 2154 (1996) (cit. on p. [7](#)).
63. Iinuma, M., Suzuki, Y., Taguchi, G., Kadoya, Y. & Hofmann, H. F. Weak measurement of photon polarization by back-action-induced path interference. *New J. Phys.* **13**, 033041 (2011) (cit. on p. [7](#)).
64. Kinoshita, R. *Development of photon pairs source having quantum correlations* 2015 (cit. on p. [13](#)).
65. Schrödinger, E. Discussion of Probability Relations between Separated Systems. *Mathematical Proceedings of the Cambridge Philosophical Society* **31**, 555–563 (1935) (cit. on p. [25](#)).
66. Schrödinger, E. Probability relations between separated systems. *Mathematical Proceedings of the Cambridge Philosophical Society* **32**, 446–452 (1936) (cit. on p. [25](#)).
67. Wiseman, H. M., Jones, S. J. & Doherty, A. C. Steering, entanglement, nonlocality, and the Einstein-Podolsky-Rosen paradox. *Physical review letters* **98**, 140402 (2007) (cit. on p. [25](#)).
68. Iinuma, M., Nakano, M., Hofmann, H. F. & Suzuki, Y. Experimental evaluation of the nonclassical relation between measurement errors using entangled photon pairs as a probe. *Phys. Rev. A* **98**, 062109 (6 2018) (cit. on p. [57](#)).
69. Matsuyama, K., Hofmann, H. F. & Iinuma, M. Experimental investigation of the relation between measurement uncertainties and non-local quantum correlations. *Journal of Physics Communications* **5**, 115012 (2021) (cit. on p. [76](#)).
70. Matsuyama, K., Ji, M., Hofmann, H. F. & Iinuma, M. Quantum contextuality of complementary photon polarizations explored by adaptive input state control. *arXiv preprint arXiv:2306.06831* (2023) (cit. on p. [77](#)).
71. Neumann, J. V. *Mathematical Foundations of Quantum Mechanics* (Princeton Univ. Press, 1955) (cit. on p. [89](#)).

72. Hardy, L. Quantum mechanics, local realistic theories, and Lorentz-invariant realistic theories. *Physical Review Letters* **68**, 2981 (1992) (cit. on p. 99).
73. Louisell, W. H., Yariv, A. & Siegman, A. E. Quantum Fluctuations and Noise in Parametric Processes. I. *Phys. Rev.* **124**, 1646–1654 (6 1961) (cit. on p. 151).
74. Gordon, J. P., Louisell, W. H. & Walker, L. R. Quantum Fluctuations and Noise in Parametric Processes. II. *Phys. Rev.* **129**, 481–485 (1 1963) (cit. on p. 151).
75. Wagner, W. G. & Hellwarth, R. W. Quantum Noise in a Parametric Amplifier with Lossy Modes. *Phys. Rev.* **133**, A915–A920 (4A 1964) (cit. on p. 151).
76. Harris, S. E., Oshman, M. K. & Byer, R. L. Observation of Tunable Optical Parametric Fluorescence. *Phys. Rev. Lett.* **18**, 732–734 (18 1967) (cit. on p. 151).
77. Brown, R. H. & Twiss, R. Q. Correlation between photons in two coherent beams of light. *Nature* **177**, 27–29 (1956) (cit. on p. 169).
78. Clauser, J. F. Experimental distinction between the quantum and classical field-theoretic predictions for the photoelectric effect. *Phys. Rev. D* **9**, 853–860 (4 1974) (cit. on p. 169).
79. Grangier, P., Roger, G. & Aspect, A. Experimental Evidence for a Photon Anticorrelation Effect on a Beam Splitter: A New Light on Single-Photon Interferences. *Europhysics Letters* **1**, 173 (1986) (cit. on p. 169).